The Impact of In-Cylinder Conditions on a Turbocharged Gasoline Pre-Chamber Ignited Engine

Priyadarshi Sahu

School of Engineering

London South Bank University

A thesis submitted in partial fulfilment of the requirements for the degree of Doctor of Philosophy.

June 2020

Acknowledgements

I would like to thank:

Dr Mark Ellis and Prof Marouan Nazha for giving me the opportunity to work on this project and for their supervision- providing expert technical guidance and out of the box thinking throughout the research project.

Advanced Engine Research Ltd for supporting and funding this research project.

AVL, Gamma Technologies and Convergent Science for providing simulation and analysis software and technical support throughout the research project.

Muhammed Fayaz, my colleague and a friend who contributed to endless discussions that helped shape this research project.

My colleagues- Dr Zoe De Grussa, Dr Antigoni Paspali, Harriet Cavanagh, Dr Ertan Siddiqui, Dr Tara Singh Ghatauray, Dr Hasan Zabihi, Dr Ridouan Chaouki, Dr Ousmane Oumar, Dr Linghao Zhao, Dr Kwame Sarkodie and Dr Nura Makawashi for providing necessary distractions in our office.

Graham Bird, Paul Elsdon and Mehdi Zahir for their help and contributions in setting up the engine test facility at the university.

My mother, Mamata Sahu, and father, Pradyumna Sahu for their continuous support and for always encouraging me to new heights.

Abstract

Turbulent Jet Ignition is a novel ignition technology that has demonstrated high thermal efficiency, especially at full loads, for lean burn IC engine applications. This technology has been extensively utilised in high speed motorsport engines such as Formula 1 and LMP1 where fuel flow rate is restricted thus driving motorsport engine manufacturers to improve fuel conversion efficiency making turbulent jet ignition technology very attractive for motorsport application. Thermal efficiency figures of over 50% have been claimed by certain Formula 1 engine manufacturers, however, the products of R&D are seldom publicised which make it difficult for novel technologies to enter the passenger car industry where improving fuel efficiency is critical to reduce global tailpipe emissions to protect the environment.

Over the years, numerous researchers have studied the turbulent jet ignition system however limited knowledge exists on the impact of in-cylinder conditions on the jet ignition system. This research focuses on studying the impact of in cylinder flow via port design, piston crown shapes and studying the impact of compression ratio and backpressure on a pre-chamber ignition system on a turbocharged lean burn high speed gasoline powered motorsport engine operated at full load conditions. Research findings include discovery of positive impact of tumble flow on main-chamber combustion processes, a novel piston crown design which assists combustion processes via pre-chamber enrichment and enhancing main-chamber tumble flow. A positive impact of increasing compression ratio and the diminishing effect of increasing residual concentration on combustion have been discussed.

Abbreviations

AMR	Adaptive Mesh Refinement
ATDC	After Top Dead Centre
BMEP	Brake Mean Effective Pressure
BSFC	Brake Specific Fuel Consumption
BTDC	Before Top Dead Centre
CA	Crank Angle
CAD	Crank Angle Degree
CFD	Computational Fluid Dynamics
COV	Coefficient of Variation
CW	Counterweight
DI	Direct Injection
EGR	Exhaust Gas Recirculation
GDI	Gasoline Direct Injection
HC	Hydrocarbons
HRR	Heat Release Rate
IC	Internal Combustion
IHRR	Integrated Heat Release Rate
IMEP	Indicated Mean Effective Pressure

ISFC	Indicated Specific Fuel Consumption
LES	Large Eddy Simulation
MAPO	Maximum Amplitude of Pressure Oscillations
MBT	Minimum Advance for Best Torque
MFB	Mass Fraction Burned
PFI	Port Fuel Injection
PRF	Primary Reference Fuel
RANS	Reynolds Averaged Navier Stokes
RCM	Rapid Compression Machine
RNG	Renormalization Group
rpm	Revolutions per Minute
SCE	Single Cylinder Engine
SI	Spark Ignition
TDC	Top Dead Centre
TJI	Turbulent Jet Ignition
TKE	Turbulent Kinetic Energy
TPS	Throttle Position
WOT	Wide Open Throttle

List of Figures

List of Tables

Table of Contents

1. Introduction

Internal combustion engines currently power at least 97% of automobiles in the world either in standalone form or coupled with hybrid technology. Electrification of automobiles is often cited as the ultimate solution to reduce emissions and protect the environment. However, electric vehicles are far from perfect in their current form.

Production of electric cars are known to use a lot of energy. The emissions generated during the production of an electric car has been known to be far higher than a conventional car (EDF Energy, 2019). This is due to the manufacture of lithium ion batteries and utilisation of neodymium magnets for electric motors which form the essential parts of an electric car, where both lithium and neodymium are rare earth metals. Currently more than a third of the CO_2 emissions from an electric car, during its lifetime, comes from the energy used to make the car itself (EDF Energy, 2019). The general expectation is that with advancing technology and more efficient manufacturing techniques, the amount of emissions created during the production of batteries and motors would reduce. However, due to a lack of range, infrastructure for charging electric vehicles and high manufacturing costs – electric vehicles are still far from attractive for the average consumer in their current form and thus IC engines are expected to power automobiles for the foreseeable future. Thus, it is imperative to continue research on improving the thermal efficiency of IC engines which would lead to lower fuel consumptions and thus lower CO_2 emissions.

At present, the development of direct injection spark-ignition (SI) engines focuses on downsizing, with the reduction in engine displacement and the use of turbo-charging to give better control of the air flow over the full power range, as a means of improving efficiency. Lean combustion is an increasingly explored method as it has shown an increase in net thermal efficiency in IC engines when operating at lambda values greater than 1.5 (Bunce et al., 2014).

Downsized spark ignition engines are characterized by high efficiencies but favour abnormal combustions like pre-ignition and knocking. Pre-ignition and heavy knocking limits the maximum load of SI engines and thus the scale of downsizing (Kalghatgi and Bradley, 2012).

Turbo-charging and direct injection coupled with lean burn technology hold the potential of enhanced power density and fuel consumption in the development of gasoline engines, however inherent issues such as pre-ignition and heavy knocking will have to be drastically reduced to unlock the full potential of this technology.

The current peak brake thermal efficiency of the best light duty gasoline engines in production utilised in passenger cars is around 40% (Joshi, 2020). Motorsport engines such as Formula 1 engines are known to possess a full load brake thermal efficiency greater than 50% (Mercedes AMG HPP, 2017).

The higher efficiency of the motorsport engine at full load when compared with a passenger road car engine is achieved by extreme downsizing which is known to reduce frictional and thermal losses. Operating the motorsport engine in lean conditions at high engine speeds contributes towards improving

the cycle thermal efficiency, extends knock limits due to exposing the end gas to a shorter residence time and results in faster combustion due to high turbulence at high engine speeds. The cycle thermal efficiency is also further improved by utilising a high compression ratio combustion chamber.

As strongly charge-diluted combustion presents a challenge for a conventional spark ignited engine due to high flow velocities which has the ability to extinguish the flame kernel and the higher ignition energy required to breakdown the increasing dielectric strength of the fluid - a consequence of downsizing of engines, alternative ignition systems were researched upon to find the ideal ignition system. One such ignition system that has shown potential is the pre-chamber jet ignition technology which has been proven to reduce fuel consumption, increase knock limits and extend lean combustion limits (Attard et al., 2010).

The pre-chamber ignition system is also known to significantly reduce CO_2 emissions due to a reduced fuel consumption. Joshi (2020), in his review of current vehicle engine efficiency and emissions had shown that the pre-chamber concepts tested have shown a reduction of CO_2 by 20% compared to a normal turbocharged GDI stoichiometric burn engine ignited by spark ignition system.

In-cylinder conditions such as flow motion, charge temperature, exhaust gas recirculation of a gasoline engine - over the years, have been optimised for a spark plug based ignition system where the combustion chamber was developed to support spark ignited combustion processes. However, little

research has been done to study and quantify the impact of in-cylinder conditions on the combustion processes for a pre-chamber ignited engine.

As the pre-chamber ignition system is at its nascent stages in research, this research aims to study various in-cylinder parameters that affect a pre-chamber ignitor's performance to address the current gaps in current literature.

2. Literature Review

2.1 Lean Burn Technology

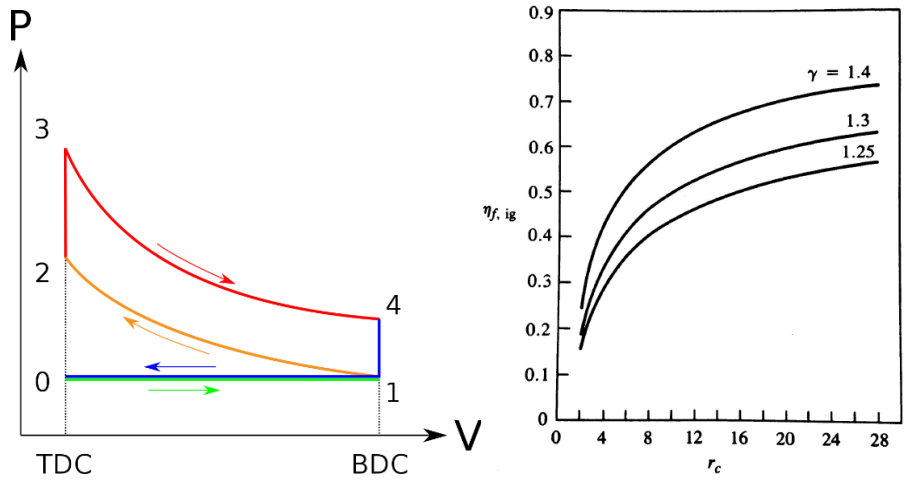

Figure 2-1 Pressure-Volume Diagram of Otto Cycle (Left) and Otto Cycle Fuel Conversion Efficiency as a Function of Compression Ratio (Right)

As a spark ignited gasoline engine is governed by the Otto cycle, engine fuel conversion efficiency depends on compression ratio and specific heat ratio of the fluid as shown in equation 2-1.

$$\eta_{th} = 1 - \frac{1}{r_c^{\gamma-1}} \qquad \text{Eqn (2-1)}$$

Where η_{th} = indicated fuel conversion efficiency

r_c = compression ratio

γ = specific heat ratio

Increasing the compression ratio and specific heat ratio results in increasing the fuel conversion efficiency. As the charge air mixture becomes leaner – the specific heat ratio increases due to higher stoichiometric air to fuel ratio coupled with low temperature combustion. However, the major limitations in implementing lean and ultra-lean combustion systems are large cyclic

variations due to unreliable ignition of the air-fuel mixture in some cycles and long combustion durations due to decreased flame speeds. Misfiring also results in very high HC emissions (Swamy et al., 2001). To counter misfires, numerous higher-energy ignition sources have been researched on such as pre-chamber ignition, laser ignition, plasma jet igniters, rail plugs. There is, however, still more work to be done for these ignition methodologies to be commercially viable.

2.2 Alternative Ignition Methods

Many methods for initiating combustion in spark-ignition engines with electrical discharges, have been proposed and examined over the years. These include different designs of spark plug, use of more than one plug, utilisation of higher power, higher energy, or longer-duration discharges, and ignition systems that initiate the main combustion process with a high-temperature reacting jet, plasma-jet and flame-jet ignition systems.

Conventional ignition systems normally ignite the unburned fuel, air, burned gas mixture within the cylinder and perform satisfactorily under stoichiometric conditions but struggle to perform under lean conditions. This is because conventional ignition systems, such as spark plugs, when igniting a lean mixture in a combustion chamber, results in slower flame speeds thus having an increased chance of misfiring and/or detonation. Thus, the alternative ignition approaches have the goal of extending the engine stability limit and/or of reducing the cyclic combustion variability, usually by achieving a faster initial burning rate compared to conventional ignition systems (Heywood, 1988).

Using gasoline in a compression ignition engine has the capability to be as efficient as a diesel engine. However, the inherent resistance of gasoline to autoignition presents a challenge to sustain low load operation (Joshi, 2020). Various approaches have been pursued in recent times to overcome some of the challenges such as the use of spark ignition to assist the compression ignition process in Mazda's Skyactiv-X engine. The engine relies on a Mazda-patented technology called Spark Controlled Compression Ignition (SPCCI) where a lean mix of fuel and air are compressed to a high pressure. The spark ignition system then ignites a very small, dense amount of fuel, which further raises the heat and pressure in the cylinder, causing the remaining fuel to ignite under pressure which results in faster and more efficient combustion process compared to a normal spark ignited engine. (Mazda, 2019)

However, Mazda have noted that when a higher load is applied on the engine, the engine switches to normal spark ignition mode due to the inherent issues in controlling the combustion process in a gasoline compression engine.

Novel combustion methods such as the pre-chamber ignition system for lean combustion has also demonstrated benefits at part load and especially at high load towards knock limit extension, increased thermal efficiency and reduced NOx emissions due to cold gas temperatures associated with combustion with high levels of dilution and multiple ignition sites in the combustion chamber (Attard and Blaxill, 2012).

2.3 Pre-chamber Ignition System

A pre-chamber ignition system is an alternative approach to ignite lean mixtures in the combustion chamber. The pre-chamber ignition system is a strategy that utilizes a standard spark to initiate combustion, which has two separate combustion chambers connected to each other by one or more small passageways. The passages are usually cylindrical orifices which are also termed as nozzles. The larger of the two chambers is called the main chamber while the smaller of the two is designated as the pre-chamber. The pre-chamber surrounds a spark plug - where the combustion is first initiated. The hot turbulent jet is generated by burning a small quantity of stoichiometric or near-stoichiometric fuel/air mixture in the pre-chamber. The higher pressure resulting from pre-chamber combustion pushes the combustion products into the main chamber in the form of a hot turbulent jet, which then ignites the main chamber contents. The hot jet has a much larger surface area, compared to a flame kernel generated in case of a conventional spark plug, leading to multiple ignition sites on its surface which can enhance the probability of successful ignition and cause faster flame propagation and heat release (Attard and Blaxill, 2012; Biswas, 2018).

There are two modes via which the pre-chamber ignition system ignites the main-chamber contents.

1. Flame Ignition (Ignition by a Reacting Jet) Mechanism

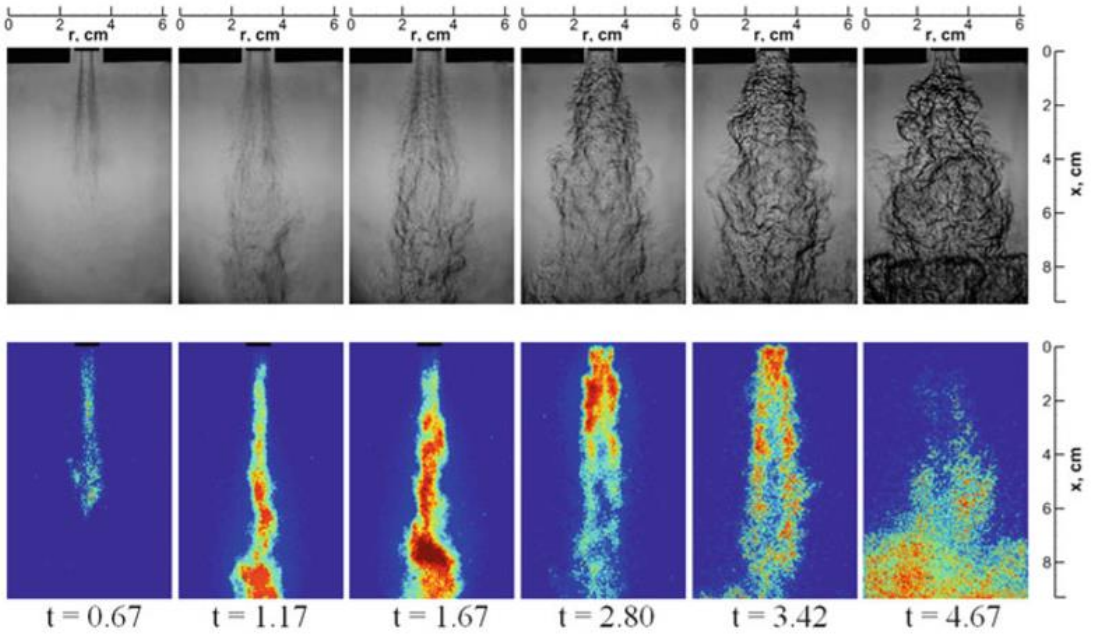

Figure 2-2 Time Sequence of Simultaneous Schlieren (Top) and OH* Chemiluminescence (Bottom) Images Showing flame Ignition Process for CH4/air with Test Conditions - $V_{pre\text{-}chamber}$ = 100 cc, $d_{orifice}$ = 4.5 mm, $P_{initial}$ = 0.4 MPa, $T_{initial}$ = 500 K, $\phi_{pre\text{-}chamber}$ = 1.0, $\phi_{main\text{-}chamber}$ = 0.9, ignition delay = 2.80 ms (Biswas, 2018)

In flame ignition mode, the hot jet contains remnants of the pre-chamber flame. This occurs due to the pre-chamber flame not being quenched by the wall heat loss and high stretch rate through the orifice. The flame that passes through the orifice can be either laminar or turbulent which depends on the pre-chamber pressure, temperature, equivalence ratio, and orifice diameter. The small turbulent flames contained by the hot jet penetrates into the main chamber causing an instantaneous ignition of the main chamber contents. (Biswas, 2018)

2. Jet Ignition (Ignition by a Reacted Jet) Mechanism

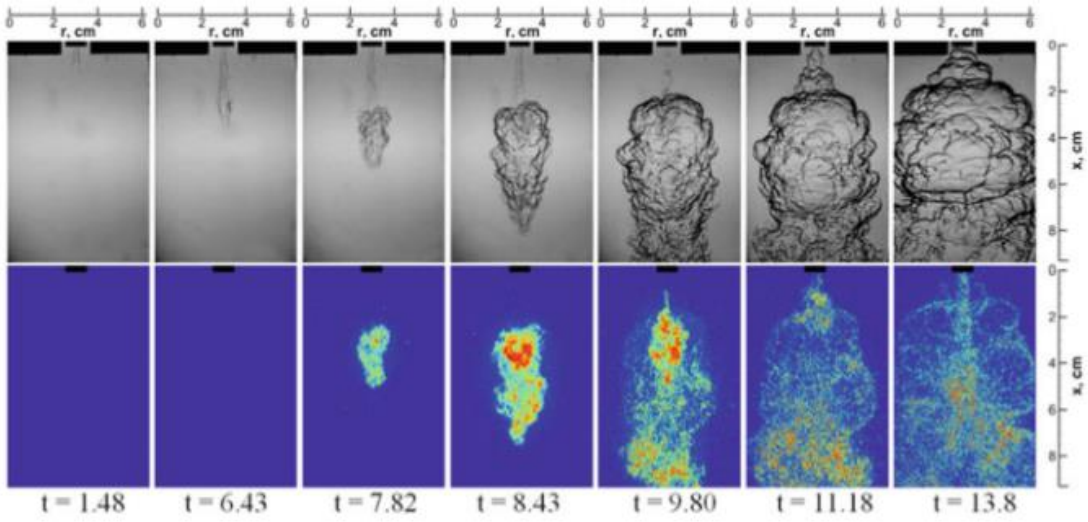

Figure 2-3 Time Sequence of Simultaneous Schlieren (Top) and OH* Chemiluminescence (Bottom) Images Showing Jet Ignition Process for CH4/air with Test Conditions - $v_{pre\text{-}chamber}$ = 100 cc, $d_{orifice}$ = 4.5 mm, $P_{initial}$ = 0.1 MPa, $T_{initial}$ = 500 K, $\phi_{pre\text{-}chamber}$ = 1.0, $\phi_{main\text{-}chamber}$ = 0.8, ignition delay = 7.82 ms (Biswas, 2018)

In jet ignition mode, the hot jet coming from the pre-chamber contains hot combustion products only. This means the pre-chamber flame had been extinguished while passing through the orifice due to heat loss and/or high stretch rate. Because the jet contained very little or no radicals, OH* signal was not detected immediately at the orifice exit as shown in Figure 2-3 (Biswas, 2018). Biswas (2018) also observed in his experiments that as the hot jet penetrated into the main chamber, the jet surface contained many small eddies. These eddies helped to mix the hot jet with the cold, unburned fuel/air mixture in the main chamber. The temperature of the hot jet dropped during the penetrating process as turbulent eddies dissipated energy. If the jet temperature dropped too rapidly, main chamber ignition was not possible. The competition between the turbulent mixing time scale (τ_F) and the chemical timescale (τ_C), which was characterized by the Damköhler number (Da), as shown in Eqn 2-2, had a deterministic effect on the ignition outcome.

$$Da = \frac{\tau_F}{\tau_C} \qquad \text{Eqn (2-2)}$$

The hot jet produced by the turbulent jet ignition (TJI) system was found to have two effects on the combustion in the main chamber. First, the generation of turbulence produced by the shear of the jet flow increased flame propagation speeds. Second, the jet distributed hot gases over a wide region in the main chamber which generated dispersed ignition throughout the chamber at the vicinity of the jets. As a result of these two effects, the TJI system was found to be well suited to mitigate the negative effects of the slower flame speeds associated with lean mixtures. Thus, TJI was found to have the potential to facilitate lean operation of an SI engine beyond what could be achieved with a standard spark plug. Also, the division of the combustion system into separate chambers facilitates mixture stratification. In some applications, additional fuel may be added to the pre-chamber to create a rich mixture within the small volume. The rich mixture is easy to ignite reliably and produces strong combustion in the pre-chamber, but the overall λ of the entire system is kept lean since the bulk of the gas in the system is contained in the still very lean main chamber leading to higher thermal efficiencies (Attard and Blaxill, 2012).

Pre-chamber ignition systems are classified as active or passive pre-chamber ignition systems based on the presence or absence of an auxiliary fuelling system for the pre-chamber. Active pre-chamber systems are characterized by an additional fuel injector attached to the pre-chamber, usually DI, in addition to the main chamber fuel injection. As the volume of pre-chamber is small compared to the main chamber volume, a small quantity of fuel provides a rich region around the spark, thus increasing the stability and reliability of

ignition and combustion process. During compression stroke, the lean mixture formed in main chamber is forced into the pre-chamber via nozzles, where the mixture is further enriched with a low flow fuel injector. The purpose of this method is to benefit the combustion process by creating regions with different air-fuel ratios with the main combustion chamber being lean, and the pre-chamber being richer. The active pre-chamber systems are however difficult to package in the limited space available in the engine head due to the additional low flow fuel injector next to the spark plug for pre-chamber fuelling when compared to the passive pre-chamber systems.

In a passive system, fuel injection occurs only in the main chamber, using either port fuel injection (PFI) or direct injection (DI) where the air-fuel mixture enters the pre-chamber via orifices or nozzles from the main chamber only as there is no additional fuel added into the pre-chamber due to the absence of additional fuel injector when compared with the active pre-chamber ignition system. In PFI engines, the relative air/fuel ratio is nearly the same in both chambers, whereas in GDI engines, the differences in relative air/fuel ratio between chambers can be indirectly induced by utilising stratified-charge operation using wall-guided, air-guided and spray-guided techniques. (Spicher and Heidenreich, 2009; Benajes et al., 2019)

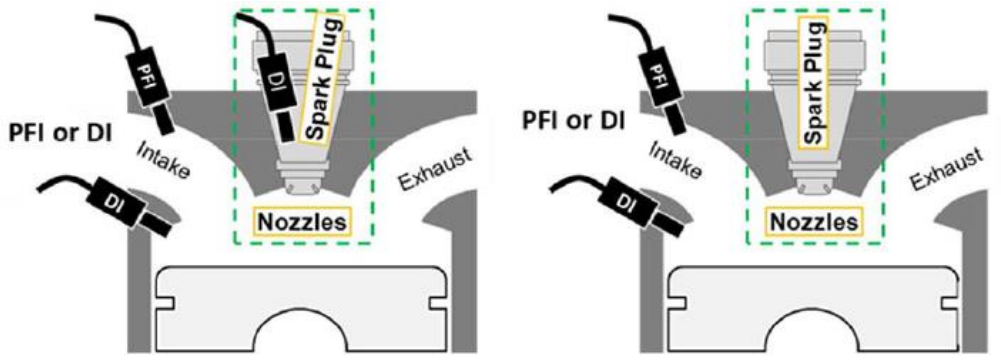

Figure 2-4 Active and Passive Pre-chamber Configurations (Cooper et al., 2020)

2.4 Influence of Pre-Chamber Ignition System on Combustion

Various studies carried out by Robinet et al. (1999), Ayala (2006), Uyehara (1995), Hynes (1986), Toulson et al. (2007) found that the main problems of working with lean mixtures is low energy provision at the start of combustion and low flame propagation speed. Use of pre-chamber ignition systems has shown improvement in lean combustion ignition due to the greater amount of energy available in the main chamber at start of combustion. Increase in available energy for mixture ignition affects the lean limit, the spark timing, start of combustion, flame propagation speed and heat release rate. The essential combustion parameters are discussed below.

2.4.1 Lean limit and Combustion Stability

Anderson et al. (2013) compared the performance of a turbocharged Rotax 914 aircraft engine with a conventional spark and an unfuelled pre-chamber ignitor at full load. Engine performance results indicated that the combustion stability was improved as the pre-chamber ignition system demonstrated a lower COV of gross IMEP, which was calculated using the ratio of standard deviation of IMEP and mean IMEP, for a higher net IMEP when compared with the spark ignition case as shown in Figure 2-5 and 2-6.

COV of gross IMEP were recorded to be generally less than 1% across the speed range. Some slight improvements in combustion stability was observed with the pre-chamber jet igniter which the author credits to the improved flame initiation associated with the propagating jets and hence the reduced dependence on the flame kernel initiation and development as in conventional

spark ignition combustion. The author states that the combustion stability results also highlight significant capability for combustion phasing retard for further knock mitigation for the pre-chamber system (Anderson et al., 2013).

At the jet ignition maximum load of ~17 bar net IMEP, a 0.6% COV of gross IMEP was observed at 4500 rpm, demonstrating that the higher loads are attainable with the pre-chamber ignition system. With a COV of gross IMEP at less than 1% at the maximum engine speed of 5500 rpm the pre-chamber ignition system demonstrated that combustion stability at higher speeds are attainable for the jet ignition combustion system. (Anderson et al., 2013)

Attard et al. (2010) also tested a fuelled pre-chamber ignitor in a naturally aspirated single cylinder engine at full load at 1500 rpm. A clear extension of lean limit was observed via a lower COV of gross IMEP and a higher thermal efficiency for the pre-chamber ignition case compared to spark ignition case as shown in Figure 2-7.

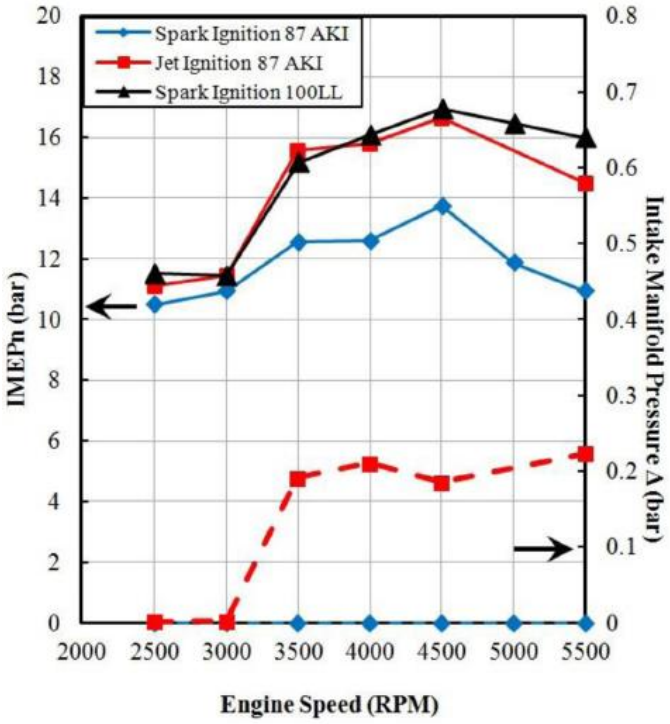

Figure 2-5 Boosted maximum load (IMEPn) and resultant changes in boost pressure for spark ignition (blue) and jet ignition (red) combustion operating on unleaded 87 AKI gasoline. Results for the spark ignition OEM engine operating on 100 LL Avgas (black) are also shown as a baseline target for performance. (Load limited by boost or knock limits at MBT combustion phasing, 49°C intake temperature, Φ=1.0) (Anderson et al., 2013)

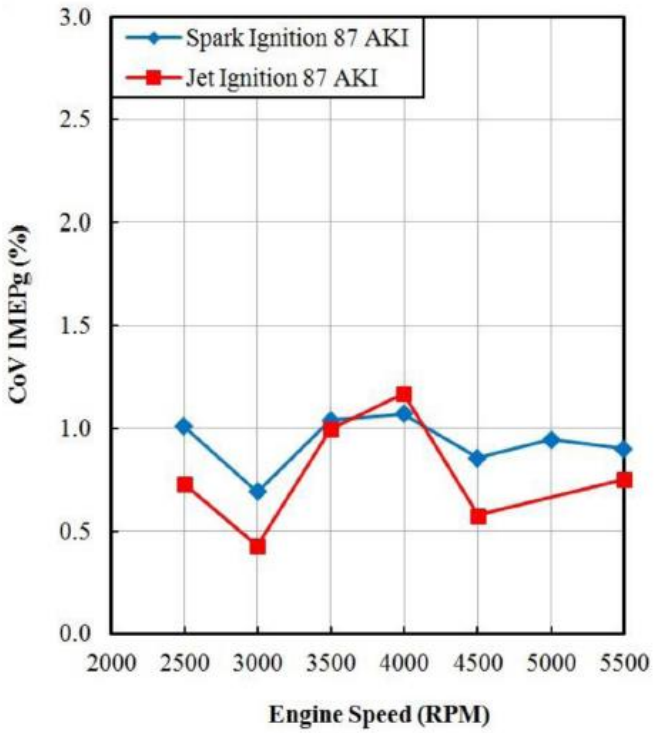

Figure 2-6 CoV IMEPg across maximum boosted loads for spark ignition and jet ignition combustion using 87 AKI unleaded gasoline (49°C intake temperature, Φ=1.0) (Anderson et al., 2013)

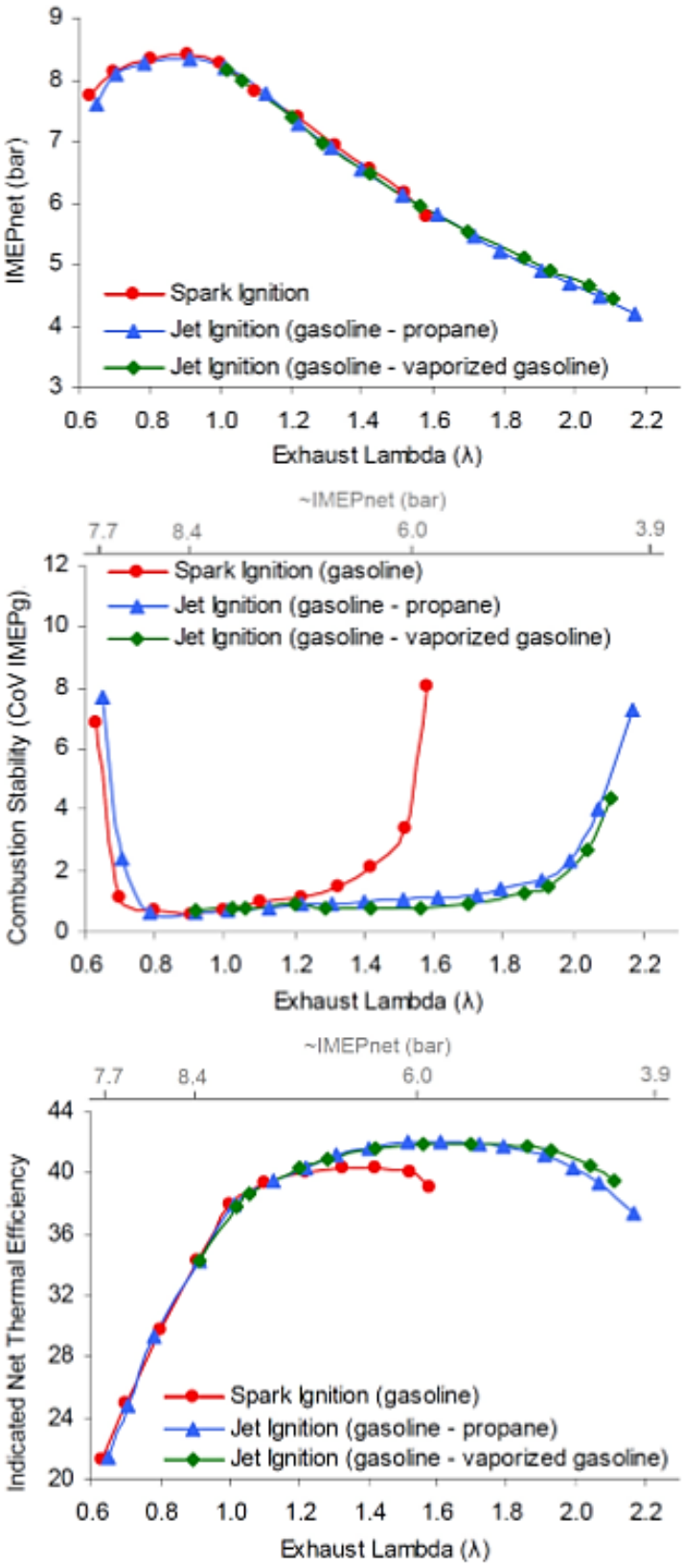

Figure 2-7 IMEP and thermal efficiency comparisons of spark ignition (gasoline), jet ignition dual fuel (gasoline - propane) and jet ignition sole fuel (gasoline - vaporized gasoline) combustion systems. 1500 rev/min, unthrottled (~ 98 kPa MAP), varying load due to dilution variations, (main chamber fuel - pre chamber fuel) (Attard et al., 2010)

2.4.2 Ignition Delay

A pre-chamber ignition system was studied by Robinet et al. (1999) to compare the operation of a baseline SI engine and a system with APIR (fuelled pre-chamber ignition) device. Figure 2-8 shows the section of the APIR with 4 pre-chamber nozzles.

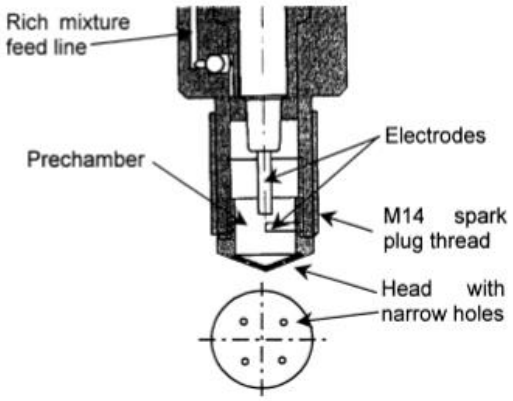

Figure 2-8 Section of the APIR Device & Top-View of the Head (Robinet et al., 1999)

Figure 2-9 shows an optimization of spark timing for a conventional engine and an engine with a pre-chamber ignition system or APIR. For MBT condition, the conventional engine has a spark timing of 32 deg BTDC whereas the APIR engine has a spark timing of 10 deg BTDC for the same MBT condition which indicates a shorter ignition delay for the APIR device due to distributed ignition sites.

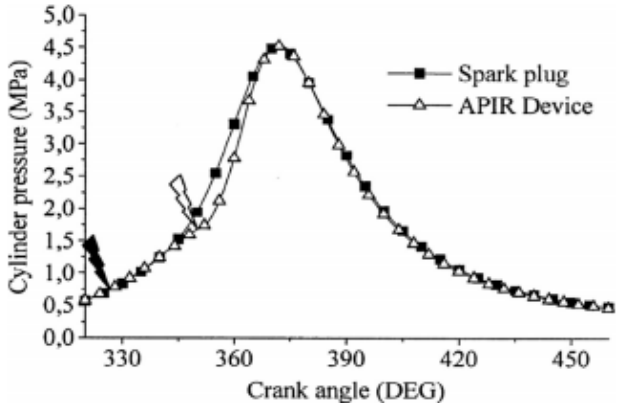

Figure 2-9 Spark Timing of Conventional and APIR (Passive Pre-chamber Ignition) engine for Same MBT Condition (Robinet et al., 1999)

Gentz et al. (2015) compared 0–10% burn rate or ignition delay of a baseline propane fuelled SI engine with TJI system in a Rapid Compression Machine (RCM) in their experiment where the pre-chamber was unfuelled. It was observed that for a SI engine the propagation of burned fraction was slower than almost all TJI tested cases, indicating that TJI improved the start of combustion. In one case where λ = 1.65 and nozzle diameter was 3mm, the TJI system had its 0–10% burn duration longer than SI system. According to the author poor fuel enrichment and consequently the reduction in jet speed and combustion instability were the causes for the longer delay in ignition in the TJI system for the nozzle diameter of 3mm.

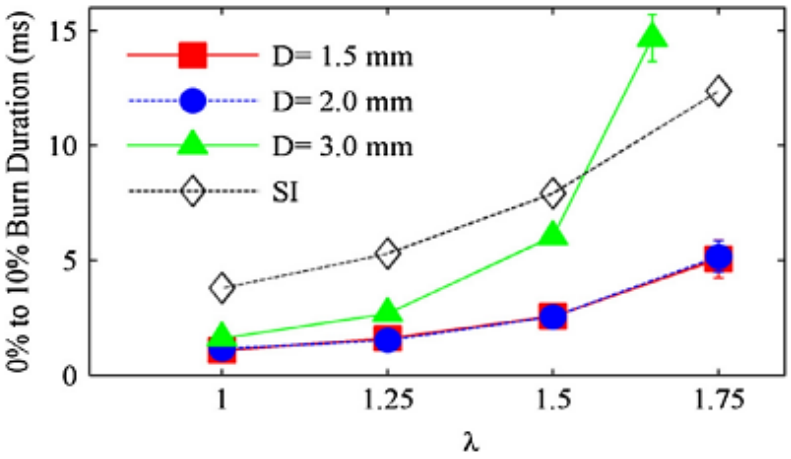

Figure 2-10 Variation in 0-10% Burn Duration vs λ for Various Nozzle Diameters and SI Engine (Gentz et al., 2015)

2.4.3 Flame propagation speed

Gentz et al. (2015) compared the 10%-90% burn duration of a baseline propane fuelled SI engine with an unfuelled pre-chamber with different nozzle diameters in an RCM.

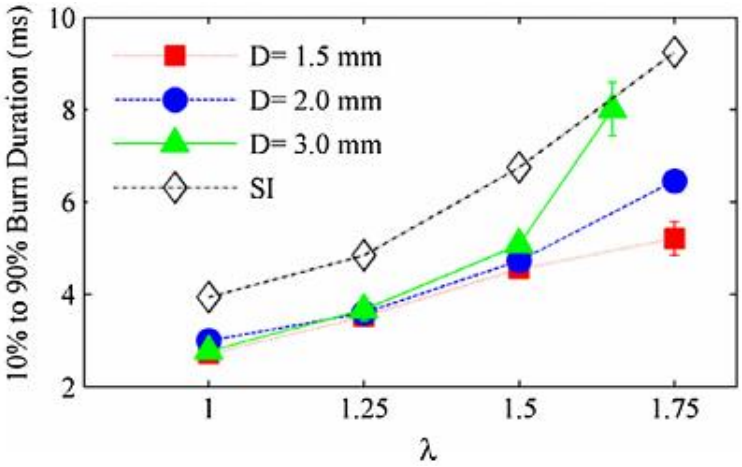

Figure 2-11 Variation in 0-10% Burn Duration vs λ for Various Nozzle Diameters and SI Engine (Gentz et al., 2015)

Figure 2-11 compares burn duration, using MFB 10–90% as evaluation parameter, for the SI system and three pre-chamber ignitors with different nozzle diameters. The authors identified minor variations in burn duration for different nozzle diameters until λ = 1.5. Beyond λ = 1.5, the burn duration was observed to increase as the nozzle diameter was increased. The authors concluded that the nozzle diameter had a reduced effect on flame propagation speed for conditions near stoichiometric. However, for mixtures leaner than λ = 1.5 the use of smaller nozzle diameters becomes advantageous due to increase in turbulence due to higher jet velocity and the resulting penetration. The use of PC ignition system proved to be satisfactory since 10–90% burn duration was faster than the SI system for all A/F ranges, indicating that the flame propagation speed was faster.

Gentz et al. (2015) and Attard et al. (2012) in their studies have suggested that one of the factors of fast 10–90% burn duration can be attributed to multiple flame fronts propagating in the main-chamber.

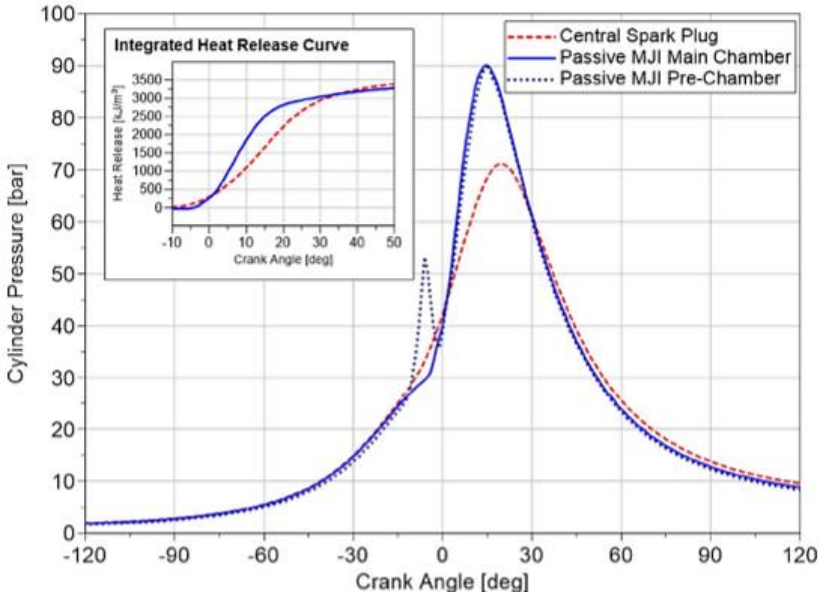

	MFB 50%	10-90% Burn Duration	PMax	RMax	COV NMEP
	[°ATDC]	[°CA]	[bar]	[bar/°]	[%]
Central Spark Plug	17.4	25.9	71.2	1.98	2.54
Passive MJI	8.6	15.4	90.9	5.2	0.85

Figure 2-12 Comparison of Passive MJI Combustion to a Conventional Central Spark Plug at 4000 rpm and 18 bar BMEP (Cooper et al., 2020)

Experiments conducted by Cooper et al. (2020) on a 3 cylinder turbocharged gasoline engine using a spark and pre-chamber ignition system showed that the 10-90% burn duration was significantly reduced by 10.5 degrees when utilising a pre-chamber ignition system as a consequence of faster combustion.

2.4.4 Knocking Combustion in a Pre-chamber Ignited Engine

The use of pre-chambers makes it possible to increase compression ratios and lean burn operation due to knock limit extension capability offered by a pre-chamber ignition system. Knock limits are known to be extended for pre-chamber ignited engines as the end gas, that typically causes engine knock via autoignition, can be burned before it ignites itself. This is due to increased flame propagation or reduced flame travel path reduces the likelihood of end gas knock. Lower combustion temperatures from lean mixture ignition in main chamber, at full loads, also contribute to knock control. (Attard et al., 2012)

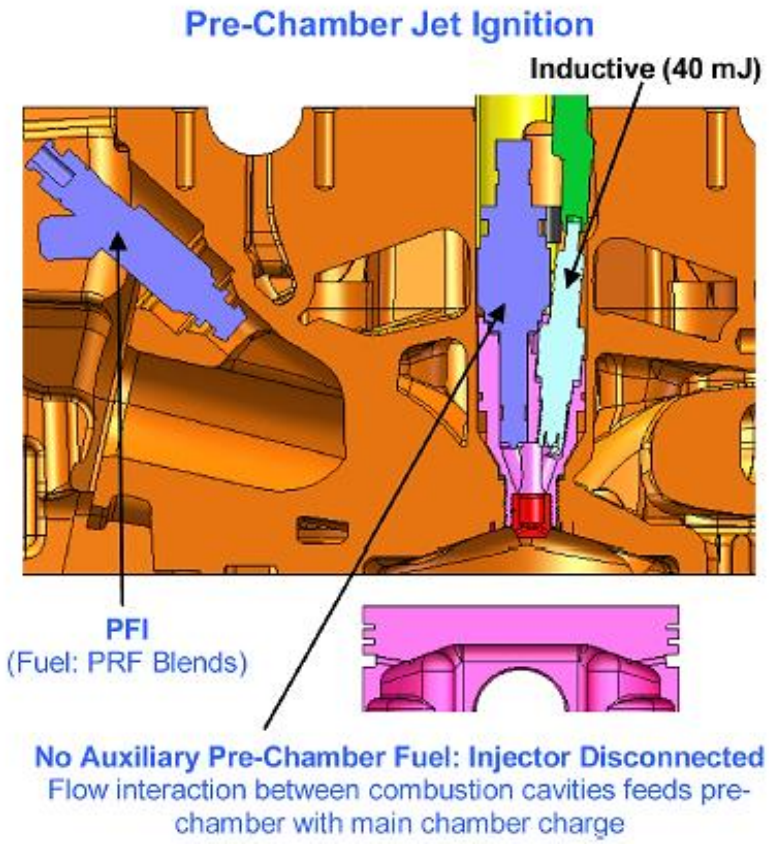

Figure 2-13 Combustion System Utilized for Knock Evaluation with Reducing Fuel Octane (PRF Blends) Pre-Chamber Turbulent Jet Ignition (Without Pre-Chamber Auxiliary Fuelling) (Attard et al., 2012)

Attard et al. (2012) conducted experiments on a normally aspirated single cylinder, 4 stroke, liquid-cooled, aluminium block engine whose displacement was 0.6 litre which had a bore and stroke of 88mm and 98mm respectively, to compare the performance of pre-chamber based ignitor vs a spark based ignitor in terms of knock limits. The setup is shown in Figure 2-13.

The author found that at optimal combustion phasing equating to MBT, the un-fuelled pre-chamber jet ignitor had a 10 Octane Number Requirement improvement due to the burn rate enhancement associated with the distributed ignition system as shown in Figure 2-14. At maximum spark retard (3% CoV IMEPg), a greater than 15 Octane Number Requirement improvement was recorded at the set operating conditions with jet ignition combustion. This was found to be due to the jet igniter's ability to create turbulent jets which entrain and ignite the main chamber mixture at multiple ignition sites. This allowed a later energy release when compared to conventional spark ignition combustion, while still maintaining adequate combustion stability.

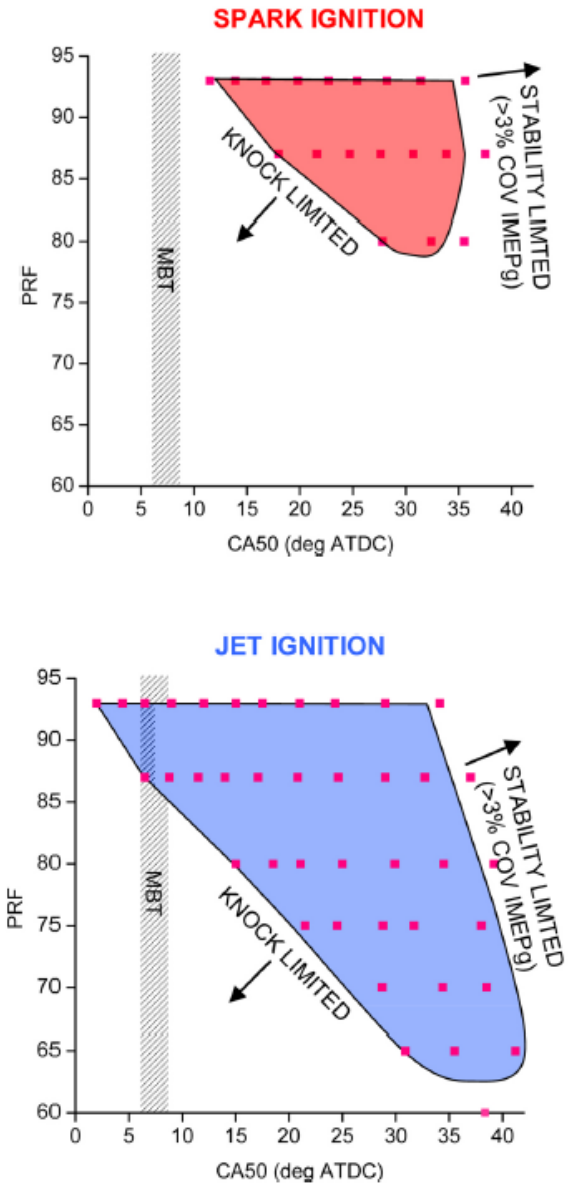

Figure 2-14 Spark ignition and Turbulent Jet Ignition (without pre-chamber auxiliary fueling) combustion operating maps with varying fuel octane and combustion phasing. 1500 rev/min, 98 kPa MAP (~ WOT), stoichiometric conditions (Attard et al., 2012)

Figure 2-15 shows the maximum knock amplitude recorded over the test sequence for each operating point with both the spark ignition and pre-chamber ignition system. The author noted a significant knock limit extension with the pre-chamber ignition system across the tested domain.

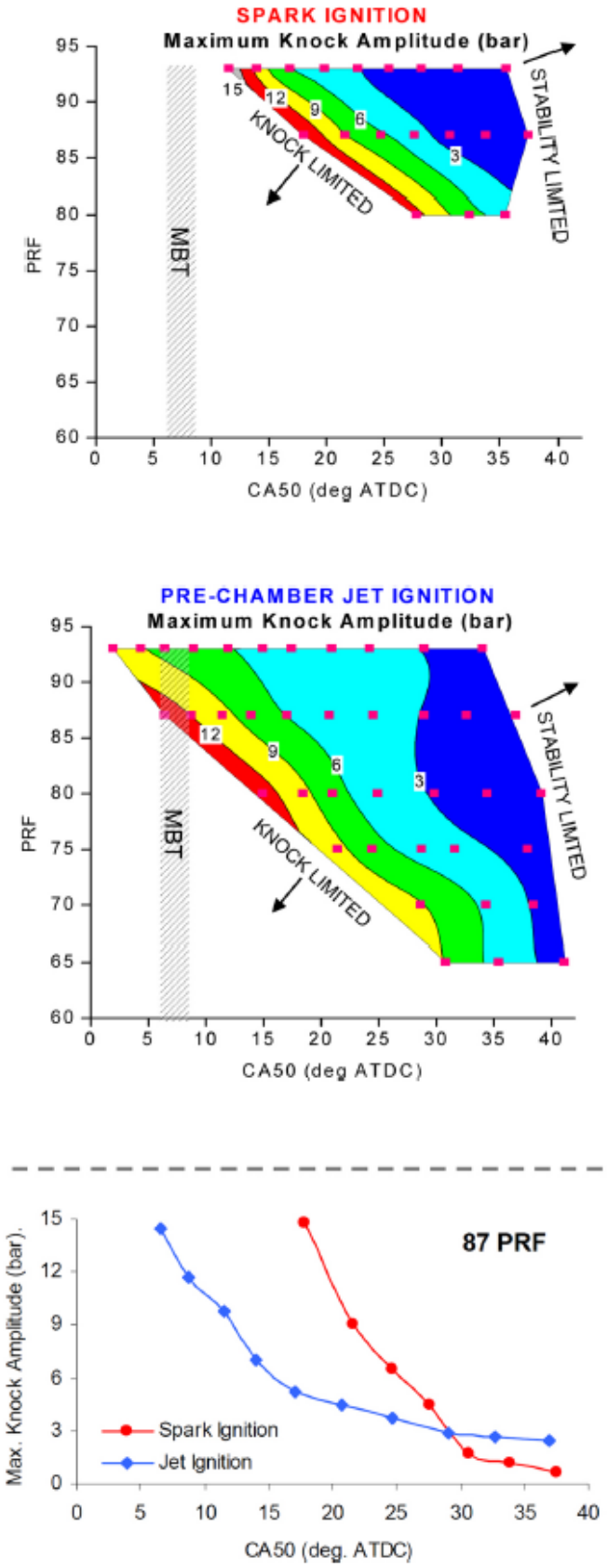

Figure 2-15 Maximum knock amplitude variation for spark ignition and jet ignition (without pre-chamber auxiliary fueling) combustion, 1500 rev/min, 98 kPa MAP (~ WOT), stoichiometric conditions. Upper: Varying fuel quality and combustion phasing. Lower: Comparisons using 87 PRF (Attard et al., 2012)

Direct comparisons between the spark ignition and jet ignition systems at 87 PRF revealed elevated knock amplitude levels with jet ignition combustion, in regions where the spark ignition system showed no signs of knocking combustion (e.g. at heavily retarded combustion phasing).

The amplitudes of the knocking combustion were found to be low (<3 bar) and the author noted that the pressure oscillations were not associated with typical end-gas knock, but were thought to be due to a phenomenon called ‘jet knock’.

Jet knock is characterized by small pressure oscillations similar to conventional end-gas knock, only significantly smaller in magnitude and which initiates just after the start of ignition instead of towards the end of combustion. Numerous researchers such as Soltic et al. (2019), Hua et al. (2020), Wakai (1993), Gupta and Bracco (1982), Hamori (2006), Biswas (2018) have also mentioned seeing pressure oscillations that seemed knock-like but were not because of end gas auto-ignition. Jet knock is known to be a function of the high pre-chamber jet velocities generated at relatively small throat areas by a large pressure ratio between the jet source and the main chamber. When the jet velocity is equal to or exceeds sonic velocity could result in the formation of a hemispherical or conical shock wave in the combustion chamber, which is detected as a small pressure oscillation. The maximum knock amplitude comparison as shown in Figure 2-15 highlighted that the pre-chamber ignition system had difficulty operating at near zero amplitude levels, where the occasional jet knocking cycle displayed some pressure oscillation which is barely audible with an engine stethoscope. (Attard et al., 2012)

Anderson et al. (2013) investigated the possibility of relaxing the octane requirement of a turbocharged Rotax 914 aviation engine by utilising a pre-chamber jet ignition system. A passive pre-chamber jet igniter- with six orifices having a hole diameter of 1.25mm and having a volume of 0.84 cm^3 which represented 2.20% of the clearance volume, was designed to replace the spark plug in a cylinder of the test engine with swirl ports and was evaluated across engine speeds ranging from 2500 to 5500rpm.

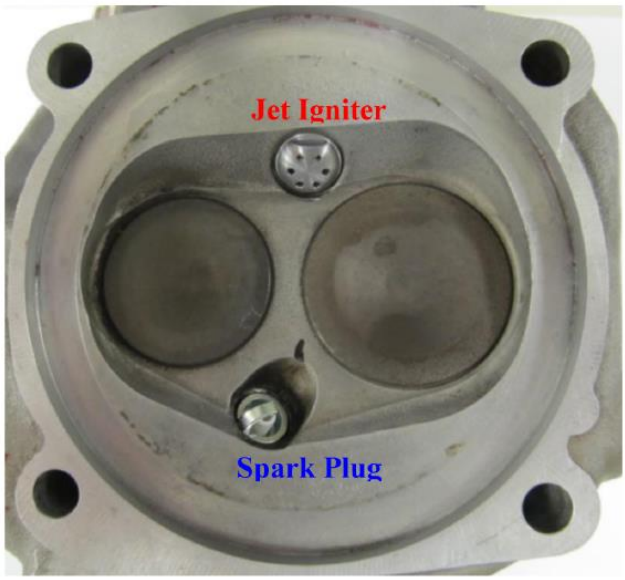

Figure 2-16 Jet Igniter and Spark Plug Hardware and Locations Used Across All Experiments (Anderson et al., 2013)

Anderson et al. (2013) found that the jet ignition power output on 87 AKI unleaded gasoline was near identical to the spark ignition system on 100 LL Avgas as shown in Figure 2-17, except at maximum engine speed, where a 9% reduction of power output was observed due to the associated reduced manifold pressure, which was knock limited. According to the author the reduced output of the jet igniter at high engine speeds was thought to be related to the increased in-cylinder charge motion having a negative effect on the jet penetration due to the very high swirl rates. Hence, the full effect of the propagating jet was not realized at high engine speeds. It was estimated that

the jet igniter offered a greater than 10 octane number improvement over the baseline spark ignition system when compared with the octane rating of the 100 LL Avgas.

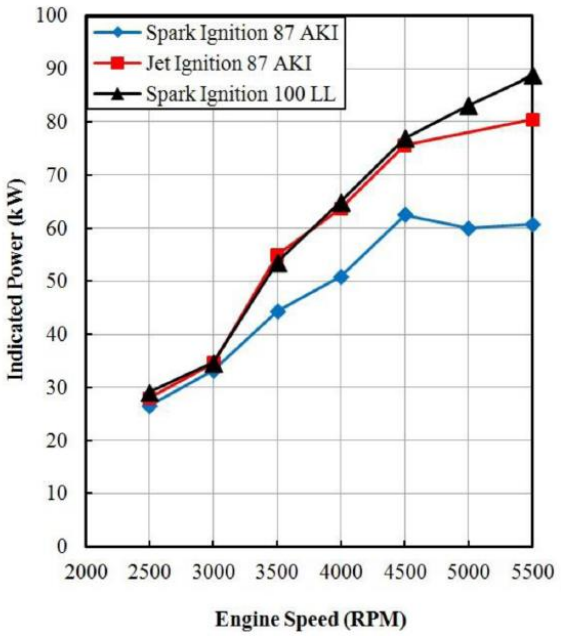

Figure 2-17 Boosted maximum indicated power for spark ignition (blue) and jet ignition (red) combustion using 87 AKI gasoline. Results from the spark ignition OEM engine operating on 100 LL Avgas (black) are also shown as a baseline target for performance. (Load limited by boost or knock limits at MBT combustion phasing, 49°C intake temperature, Φ=1.0) (Anderson et al., 2013)

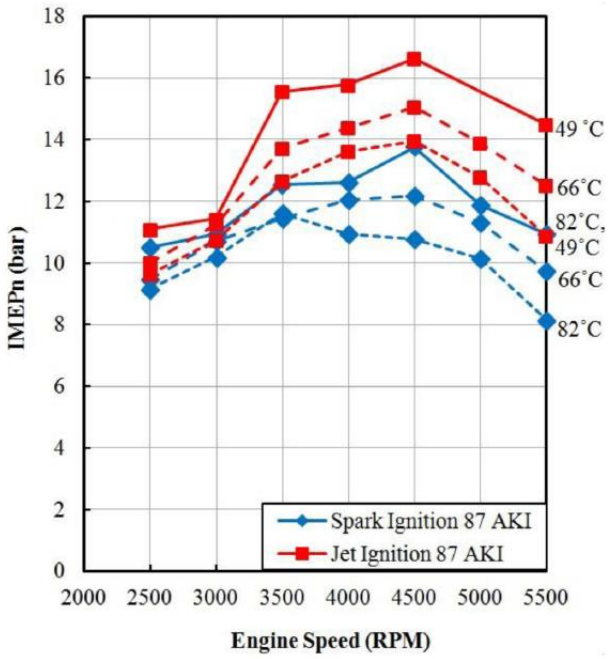

Figure 2-18 Net IMEP for spark ignition and jet ignition combustion with varying intake-air temperature using 87 AKI unleaded gasoline (Load limited by boost or knock limits at MBT combustion phasing, Φ=1.0) (Anderson et al., 2013)

A study varying the intake air temperature up to 82°C was conducted by Anderson et al. (2013) for both spark ignition and jet ignition systems to determine how the maximum load limits were affected by intake charge air temperatures. Figure 2-18 displays the performance of the jet igniter compared to that of the spark ignition system at 49, 66 and 82°C intake temperatures. The experiments were conducted by operating the engine at optimized MBT combustion phasing (no ignition retard) and increasing the manifold pressure until maximum airflow (turbocharger limited) or maximum knock limits were exceeded. For both spark ignition and jet ignition modes, MBT corresponded to a 50% mass fraction burn location of 7-8 deg ATDC. Results showed a 3 bar net IMEP load increase above 3500 rpm across all equivalent intake air temperatures, which were all knock limited. To quantify the effect of the jet igniter in terms of intake air temperature improvement the author found that the pre-chamber combustion system can match spark ignition load with approximately 35°C increase in intake air temperature due to superior knock resistance and reduction of ignition phasing loss.

Figure 2-19 displays the maximum knock amplitudes recorded for boosted conditions across the range of speeds tested for both combustion systems. For the pre-chamber jet ignition system, knock limits were observed not to exceed until 4000 rpm, indicating that the combustion system could tolerate higher levels of boost if the turbocharger system were able to deliver higher air flow rates. For the spark ignition system, knock limits exceeded at first at the lowest operating speed of 2500 rpm, with knock levels then decreasing as the engine speed increased to 3000 rpm because of the reduced end-gas residence time at elevated pressure and temperature as the engine speed

increases. Knock levels were found to be higher than the pre-chamber ignition system above 3000 rpm due to the likelihood of end-gas autoignition due to slower combustion speed of the spark ignition system. The study conducted thus shows exceptional knock limit extension capabilities of the pre-chamber system when compared with that of a spark ignitor based system when utilised in a turbocharged engine. (Anderson et al., 2013)

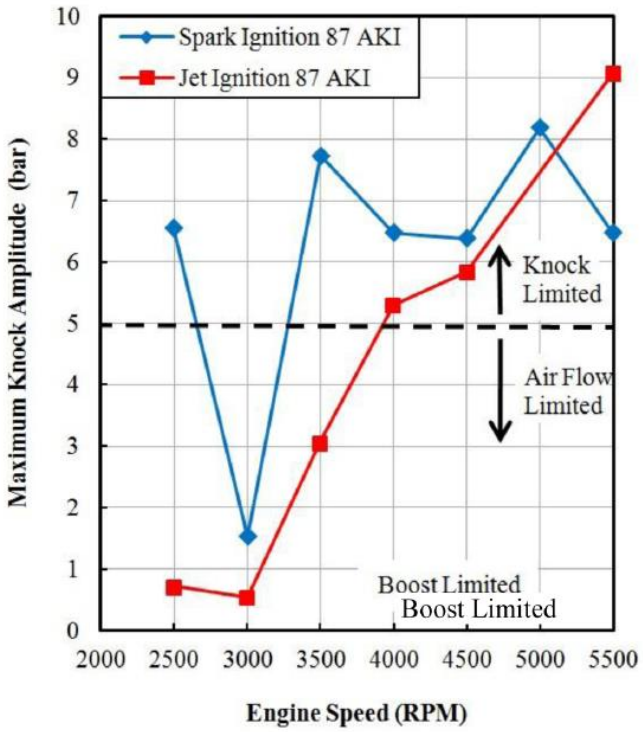

Figure 2-19 Maximum knock amplitude across boosted loads for spark ignition and jet ignition combustion using 87 ON unleaded gasoline (49°C intake temperature, Φ=1.0) (Anderson et al., 2013)

Hua et al. (2020) studied the effect of knocking combustion on gasoline fuelled engine operating at 1500 rpm. The authors tested single and twin spark ignition systems along with jet ignition with 1 and 7 holes at advanced spark timings to generate knocking combustion. The mean MAPOs of jet ignited engine under non-knocking conditions were found to be higher than the spark ignited engine as shown in Figure 2-20, which was caused due the pressure oscillations originating from the jet process. The authors also found that when

spark timing was advanced to reach knock condition, the increase slopes of jet ignition MAPO values were found to be significantly lower than the spark ignited engine thus indicating that the knocking combustion was less sensitive to spark timings when jet ignition method was used.

Statistical parameters - μ, σ, RSD and R, were utilised to study the MAPO distribution for a single spark ignited engine and a single hole jet ignited engine as shown in Figure 2-21. It was observed that knocking in the spark ignition mode resulted in the distribution being discrete with random cycles of high knock intensity showing high deviation, which resulted in significant increase of the RSD and the R value. However, the MAPO distribution of jet ignited engine had shown that the distribution patterns remained almost the same for both normal and knocking combustions, where the RSD values were between 0.4 & 0.5. This phenomenon indicated that the randomness of jet ignited engine was very low even under knocking conditions. The authors concluded that the turbulent jet ignition mode had better combustion stability with low cycle-to-cycle variation than the spark ignited engine.

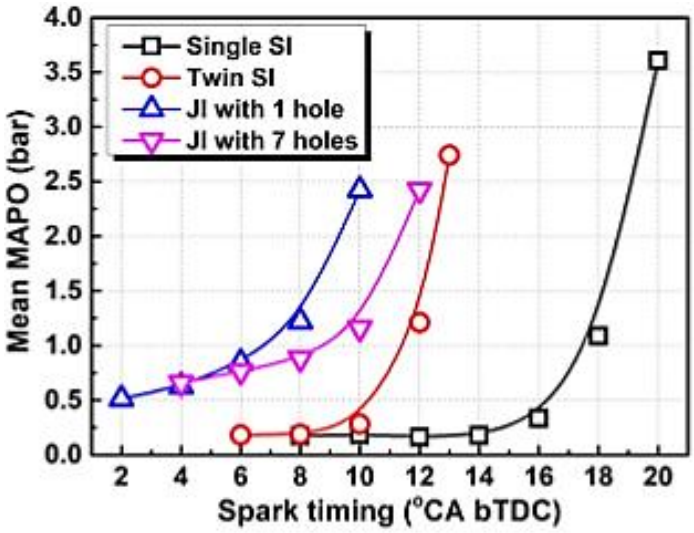

Figure 2-20 Knock Intensity Against Spark Timing with Different Ignition Methods (Hua et al., 2020)

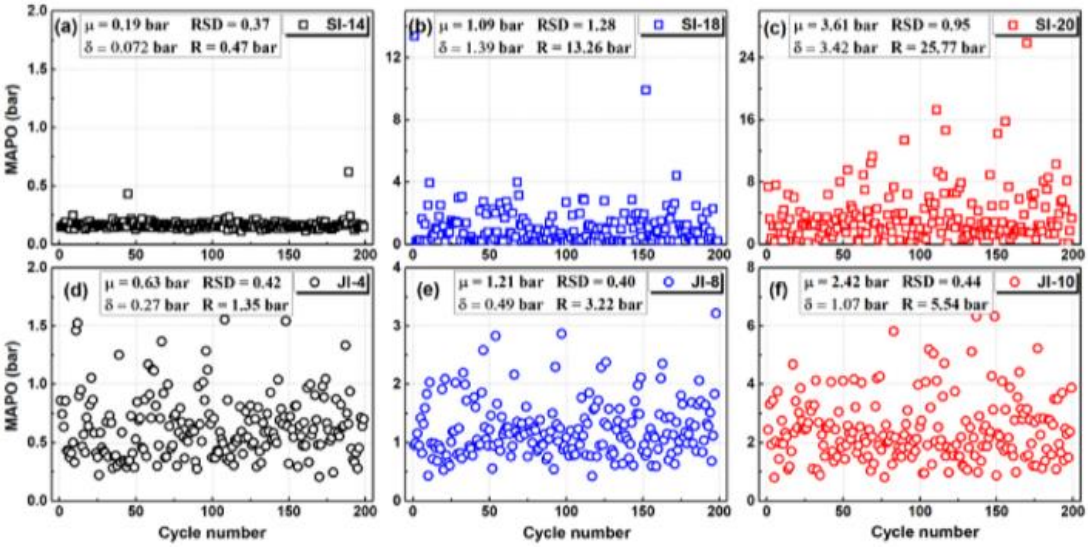

Figure 2-21 MAPO Distributions of JI Combustion and SI Combustion Under Conditions from Normal to Knock (Hua et al., 2020)

Hua et al. (2020) also reported observing two stage pressure oscillations for the jet ignited engine in knocking condition. The authors argued that out of the two stages- the first stage of pressure oscillations were caused due to ejection of jets and the second stage of oscillations were caused due to auto-ignition of unburned gas. The authors observed different frequencies of the two stages of pressure oscillations.

The different frequencies of the pressure oscillations were attributed to the changing main-chamber temperature throughout the combustion process. When the pressure oscillations are generated by jet ejection into the main-chamber, the ambient temperature is low thus resulting in lower speed of sound and thus the low frequency of pressure oscillations. As combustion took place in the main-chamber, the temperature gradually increased, and the speed of sound also increased. When the auto-ignition occurred in the unburned region, the temperature in the main-chamber was relatively high, thus leading to a higher speed of sound and resulted in high frequency of pressure oscillation, shown in Figure 2-22.

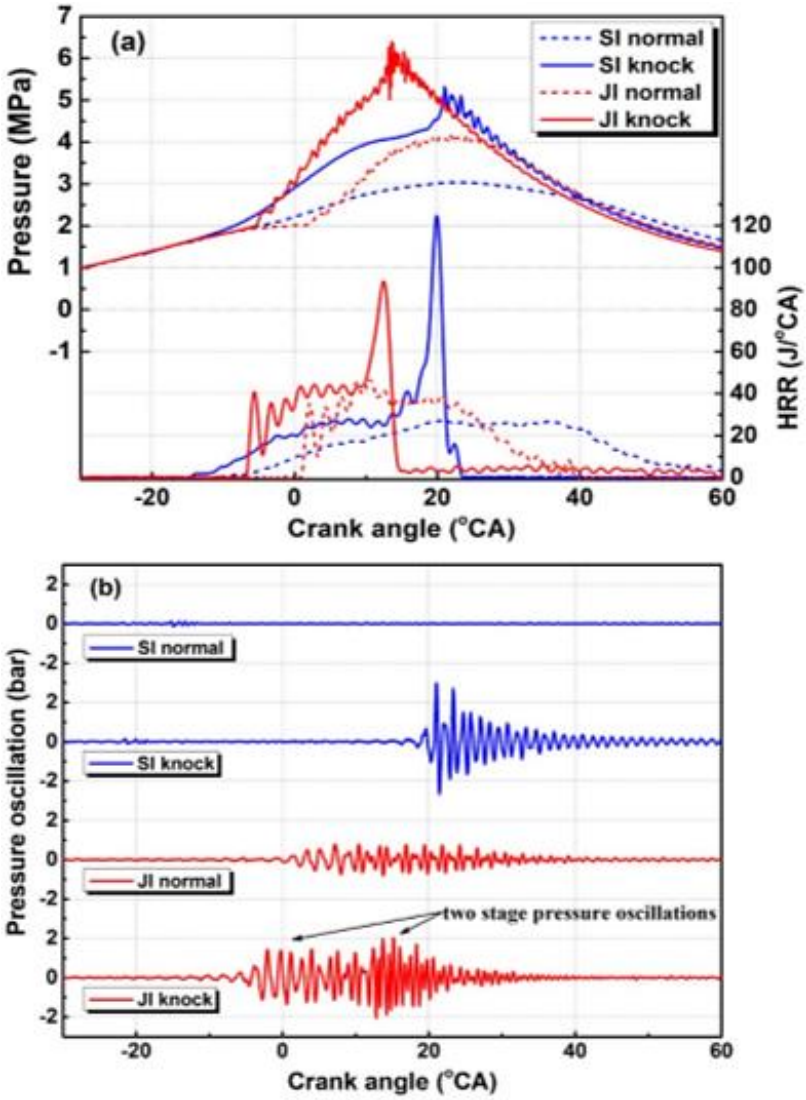

Figure 2-22 In-cylinder pressure, HRR and pressure oscillations of several typical combustion cycles (including SI normal, SI knock, JI normal and JI knock combustions) (Hua et al., 2020)

2.5 Influence of Main Chamber Conditions on a Pre-chamber Ignited Engine

2.5.1 In-cylinder Flow Motion

Flow motion in the cylinder of internal combustion engines has a fundamental effect on combustion and thus on engine performance and exhaust emissions. Large-scale flow structures, like swirl and tumble, is utilised to maintain the flow's kinetic energy until the late stage of the compression stroke just before combustion, when it dissipates or breaks up into micro-scale turbulence to promote the early flame kernel growth and to speed up the flame propagation. In spark ignited engines, the enhanced turbulent flow generated towards the end of compression stroke can considerably improve the combustion process, extend lean limits and decrease cycle-to-cycle combustion variation at ultra-lean conditions (Li et al., 2001). However, few studies on impact of flow motion have been carried out on pre-chamber ignited engines thus leaving a gap in literature especially for gasoline fuelled engines. The few studies available have been reviewed below.

Kimura et al. (2018) studied the impact of in-cylinder flow on a fuelled pre-chamber ignited supercharged Honda engine at 2000 rpm and 5.1 bar IMEP at various air/fuel ratios with two tumble ports. Port A and B had a tumble ratio of 0.4 and 1.8 which were determined by 3D CFD results. Engine testing results, as shown in Figure 2-23, showed that the MFB 10-90% burn duration was slightly reduced for the high tumble port case and COV of IMEP was 0.5 percentage higher on average at varying air/fuel ratios. The authors concluded in their study that in-cylinder flow has no impact on the combustion process

for a pre-chamber ignited engine as there was no need for early flame kernel development for a pre-chamber ignited engine. The authors argued that due to residual tumble flow in Port B at compression stroke as shown in Figure 2-24, resulted in leakage of the injected pre-chamber fuel into the main-chamber which led to differing amounts of pre-chamber fuel at the start of combustion at each cycle thus leading to increased cyclic variation.

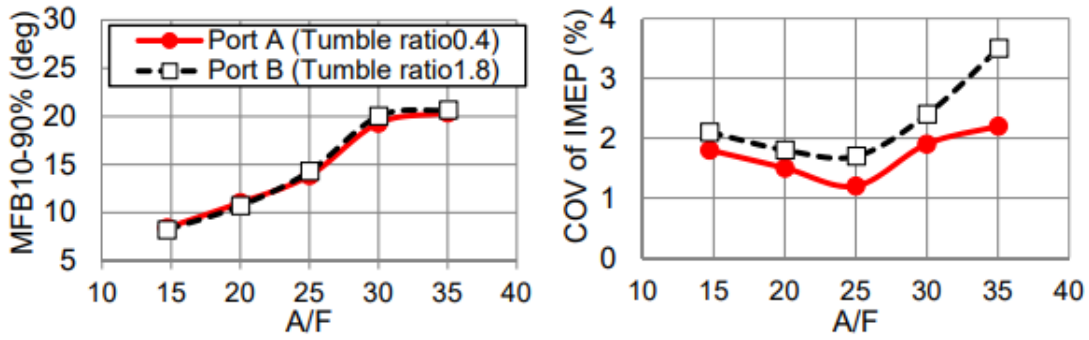

Figure 2-23 Performance Result of Intake Ports with Different Tumble Ratios (Kimura et al., 2018)

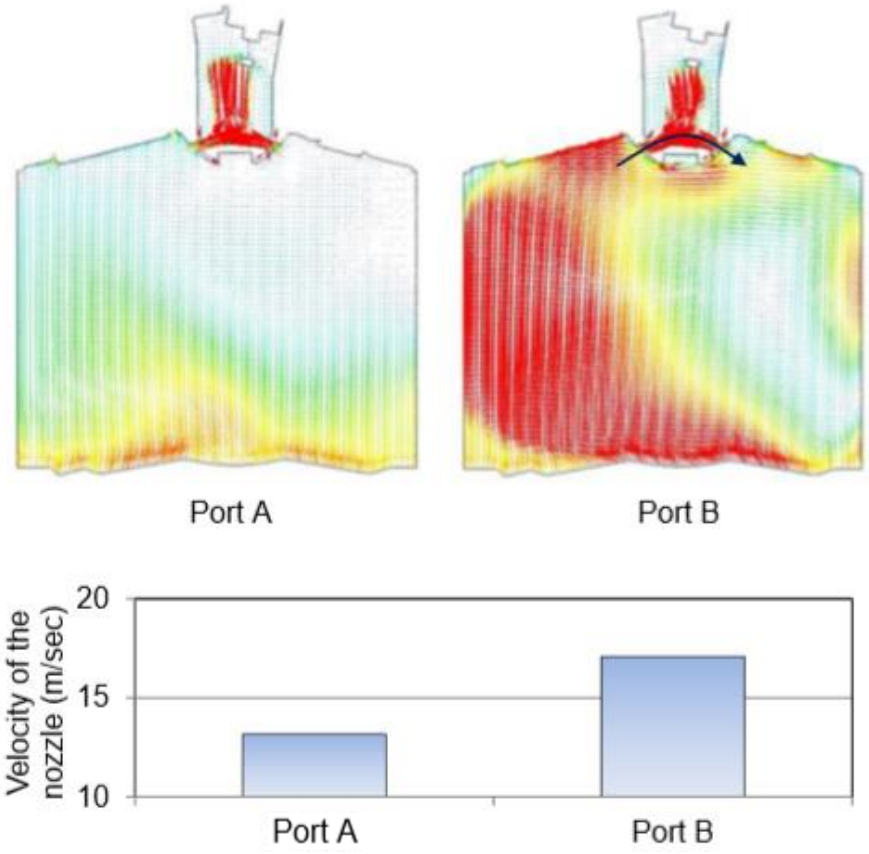

Figure 2-24 In-cylinder Flow by CFD at Crank Angle 80 deg BTDC (Kimura et al., 2018)

Serrano et al. (2019) studied the influence of charge motion in the engine cylinder of a fuelled pre-chamber ignited low speed gasoline engine via numerical studies. Studies concluded that although the strong tumble motions and high turbulent kinetic energy in spark-ignited engines supported a faster flame propagation process and hence enhance the efficiency, however, in the case of a pre-chamber engine, results of numerical investigation had shown that the turbulence level in the vicinity of the flame front and the overall combustion performance were mainly related to the jets coming out of the pre-chamber holes and to a much lesser extent to the charge motion in the main chamber generated by the intake ports thus only requiring a low tumble motion in the main-chamber.

Novella et al. (2020) studied the effect of air and EGR dilution on a passive pre-chamber ignited engine via experimental and numerical studies with the engine operating at 2000 rpm and 4500 rpm. The authors concluded via numerical study that due to the inherent worsening of the PC flow and thermochemical conditions when advancing the spark timing, in combination with the impact of external dilution strategies which have a negative impact on the laminar flame speed and combustion rates – these factors deteriorate the combustion in the pre-chamber. The jet ejection process from the pre-chamber is thus compromised and thus the onset of MC ignition is negatively affected. The combination of these negative effects limits the strength of dilution that can be admitted by the engine. However, the authors argued that if thermodynamic and turbulence conditions in the MC were still favourable for assuring a reasonable combustion rate, the overall operation of the engine

may not be compromised. However, this was not confirmed via any flow altering parametric studies.

Roethlisberger and Favrat, 2002, researched on the effects of engine geometrical parameters on a turbocharged passive pre-chamber based spark ignition natural gas engine manufactured by Liebherr- which had six cylinders inline and operated with a compression ratio of 12:1 at 1500rpm, a swirl ratio of 2.0 and λ = 1.61. To evaluate the effects of main combustion chamber geometry on the combustion process, two piston bowl configurations were investigated- a base piston (A) and a high turbulence piston (B) as shown in Figure 2-25.

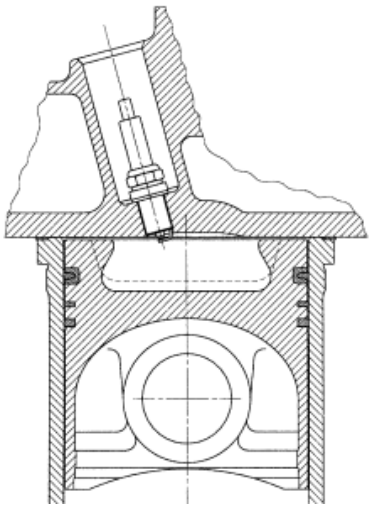

Figure 2-25 Base Piston (A) (Dotted line) and High Turbulence Piston (B) (Solid Line) (Roethlisberger and Favrat, 2002)

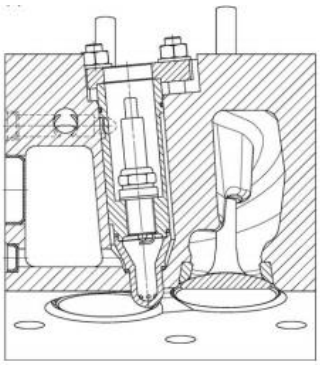

Figure 2-26 Spark Plug Replaced with Pre-chamber (Roethlisberger and Favrat, 2002)

The authors noted that at a constant relative air to fuel ratio, the transition from piston A to B slightly reduces the intensity and duration of the pre-chamber pressure pulse, which is illustrated by the difference between the pre-chamber and the main chamber pressure as shown in Figure 2-27(c). This difference in pre-chamber and main chamber pressure is expected to decrease the penetration of the gas jets into the main combustion chamber. However, the higher turbulence generated by piston B strongly intensifies and accelerates the main chamber combustion process, particularly in the late stage as shown in Figure 2-27(b). The faster combustion process induced by piston B causes a significant increase in peak cylinder pressure as can be seen in Figure 2-27(a).

The authors concluded that the significantly shorter combustion duration characterising piston B caused an increase in fuel conversion efficiency, particularly for the highest values of relative air to fuel ratio as shown in Figure 2-27(e). They also found that the more rapid late stage of the combustion process reduces the cycle-by-cycle variation. This is indicated by a somewhat lower coefficient of variance of IMEP. In comparison to the original piston, the use of a piston generating significantly more turbulence lead to an approximately 0.5% higher fuel conversion efficiency.

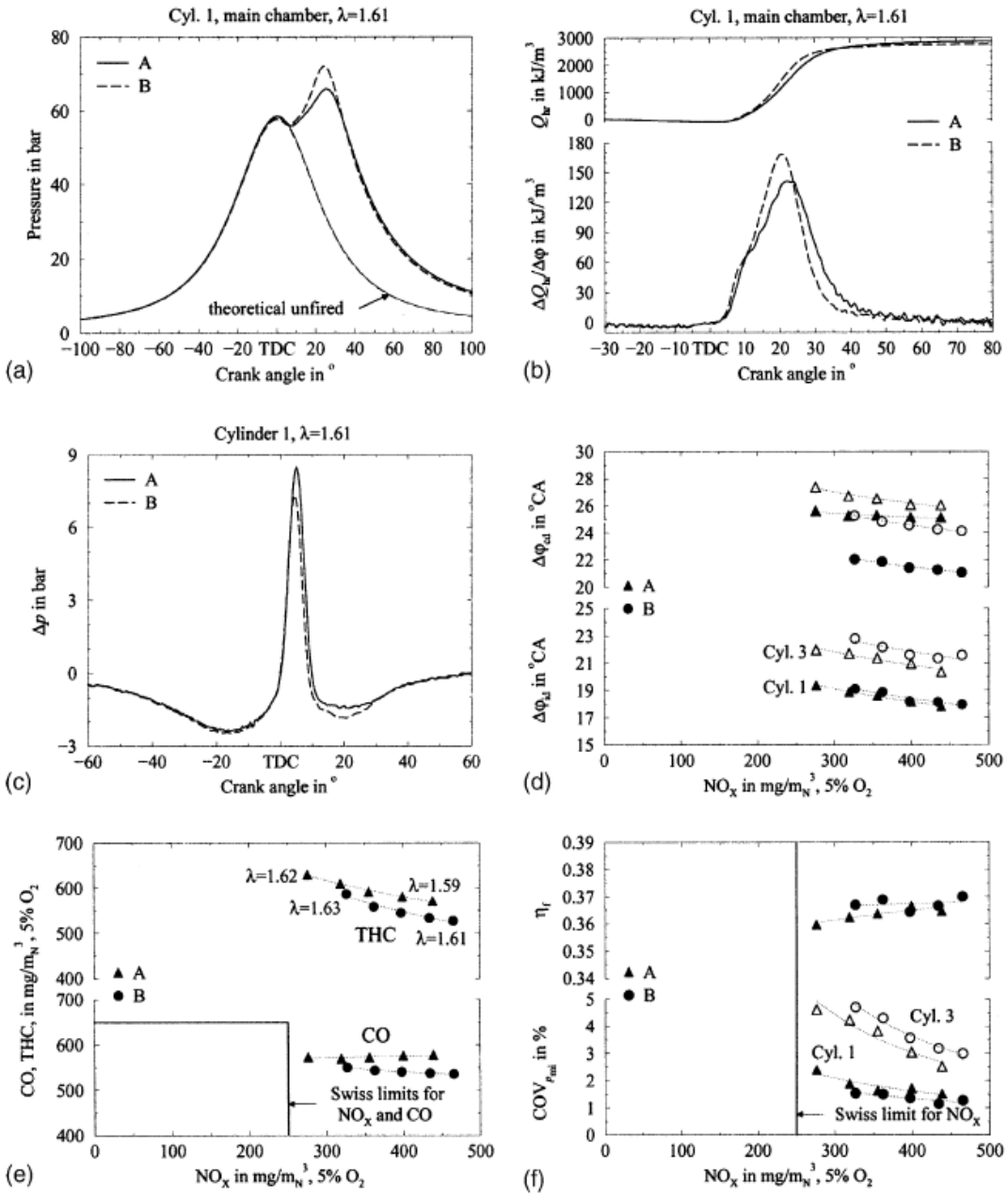

Figure 2-27 Prechamber ignition, influence of the main combustion chamber on the engine performance and emissions; main chamber pressure (a), heat-release rate and integral (b) and pressure difference between pre- and main chamber (c) at constant relative air to fuel ratio; ignition delay and combustion duration (d) CO and THC emissions (e) and fuel conversion efficiency and coefficient of variance of pmi (f) as function of NOx emissions; Vp = 4540 mm^3, An = 14.10 mm^2, Nn = 4, an = 78 deg, ST = 8.3 deg CA BTDC, NG7. (Roethlisberger and Favrat, 2002)

2.5.2 Effect of Compression Ratio

Stadler et al. (2020) studied the effect of compression ratio on a spark and pre-chamber ignited engine operating at 1500 rpm with both fuelled and unfuelled pre-chambers. Two compression ratios were studied where the change in compression ratio was obtained via changes to the piston crown shape. Compression ratios of 10.92 and 14.91 were compared for the spark ignition case and compression ratios of 10.54 and 14.18 were compared for the pre-chamber ignition case.

The authors concluded that due to the need to retard combustion, conventional SI operation showed a decreased thermal efficiency for elevated compression ratio case. The passive pre-chamber operation extended knock limits and benefitted from elevated compression ratio in terms of efficiency. Although the authors argued that increased heat losses at stoichiometric case resulted in no improvement in thermal efficiency when compared to the spark ignition case. For the fuelled pre-chamber operation mode, lean combustion increased efficiency by +2.5 % compared to conventional, stoichiometric spark ignited operation at low compression ratios. The efficiency was further increased to +5.4 % when the compression ratio was increased.

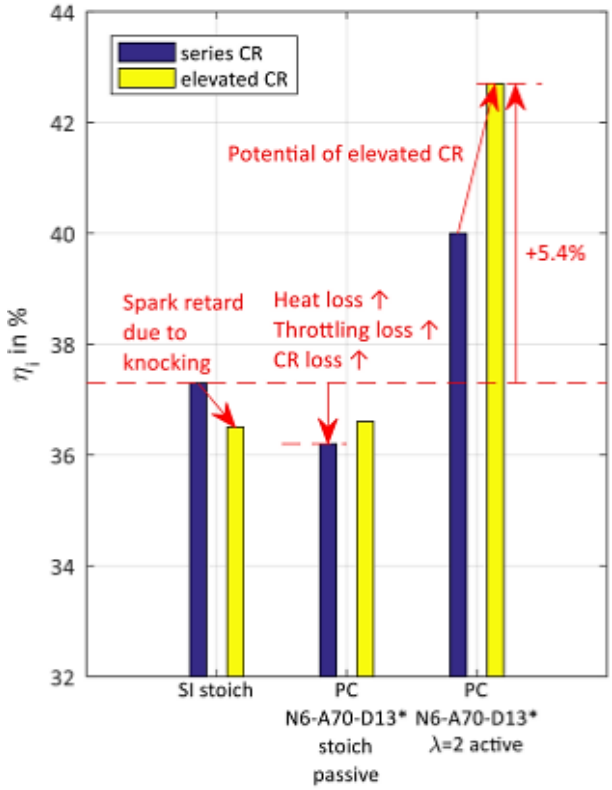

Figure 2-28 Overview of Indicated Efficiency Potential of the PC Ignition System at 9 bar IMEP, 1500 rpm (Stadler et al., 2020)

2.5.3 Effect of Residual Concentration

Novella et al. (2020) numerically studied the influence of residual concentration in the pre-chamber and main-chamber on combustion. The authors studied the influence of 10% EGR compared to no EGR on a passive pre-chamber ignited engine operating in stoichiometric condition at 4500 rpm. Figure 2-29 shows the laminar flame speed evaluated in the flame front, the HRR and the relative pressure (Δp) defined as the pressure difference between the pre-chamber and the main chamber. The authors observed that the laminar flame speed values, depicted in the top graph start to decrease as the dilution rate increases. As a result, the HRR profiles, plotted in the middle graph, showed that the maximum energy released due to combustion in the pre-chamber was notably reduced and which led to longer combustion

duration. The bottom graph showed that maximum pressure difference among both chambers was reduced for the 10% EGR case thus compromising the jet ejection process and negatively affecting the ignition of the main chamber.

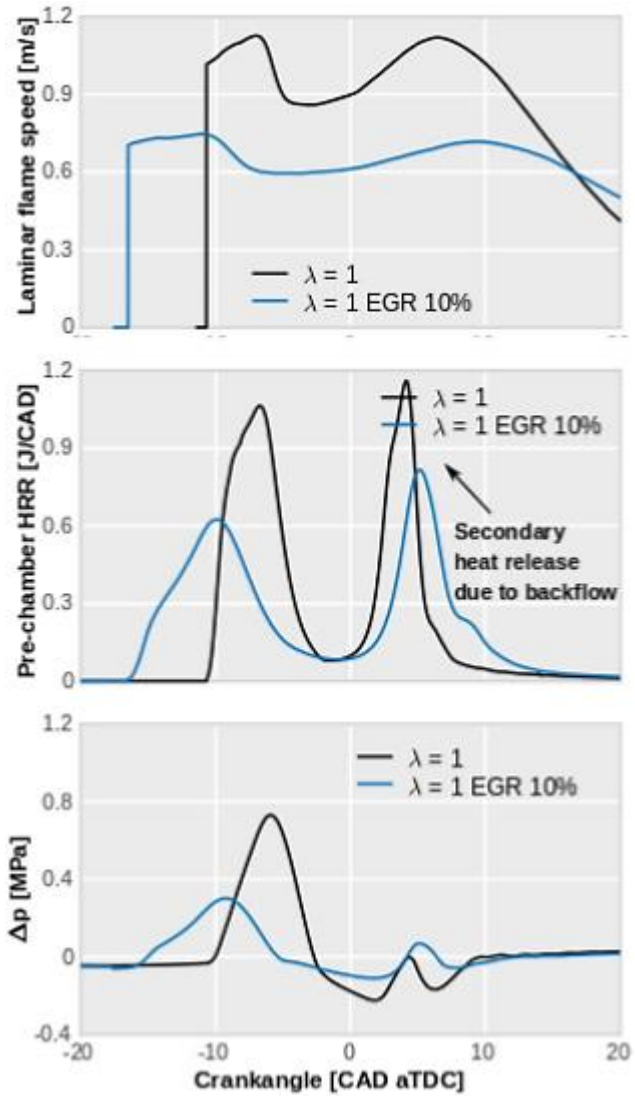

Figure 2-29 Comparison Among Diluted and Non-Diluted Simulations. The Laminar Flame Speed Evaluated in The Flame Front, HRR Traces In The Pre-Chamber And Pressure Difference (Δp) Profiles Are Shown (Novella et al., 2020)

The authors also concluded that with the addition of 10% EGR, the flame began in a less favourable region- the thickened flame regime where some eddies could penetrate the diffusive layer of the flame, enlarging it and compromising the flame stability (the combustion duration was 7 CAD) as

shown in Figure 2-30. Combustion inside the pre-chamber without EGR began in the thickened wrinkled flame regime where the Kolmogorov scales are larger than the flame thickness thus leading to a faster combustion process (the combustion duration was 3 CAD).

The authors note that before the end of pre-chamber combustion the flame shifted to a favourable region with Damköhler numbers over 1, thus achieving a more stable combustion for both no EGR and 10% EGR. The main-chamber combustion process had shown a very similar trend, becoming more stable and moving towards the corrugated flame regime after approximately 25 and 15 CAD for the cases with and without EGR dilution, respectively. Results thus showed that increasing residual concentration results in increasing the burn durations.

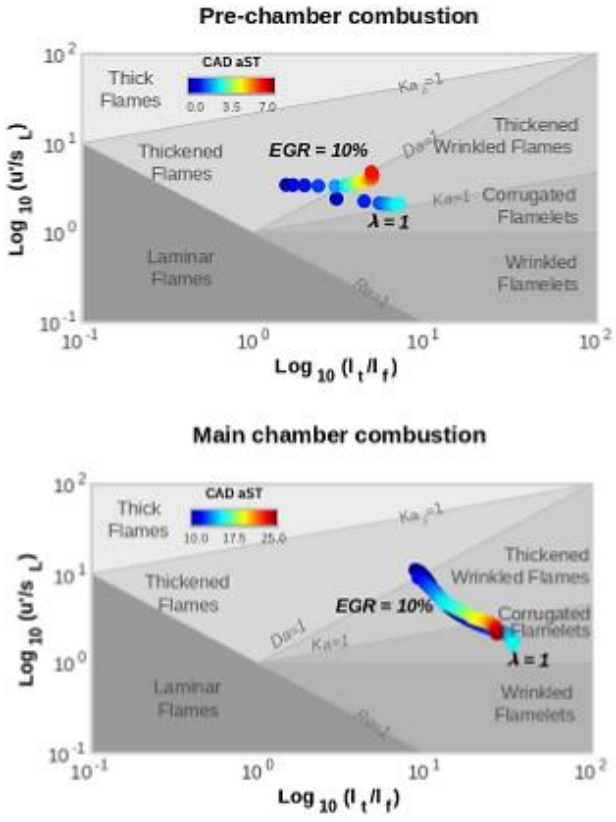

Figure 2-30 Evolution of the Combustion Progress in the Flame Regime Diagram. The PC Combustion is shown in the Top Graph and the Main-chamber Combustion is shown in the Bottom Graph (Novella et al., 2020)

2.6 Objectives of Research

In the literature review presented in this section, it is evident that gasoline based pre-chamber system is a novel and promising concept and gaps exist in the available literature in the areas of charge motion, residual concentration and compression ratio and their impact on the combustion process of a gasoline fuelled pre-chamber ignited turbocharged lean burn engine.

Although few studies have focused on main chamber charge motion in a pre-chamber ignited gasoline fuelled low speed engine – the general conclusion of all these studies are that main chamber charge motion has no impact or negatively impacts combustion. The first objective of the research is to study the impact of charge motion in the main-chamber of a high speed pre-chamber ignited engine. Based on the findings of the first objective – a redesign of the piston crown shape is to be explored to support a pre-chamber ignition system. The third objective is to determine the effects of residual concentration in the main-chamber and pre-chamber on combustion in lean operating conditions, as current literature only addresses the effect of residual concentration on the pre-chamber ignition system at stoichiometric air/fuel ratio conditions on a low speed engine. The effect of residual concentration is studied by varying the exhaust back-pressure. The fourth objective is to determine the effect of increasing compression ratio on the passive pre-chamber ignited engine at lean operating conditions as current literature only addresses the effect of increasing compression ratio at stoichiometric condition for a passive pre-chamber ignited engine.

It is worth noting that most of the research work carried out on pre-chamber ignition systems have focused on low speed naturally aspirated engines and moderately downsized engines and little has been done in the field of highly downsized turbocharged high speed engines, one which this thesis focuses upon.

The impact of in-cylinder conditions on a gasoline based pre-chamber ignition system has not been widely researched upon and there remains many questions to be answered. This thesis summarises research work to determine the impact of in-cylinder conditions on a high speed turbocharged gasoline pre-chamber ignited engine to add to or fill the existing gap in literature.

3. Development of a Boosted High Speed Knock Limited Single Cylinder Research Engine

Single cylinder engines are traditionally utilised in the early stages of engine development such as testing of new individual components to directly assess its performance contribution without interference from other cylinders such as in the case of multi-cylinder engines. However, in a fast paced industry such as the motorsport industry- the design and manufacture of prototype parts required to build, in many cases- most of which are manufactured from exotic and long lead time materials, tend to be very expensive. In addition to this, correlation of the performance of the single cylinder engine seldom matches with that of the equivalent multi-cylinder engine at the first instant without tuning of certain parameters such as coolant and oil temperatures to match the heat rejection of the single cylinder engine with that of the equivalent multi-cylinder engine.

In order to overcome the cost and time barriers associated with the construction of a single cylinder engine from scratch, a methodology is presented in this dissertation which utilises an existing V6 motorsport engine and utilises the existing V6 engine head, block and crankshaft components to manufacture a single cylinder engine for the purpose of combustion research.

A V6 motorsport engine was utilised for the conversion into a single cylinder engine as a V6 type is the engine of choice for tier 1 motorsport engine

manufacturers/regulations such as Formula 1 (F1) and Le Mans Prototype (LMP1) class of racing cars. (FIA, 2019; AER Ltd, 2016; Toyota, 2018)

3.1 Experimental Setup

Table 3-1 and 3-2 provides the specifications of the 4-stroke multi-cylinder V6 engine, 4-stroke single cylinder engine and the test cell. The single cylinder engine was derived from the multi-cylinder V6 engine, details of conversion are discussed in the following chapters.

	V6 Engine	**Single Cylinder Engine**
Max Engine Power	>500 kW	>50 kW
BMEP	>25 bar	
Max Engine Speed	>8000 rpm	
Fuel Delivery	Gasoline Direct Injection - 500 bar Max Inj Pressure	
Fuel	80% Gasoline and 20% Ethanol	
Max Fuel Consumption Rate	≥80 kg/h	13.33 kg/h

Table 3-1 Multi-cylinder and Single Cylinder Engine Specifications

Item	**Specification**
Dynamometer (SCE)	SCHORCH AC 140 kW
Air Flow Meter	Sierra Instruments FastFlo 620S 900 kg/h
Fuel Flow Meter	Sierra Instruments FMS1000
Temperature Sensors	4X PRT, 8X K-Type Thermocouples
Pressure Sensors	GE 10X 0-10 bar, 2X Bosch TMAP
Instantaneous Pressure Measurement System	AVL Indimodul with Kistler Instantaneous Intake and Exhaust Manifold Pressure Sensors

Engine Boosting System	2 Stage In-Series Eaton TVS410 and TVS900 Superchargers
Engine Air Intercoolers	2 Stage Bowman Air to Water

Table 3-2 Test Cell Specifications

Figure 3-1 shows the setup of the test cell which was developed and commissioned from scratch by the two students involved in this research project- only the work undertaken by the author of this thesis has been presented in this chapter. A supercharger rig was utilised to provide pressurised air to the engine which was driven by the rear end of the dynamometer, where the pressure was controlled to a set value by controlling the bypass valve. Figure 3-2 shows the supercharger rig connected to the rear end of the dynamometer. The hot compressed air was cooled using 2 stage intercoolers which controlled the temperature of the charge air to a set temperature by varying waterflow into the intercoolers. The charge air was then fed into the engine utilised for combustion.

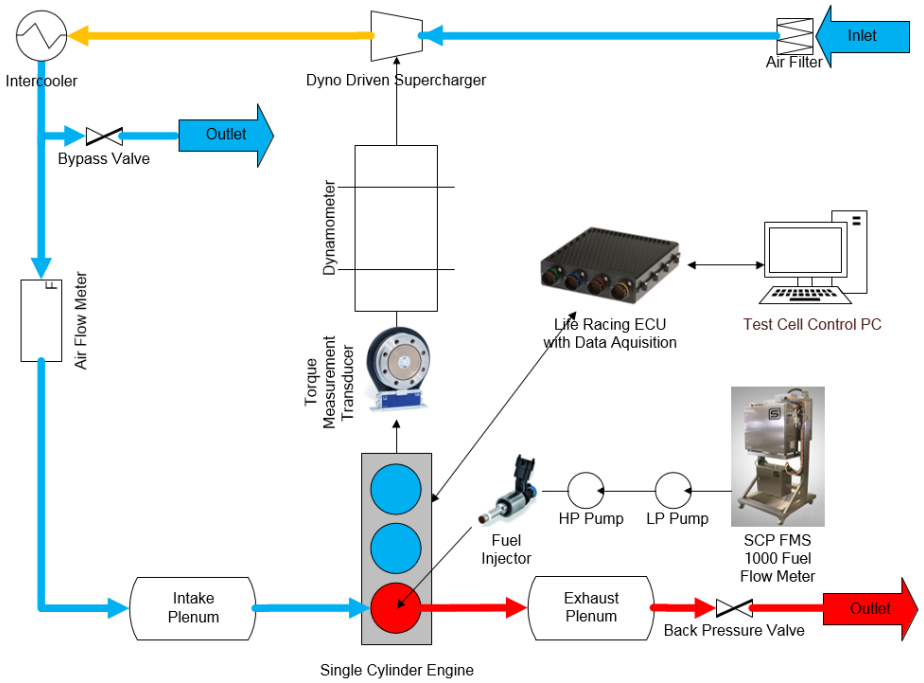

Figure 3-1 Test Cell Setup

The combination of the supercharger rig and back-pressure valve was utilised to simulate a turbocharged engine where the back-pressure valve was controlled to a set back-pressure to simulate the turbine inlet conditions for the single cylinder engine similar to that of a V6 engine.

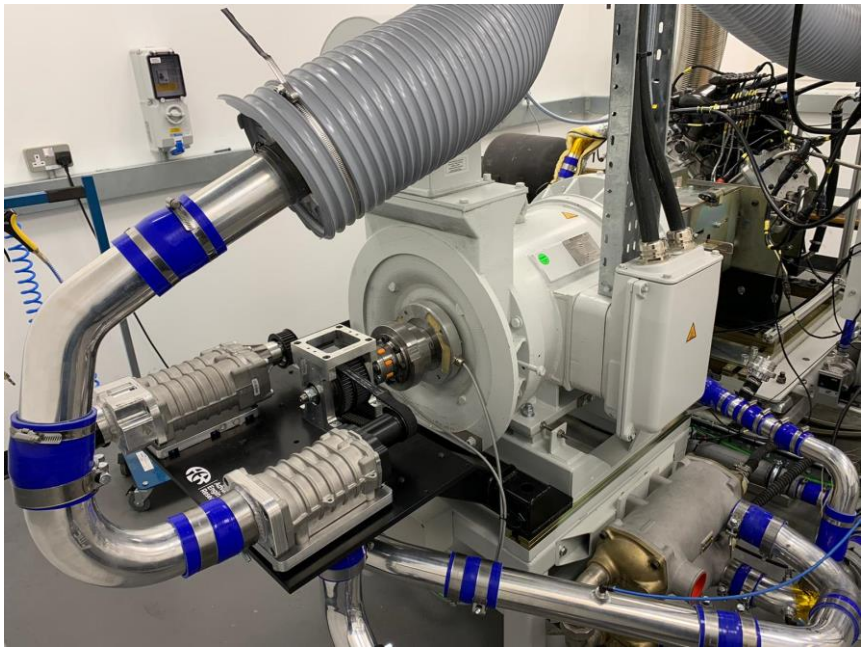

Figure 3-2 Supercharger Rig Connected to the Rear End of the Dynamometer

3.2 Physical Design of Single Cylinder Engine

A V6 engine was converted to a single cylinder engine by removing reciprocating components from bank 1 and leaving the pistons and connecting rods as is on bank 2 of the engine. Figure 3-4 shows all the connecting rods of the V6 engine connected to the crankshaft on the left image and only 3 connecting rods belonging to one bank of the engine and spacers replacing the other bank's connecting rods on the right image. The head in the redundant bank of the engine was replaced with a deck plate so as to reduce coolant and oil flow circuit lengths which would result in the reduction of heat rejection of the engine due to reduced contact surface areas for the oil and coolant circuits.

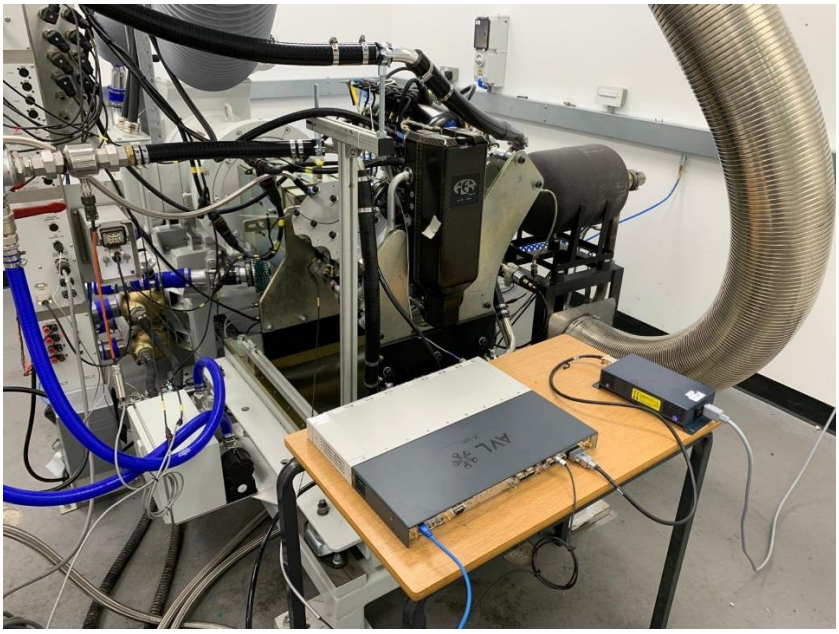

Figure 3-3 Single Cylinder Research Engine Setup

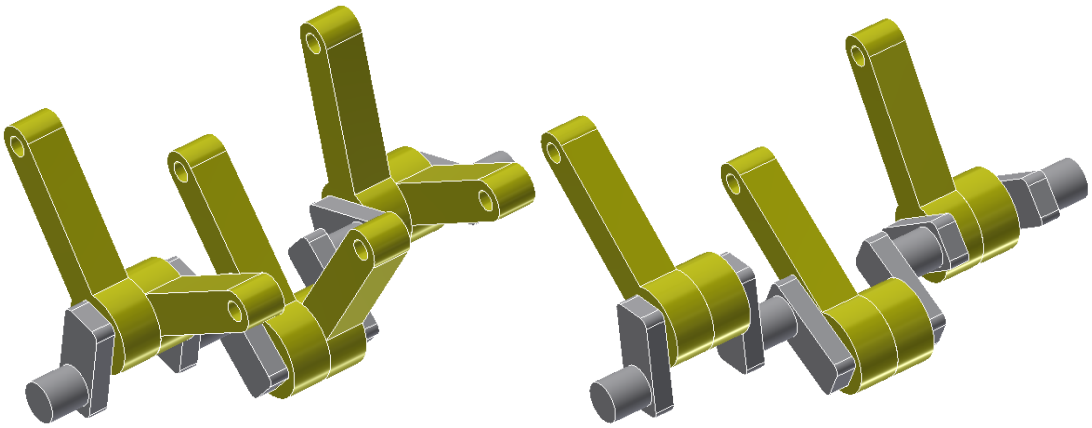

Figure 3-4 Connecting Rods Arrangement on the V6 Engine (Left) and Single Cylinder Engine (Right)

3.2.1 Engine Balancing- Reciprocating Inertia Forces

The V6 engine under consideration can be visualized as two three-cylinder in-line engines inclined 90 degrees to each other with the crank throws for each cylinder bank alternately staggered along the crankshaft length. Primary and secondary forces for an in-line three cylinder engine are balanced. Thus, a V6 engine, which is a combination of two in-line three cylinder engine is also balanced. (Heisler, 1995)

As the V6 engine, which is to be converted to a single cylinder research engine, has a common pin crankshaft for both the banks, the now-removed connecting rods were replaced with spacers. Since the counterweights of the engine crankshaft were optimized for the parent V6 engine, the single cylinder engine which is based on an I3 will need to have its counterweight mass reduced to prevent over-balancing and thus prevent higher main journal bearing loads.

The reduction in counterweight mass was assessed via a 1D Cranktrain simulation model of the engine in GT Suite. Figure 3-5 demonstrates the influence of different counterweight masses on the bearing loads of the journal bearing closest to the firing cylinder.

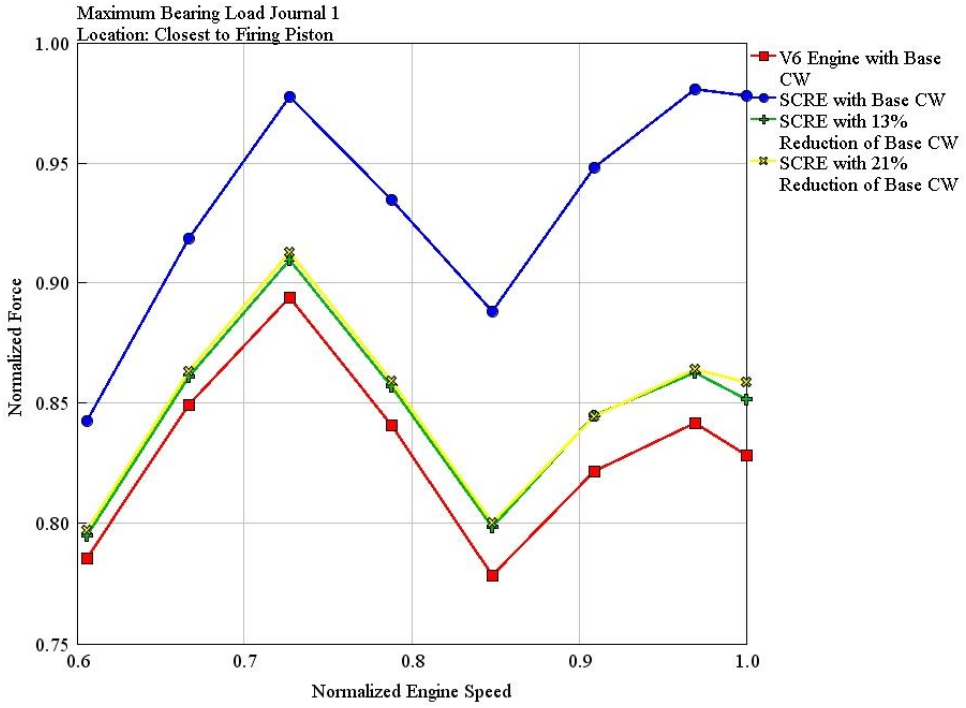

Figure 3-5 Comparison of Maximum Bearing Loads of V6 Engine with Base CW vs SCE with CW Mass Iteration

It was determined that the SCE equipped with a CW mass – 13% less than the base CW would be sufficient to reduce the bearing loads arising from an over-balanced condition.

3.2.2 Flywheel Inertia

Since a single cylinder engine will have higher speed and torque fluctuations as the converted engine would now have a single firing cycle as opposed to six firing cycles in 720 CAD, the higher speed and torque fluctuations may cause instability and unwarranted vibrations. To mitigate this condition, the flywheel inertia of the engine was increased as the flywheel of an engine is designed to store rotational energy and thus smoothen the power output.

The rotational energy contained in a flywheel is dictated by:

$$K = \frac{1}{2} I\omega^2 \qquad \text{Eqn (3-1)}$$

a higher inertia of the flywheel of single cylinder engine would allow for increased storage capacity of rotational energy which would aid in stabilising the torque output of the engine.

To achieve this, the coefficient of speed fluctuation of the flywheel for the V6 engine was calculated at the idle rpm of engine, using the following expression:

$$C_f = \frac{Range\ of\ Speed}{Average\ Speed} \qquad \text{Eqn (3-2)}$$

Where: $Range\ of\ Speed = Max\ Speed - Min\ Speed$ Eqn (3-3)

$$Average\ Speed = \frac{Max\ Speed + Min\ Speed}{2} \qquad \text{Eqn (3-4)}$$

The figure obtained from the above expression for the V6 engine was then utilised as a benchmark for the parametric study of the flywheel inertia required- for the design of a new flywheel for the single cylinder engine.

Figure 3-6 compares the 1D simulated flywheel speed fluctuations of V6 engine with the SCE along with various iterations of flywheel inertia.

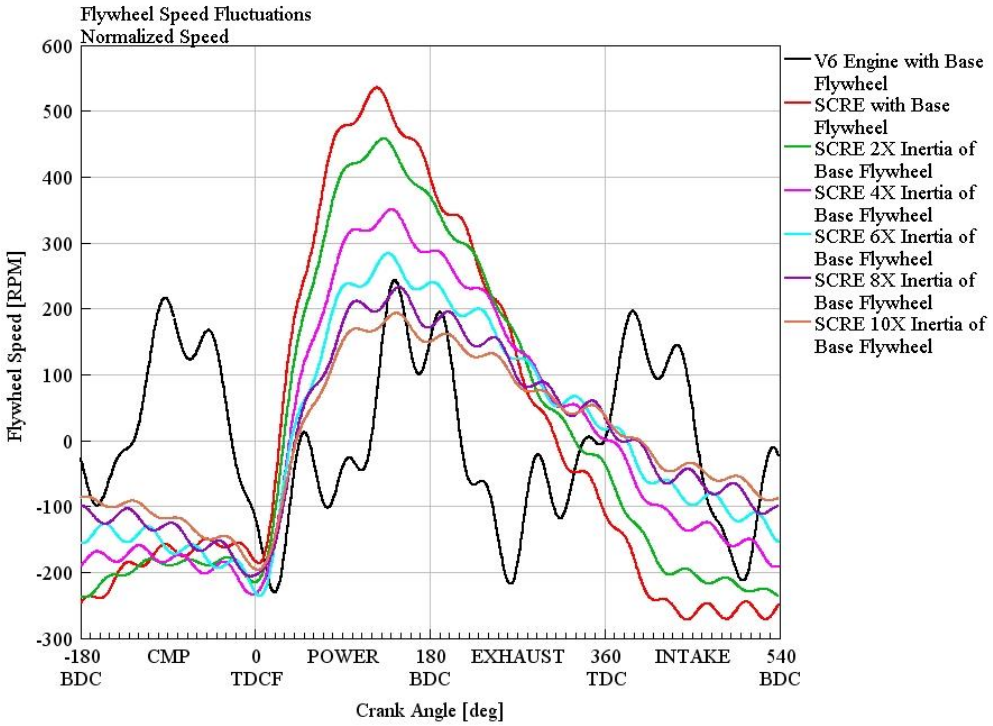

Figure 3-6 Comparison of Flywheel Speed Fluctuations of V6 Engine with Base Flywheel vs SCE with Flywheel Inertia Iteration

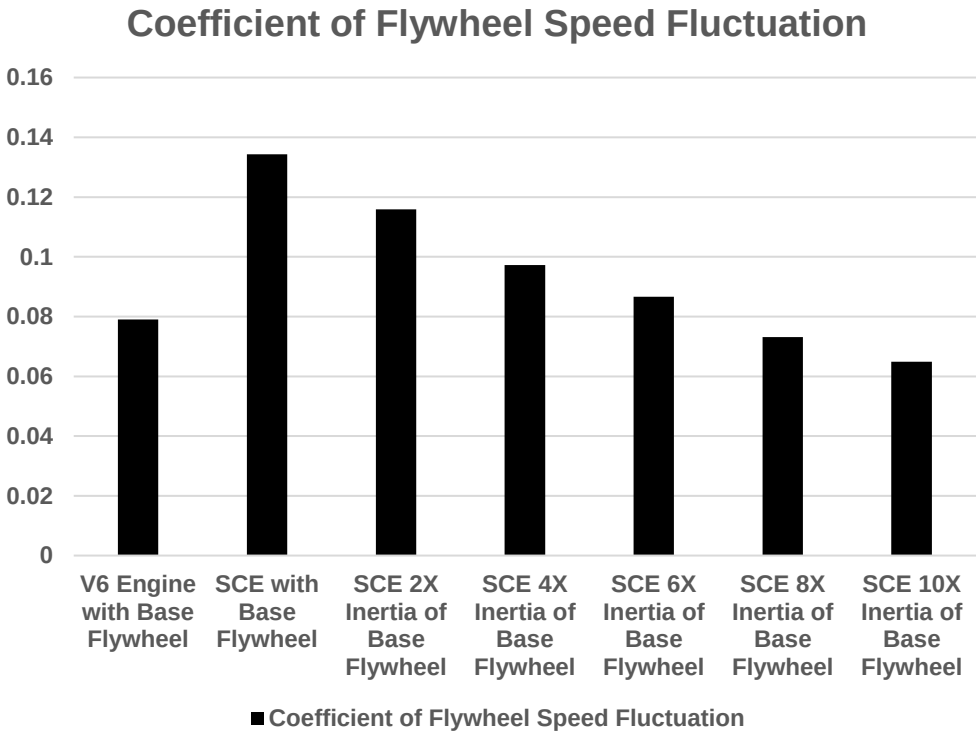

Figure 3-7 Comparison of the Flywheel Speed Fluctuations of Various Flywheel Inertias

Figure 3-7 compares the V6 engine and SCE's speed fluctuations with varying flywheel inertias. It was found that the SCE with a minimum of 8 times the inertia of the base flywheel has its coefficient of flywheel speed fluctuation comparable to that of the V6 engine with the base flywheel and hence it was decided that a flywheel of 8 times the inertia of the base flywheel should be installed on the SCE.

3.2.3 Pumping Losses from Redundant Cylinders

It was known that the redundant cylinders would greatly increase the friction power of the SCE. To reduce the losses arising from the redundant cylinders, utilization of cylinder valve deactivation method was explored.

Shutting valves permanently for all the strokes of the engine results in recovering the pumping power during the intake and exhaust stroke of the engine. Deactivation of valves was achieved by machining the cam lobes and by using high stiffness springs on the valves.

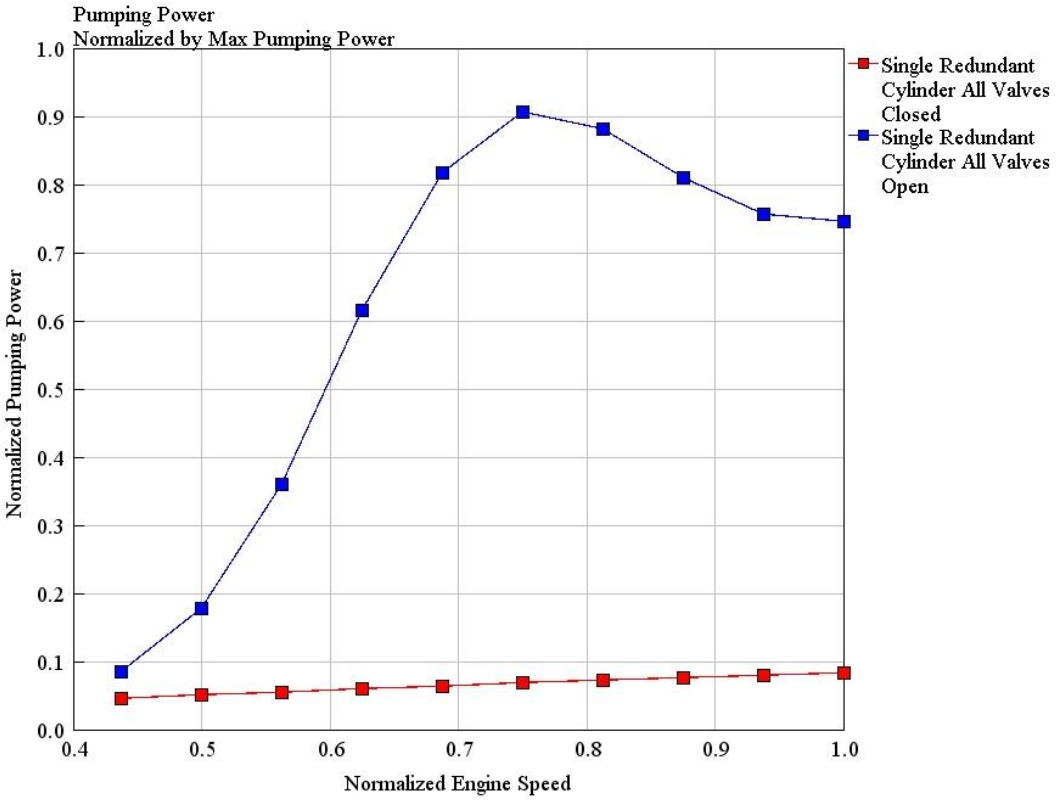

Figure 3-8 Comparison of Simulated Pumping Power vs Engine Speed for All Valves Closed and All Valves Open

Figure 3-8 shows the 1D computed comparison of the pumping power losses when valves of 2 redundant cylinders were deactivated and in the second case, left activated. The case where all valves were deactivated shows reduced pumping power losses which can be attributed to the recovery of the pumping energy from the compression stroke at the expansion stroke and recovery of the pumping energy from the exhaust stroke at the intake stroke.

3.2.4 Engine Gas Path

The intake and exhaust system of the single cylinder engine is to be designed such that it matches the instantaneous intake and exhaust port pressures of the multi cylinder engine so as the match the volumetric efficiency ensuring that the exact charge mass is contained in the combustion chamber and exact percentage of residuals is contained in the combustion chamber of the single cylinder engine when compared with the multi cylinder engine.

3.2.4.1 Intake System

To achieve an optimized intake path for the SCE, 1D gas path optimization simulation study was carried out on the intake manifold system of the engine. Various authors such as Asad et al. (2011) and Harrison and Dunkley (2004) recommend using an intake plenum or an intake buffer tank before the engine's intake manifold, however these methods hold true and valid for naturally aspirated engines as these engines rely on the intake stroke of the piston to draw air charge. Since forced induction methods are utilised in this engine, the need for an intake buffer tank is redundant as the boosting system is capable of offsetting the minor reductions in the volumetric efficiency of the engine.

The intake system of the V6 engine was first modelled in 1D to generate baseline data of the intake port pressure pulsations. Figure 3-9 demonstrates the correlation of the modelled intake port pressures with test data at Runner 3.

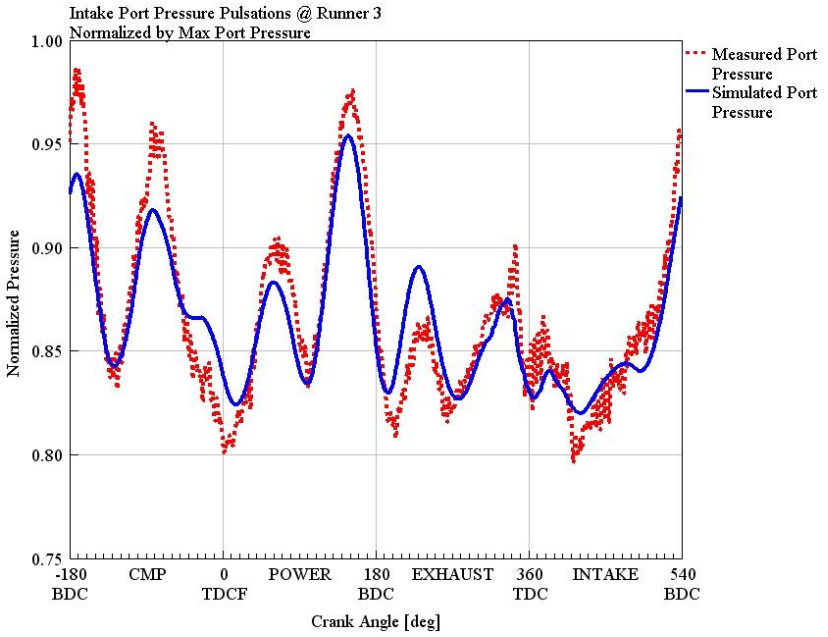

Figure 3-9 Simulated Intake Port Instantaneous Pressure Correlation with Measured Test Data

It was determined via 1D optimization study that removing the two runners (Runner 2 and Runner 3) of the redundant two cylinders of the engine sufficed in matching the single cylinder engine's intake port pressure fluctuations during intake valve opening period, comparable to that of the multi cylinder engine.

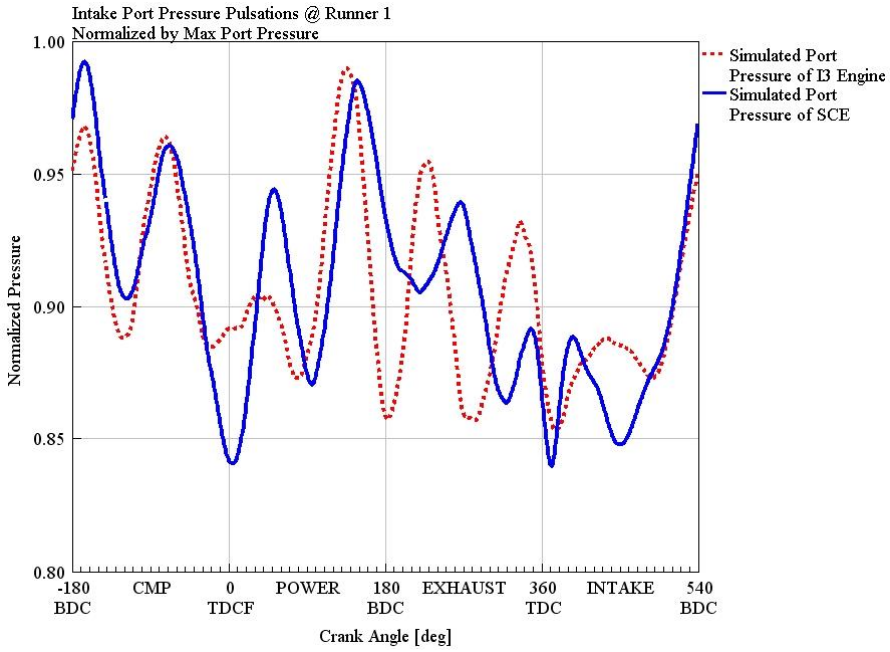

Figure 3-10 Comparison of Intake Port Instantaneous Pressure of a Cylinder in One Bank of the V6 Engine and the SCE

3.2.4.2 Exhaust System

The exhaust system of the single cylinder engine was to be designed such that it matched the instantaneous exhaust port pressures of the multi cylinder engine so as to match the residuals in the combustion chamber which would aid in matching the combustion characteristics of the single cylinder engine with the multi cylinder engine. In addition to matching the exhaust port pressures, the highly boosted single cylinder engine was found to produce high exhaust pressure fluctuations which resulted in highly fluctuating lambda sensor output which severely impacted the normal functioning of the engine as the fluctuating lambda sensor output caused the closed loop fuel control system to make changes to the quantity of fuel injected which resulted in an unstable engine.

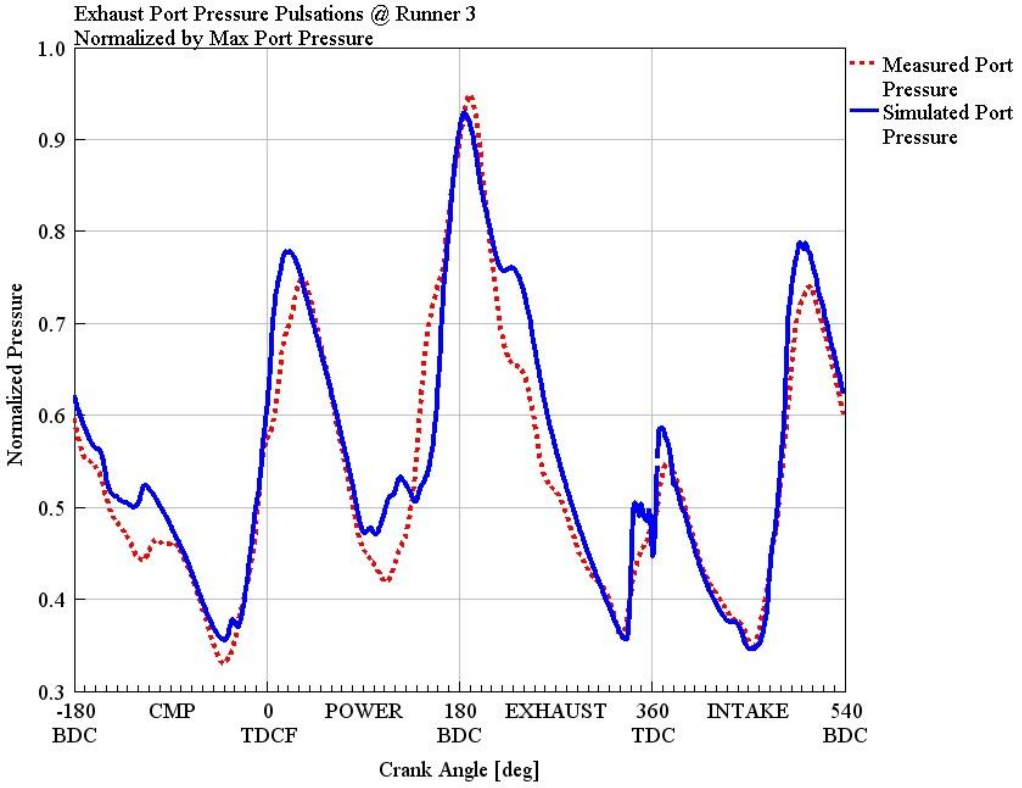

Figure 3-11 Simulated Exhaust Port Instantaneous Pressure Correlation with Measured Test Data

The exhaust system of the V6 engine was first modelled in 1D to generate baseline data of the exhaust port pressure pulsations. Figure 3-11 demonstrates the correlation of the modelled exhaust port pressures with test data at Runner 3.

To cope with the high exhaust pressure fluctuations, an exhaust plenum was utilised with tuned exhaust runner lengths based on 1D gas path optimization simulation study of the single cylinder engine which resulted in dampening of the excess exhaust pressure fluctuations thus stabilizing the lambda sensor output, but also matching the instantaneous exhaust port pressure pulsations at exhaust valve open timing.

A backpressure valve in the form of an independent turbocharger wastegate with a closed loop control system controlling to a set target back pressure was utilised to simulate exhaust back pressure to replicate a turbocharged engine.

Figure 3-12 shows the comparison of simulated exhaust port pressure fluctuations of one bank of the V6 engine compared with the SCE with and without an exhaust plenum. It can be deduced from the results that without the exhaust plenum the instantaneous exhaust pressure exceeds the maximum instantaneous pressure of the base V6 engine by 1.3 times.

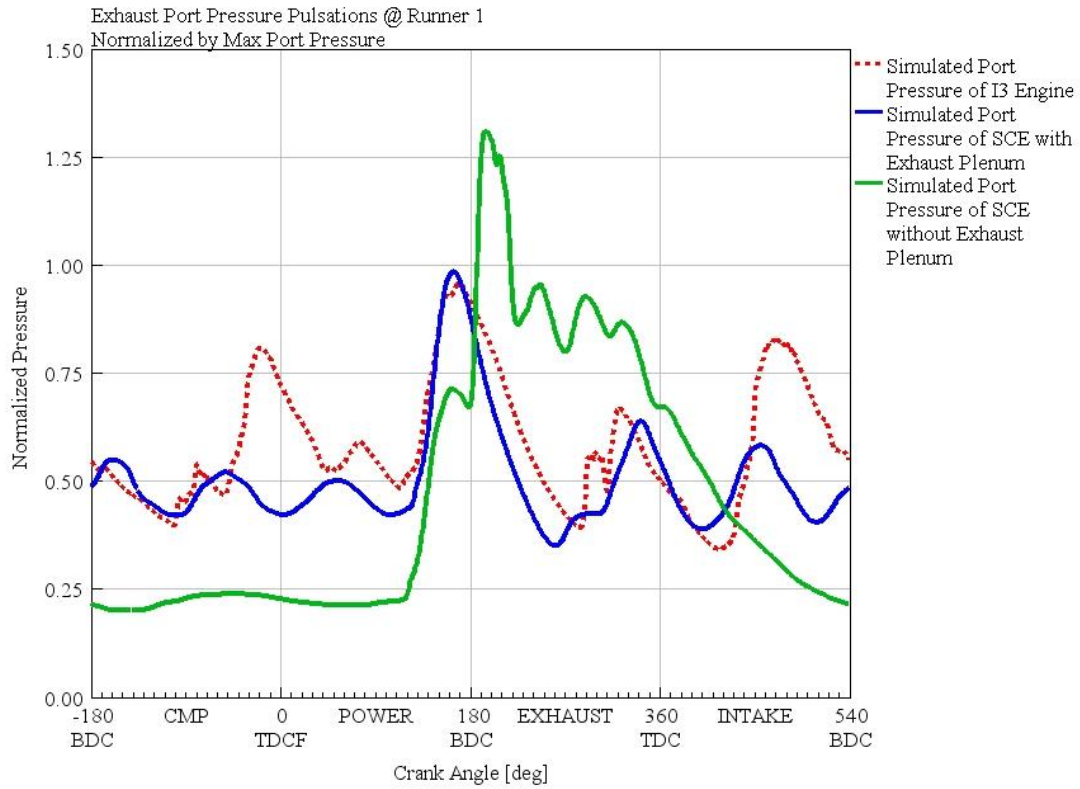

Figure 3-12 Comparison of Exhaust Port Instantaneous Pressure of a Cylinder in One Bank of the V6 Engine and the Single Cylinder Research Engine

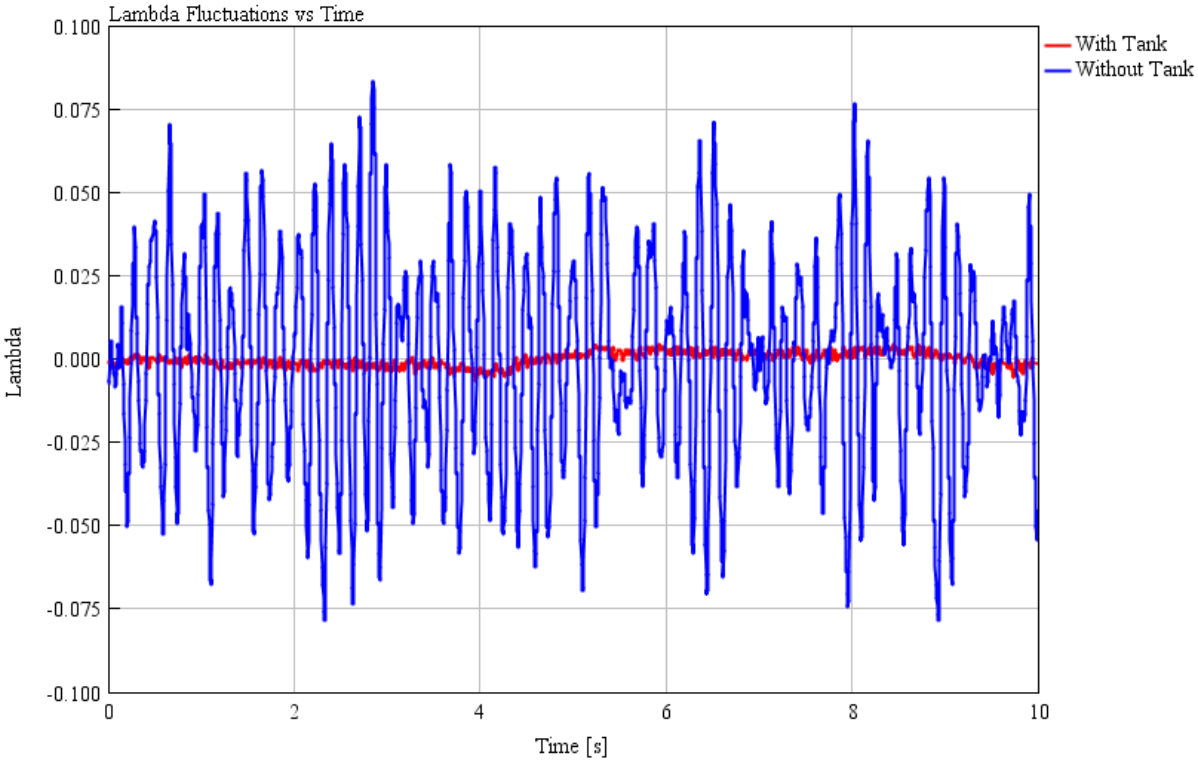

Figure 3-13 Comparison of Sensor Output of Instantaneous Lambda vs Time for With and Without Exhaust Buffer Tank Configurations

Figure 3-13 shows the comparison of the highly fluctuating instantaneous lambda sensor output of the SCE when it is without the exhaust buffer tank and a stabilized lambda sensor output when it was fitted with the exhaust buffer tank. These two cases were simulated in 1D, shown in Figure 3-14, and it was found that the instantaneous pressure fluctuations at the lambda sensor location was very high without the exhaust buffer tank than when the SCE with fitted with exhaust buffer tank.

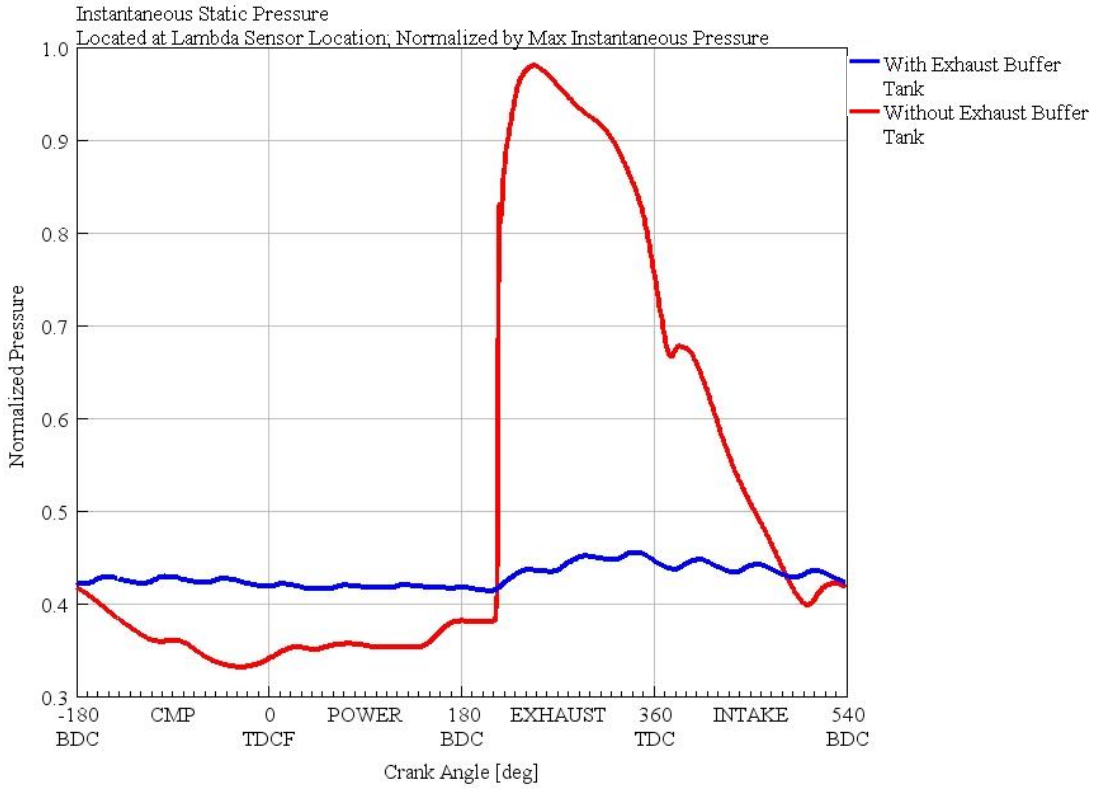

Figure 3-14 Comparison of Simulated Instantaneous Static Pressure at Lambda Sensor Location for With and Without Exhaust Buffer Tank Configurations

3.2.5 In-Cylinder Pressure Measurement and Simulation

A predictive SITurb 1D combustion model for the V6 engine was developed in GT Power using- 100 cycle-averaged in-cylinder, intake and exhaust manifold instantaneous pressure measurements, which predicts the burn rate of the charge mass in the combustion chamber for varying operating ranges. The model takes into account the cylinder's geometry, spark location, spark timing, air motion in the cylinder, charge mass and fuel properties (S. D. Hires et al., 1978; Norman C. Blizard and James C. Keck, 1974; T. Morel et al., 1988). Using a SITurb predictive combustion model to compare and predict in-cylinder pressure of the SCE is advantageous in the conversion of the V6 engine into a SCE, as the impact of the changes to volumetric-efficiency/engine-breathing (due to changes of gas path design for SCE) on combustion can be more accurately predicted when using a predictive model as opposed to a non-predictive or commonly used Wiebe combustion model.

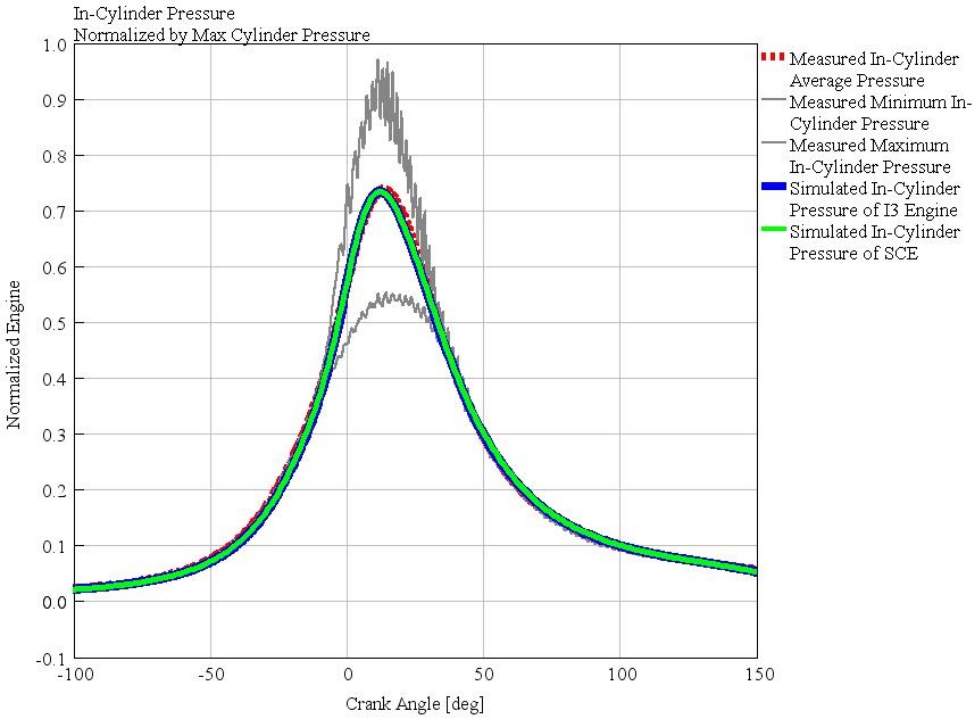

Figure 3-15 Simulated In-cylinder Instantaneous Pressure Correlation with Measured Test Data

Figure 3-15 shows the measured in-cylinder pressure against the simulation datasets. A good correlation was achieved between the simulated and measured data of the V6 engine. The simulated SCE in-cylinder pressure was found to match with the V6 engine's in-cylinder pressure for the same ignition timing and same knock index.

3.3 Engine Testing Results and Discussion

During the initial performance testing of the engine on the dynamometer, it was found that the performance of SCE was much lower than the performance of a single cylinder of the V6 engine as shown in Figure 3-16. The SCE power was found to be 8.6% and 16.57% lower than that of a single cylinder of the V6 engine at lower and higher engine speed sites, respectively.

It was anticipated that the redundant two cylinders on the SCE would result in additional parasitic losses via friction between the redundant pistons and liners. To quantify the friction power loss of the SCE, a motoring test was conducted to compare the friction power of the SCE with that of the single cylinder of a V6 engine.

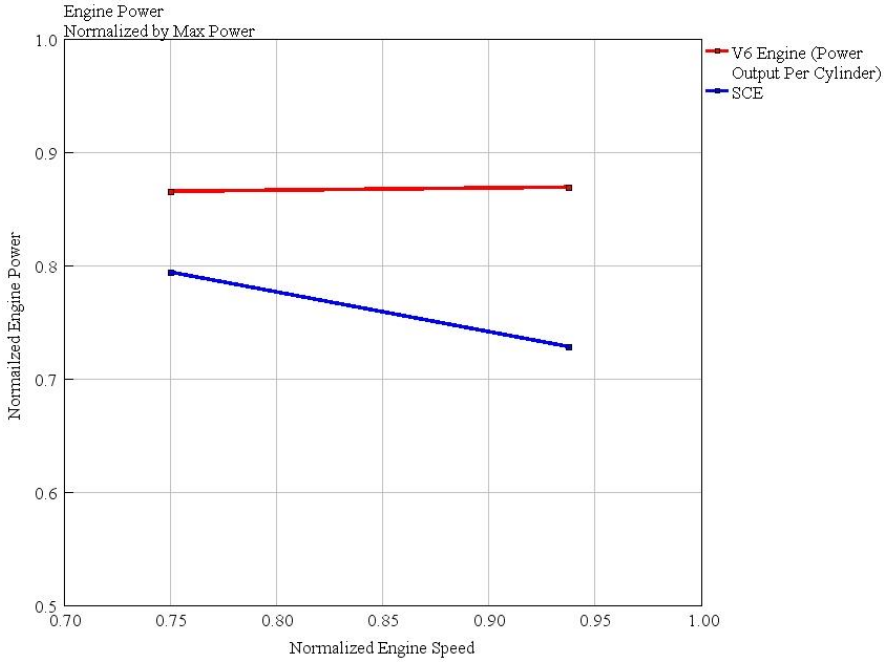

Figure 3-16 Comparison of Measured Engine Power Output of a Single Cylinder of V6 Engine and SCE

Figure 3-17 shows the comparison of measured friction power of the SCE with a single cylinder of the V6 engine, both of which have been corrected for pumping power losses. The friction power of the SCE was found to be 1.23 times and 1.58 times per cylinder of the V6 engine at the lower and higher engine speed sites. Based on the measured friction data, a novel power correction method was devised for the SCE to calculate the SCE's equivalent power output comparable to that of a single cylinder power output of the V6 engine.

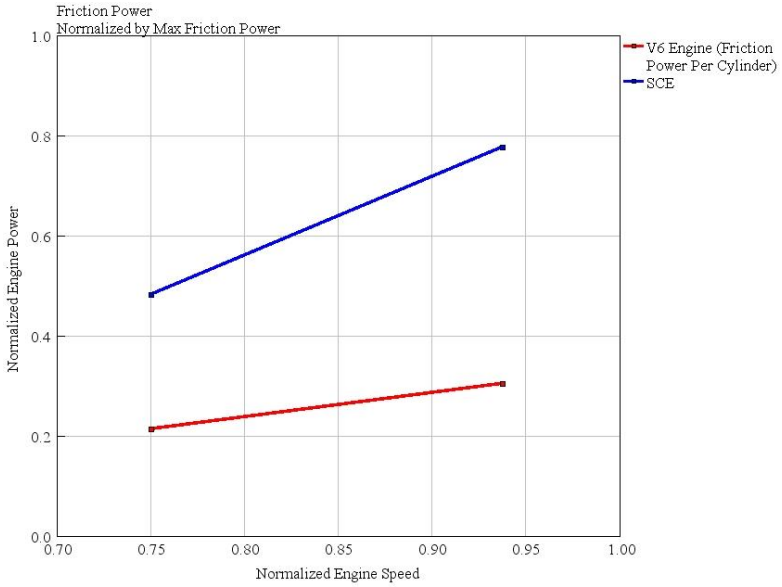

Figure 3-17 Comparison of Measured Engine Friction Power Output of a Single Cylinder of V6 Engine and SCE (Pumping Power Corrected)

The friction power correction factor was calculated by first adding the friction power of SCE to the measured brake power output of the SCE so as to obtain the indicated power and then adding the friction power of the single cylinder of a V6 Engine to the indicated power of the SCE as calculated previously.

$$SCE_{BP} + SCE_{FP} = SCE_{IP} \qquad \text{Eqn (3-5)}$$

$$SCE_{IP} - \frac{1}{6}V6_{FP} = SCE_{Corr\,BP} \qquad \text{Eqn (3-6)}$$

Where:

SCE_{BP} = Brake Power Output of Single Cylinder Engine

SCE_{FP} = Friction Power of Single Cylinder Engine

SCE_{IP} = Indicated Power of Single Cylinder Engine

$V6_{FP}$ = Friction Power of V6 Engine

$SCE_{Corr\,BP}$ = Corrected Brake Power Output of Single Cylinder Engine representing the Power Output of a Single Cylinder of the V6 Engine

Figure 3-17 and 3-18 demonstrate the effectiveness of the friction power correction factor in correlating with 1/6th of measured V6 engine power and BSFC figures at low and high speeds.

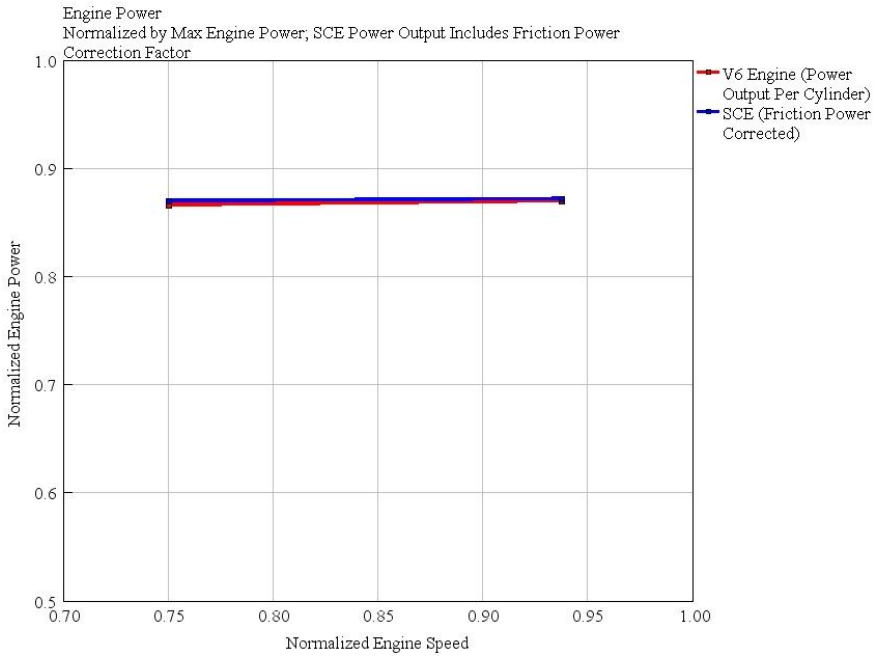

Figure 3-18 Comparison of Measured Engine Power Output of a Single Cylinder of V6 Engine and SCE (Friction Corrected)

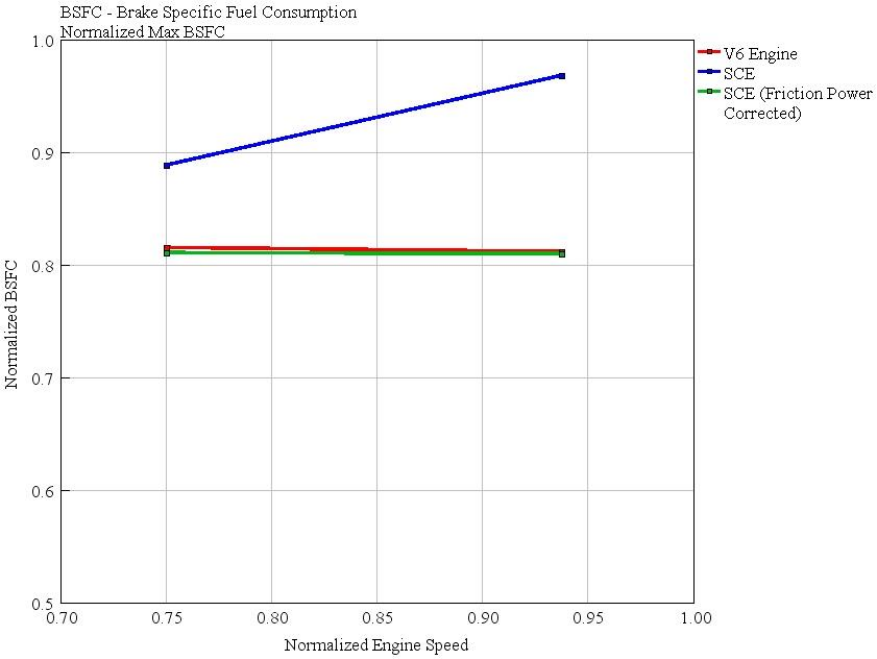

Figure 3-19 Comparison of Measured Engine BSFC of V6 Engine and SCE

The engine power and BSFC figures of the single cylinder engine were found to be within 1.2% of the multi-cylinder engine.

3.4 Conclusions

The methodology presented was shown to be cost effective and the performance of the Single Cylinder Engine (SCE) was tested and it was demonstrated that with the utilisation of the friction correction factor in the power output of the SCE, calculated from measured friction power of the SCE and the V6 engine, the power and BSFC figures for the SCE were within 1.2% of the multi-cylinder engine.

4. Experimental Setup and Methodology

4.1 Research Methods

A combination of engine testing and simulation was utilised to achieve the objectives set out for this research. The engine was first tested with a spark ignition system at various relative air/fuel ratios at full load condition to generate baseline performance data of the engine. A 1D CFD simulation model was developed which was correlated to the baseline performance data obtained from engine testing. A 3D CFD simulation model was then developed with boundary conditions obtained from the 1D CFD simulation model to build and study various prototype parts- such as the pre-chambers and piston crown designs. The prototype parts were then fitted onto the engine for testing to generate performance data at full load condition. The engine testing results with the prototype parts installed were then utilised to correlate 1D and 3D CFD simulation models with test data to study performance improvements or losses at various operating conditions with the pre-chamber ignition system to meet the objectives of the research.

The engine testing methods and simulation models utilised have been described in detail in the forthcoming sections of this chapter.

4.2 Engine Test Setup

4.2.1 Engine Test Schedule

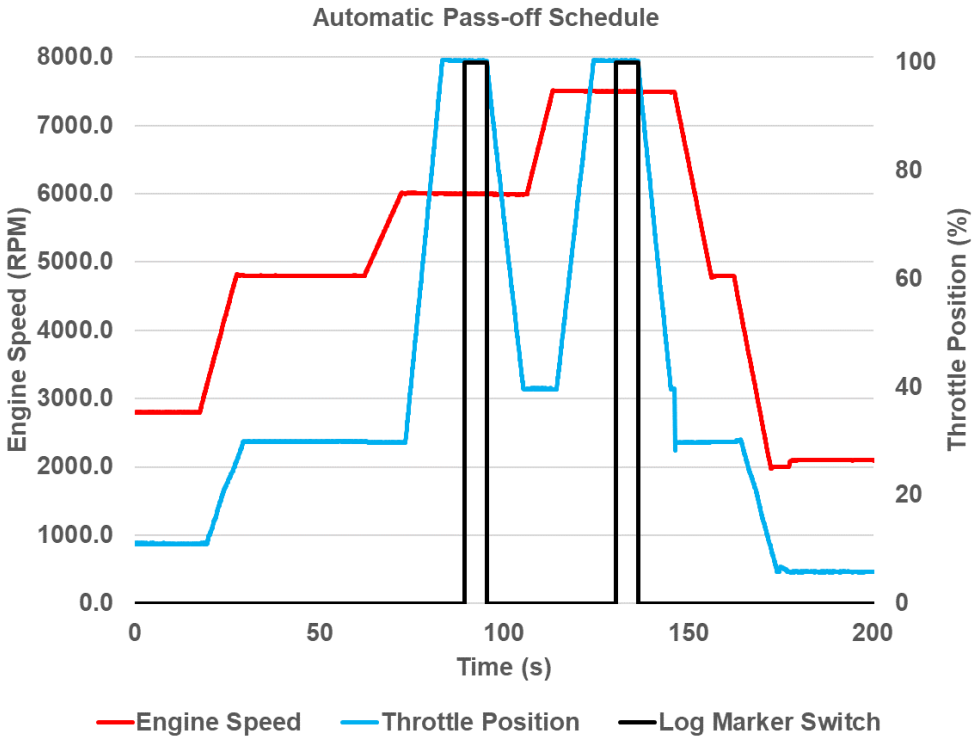

Figure 4-1 Engine Test Automatic Pass-off Schedule

Engine testing was automated with a set schedule to ensure repeatability of tests. Figure 4-1 shows the engine pass-off schedule where the engine was warmed up at 4800 rpm and 30% throttle to attain and stabilise to set target oil and coolant temperatures - which were set to 85 °C. The engine was then scheduled to ramp up to 6000 rpm and subsequently ramp up throttle to 100% where the engine was set to operate at full load for 12 seconds to stabilise all parameters before recording the engine performance parameters. The various engine performance parameter readings were recorded for the last 5 seconds of the engine test at full load which was synced with all data acquisition systems with a log marker switch as shown in Fig 1. The aforementioned steps were repeated when the engine was then ramped up to 7500 rpm.

4.2.2 Engine Calibration

The engine was calibrated to operate at set fuel flow targets as opposed to fixed load. For the experiments conducted as presented in this thesis, Le Mans Prototype Hybrid (LMP1-H) fuel flow limits were utilised as fuel flow targets for all the experiments. The LMP1-H fuel flow limit was 80 kg/h which is determined by FIA (FIA Sport / Technical Department, 2019). As 80 kg/h fuel flow limits applies to the whole engine, a V6 engine in this case, the single cylinder engine's fuel flow limit was calculated to be 13.33 kg/h was set as the fuel flow target for all the experiments.

A closed loop lambda control system was utilised which controlled the manifold pressures to attain the set lambda target and set fuel flow target. The intake air temperatures were controlled to 35 °C by charge air coolers for all test conditions.

The engine performance was tuned for lowest BSFC at all operating points. Ignition timings were knock limited.

4.2.3 Ignition Systems

An M12 conventional spark plug with a conventional gap and >70mJ ignition energy was utilised to test the engine in spark ignition mode. The pre-chamber ignition system was developed in a parallel study. Figure 4-2 shows the pre-chamber assembly. The pre-chamber was designed to be a direct replacement for the spark plug utilised in the spark ignition tests thus requiring no modifications. A standard M10 NGK spark plug >70J was utilised in the pre-chamber. Different thickness of washers was utilised to ensure that the nozzle orientation was the same every time the pre-chamber was removed and fitted again on the engine.

Figure 4-2 M10 Spark Plug Utilised in the Pre-chamber (Left) and Pre-chamber Spark Plug Assembly with Control Washer (Right)

4.2.4 In-cylinder Pressure Instrumentation

AVL X-ion high-speed data acquisition system was utilised to record and monitor in-cylinder pressure signals from the single cylinder engine. An AVL GO15DK Gen1 piezoelectric 0-1000 bar pressure sensor was utilised for this project. As the engine to be tested was a high BMEP motorsport engine which was calibrated to run at the knock limit and can result in high amplitude knocking combustion cycles, the high range sensor was chosen due to its ruggedness ability to withstand knocking cycles. An example of recorded knocking cycles is shown in Figure 4-3. Specification of the in-cylinder pressure sensor is provided in Appendix section of this dissertation.

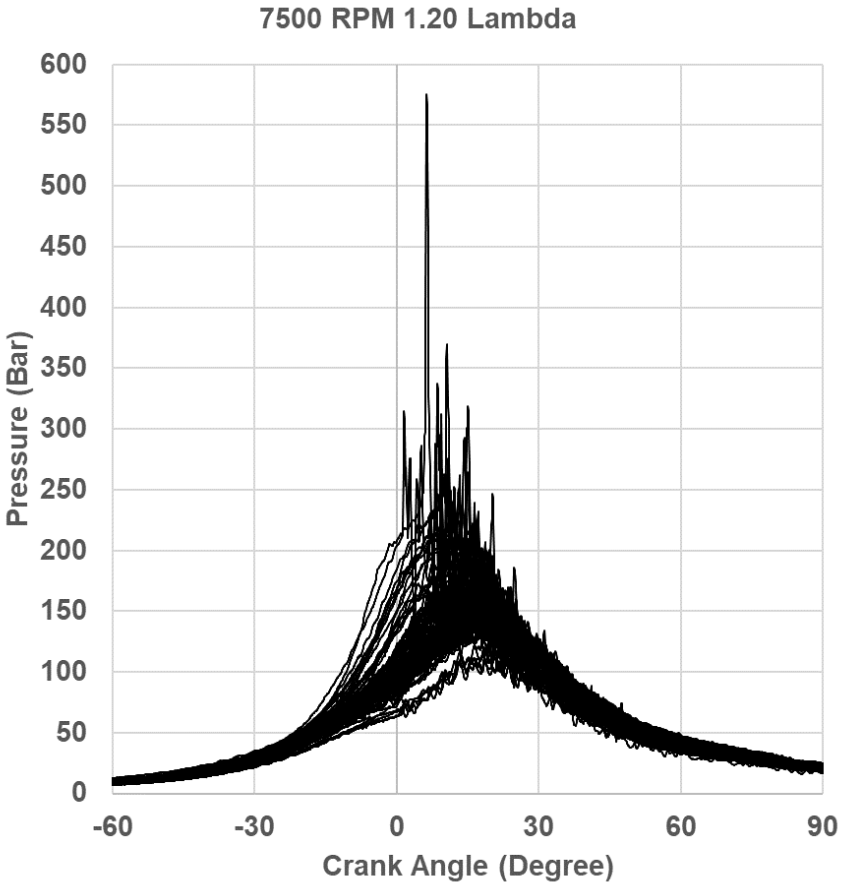

Figure 4-3 Recorded Knocking Cycles at 7500RPM with Relative air/fuel ratio of 1.20

4.3 In-cylinder Pressure Data Processing and Analysis

Heat release calculations from the recorded in-cylinder pressure data were conducted via AVL Concerto 5 software.

The pressure signal was filtered using low pass and high pass filters for combustion calculations and knock signal processing, respectively. The filtering frequency was determined via utilising the draper equation as shown in Equation 4-1 for the first mode where (m,n) = (1,0).

$$f_{m,n} = \alpha_{m,n} \frac{c_s}{\pi B} \qquad \text{Eqn (4-1)}$$

To calculate various combustion performance parameters from the in-cylinder pressure data, the Thermodynamics2Mass function was utilised in AVL Calcgraf – which is a graphical editor designed to create calculation models to process the raw in-cylinder pressure signals.

A simplified process was utilised to calculate the heat release where the energy effectively delivered to the gas from the cylinder pressure is computed. The polytropic coefficient curve is also taken into account in relation to the temperature by an approximation formula. Surface losses are neglected, the displayed heat release is therefore accordingly lower than the actual energy released. The calculation of heat release which is based on the first law of thermodynamics is shown in Equation 4-2. (AVL List GmbH, 2020)

$$Q_i = \frac{K}{\kappa_i - 1} V_{i+n} \left[p_{i+n} - p_{i-n} \left(\frac{V_{i-n}}{V_{i+n}} \right)^{\kappa_i} \right] \qquad \text{Eqn (4-2)}$$

$$Q_0 = 0, X_0 = 0$$

Where κ_i = Polytropic coefficient

n = Interval (degree)

C = Constant

p = Pressure

V = Volume

The calculation of polytropic coefficient which is dependent on temperature is shown in Equation 4-3.

$$\kappa_i = \frac{0.2888}{Cv_i} + 1 \qquad \text{Eqn (4-3)}$$

Where Cv_i is the specific heat at constant volume. Calculation of Cv_i shown in Equation 4-4.

$$Cv_i = 0.7 + T_i(0.155 + A_i)10^{-3} \qquad \text{Eqn (4-4)}$$

Where A_i is the coefficient which takes into account the internal EGR rate in the case of gasoline engines which has a value of 0.1.

T_i = Temperature

The temperature was calculated by utilising equation 4-5.

$$T_i = \frac{p_i.V_i}{m.R} \qquad \text{Eqn (4-5)}$$

Where R = Universal gas constant = 287.12kJ/kg/K

m = mass of air (kg)

The charge mass m present in the combustion chamber was calculated from measured lambda and measured fuel flow rate.

4.4 Simulation Methodology

4.4.1 1D CFD

GT Power engine simulation software was utilised to model the V6 and single cylinder engine in 1D for various studies. The 1D CFD model was utilised to provide boundary conditions for 3D CFD studies such as instantaneous intake and exhaust port pressures and temperatures. The 1D CFD model was correlated to test data as described in Section 3.2.5. In the earlier stages of the research, a predictive 0D combustion model, which was calibrated to V6 engine test data, was utilised to predict combustion parameters and performance of the single cylinder engine during development phase as the predictive combustion model takes into account the effects of intake and exhaust acoustics and its subsequent influence on the in-cylinder flow and turbulence parameters via 0D Flow and Turbulence models – all of which affect combustion. This combustion model was subsequently replaced with a spark-ignition Wiebe combustion model ('EngCylCombSIWiebe') whose parameters such as MFB50% anchor angle and MFB10-90% burn durations were matched with the single cylinder engine test data to study instantaneous residual concentrations in the combustion chamber and provide boundary conditions for 3D CFD numerical models of the single cylinder engine.

The SI Wiebe combustion model imposes the burn rate for spark-ignition engines using a Wiebe function, which approximates the typical shape of an SI burn rate. The following equations are utilised in the SI Wiebe combustion model. (Gamma Technologies, 2019)

Inputs:

AA = Anchor Angle (deg)

D = Duration (deg)

E = Wiebe Exponent ("def" = 2.0)

CE = Fraction of Fuel Burned (also known as "Combustion Efficiency")

BM = Burned Fuel Percentage at Anchor Angle ("def" = 50%)

BS = Burned Fuel Percentage at Duration Start ("def" = 10%)

BE = Burned Fuel Percentage at Duration End ("def" = 90%)

Calculated Constants: BMC = -ln(1-BM) Burned Midpoint Constant

BSC = -ln(1-BS) Burned Start Constant

BEC = -ln(1-BE) Burned End Constant

$$WC = \left[\frac{D}{BEC^{1/(E+1)} - BSC^{1/(E+1)}}\right]^{-(E+1)}$$ Wiebe Constant Eqn (4-6)

$$SOC = AA - \frac{(D)(BMC)^{1/(E+1)}}{BEC^{1/(E+1)} - BSC^{1/(E+1)}}$$ Start of Combustion (deg) Eqn (4-7)

Burn Rate Calculation

Θ = Instantaneous Crank Angle

The cumulative burn rate is calculated, normalized to 1.0. The combustion starts at 0.0 (0.0% burned) and progresses to the value specified by the "Fraction of Fuel Burned Attribute", which is typically close to 100% for a lean burn engine.

$$Combustion(\theta) = (\mathrm{CE})\left[1 - e^{-(WC)(\theta - \mathrm{SOC})^{(E+1)}}\right]$$ Eqn (4-8)

4.4.2 3D CFD

CONVERGE CFD was utilised to study combustion and in-cylinder flow via 3D computational fluid dynamics (CFD). CONVERGE CFD was utilised over the other commercially available 3D CFD programs due to the fact that the program eliminates the grid generation bottleneck from the simulation process. CONVERGE CFD automatically generates a perfectly orthogonal, structured grid at runtime based on simple, user-defined grid control parameters. A modified cut-cell Cartesian method is utilised that eliminates the need for the body fitted computational cells for the geometry of interest. This method allows for the use of simple orthogonal grids and completely automates the mesh generation process and thus eliminates the need to manually generate a grid thus significantly improving workflow.

An in-cylinder 3D CFD model of the single cylinder research engine was developed and further modified to evaluate different piston shapes and tumble generation strategies to study their effect on combustion for both spark and pre-chamber ignited engines.

4.4.2.1 Turbulence Modelling and Flow Motion

The RANS based RNG k−ε turbulence model was utilised to capture the sub-grid scale influence of turbulence on the momentum, energy and species transport fields due to the model being able to account for higher scales of motion compared to the other turbulence models available. A summary of the applications, advantages and disadvantages of various turbulence models considered is shown in Table 4-1.

Model Name	Applications	Advantages	Disadvantages
Standard k-ε	Planar shear layers, internal recirculating flows	Robust, good convergence rate, low memory requirements	Performs poorly in adverse pressure gradients, separation, jet flows
RNG k-ε	Rotating cavities, indoor air simulation, IC engines	Accounts for more scales of motion	Less numerically stable
Realizable k-ε	Rotational flows	Prevents non-physical values for turbulence quantities	Possibly more dissipative
v^2-f and $\zeta-f$	Low Re wall-bounded flows	Superior behaviour with highly resolved walls	More costly, not appropriate for high Re
Standard k-ω	- Wall-bounded flows, free shear, low Reflows - Suitable for complex boundary layers under adverse pressure gradient and separation	Use to predict transition	Sensitive to free-stream conditions
k-ω SST	Gas turbines, external flows, low Re flows	Good resolution of flow near wall	Dependence on wall distance makes it less suitable for free shear flows
RSM	Jet impingement, cyclone separators, swirl combustors, other highly 3D flows	Superior performance in flows with strong anisotropy	Most costly

Table 4-1 Comparison of RANS Turbulence Models (Convergent Science, 2017)

The tumble ratio in X direction was defined as the ratio of the angular speed of the flow about the centre of mass in the X direction, ω_1, to the angular speed of the crankshaft, $\omega_{crankshaft}$, as shown in Equation 4-9.

$$tumble\_ratio_X = \frac{\omega_1}{\omega_{crankshaft}} \qquad \text{Eqn (4-9)}$$

4.4.2.2 Near Wall Behaviour

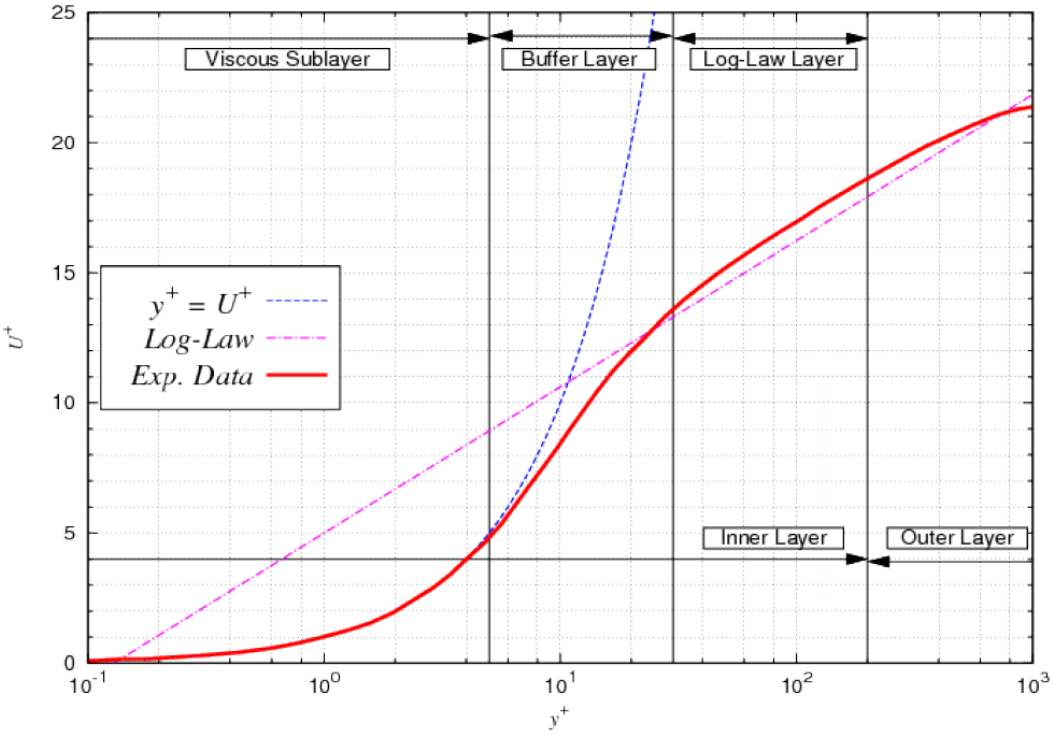

Figure 4-4 Comparison of Non-dimensional Velocity, Wall Distance and Law of Wall with Experimental Data

A law of wall model was utilised to estimate the local velocity in the boundary layer. In turbulent flows, the velocity adjacent to walls changes rapidly. To quantify this strong velocity change, non-dimensional wall distance and velocity were utilised as shown in Equations 4-10, 4-11 and 4-12.

$$u^+ = \frac{u}{u^*} \qquad \text{Eqn (4-10)}$$

$$y^+ = \frac{yu^*}{v} \qquad \text{Eqn (4-11)}$$

$$u^* = \sqrt{\frac{\tau_{wall}}{\rho}} \qquad \text{Eqn (4-12)}$$

Where τ_{wall} is the shear stress at the wall, ρ is density and v is the kinematic density. The y+ values relate the cell size adjacent to the wall to the physical location in the boundary layer based on the local velocity. Resolving the flow

to the viscous sublayer would require a very small y+ and is thus very computationally expensive. Law of wall model was utilised to estimate the local velocity in the boundary layer without resolving the viscous sublayer as this method is computationally efficient. The law of the wall states that the average velocity of a turbulent flow at a certain point is proportional to the logarithm of the distance from that point to the wall of the fluid region. The single cylinder engine's combustion chamber model in 3D CFD was setup such that the adaptive mesh refinement (AMR) at the walls of the combustion chamber limited the mesh refinement to target a y^+ value of 100 to attain realistic estimation of boundary layer velocities. (Convergent Science, 2017)

4.4.2.3 Mesh Generation

A base cell size of 2 mm was utilised for the engine cylinder. Local grid refinements, such as AMR and fixed embedding, were utilised at regions where sharp gradients of flow variables were expected such as spark plug, valves and piston. Velocity AMRs were utilised in intake region during intake stroke and the cylinder region throughout the engine cycle which targeted a mesh size of 0.5 mm for a minimum velocity sub-grid value of 1m/s. Temperature AMR was utilised in the cylinder region during combustion phase which targeted a mesh size of 0.25 mm for a minimum temperature sub-grid value of 2.5 K.

The smallest cell size utilised was 0.125 mm which was utilised at the spark plug electrodes in spark ignition case and the 0.125mm cell size was utilised inside the entire pre-chamber for the pre-chamber case to accurately model and visualise flame kernel growth for both spark and pre-chamber ignition

cases. The mesh was not refined further as increasing the mesh resolution beyond 0.1 mm would not improve accuracy as there are no more scales to resolve in a RANS based turbulence model (Pomraning et al., 2014).

Figure 4-5 shows the mesh generation from spark and pre-chamber ignited engine's simulation models during combustion.

The maximum cell count was found to be 3.5 million cells during combustion phase and the pre-chamber simulation model took 12 days to complete simulation of a single 4-stroke cycle. The simulations were conducted on a 24 core, 48 thread CPU.

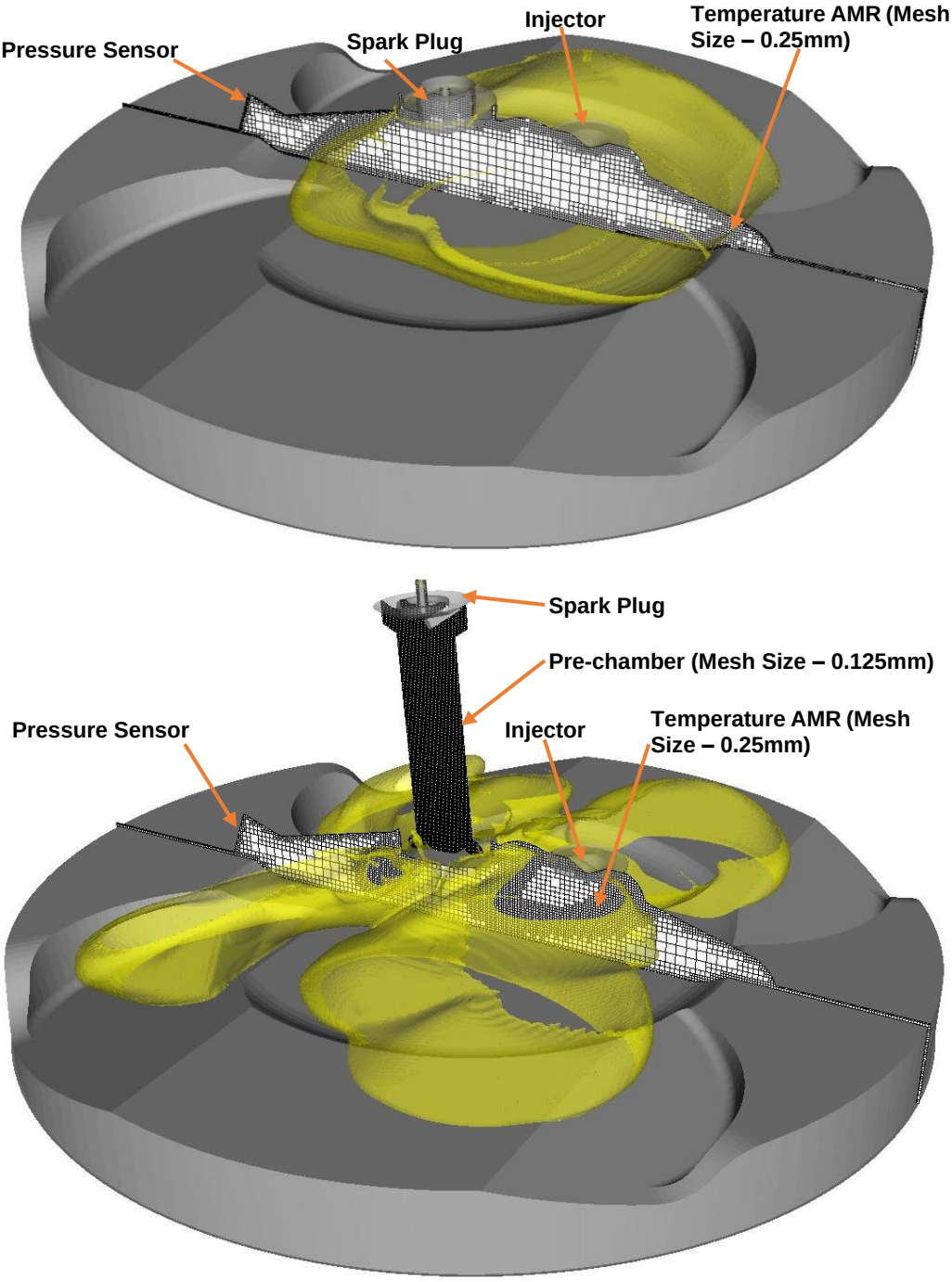

Figure 4-5 Depiction of 3D CFD Mesh Generation on X-axis Clip Plane for Spark Ignition Case (Top) and Pre-chamber Ignition Case (Bottom)

4.4.2.4 Spray Modelling

Spray modelling was conducted using a Eulerian Lagrangian approach where the Lagrangian solver was utilised to model discrete parcels and the Eulerian solver was utilised to model the continuous fluid domain- all of which were included in the software package. The parcels undergo several physical processes such as primary and secondary breakup – controlled by the Kevin -Helmholtz and Rayleigh-Taylor (KH and RT) constants, drop drag, collision and coalescence, turbulent dispersion and evaporation. However, due to the unavailability of a spray experiment setup it was not possible to tune the spray model coefficients and thus basic spray modelling options were selected without any tuning of the coefficients. The spray contained E20 fuel composition which was the fuel utilised in all experiments which consisted of 80% iso-octane and 20% ethanol.

4.4.2.5 Ignition Source Modelling

Spark ignition was modelled by introducing an energy source between the spark plug electrodes with a defined energy (based on the actual spark plug's actual energy discharge), volume and duration. This energy source was allowed to move with flow near the spark plug electrodes to simulate the plasma arc stretching.

4.4.2.6 Combustion Modelling

Combustion in the engine cylinder was simulated using the SAGE detailed chemistry solver which was available in the 3D CFD software (P. K. Senecal et al., 2003). The SAGE detailed chemistry solver utilises local conditions to calculate reaction rates based on principles of chemical kinetics and solves

detailed chemical kinetics during combustion and determines kinetically limited phenomena such as engine knock and emissions. The solver reads the reaction mechanism in CHEMKIN format and solves ODEs to find the reaction rates which then couples with the transport solver via source terms in the species transport equations. At each time-step, the chemistry solver calculates the new species mass fractions immediately prior to solving the transport equations where the change in the species mass fractions is treated as a source. The system of elementary reactions is solved using CVODES (general ODE solver). The forward reaction rate is given by

$$k_{fr} = A_r T^b e^{\left(\frac{-E_r}{R_u T}\right)} \qquad \text{Eqn (4-13)}$$

Where: A_r is the pre-exponential factor

b is the temperature exponent

E_r is the activation energy

R is the universal gas constant

The skeletal mechanism utilised in all simulation studies is built by merging a mechanism of Toluene Reference Fuel or TRF (Liu et al., 2013) and an ethanol mechanism (Marinov, 1999). The TRF mechanism contains individual mechanisms of n-heptane, iso-octane and toluene to closely represent gasoline, detailed chemical kinetics and reactions of individual components has been provided in Appendix Section A4. However, utilising all the three components to represent gasoline resulted in a higher number of species and reactions which led to a significant increase in the simulation time (Liu et al., 2013). Due to the increased simulation time only iso-octane from the TRF

mechanism was called upon to represent gasoline in simulations. Utilising the iso-octane and ethanol reaction mechanisms resulted in a total of 63 species and 207 reactions for combustion calculation.

4.4.2.7 Prediction of Cyclic Variation

LES based simulations have been utilised in various studies such as by Probst et al. (2019), Truffin et al. (2015) and Granet et al. (2012) to quantitatively predict cyclic variation, however, the RANS based 3D CFD model was also able to predict cyclic variation which was not quantitative but stayed close to the average pressure curve. This was proven by Scarcelli et al., (2016) in their numerical and experimental investigations on a gasoline direct injected single cylinder research engine at Argonne National Laboratory where they compared the effect of different concentrations of EGR on combustion stability. Simulations were conducted for 20 consecutive cycles with detailed chemistry and compared against 500 cycles of experimental data. Results concluded that the COV (IMEP) trend was captured well by the simulation as shown in table 4-2, which indicated that the phenomena leading to cyclic variation in the engine simulation model, which utilised a RANS based approach, was caused by eddies larger than those destroyed by the turbulent viscosity.

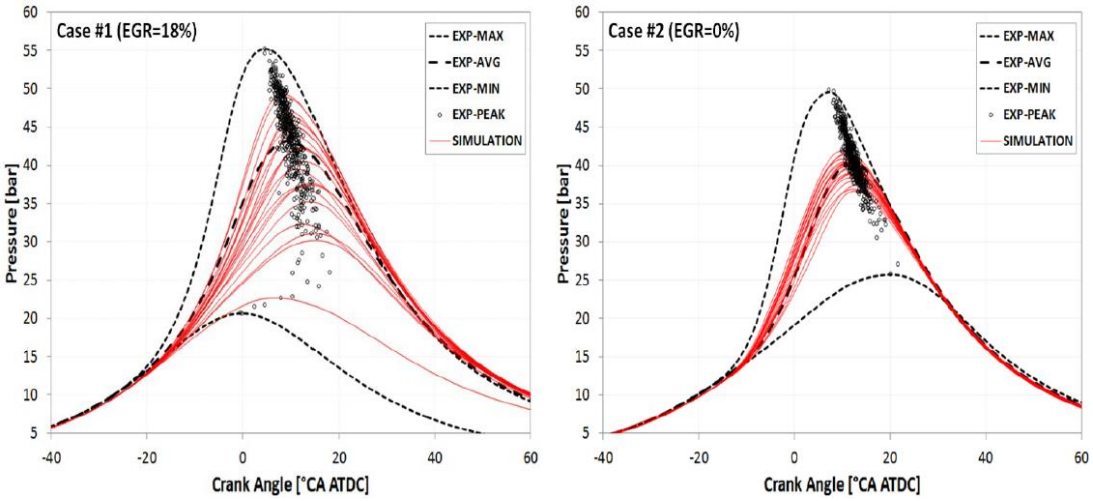

Figure 4-6 Comparison of RANS based 3D CFD Predicted Cylinder Pressures for EGR 18% and EGR 0% (Scarcelli et al., 2016)

	EGR = 18%	EGR = 0%
Experiment	7.8	1.4
Simulation	10	1

Table 4-2 Comparison of COV of IMEP between Experimental and Simulation Data at EGR 18% and 0%

5. Investigation of the Influence of Port Induced Tumble on a Pre-chamber Ignition Engine

Gas flow motion within an engine cylinder is a major factor that is known to control the combustion process in spark-ignition engines (Heywood, 1998). Many studies have shown that an in-cylinder flow motion has a positive impact on various factors such as knock limit extension, better air-fuel mixing and vaporisation, faster combustion processes thus resulting in higher engine thermal efficiencies for a spark ignited gasoline engine. However, there is a very limited knowledge on the impact of in-cylinder flow on pre-chamber ignited gasoline engine as discussed in Chapter-2.

To establish whether the flow characteristics in a cylinder affects a pre-chamber ignited gasoline engine in the same way as it does in a spark ignited gasoline engine, the impact of tumble ratio on the burn characteristics and performance of the engine were investigated via simple port induced tumble.

5.1 Port Induced Tumble Generation

The port induced tumble was to be generated using the barrel throttle of the engine which was to be set at 75% - thus masking the lower part of the ports and allowing for a higher port flow velocity which aided in increasing the tumble ratio in the cylinder. Figure 5-1 shows the throttle position at 100% and 75%. The partial closing of the barrel throttle was expected to reduce the port flow discharge coefficients thus demanding a higher manifold pressure to

overcome this restriction to obtain the necessary air charge mass in the cylinder to achieve the set lambda target at 13.33kg/h fuel flow rate. Since the engine boost rig was limited to an absolute pressure ratio of 2.5 bar, a decision was made to operate the engine without a back pressure valve to limit manifold pressure as setting the barrel throttle at 75% with back pressure may have resulted in the manifold pressure to rise and operate near to or above the boost rig's absolute pressure limit – risking the life of the boost rig components.

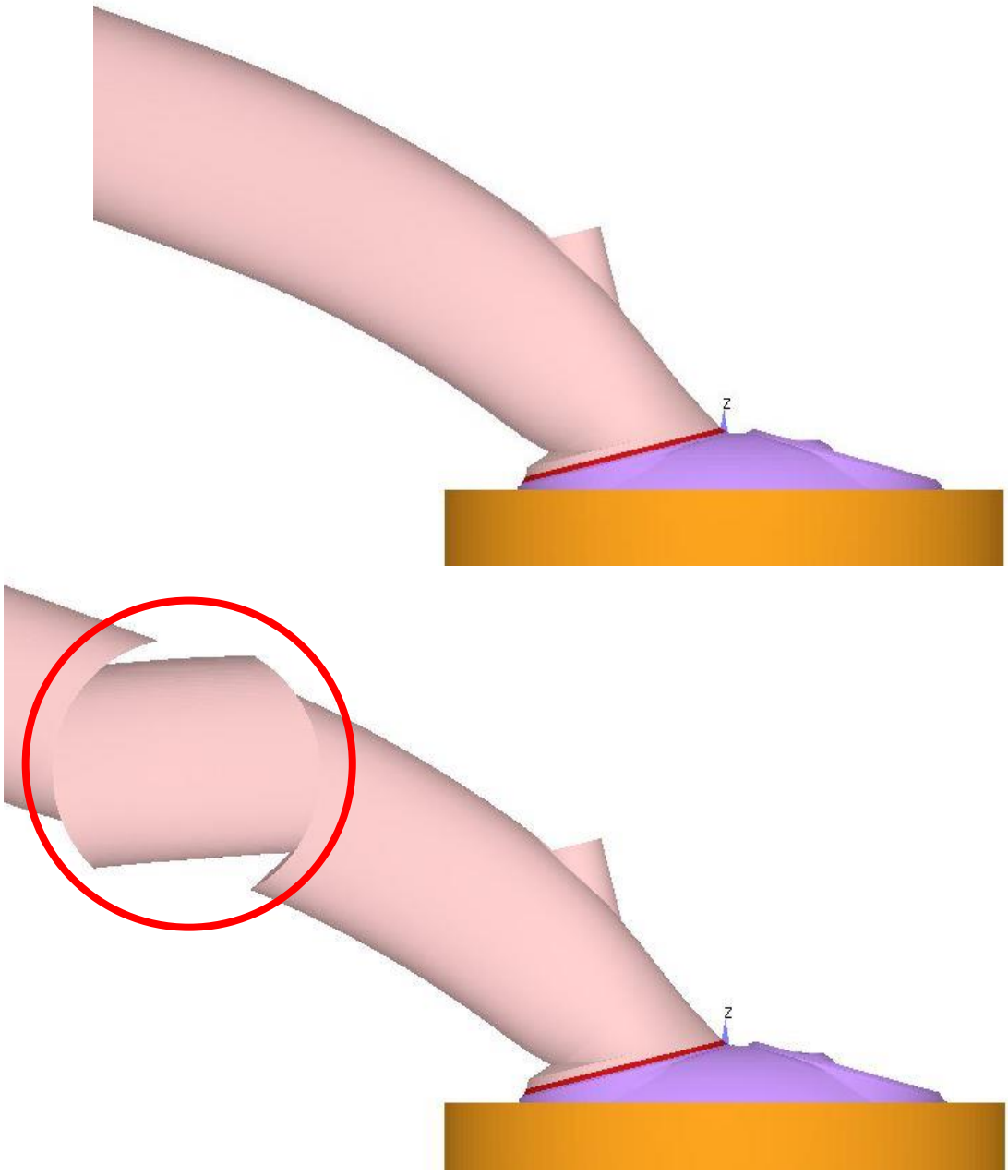

Figure 5-1 Throttle Position at 100% (Top) and 75% (Bottom) (Throttle is Circled Red)

5.2 Investigation of Port Generated Tumble Methods via Simulation

5.2.1 Flow Bench Simulations in 3D CFD

The tumble and turbulence generated by setting the barrel throttle at 75% was assessed in 3D CFD. To obtain boundary conditions for the simulation, a flow-bench case was setup to find the forward flow discharge coefficients for the throttle position at 75%- as these discharge coefficients were then utilised in 1D GT Power model of the single cylinder engine to predict the instantaneous intake and exhaust port pressures and temperatures required for the 3D CFD model.

Figure 5-2 shows the comparison of the flow through the ports and valves for the cases of 100% and 75% throttle positions at various intake valve lifts. It is evident from the simulation results that the throttle position, when set at 75%, creates a flow restriction which can be seen via reduced velocity in the vicinity of the intake valve seat area due to the pressure drop between the inflow and outflow boundary being the same in the simulation setup for the throttle position at 100% and 75%. However, when the throttle position was set at 75%, it can be seen that the flow in the ports in the maximum valve lift case is being guided to the far side of the intake valves which would aid in increasing the tumble ratio in the cylinder.

The port flow discharge coefficient at maximum valve lift for the throttle position at 75% case was found to be 13.2% lower than a fully open throttle body. A comparison of the port flow discharge coefficients is shown in Figure 3.

The tumble coefficient of the two throttle positions were compared as shown in Figure 4. The tumble coefficient was calculated using equation 5-1 and 5-2.

$$C_t = \frac{2T}{m_f \mathring{U}_{is} B} \quad \text{Eqn (5-1)}$$

$$U_{is} = \sqrt{RT_0}\left[\frac{2\gamma}{\gamma-1}\left\{1 - P_R^{\frac{\gamma-1}{\gamma}}\right\}\right]^{\frac{1}{2}} \quad \text{Eqn (5-2)}$$

Where: C_t = Tumble Coefficient

T = Tumble Torque

m_f = Mass Flow Rate

$\mathring{U}_{is}$ = Isentropic Valve Velocity

B = Cylinder Bore

P_R = Absolute Pressure Ratio (Static Outlet Pressure/Total Inlet Pressure)

R = Gas Constant

T_0 = Upstream Stagnation Temperature

γ = Specific Heat Ratio (1.4 for air at 300K)

The tumble coefficient for the throttle position at 75% case was found to be 25.1% higher than that of the throttle position at 100% case which means that the throttle position 75% case must generate higher tumble for a 4 stroke transient simulation.

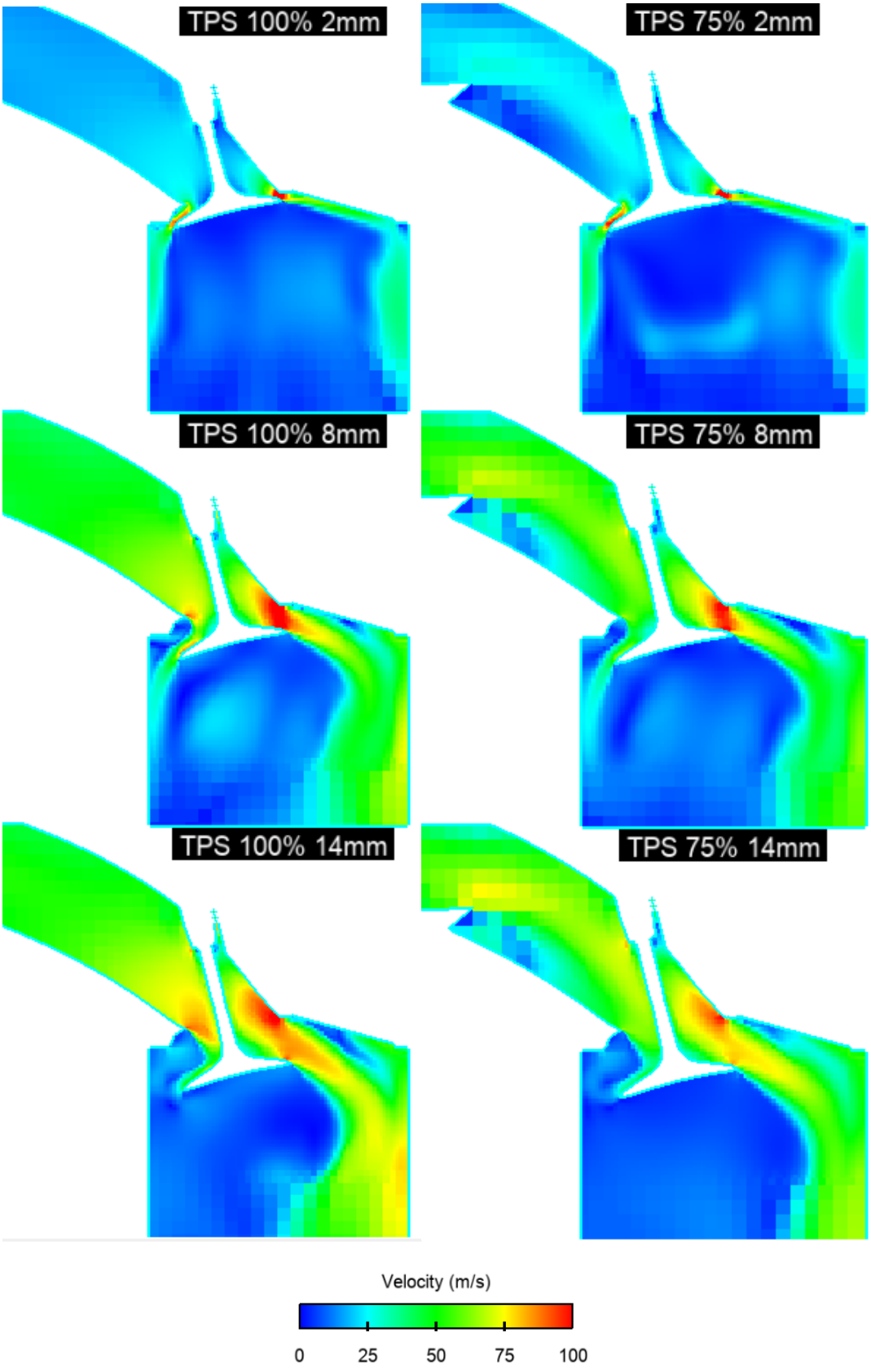

Figure 5-2 Comparison of Velocity Profile of Port Flow-bench Simulation Results at 2, 8 and 14mm Valve Lifts with Throttle Position at 100% (Left) and 75% (Right)

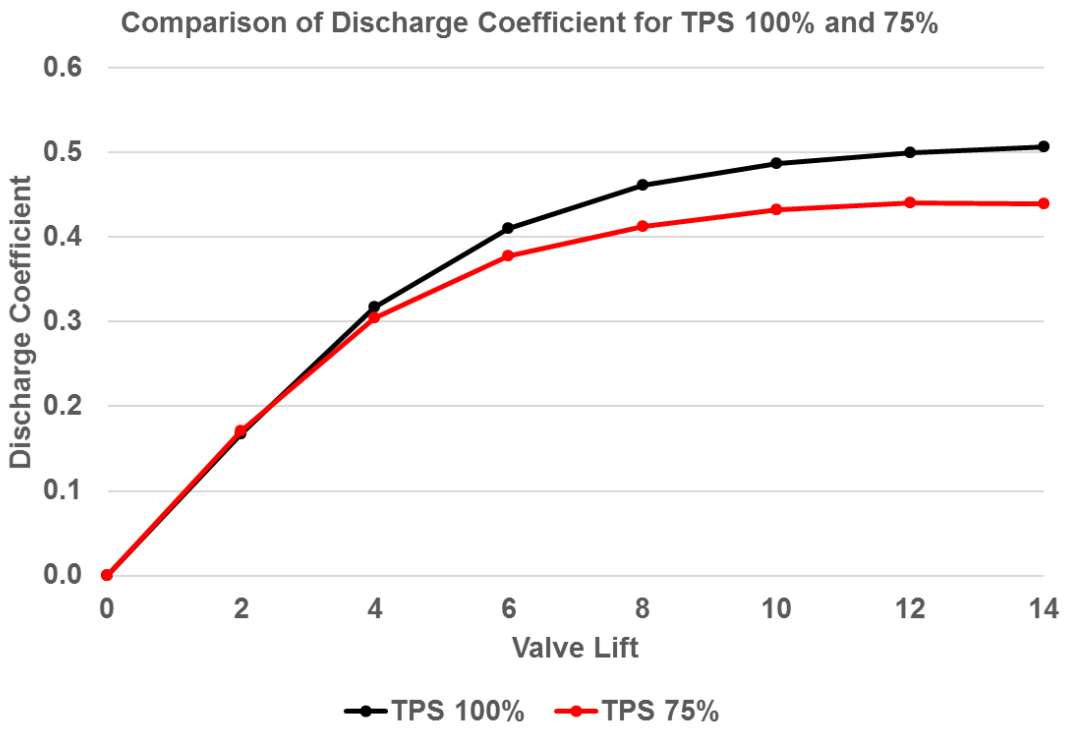

Figure 5-3 Comparison of Port Flow Discharge Coefficients for Throttle Position 100% and 75%

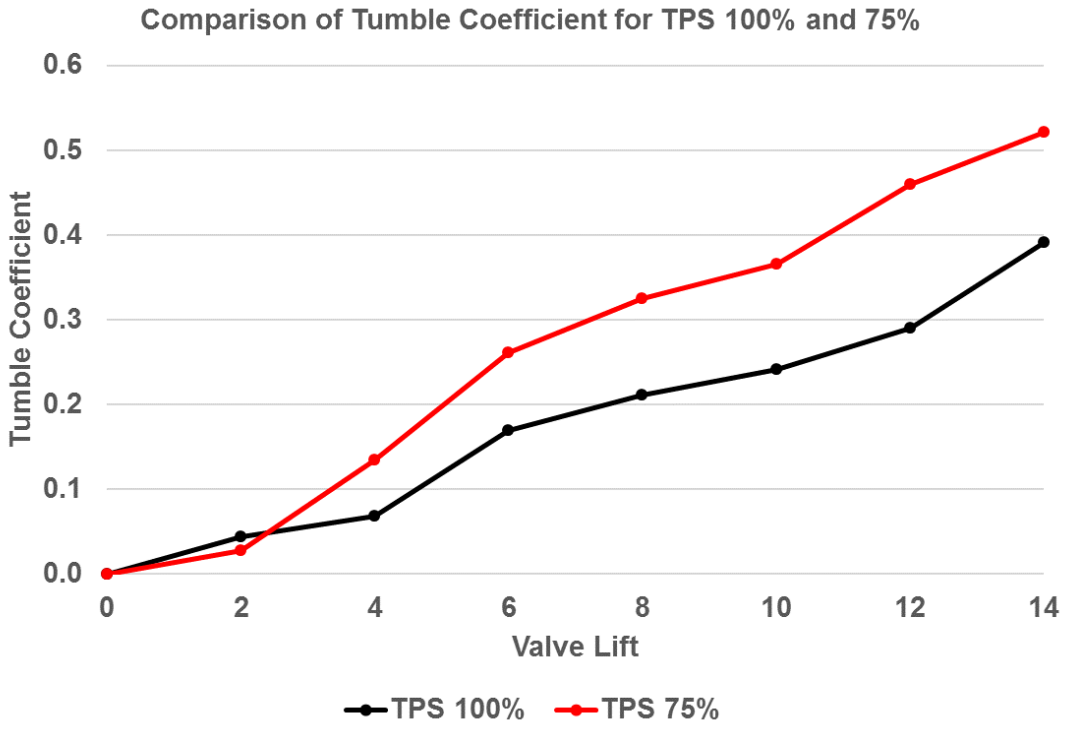

Figure 5-4 Comparison of Port Flow Tumble Coefficients for Throttle Position 100% and 75%

5.2.2 Simulation in 1D CFD

The intake port flow coefficients obtained as described in section 5.2.1 were input into the 1D CFD model of the single cylinder engine with the base engine's correlated Wiebe combustion model, and the following port pressures and temperatures were generated as shown in Figures 5-8.

Analysis of the figures show that the change in the coefficient of discharge for TPS 75% had only resulted in the increase of the intake port pressure to match the air charge mass contained in the engine cylinder as per TPS 100% case to achieve the relative air/fuel ratio of 1.20. As expected, the exhaust port pressures and temperatures were expected to be the same as the air charge mass and fuel mass were exactly the same for both TPS100% and 75% cases and as the Wiebe combustion model would not have taken into account the effect of increased tumble on combustion.

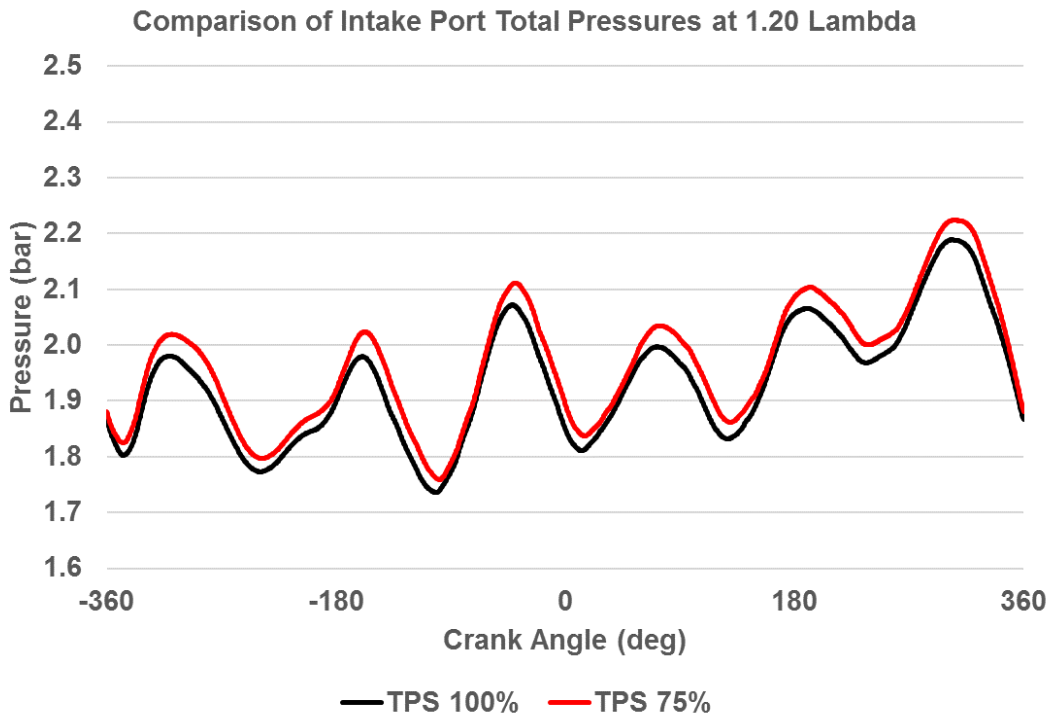

Figure 5-5 Comparison of Intake Port Total Pressures for TPS 100% and 75%

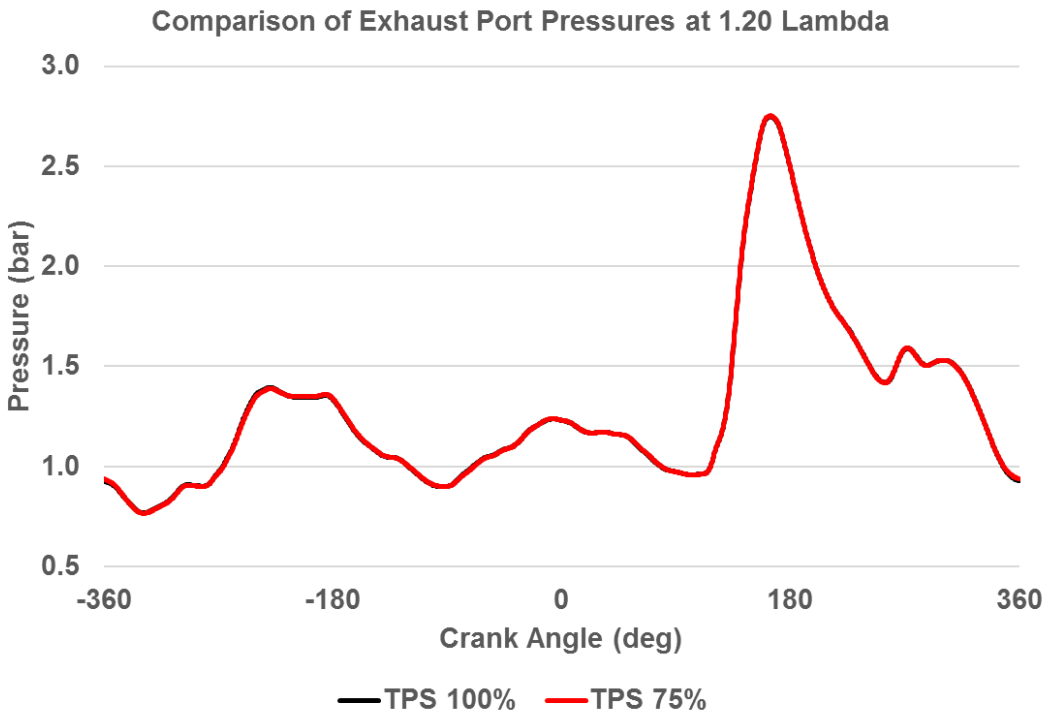

Figure 5-6 Comparison of Exhaust Port Static Pressures for TPS 100% and 75%

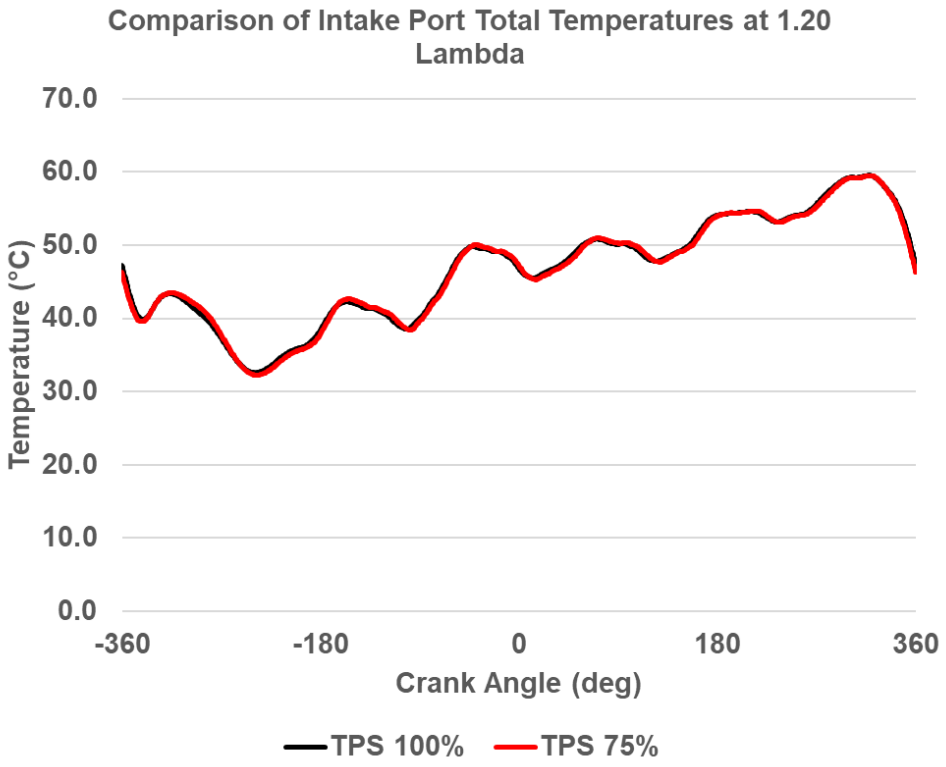

Figure 5-7 Comparison of Intake Port Total Temperatures for TPS 100% and 75%

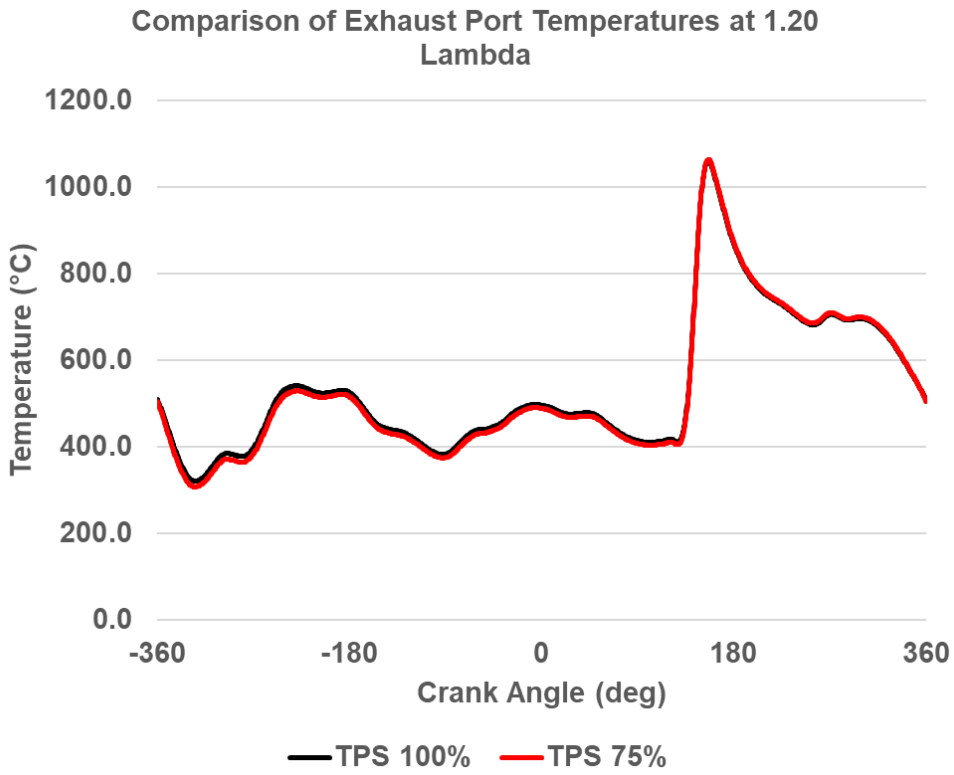

Figure 5-8 Comparison of Exhaust Port Static Temperatures for TPS 100% and 75%

5.2.3 4-Stroke Simulation in 3D CFD

Boundary conditions were input into the 3D CFD transient model which were generated from the 1D CFD model as described in section 5.2.2. The simulations were run for two consecutive 4-stroke cycles with a 6-hole pre-chamber ignitor with 1.2 cm^3 internal volume for 100% and 75% throttle position settings, with the engine operating at a relative air/fuel ratio of 1.20 at 7500 rpm. The spark timing was set to 28 deg BTDC. The aim of the simulation was to demonstrate that TPS 75% case had a higher tumble ratio and generated a higher turbulence level in the combustion chamber which aided combustion processes in a pre-chamber ignited engine.

Figure 5-9 shows the correlation between the simulated TPS 100% case and test data for the TPS 100% case. The simulated data has a slightly advanced combustion phasing which is due to the ignition timing differences used in the

test and simulation. The test data had a knock limited ignition timing of 27.7 deg BTDC whereas the simulation had a slightly advanced ignition timing of 28 deg BTDC. The 0.3 degree change resulted in a slight alteration of combustion phasing when comparing simulated and test results as a pre-chamber ignitor was found to be very sensitive to spark timing. Simulating more cycles would provide more information on cyclic variation however further cycles were not simulated due to the simulation model being computationally expensive.

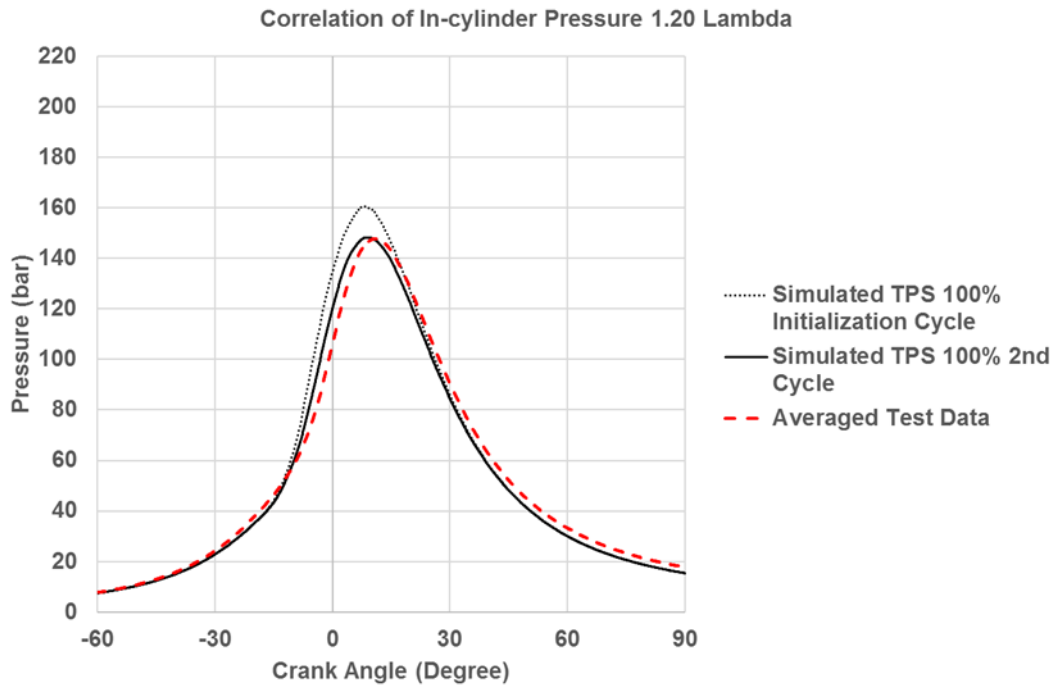

Figure 5-9 Correlation of Simulated In-cylinder Pressure for TPS 100% with Test Data

Following correlation, the TPS 75% case was simulated and an improvement of 0.05 bar improvement in IMEP was observed with non-optimised ignition timings. Optimisation of ignition timings for TPS 75% case was planned to be undertaken during testing phase as running 3D CFD simulations for ignition timing optimisation would be computationally expensive.

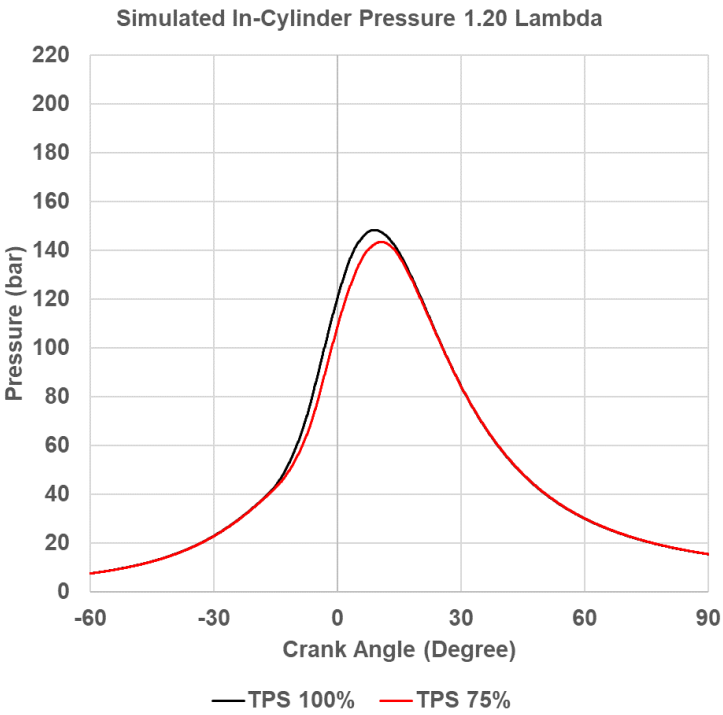

Figure 5-10 Comparison of Simulated In-cylinder Pressure for TPS 100% and 75%

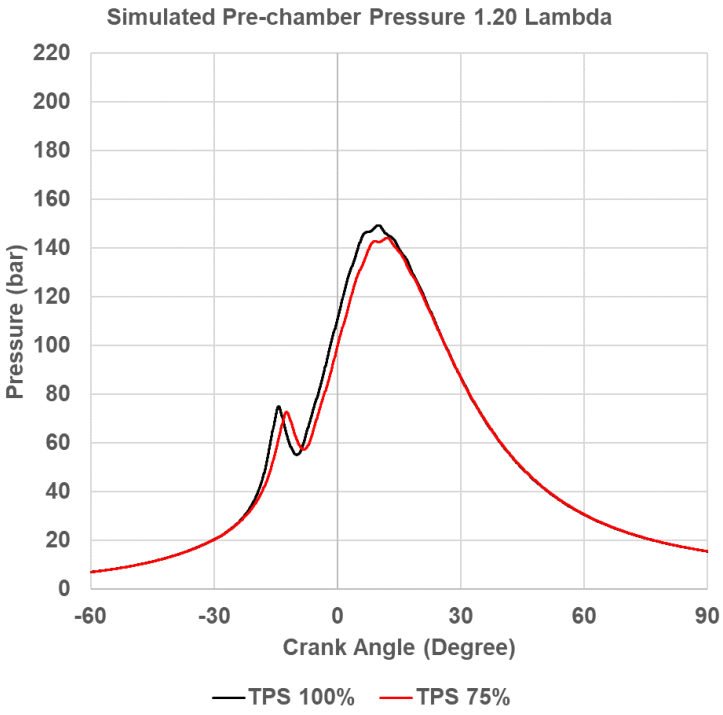

Figure 5-11 Comparison of Simulated Pre-chamber Pressure for TPS 100% and 75%

Figure 5-10 and 5-11 show the comparison of simulated in-cylinder pressure and pre-chamber pressure. The pre-chamber peak pressure for the TPS 75% case was found to be delayed and lower than the TPS 100% case which can

be attributed to a longer ignition delay due to a leaner relative air/fuel mixture in the pre-chamber at ignition timing as shown in Figure 5-12.

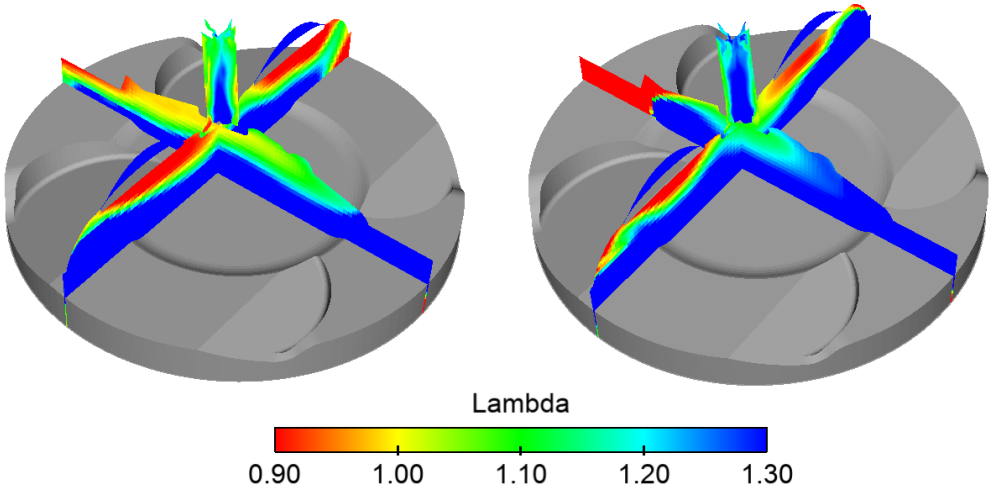

Figure 5-12 Comparison of Fuel Distribution for TPS 100% and TPS 75%

Figure 5-13 and 5-14 show that the heat release rate for TPS 75% was higher than TPS 100% case between 0 and 30 deg ATDC which resulted in a shorter burn duration even with a longer ignition delay, shown in Figure 5-15, which can be attributed to the higher turbulent kinetic energy present in the main chamber for the TPS 75% case as shown in Figures 5-18, 5-19 and 5-20. The high turbulence was a result of breaking down a higher tumble flow arising from the high port flow velocity for the TPS 75% case as shown in Figures 5-16 and 5-17.

Figure 5-21 shows the comparison of the combustion flames depicted by a 1700K temperature iso-surface at various time steps. Hot jets from the pre-chamber were observed earlier in TPS 100% case than the TPS 75% case due to pre-chamber enrichment however, the faster main chamber combustion process for the TPS 75% case improved the flame speed and thus the flame can be seen to have covered the same area as the TPS 100% case at 10 deg ATDC.

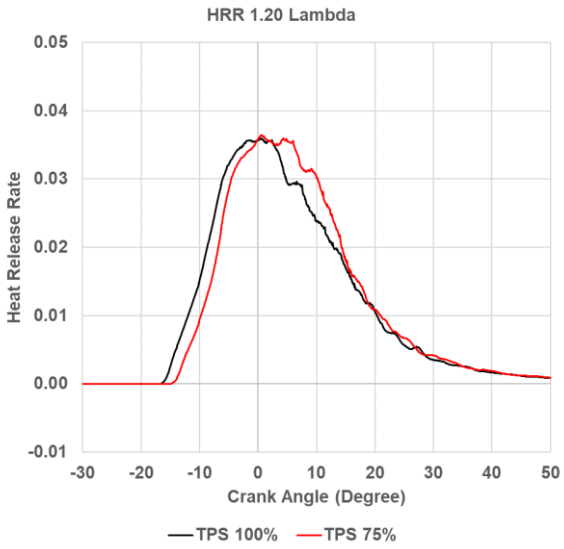

Figure 5-13 Comparison of Simulated Heat Release Rate for TPS 100% and 75%

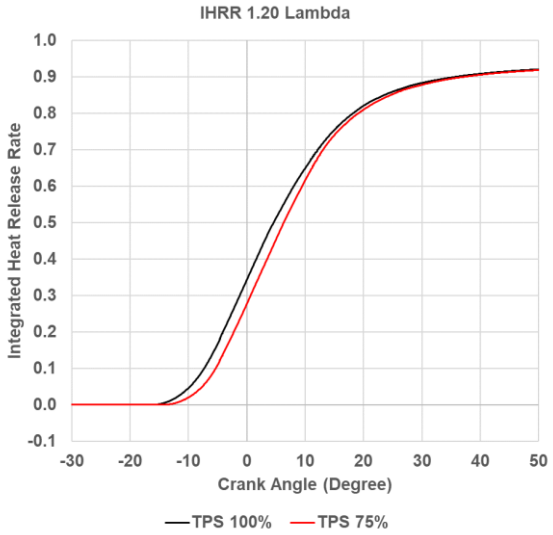

Figure 5-14 Comparison of Simulated Integrated Heat Release Rate for TPS 100% and 75%

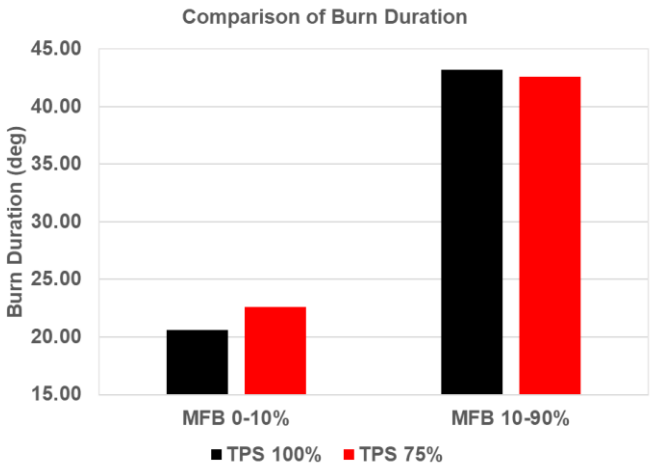

Figure 5-15 Comparison of Simulated Ignition Delay and Burn Duration for TPS 100% and TPS 75%

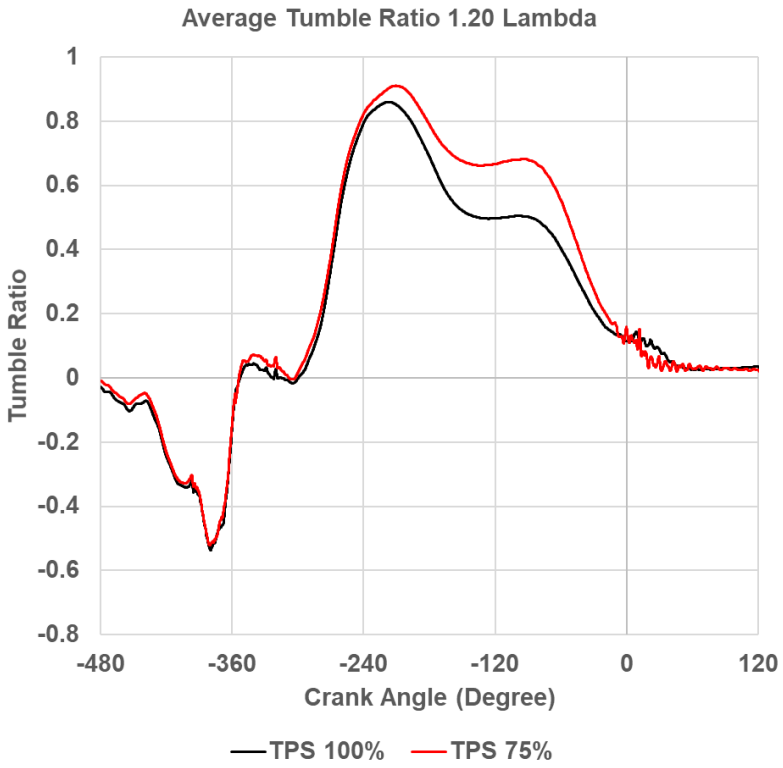

Figure 5-16 Comparison of Simulated In-cylinder Tumble for TPS 100% and 75%

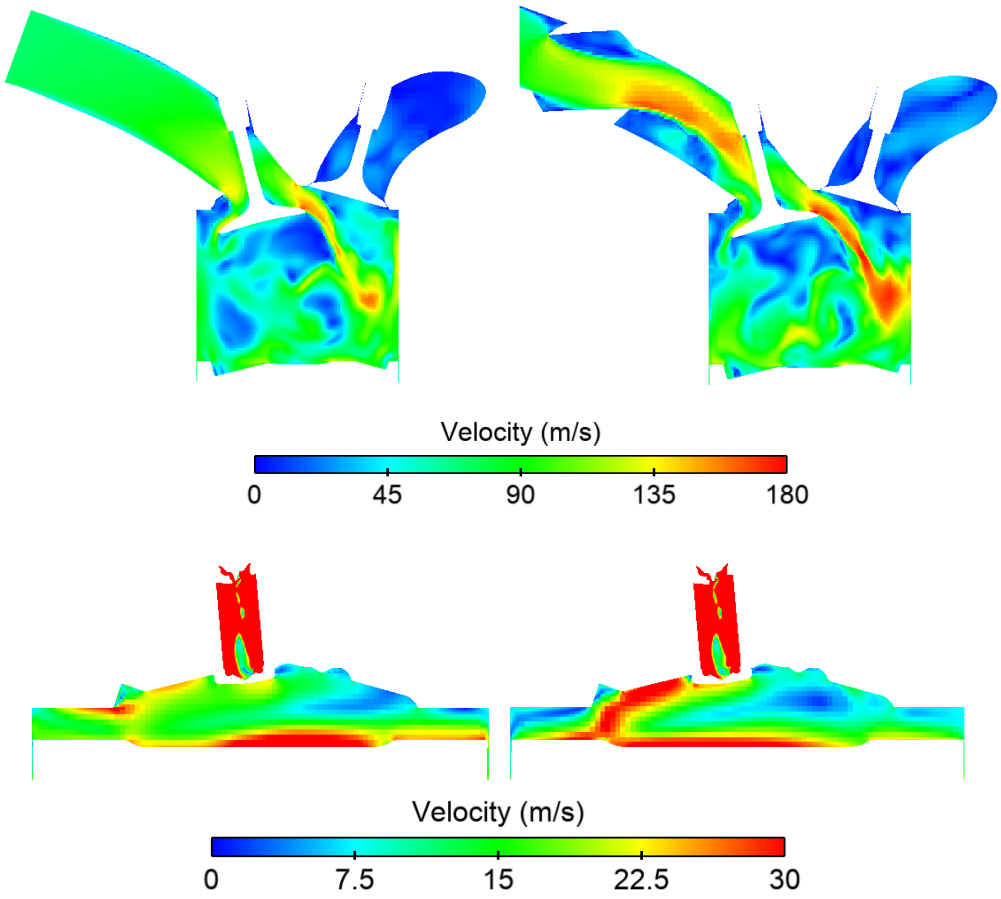

Figure 5-17 Comparison of Simulated In-Cylinder Velocities at 240 deg BTDC (Top) and 25 deg BTDC (Bottom) For TPS 100% (Left) and TPS 75% (Right)

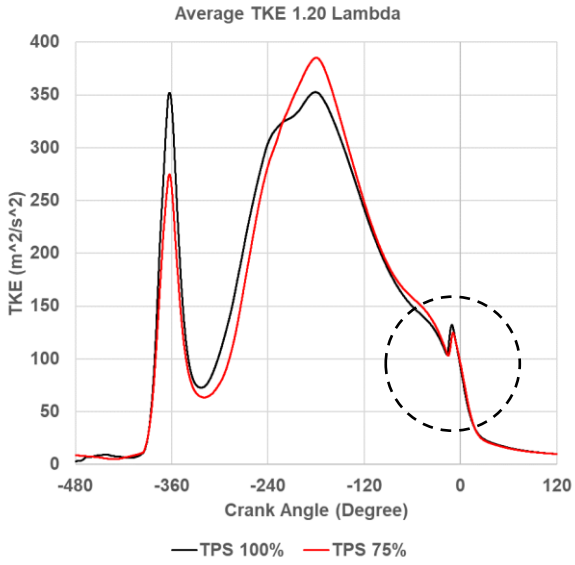

Figure 5-18 Comparison of Simulated Turbulent Kinetic Energy for TPS 100% and 75%

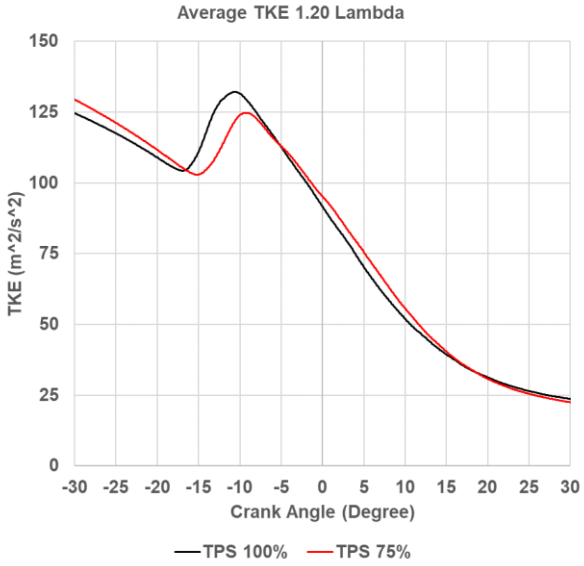

Figure 5-19 Enlarged View of Comparison of Simulated 3 Cycle Averaged Turbulent Kinetic Energy for TPS 100% and 75%

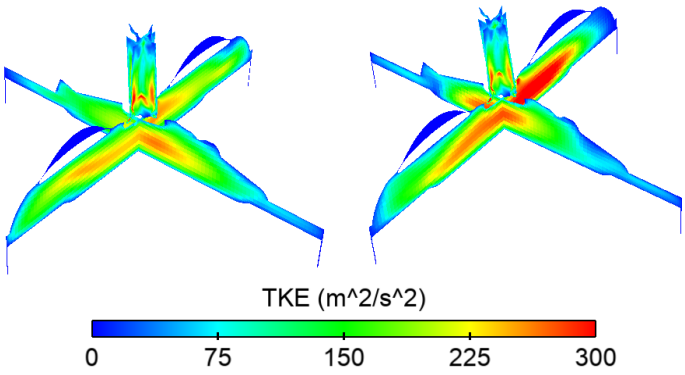

Figure 5-20 Comparison of Simulated Turbulent Kinetic Energy at 25 deg BTDC For TPS 100% (Left) and TPS 75% (Right)

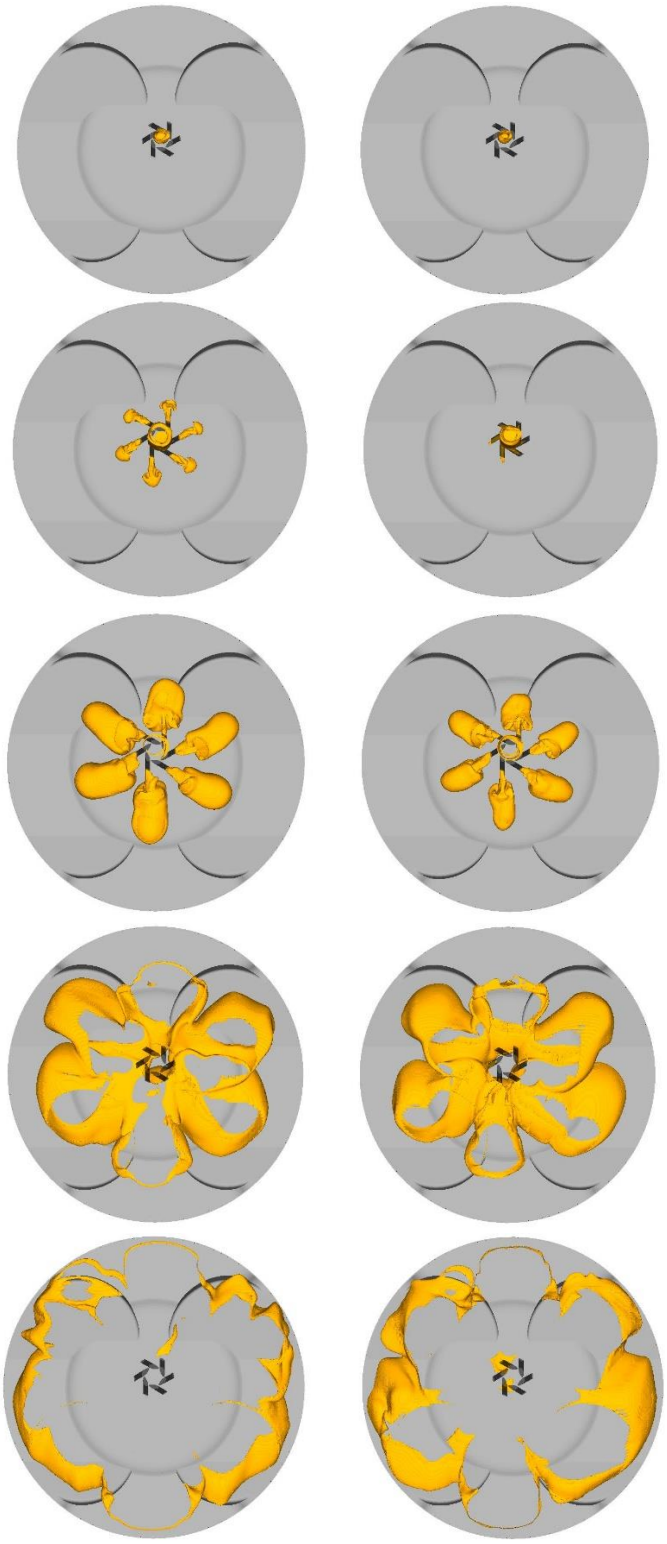

Figure 5-21 Comparison of Combustion Flames for TPS 100% (Left) and TPS 75% (Right) at 20 deg BTDC, 15 deg BTDC, 10 deg BTDC, 0 deg and 10 deg ATDC (Top to Bottom)

5.3 Experimental Results of Port Generated Tumble Methods

5.3.1 Performance Evaluation of Port Generated Tumble on Spark Ignited Engine

The first set of experiments were conducted on the single cylinder engine with a spark ignition system at 7500 rpm where ignition and fuel timings were optimised at relative air/fuel ratios of 1.20, 1.25 and 1.30 for a fuel flow rate of 13.33 kg/h to calibrate the engine for maximum indicated performance or lowest ISFC which was limited by knock. The aim was to establish the impact of in-cylinder flow on a spark ignited combustion chamber for a high-speed engine. Figure 5-22 and 5-23 show the comparison of ISFC (gross) and $COV_{IMEP(gross)}$ for the cases of TPS 100% and 75%.

It was established from the engine test results that a higher tumble ratio and resulting higher turbulence in the combustion chamber had a positive effect on combustion. The TPS 75% case resulted in a maximum improvement of 0.554 g/kWh Gross ISFC at 1.25 lambda and a reduced $COV_{IMEP(gross)}$ by a maximum of 0.41% at 1.30 lambda when compared with the TPS 100% case.

As the spark timing was knock limited, TPS 75% case had a spark timing, shown in Figure 5-24, which was retarded by 1.05 degrees on average when compared with the TPS 100% case. The retarding of spark timing along with reduction in exhaust gas temperatures, as shown in Figure 5-25, for a higher performance- confirms that the combustion was improved.

A shorter burn duration for the TPS 75% case also resulted in improving the average cylinder pressures as shown in Figure 5-26. The average pressures for the 1.25 lambda case look similar for both TPS 100% and TPS 75% cases due to fuel flow rate of TPS 75% being 0.05 kg/h lower than TPS 100% which is reflected in the gross ISFC plot in Figure 5-22. An improvement in normalized heat release rate and the integrated heat release rate was observed for the TPS 75% case as shown in Figure 5-27.

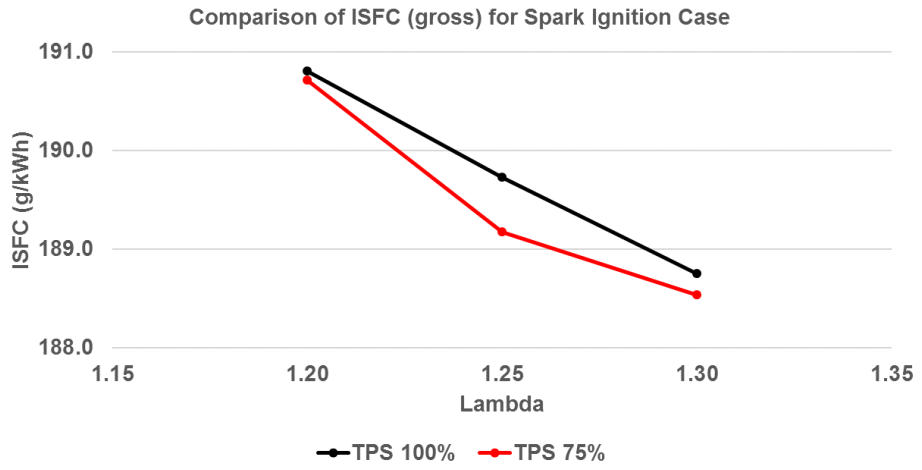

Figure 5-22 Comparison of Gross Indicated Specific Fuel Consumption for TPS 100% and TPS 75% at Lambda 1.20, 1.25 and 1.30

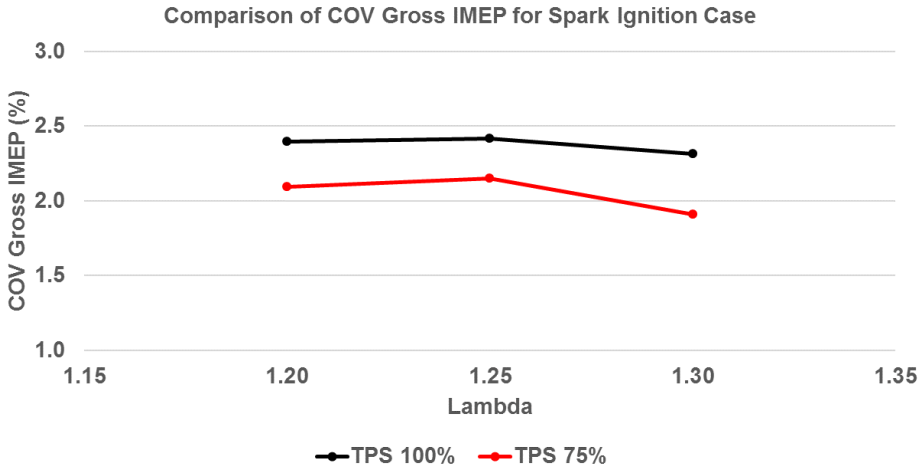

Figure 5-23 Comparison of Coefficient of Variation of Gross IMEP for TPS 100% and TPS 75% at Lambda 1.20, 1.25 and 1.30

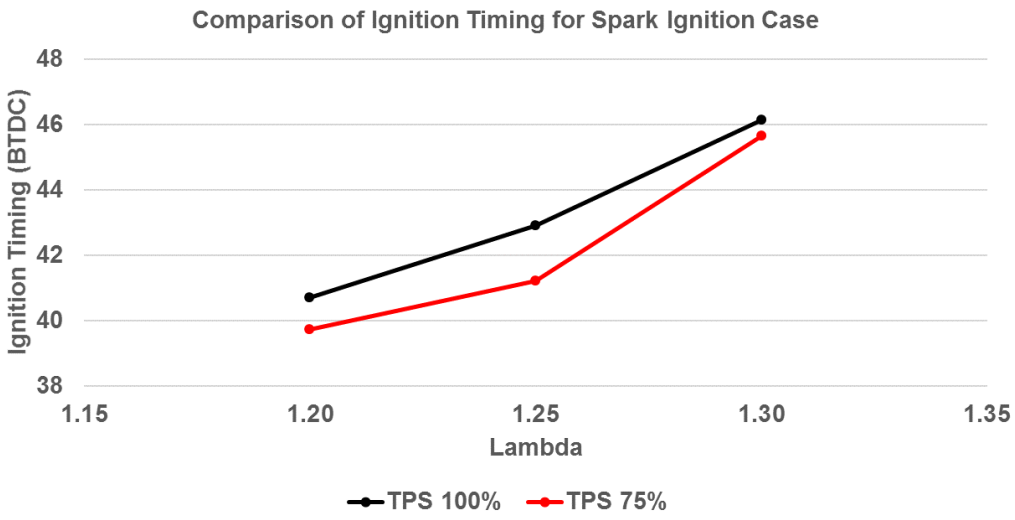

Figure 5-24 Comparison of Ignition Timing for TPS 100% and TPS 75%

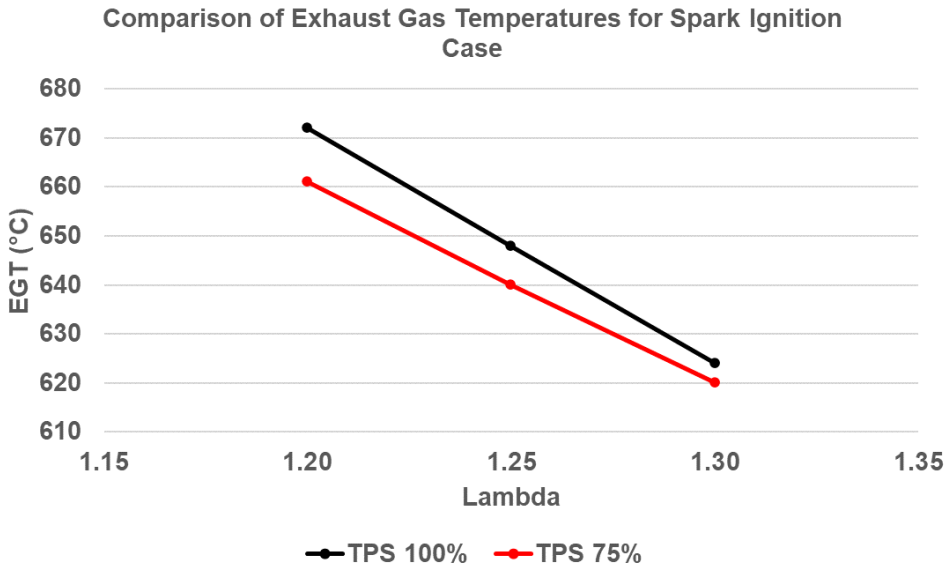

Figure 5-25 Comparison of Exhaust Gas Temperatures for TPS 100% and TPS 75%

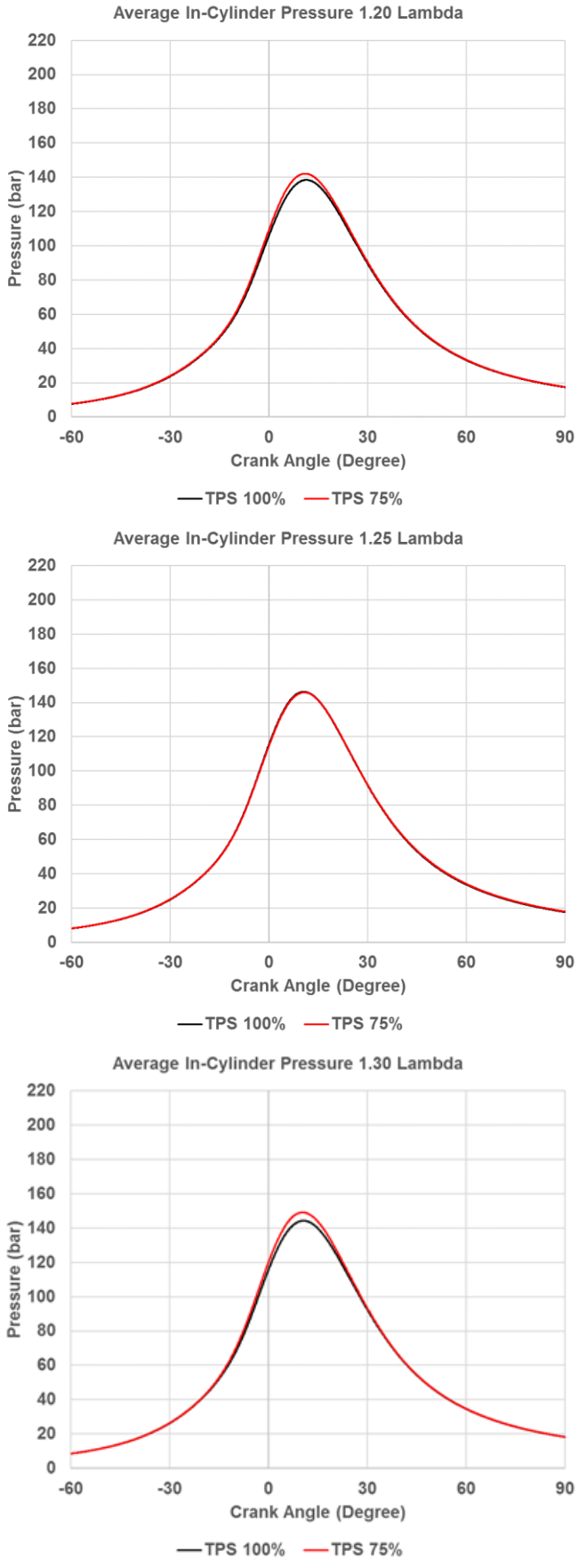

Figure 5-26 100 Cycle Averaged In-cylinder Pressure Plots for TPS 100% and TPS 75% at Lambda 1.20, 1.25 and 1.30

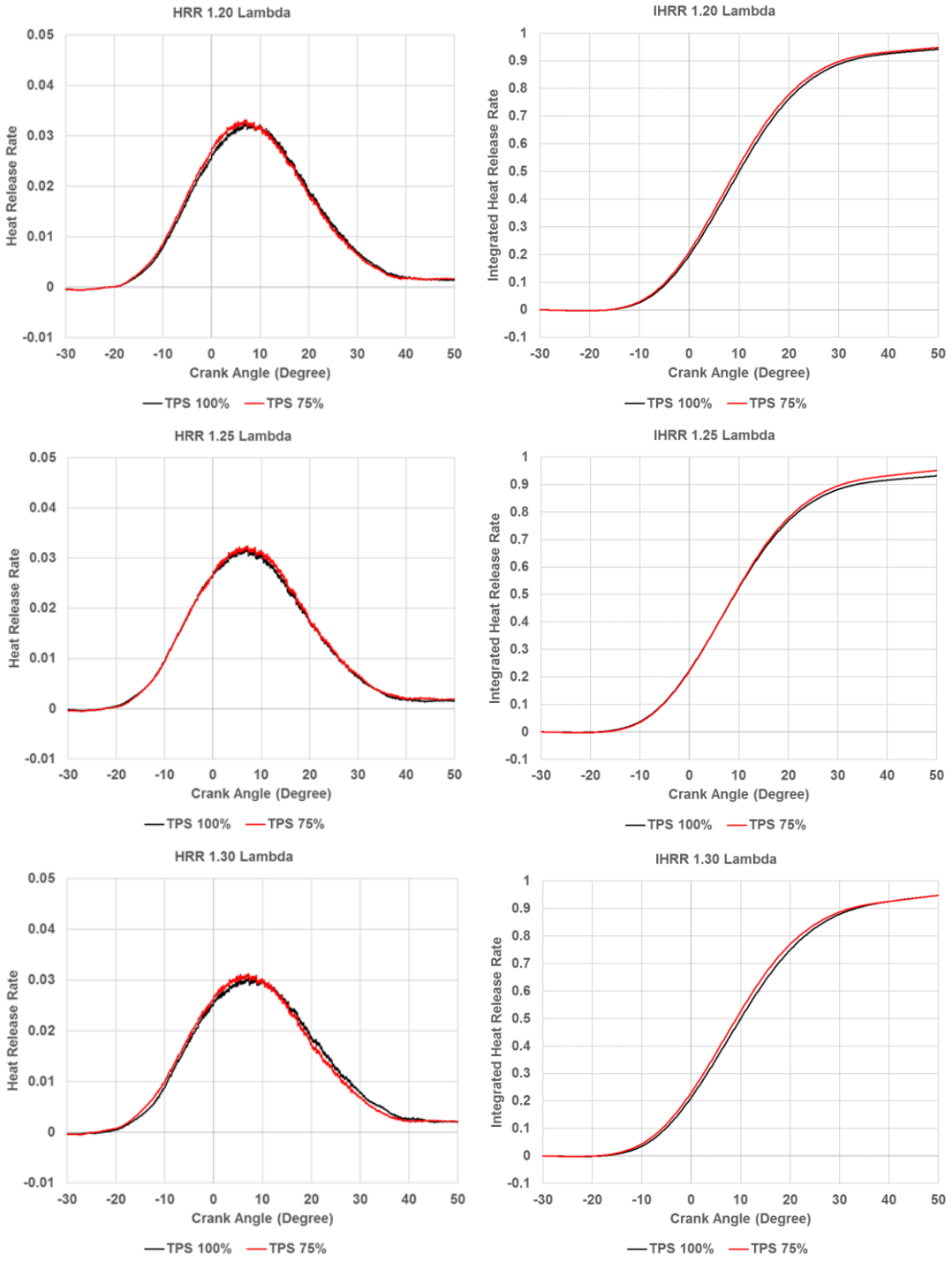

Figure 5-27 100 Cycle Averaged Normalized Heat Release Rate (Left) and Normalized Integrated Heat Release Rate (Right) for TPS 100% and TPS 75% at Lambda 1.20, 1.25 and 1.30

Figure 5-28 Comparison of Maximum Amplitude of Pressure Oscillations for TPS 100% and TPS 75% at Lambda 1.20, 1.25 and 1.30

Figure 5-28 shows the comparison of MAPO for TPS 100% and TPS 75% for 100 cycles. The average of maximum amplitude of pressure oscillations for TPS 75% were found to be slightly higher for all relative air/fuel ratios when compared with TPS 100%. Table 5-1 shows the comparison between the average MAPO for TPS 100% and TPS 75% cases.

Lambda	TPS 100% MAPO (bar)	TPS 75% MAPO (bar)
1.20	7.10	8.30
1.25	7.47	7.60
1.30	6.78	7.30

Table 5-1 Comparison of Average MAPO for TPS 100% and TPS 75% at Lambda 1.20, 1.25 and 1.30

5.3.2 Performance Evaluation of Port Generated Tumble on Pre-chamber Ignited Engine

The spark plug in the engine was replaced with an unfuelled 6 hole pre-chamber ignitor which had a volume of 1.2 cm^3. The engine was calibrated at 7500 rpm where ignition and fuel timings were optimised at relative air/fuel ratios of 1.20, 1.25 and 1.30 for a fuel flow rate of 13.33 kg/h to calibrate the engine for maximum indicated performance or lowest ISFC which was limited by knock. The aim was to establish if in-cylinder flow had an impact on combustion for a pre-chamber ignited combustion chamber in a high-speed engine. Figure 5-29 and 5-30 show the comparison of ISFC (gross) and $COV_{IMEP(gross)}$ for the cases of TPS 100% and 75%.

Engine test results had shown that a higher tumble ratio and resulting higher turbulence in the combustion chamber had a positive effect on combustion for a pre-chamber ignited engine. The TPS 75% case resulted in a maximum improvement of 3.74 g/kWh Gross ISFC at 1.20 lambda and a reduced $COV_{IMEP(gross)}$ by a maximum of 0.68% at 1.20 lambda when compared with the TPS 100% case.

As the spark timing was knock limited, TPS 75% case had a spark timing, shown in Figure 5-31, which was advanced by 0.79 degrees on average when compared with the TPS 100% case. The advancing of spark timing along with reduction in exhaust gas temperatures, as shown in Figure 5-32, for a higher performance- confirms that the combustion and knock limits were improved.

Figures 5-33 shows 100 cycles of filtered in-cylinder pressure data for all TPS 100% and TPS 75% cases tested on the engine. The TPS 75% case across

all relative air/fuel ratios shows that the pressure vs crank angle plots are more concentrated which also resulted in a lower COV of gross IMEP as shown in Figure 5-30. A shorter burn duration for the TPS 75% case also resulted in improving the average cylinder pressures as shown in Figure 5-34.

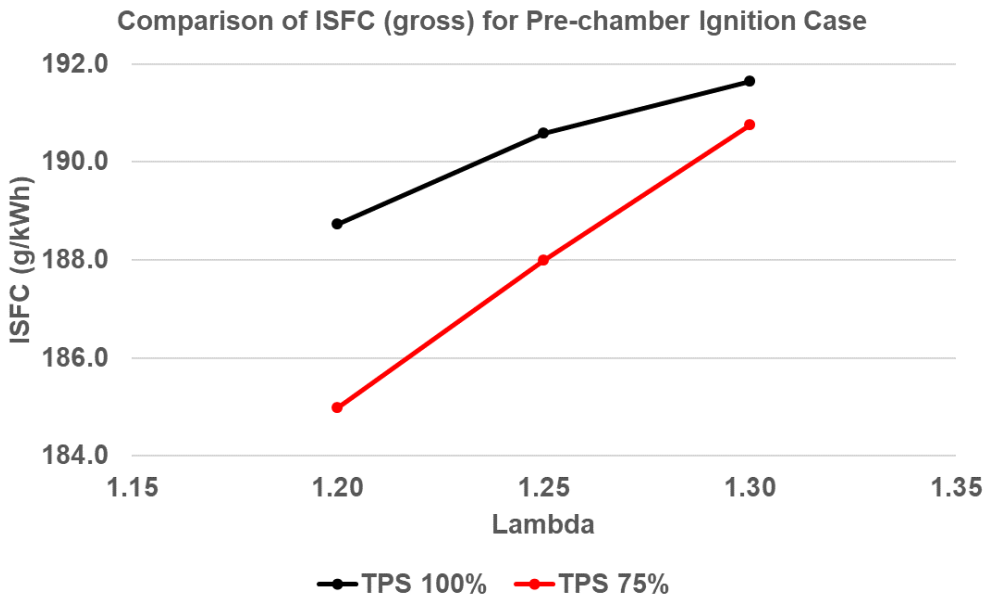

Figure 5-29 Comparison of Gross Indicated Specific Fuel Consumption for TPS 100% and TPS 75% at Lambda 1.20, 1.25 and 1.30

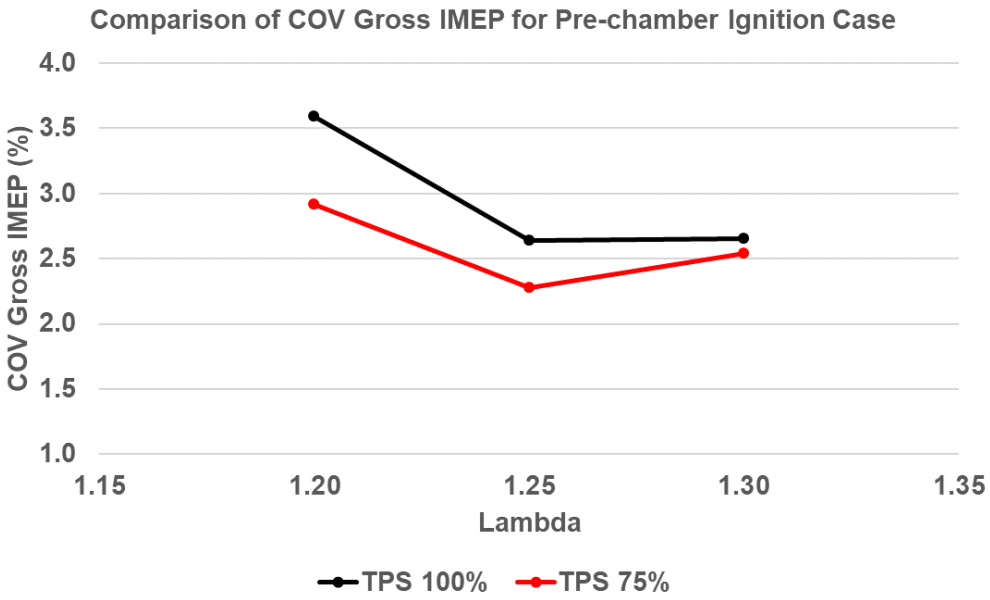

Figure 5-30 Comparison of Coefficient of Variation of Gross IMEP for TPS 100% and TPS 75% at Lambda 1.20, 1.25 and 1.30

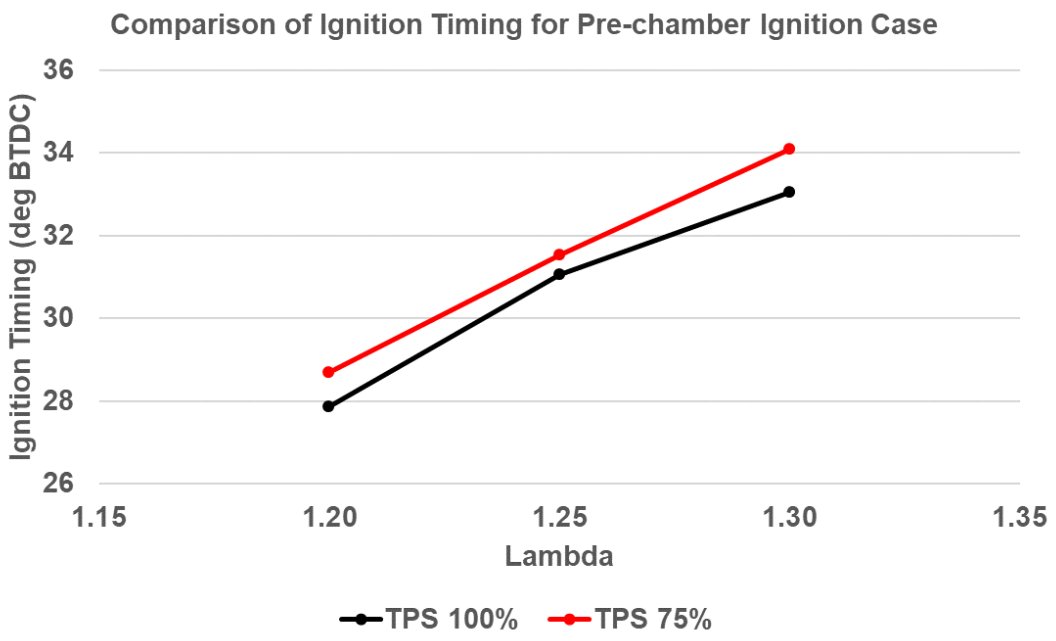

Figure 5-31 Comparison of Ignition Timing for TPS 100% and TPS 75%

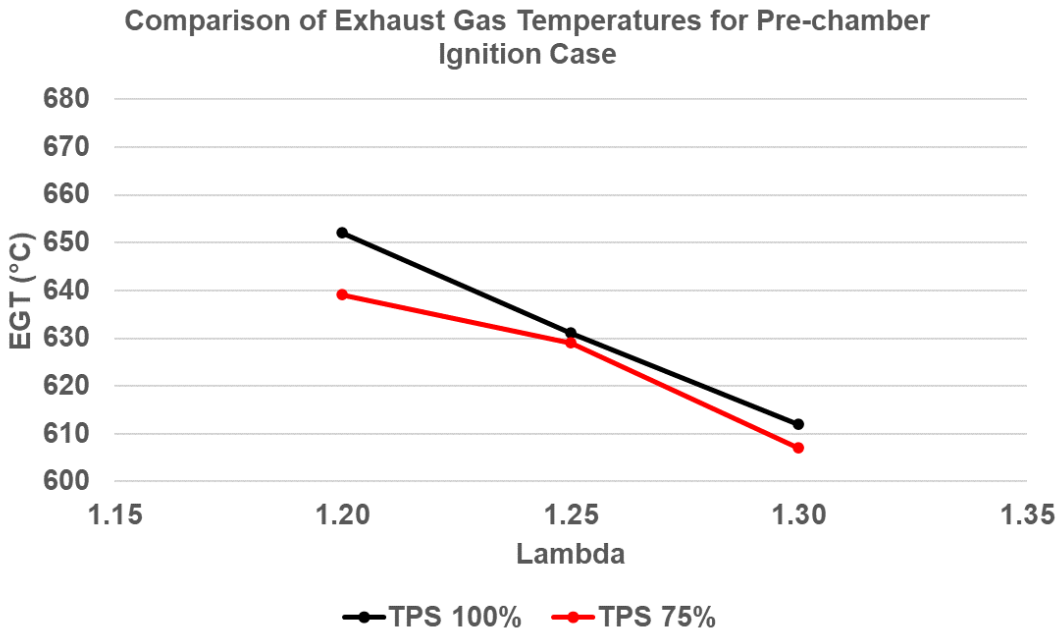

Figure 5-32 Comparison of Exhaust Gas Temperatures for TPS 100% and TPS 75%

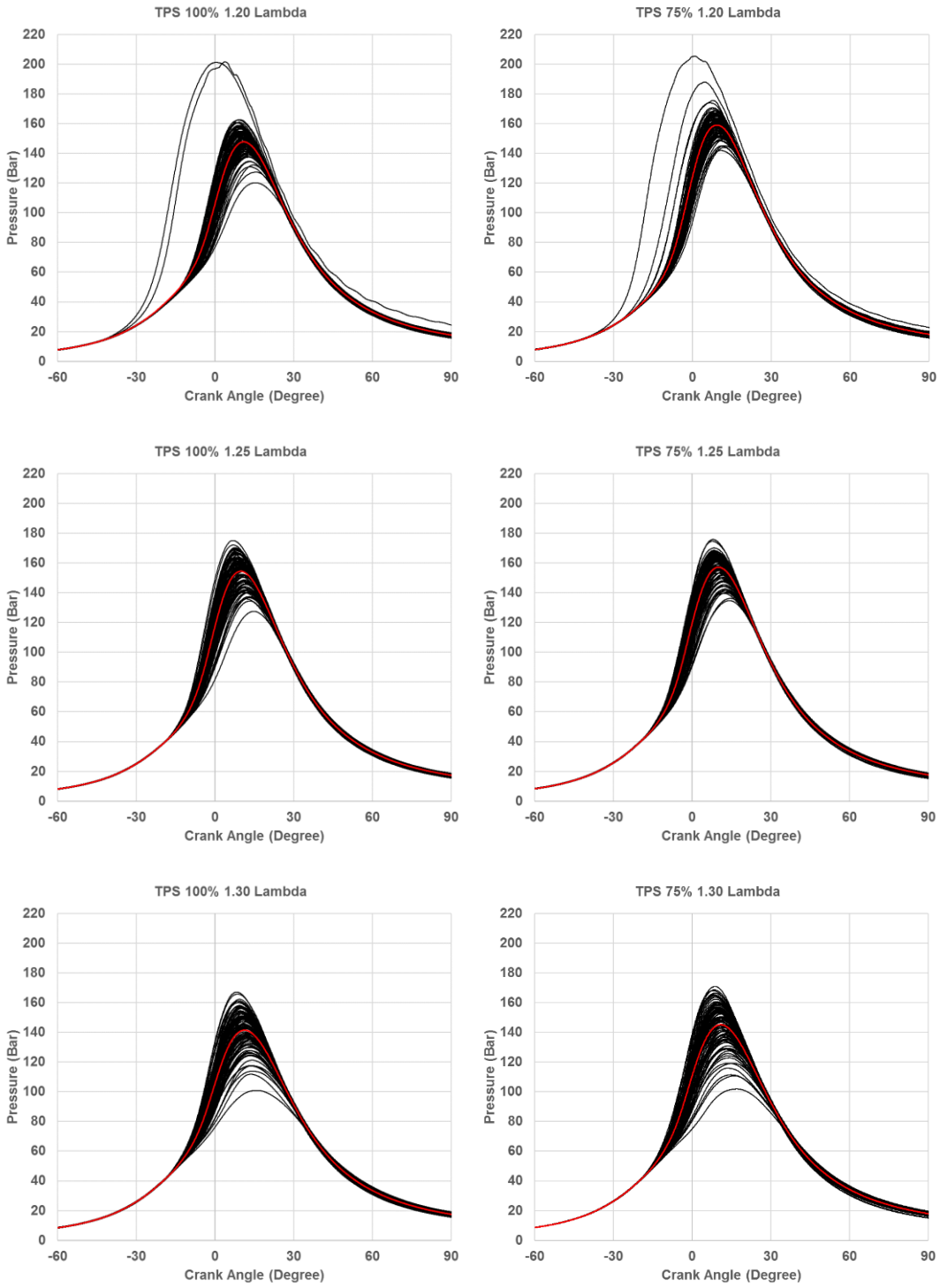

Figure 5-33 100 Cycles In-Cylinder Pressure Plots for TPS 100% and TPS 75% at Lambda 1.20, 1.25 and 1.30

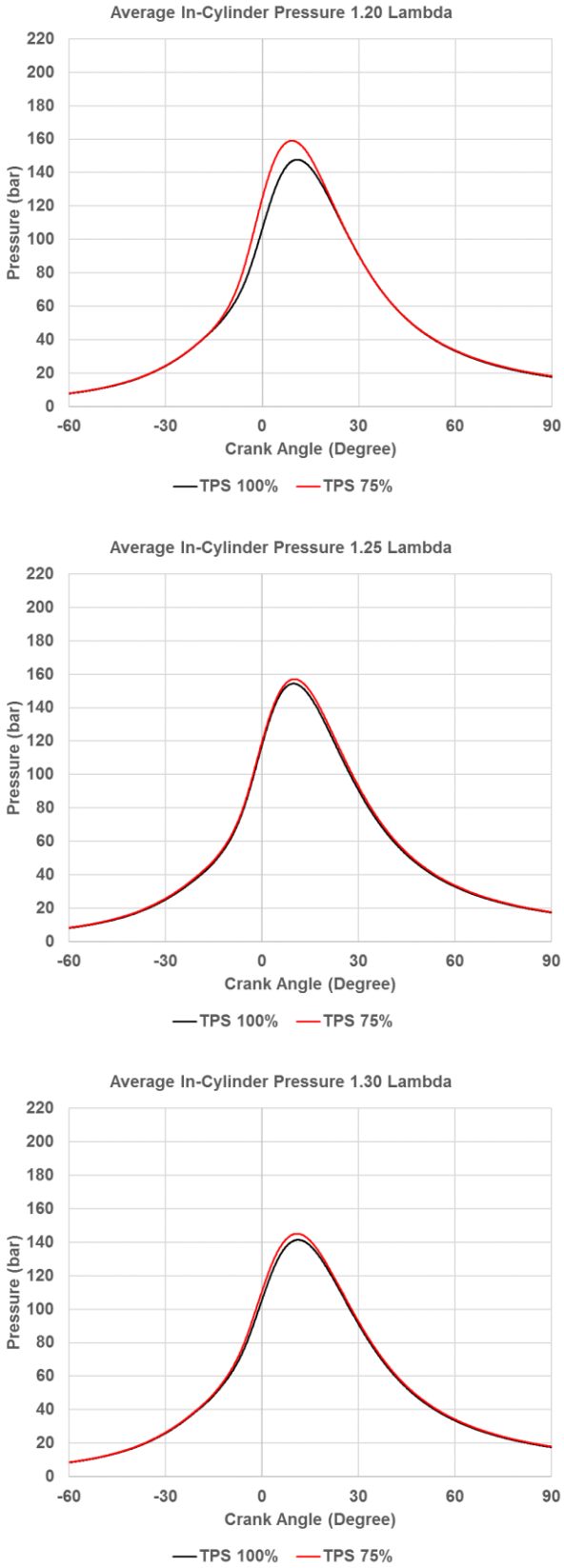

Figure 5-34 100 Cycle Averaged In-cylinder Pressure Plots for TPS 100% and TPS 75% at Lambda 1.20, 1.25 and 1.30

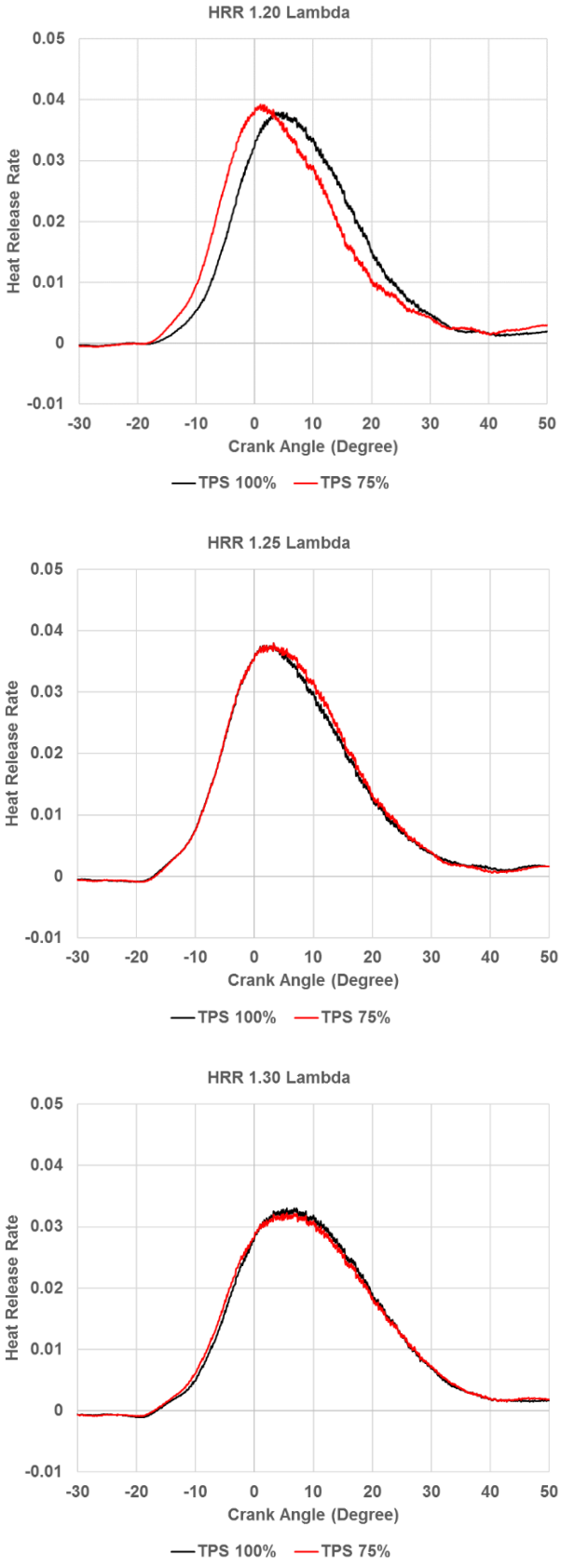

Figure 5-35 100 Cycle Averaged Normalized Heat Release Rate for TPS 100% and TPS 75% at Lambda 1.20, 1.25 and 1.30

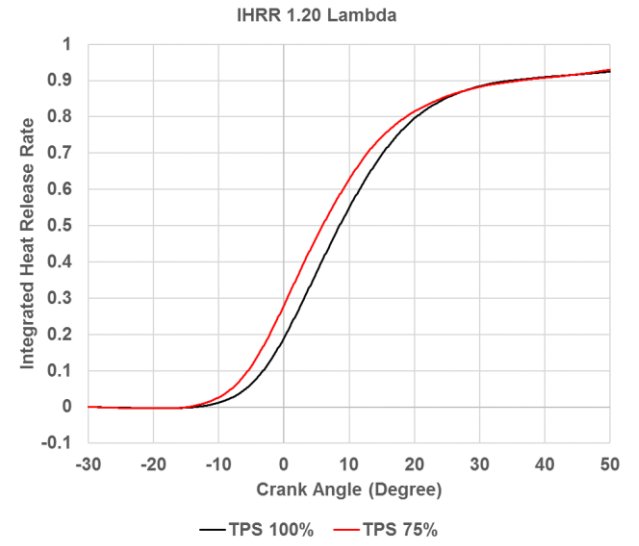

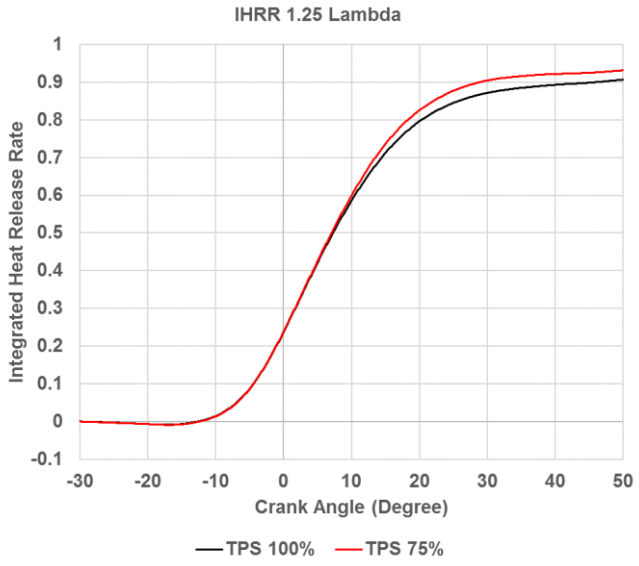

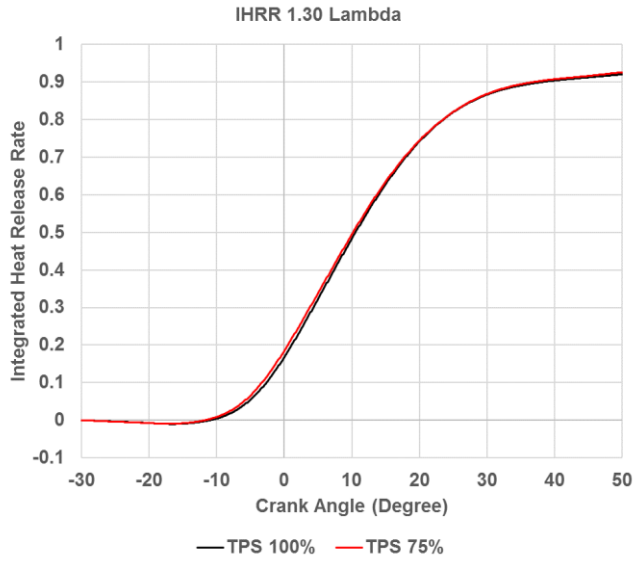

Figure 5-36 100 Cycle Averaged Normalized Integrated Heat Release Rate for TPS 100% and TPS 75% at Lambda 1.20, 1.25 and 1.30

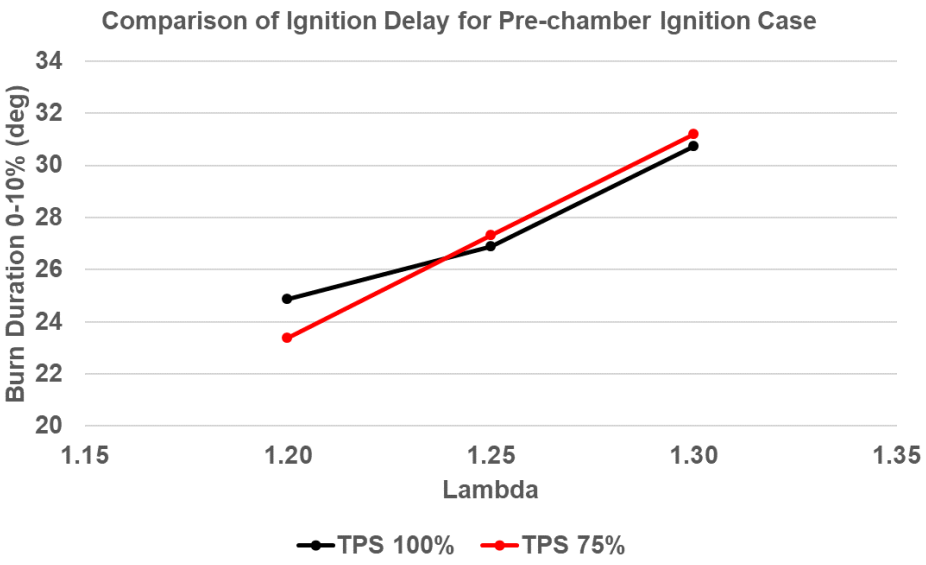

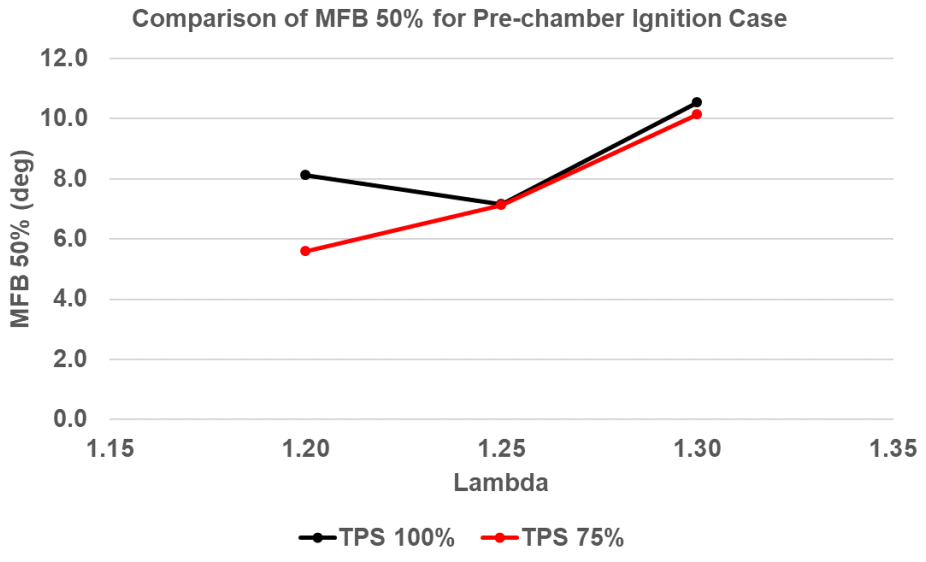

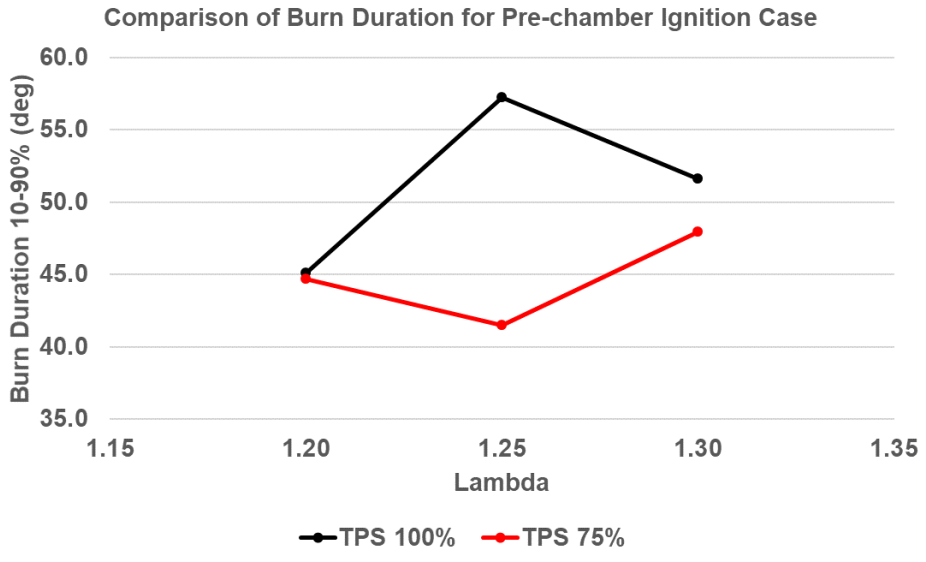

Figure 5-37 Comparison of Cycle Averaged Ignition Delay, 50% Burn Point and Burn Duration for TPS 100% and TPS 75%

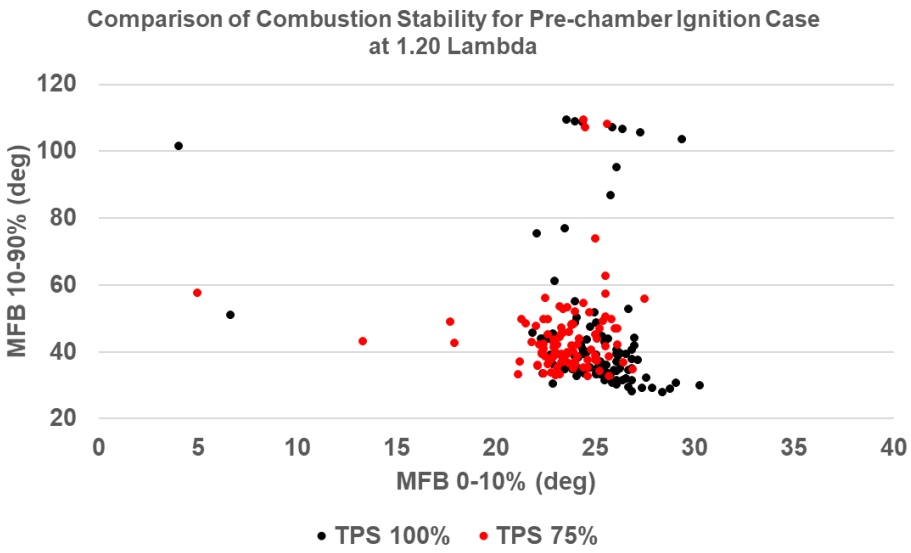

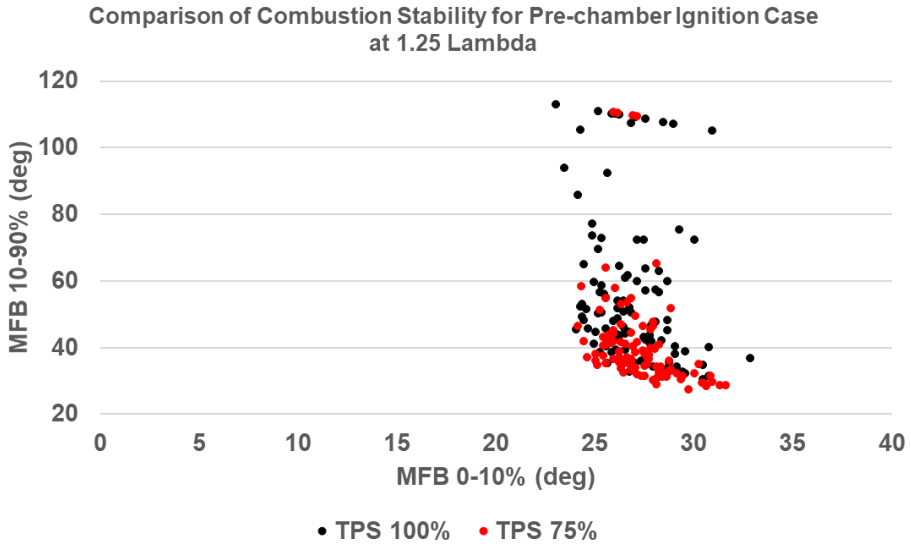

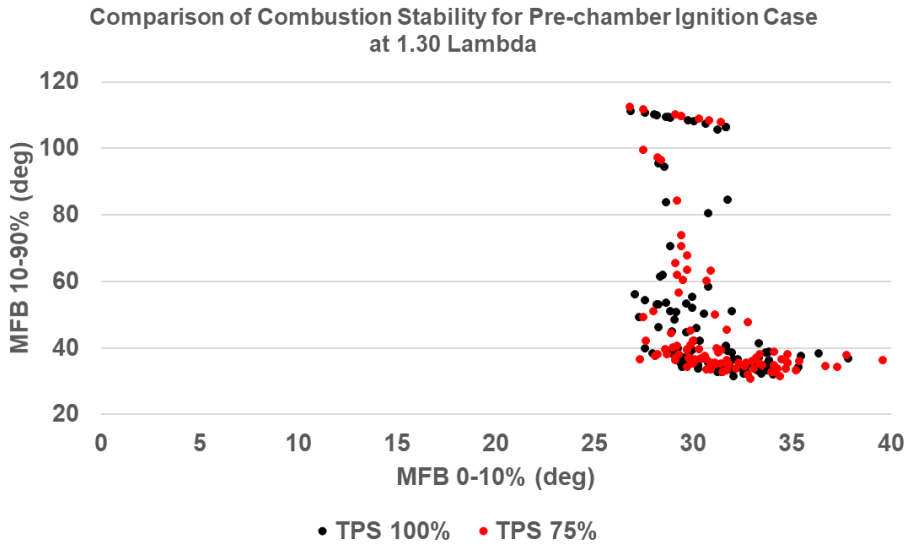

Figure 5-38 Comparison of Combustion Stability for TPS 100% and TPS 75% at 1.20, 1.25 and 1.30 Lambda Targets

Figure 5-39 Comparison of Maximum Amplitude of Pressure Oscillations for TPS 100% and TPS 75% at Lambda 1.20, 1.25 and 1.30

Figure 5-35 and 5-36 show the normalized heat release rate and the integrated heat release rate, where an improvement in both the parameters can be observed for the TPS 75% case.

Figure 5-37 shows the 100 cycle averaged burn characteristics for all relative air/fuel ratios tested. Ignition delay or burn duration of 0-10% for TPS 75% case was found to be 1.49 degree shorter at a relative air/fuel ratio of 1.20 and 0.46 degree longer at 1.25 and 1.30 than the TPS 100% case. The 50% burn point of TPS 75% case was found to be 2.54 degree lower at 1.20 relative air/fuel ratio and near identical burn points at 1.25 and 1.30 relative air/fuel ratios when compared with the TPS 100% case. TPS 75% case demonstrated a reduced burn duration across all relative air/fuel ratios with a maximum reduction of 15.78 degree at 1.25 relative air/fuel ratio.

Figure 5-38 demonstrates the combustion stability of TPS 75% where the ignition and burn characteristics were found to be more concentrated and shorter than TPS 100% case across all relative air/fuel ratios.

The average of maximum amplitude of pressure oscillations for TPS 75% were found to be near similar for all relative air/fuel ratios when compared with TPS 100%. Table 5-2 shows the comparison between the average MAPO for TPS 100% and TPS 75% cases.

Lambda	TPS 100% MAPO (bar)	TPS 75% MAPO (bar)
1.20	14.28	14.43
1.25	10.69	10.03
1.30	7.98	8.05

Table 5-2 Comparison of Average MAPO for TPS 100% and TPS 75% at Lambda 1.20, 1.25 and 1.30

5.4 Discussion of Results

5.4.1 Influence of High Tumble Flow on Pre-chamber Ignited Combustion Process

3D CFD simulation results showed that despite the lower and delayed peak pressure generated in the pre-chamber for the TPS 75% case which was due to a lean relative air/fuel ratio in the pre-chamber at ignition time. The lean relative air/fuel ratio in the pre-chamber resulted in a lower jet velocity from the pre-chamber nozzles into the main chamber- the 10-90% burn duration was relatively short compared to the TPS 100% case due to higher turbulent kinetic energy in the main chamber between 5 deg BTDC and 20 deg ATDC. The effect of turbulent kinetic energy on combustion can be visualised in terms of heat release rate, where the simulated heat release rate for TPS 75% was found to be significantly higher between 5 deg BTDC to 20 deg ATDC than the TPS 100% case due to increased flame speeds from increased turbulence.

Researchers such as (Kimura et al., 2018) who had previously studied impact of in-cylinder flow on a fuelled pre-chamber ignited engine concluded in their study that in-cylinder flow has no impact on the combustion process for a pre-chamber ignited engine as there was no need for early flame kernel development for a pre-chamber ignited engine, however this research was carried out on a low speed and low IMEP engine where the engine speed was 2000 rpm and the IMEP was limited to 5.1 bar. For the aforementioned engine, since the combustion chamber, although supercharged, is not highly downsized- the pressure difference between the main chamber and pre-chamber was expected to be high thus resulting in high jet velocities and high

jet penetration length which is why a high tumble flow did not make an impact on the combustion process in the main chamber. However, for a turbocharged high IMEP motorsport engine such as the one used in this research, engine test results had shown that a high tumble flow and the resulting high turbulence in the main combustion chamber did make a positive impact on the combustion process due a reduced pressure difference between the main chamber and pre-chamber. The reduced pressure difference between the main chamber and pre-chamber due to a high manifold pressure resulted in lower jet velocities and jet penetration thus relying on the main chamber conditions for the combustion flames to propagate in the combustion chamber as shown in the simulated results in Figure 5-21.

Engine test results had shown that there was a significant reduction in gross ISFC with a maximum reduction of 3.74 g/kWh at 1.20 relative air/fuel ratio for TPS 75% case as shown in Figure 5-29 and an upward trend of gross ISFC was observed for leaner relative air/fuel ratios as it was difficult to enrich the pre-chamber via the existing combustion chamber design at these operating points. Figure 5-38 shows the combustion stability comparison between TPS 100% and TPS 75% cases where the high turbulence can be observed to reduce the number of slow cycles for the TPS 75% case which is in-turn reflected in the lower COV of gross IMEP as shown in Figure 5-30. The combustion process for the TPS 75% case was also found to be efficient via lower exhaust gas temperatures and lower burn durations compared to TPS 100% case as shown in Figure 5-32 and 5-37.

5.4.2 Knocking Behaviour in Main Chamber for a Pre-chamber Ignition System

A reduced burn duration was observed, as shown in Figure 5-40, for the pre-chamber ignitor over a spark ignitor due to multiple ignition sites and high ignition energy offered by a pre-chamber ignitor. However, due to the pre-chamber's high volume and high surface area- heat losses could be observed in the integrated heat release rate comparison from 30 deg ATDC till exhaust valve opening time. For subsequent experiments, the pre-chamber ignitor was replaced with a 4 hole pre-chamber with a lower volume and lower surface area based on research outputs from a parallel study which was not in the scope of this project.

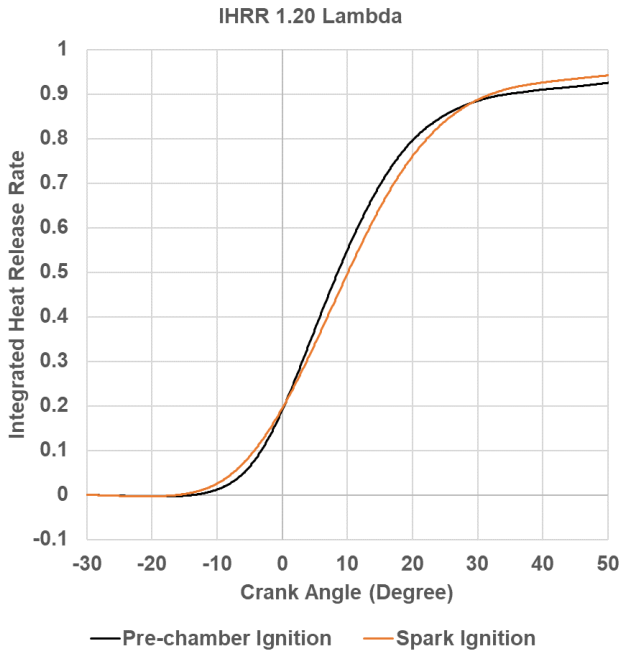

Figure 5-40 Comparison of Normalized Integrated Heat Release Rate of Pre-chamber and Spark Ignition at 1.20 Relative Air/Fuel Ratio

The in-cylinder pressure data from the pre-chamber ignited engine showed a few pre-ignition cycles at 1.20 relative air/fuel ratio for both TPS 100% and 75% which could be heard as knocking cycles via an engine stethoscope,

however, the engine operated completely free of pre-ignition and knocking cycles at 1.25 and 1.30 relative air/fuel ratio and achieved MBT or Minimum Advance for Best Torque ignition timings. The pre-ignition cycles were believed to be due to hotspots in the pre-chamber body due to its large volume and surface area, as upon inspection it was discovered that the cylinder head had locally melted onto the pre-chamber thread as shown in Figure 5-41.

Figure 5-41 Melted Aluminium on the Pre-chamber Thread

It is worth noting here that the pre-chamber ignited engine was not susceptible to end gas auto-ignition in the main chamber and no pinging noises were heard via the engine stethoscope during testing except for the pre-ignition cycles. The engine knock sensor however registered high amplitude vibrations that seemed knock-like and detected normal engine cycles as knocking cycles. The phenomenon was found to be ‘Jet Knock’ as described by Attard et al. (2012). Numerous researchers such as Soltic et al. (2019), Hua et al. (2020), Attard et al. (2012), Wakai (1993), Gupta and Bracco (1982), Hamori (2006),

Biswas (2018) have mentioned seeing pressure oscillations that seemed knock-like but were not because of end gas auto-ignition. It was found that the oscillations originated from shockwaves generated from the head of the jets from the pre-chamber as the jets rapidly compress the main-chamber contents ahead of the jets which often exceed Mach 1 leading to formation of shock structures. The formation of shock structures was simulated in 3D CFD as shown in Figure 5-42. The correlated pre-chamber ignition simulation model was utilised with a reduced Maximum Mach CFL limit to fully resolve the propagating pressure waves within the computational domain. The shock structures were depicted by a pressure difference iso-surface of 5 bar which was coloured in blue and the flame front was depicted by a 1700 K temperature iso-surface was coloured in black. The Mach number at the vicinity of pre-chamber nozzle was found to be 1.27.

Figure 5-43 shows a comparison of a typical raw cylinder pressure signal for both spark ignition and pre-chamber ignition systems which were selected based on proximity to the averaged cylinder pressure signal for either of the ignition systems from test data. A high amplitude pressure oscillation was observed for the pre-chamber ignition system. Filtering the signal with a high pass filter, as shown in Figure 5-44, had shown that the high amplitude oscillation for the pre-chamber ignition system commenced at 8 deg BTDC which correlates with the CFD simulation results as the simulation results showed that the jets first ejected from the pre-chamber into the main-chamber at 8 deg BTDC. Comparison of the maximum amplitude of pressure oscillations showed that the MAPO of pre-chamber ignition system was 15.1 bar compared to 7.2 bar of the spark ignition system. It is worth noting here

that the spark ignition system also has a low amplitude oscillation due to faster combustion due to high turbulence at 7500 rpm which is a typically high engine speed where pressure waves can be generated ahead of the flame front which reflect off the combustion chamber walls and can be seen as low pressure oscillations.

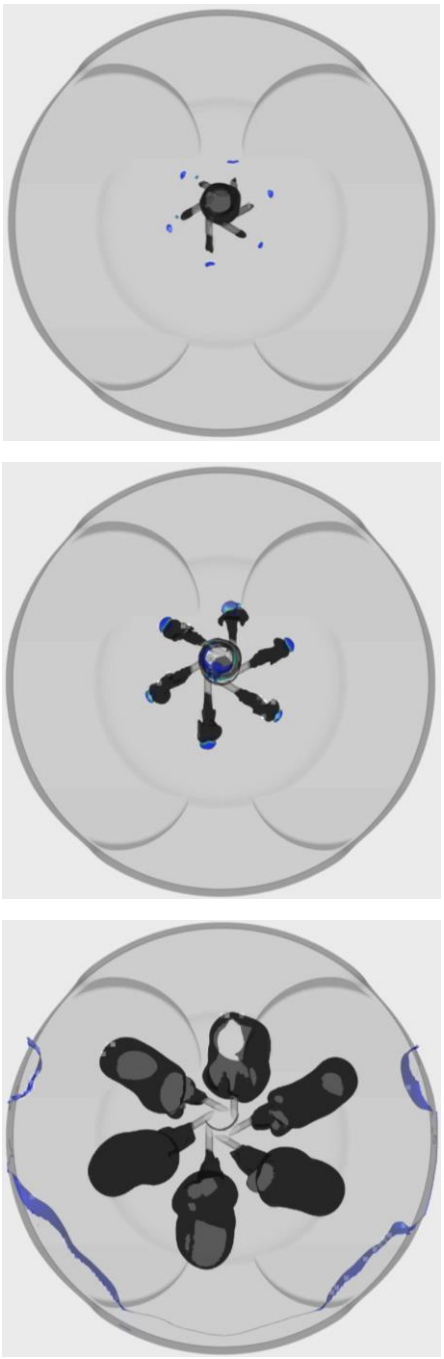

Figure 5-42 Depiction of Shock Structures at 8 deg BTDC, 7 deg BTDC and 3 deg BTDC with Flame shown in Black and Pressure Difference Iso-surface shown in Blue

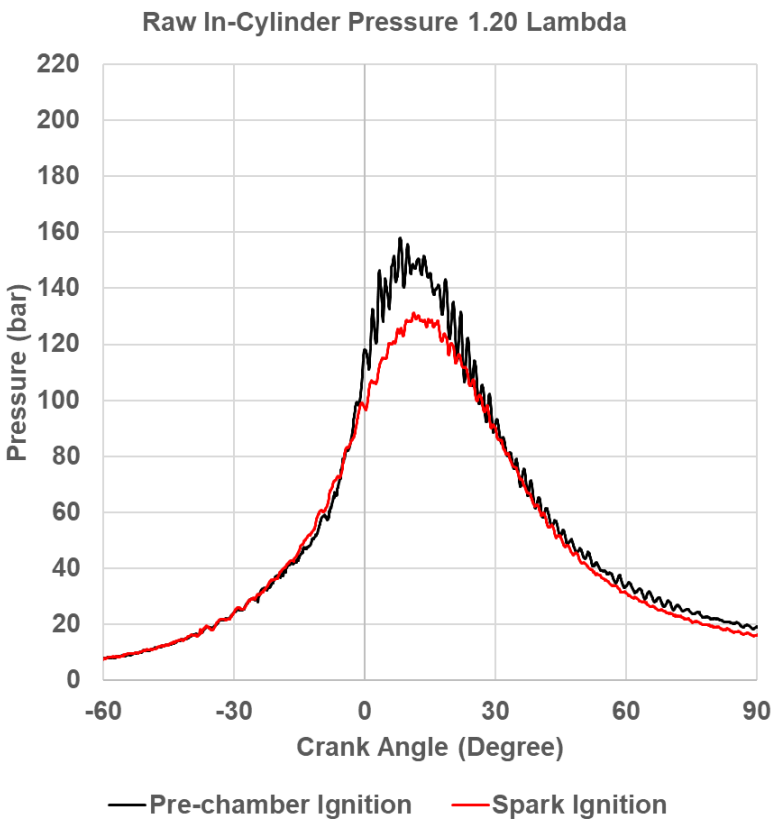

Figure 5-43 Comparison of Raw In-Cylinder Pressure Signal of Pre-chamber and Spark Ignition System

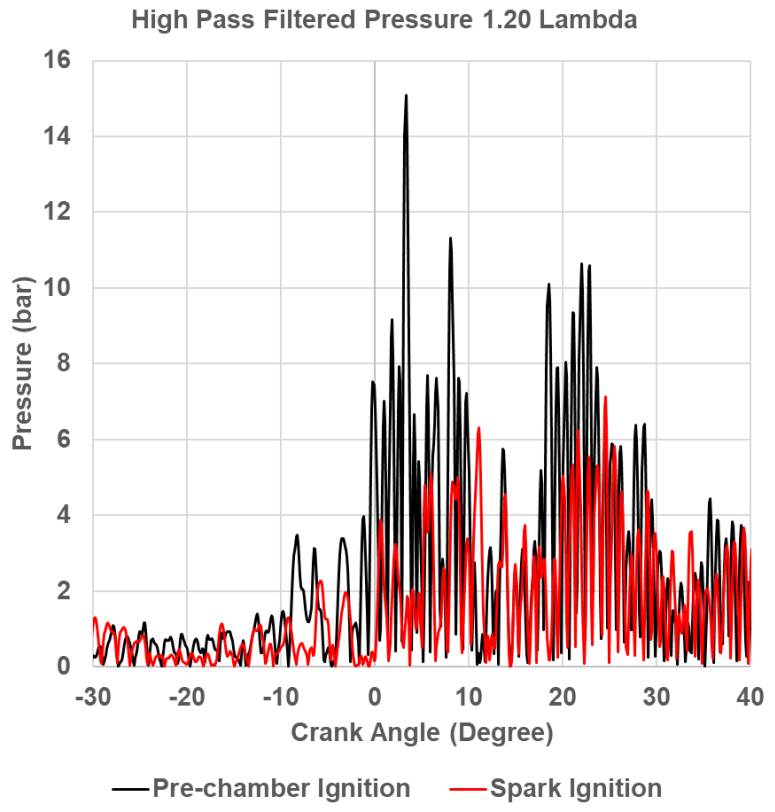

Figure 5-44 Comparison of High Pass Filtering of Raw Pressure Signal for Pre-chamber and Spark Ignition System

6. Investigation of the Influence of Piston Crown Geometry on a Pre-chamber Ignited Engine

The enrichment of the pre-chamber is known to be a key factor in pre-chamber ignited engine as an enriched pre-chamber would reduce ignition delay and result in higher flame speeds. The higher flame speed results in generating a higher pressure within the pre-chamber which would further increase the pressure difference between the pre-chamber and main chamber thus improving the jet ejection characteristics from the pre-chamber which ignite the contents of main chamber. Results from Chapter 5 showed that the main chamber charge motion does have a positive impact on the main chamber combustion processes for a pre-chamber ignited engine via high tumble and turbulence in the main chamber which affect mixture formation and flame propagation.

As the combustion chamber for a gasoline fuelled engine is suited to a spark ignited engine which has been studied and optimised for over a century, little is known about the impact of combustion chamber design for a pre-chamber ignited engine. This chapter aims to find and study an optimum piston crown shape for a pent roof style engine head which would facilitate to further study the impact of in-cylinder conditions on a pre-chamber ignited engine.

6.1 Piston Crown Development

The main aim of the piston crown shape development was to design a piston crown that provided an enriched mixture to the pre-chamber, generated high tumble during intake stroke which aided mixture formation and generated higher turbulence during compression stroke which aided combustion processes for a given compression ratio.

Following an iterative study in 3D CFD it was found that a bowl in the piston with a smaller diameter and higher depth, which was positioned towards the exhaust side resulted in an improved tumble ratio, improved turbulent kinetic energy when the piston approached TDC and improved enrichment near the spark plug electrodes- simulation results of which have been presented in this section.

Figure 6-1 shows the comparison of the design of the piston crown shapes. The piston, which was originally fitted to the engine, will be referred to as a ‘Base Piston’ and the newly developed piston will be referred to as a ‘Bowl Piston’. The bowl piston had a depth more than twice than that of the base piston and the bowl piston had a smaller diameter bowl which was 38% smaller than that of the base piston. Additional features such as removal of material from the intake and exhaust squish area were also facilitated to reduce stagnation regions between the two intake and two exhaust valve pockets which were aimed at improving combustion- as found in simulation results.

To study the differences between the two piston designs, five 4-stroke cycles were simulated for each piston design with the engine operating at 7000 rpm, 1.20 relative air/fuel ratio with a fuel flow rate of 13.33 kg/h and a 33 deg BTDC

spark timing with a compression ratio of 14.1. The simulation for piston optimisation was conducted on a spark ignited engine due to low computational cost as a pre-chamber ignited engine simulation took 5 times longer than the spark ignited engine.

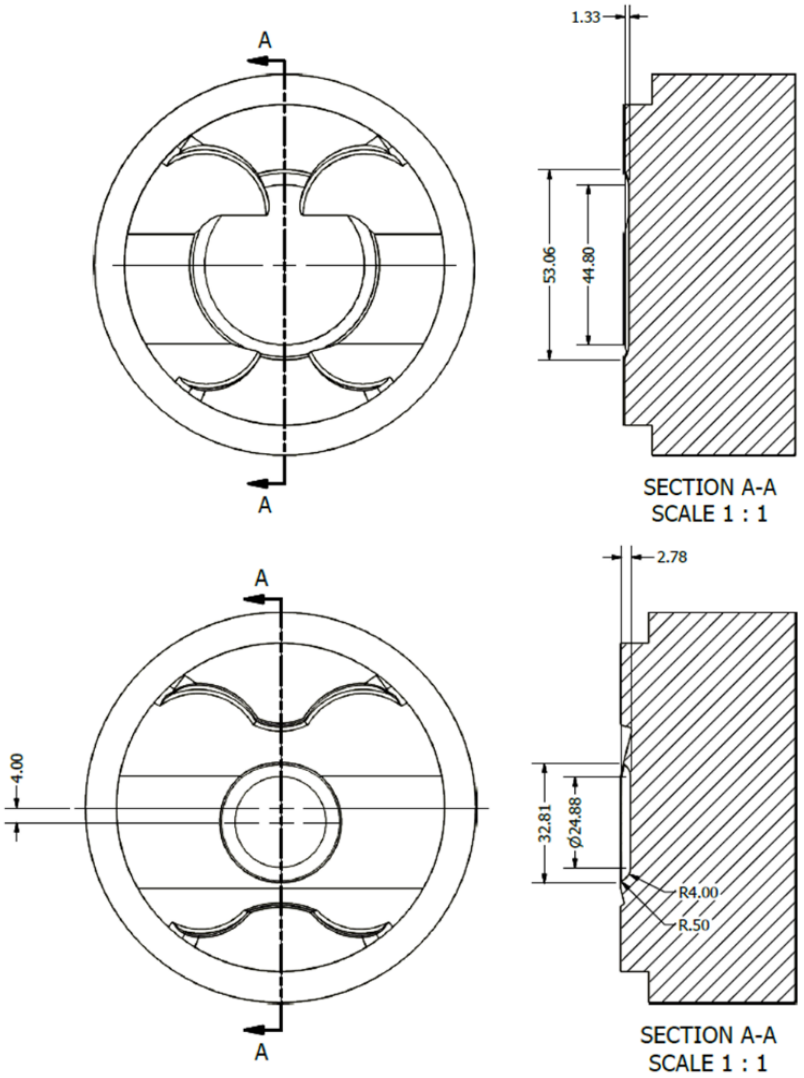

Figure 6-1 Base Piston (Top) and Bowl Piston (Bottom) Crown Designs

Figure 6-2 and 6-3 show the comparison between the simulated in-cylinder pressure for base and bowl piston. It was observed that the bowl piston resulted in a higher IMEP of 22.1 bar compared with 21.06 bar than that of the base piston. The improvement in 1.04 bar of IMEP was found to be due to reduction in ignition delay which was the consequence of enrichment near the

spark plug electrodes which also resulted in lower cyclic variation as shown in Figure 6-3 and an improvement in tumble and turbulence levels, as shown in Figure 6-11 and 6-16 which led to faster combustion. Cycle 1 was eliminated from the results as it was an initialisation cycle.

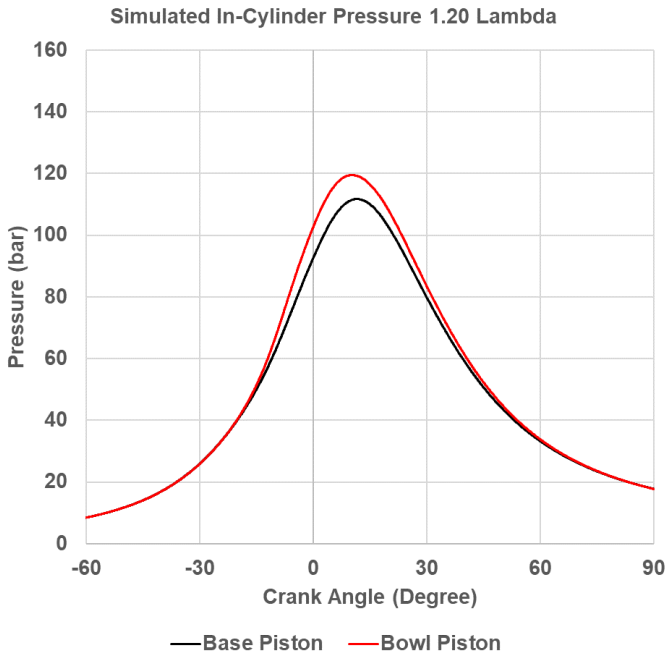

Figure 6-2 Comparison of Simulated Averaged In-cylinder Pressure for Base Piston (Black) and Bowl Piston (Red)

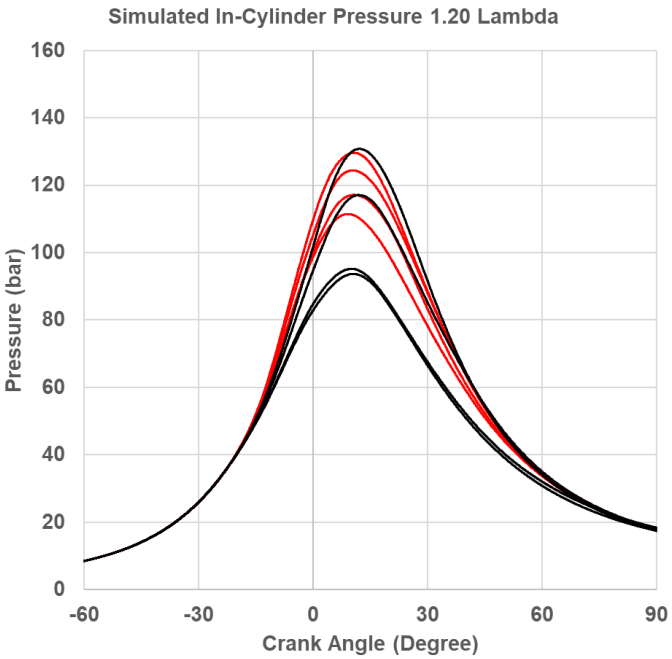

Figure 6-3 Comparison of Simulated In-cylinder Pressure Cycles 2-5 for Base Piston (Black) and Bowl Piston (Red)

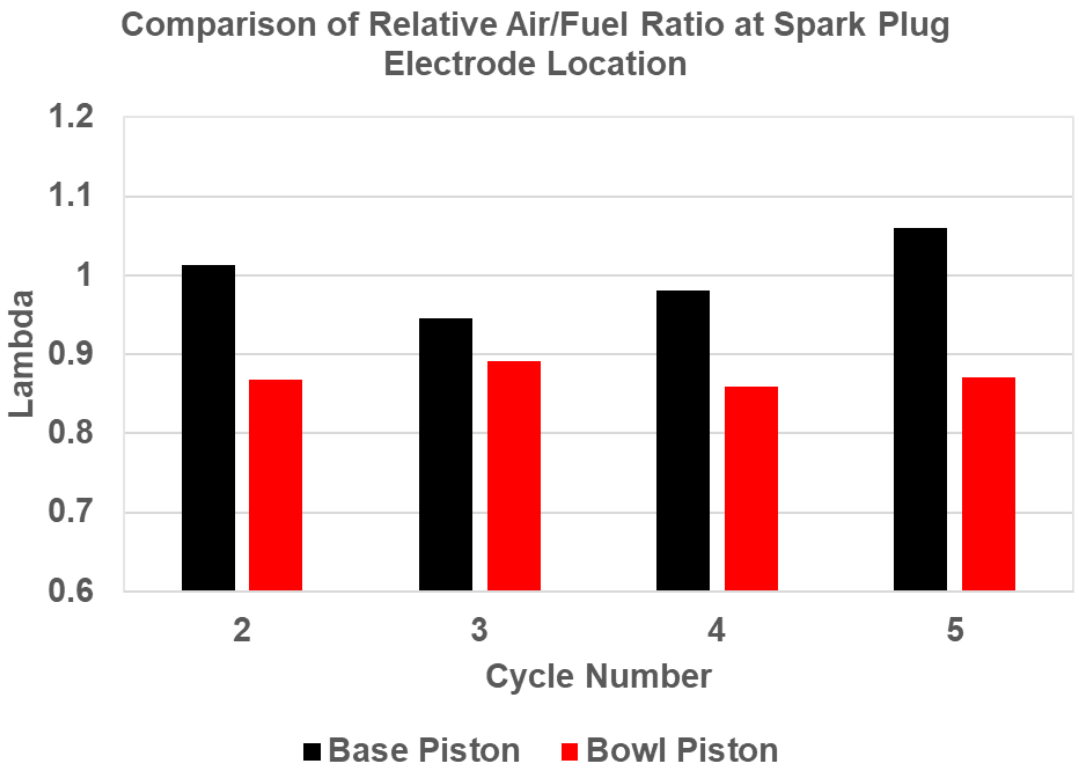

Figure 6-4 Comparison of Relative Air/Fuel Ratio at Spark Plug Electrodes at Spark Timing for Cycles 2-5 for Base Piston and Bowl Piston

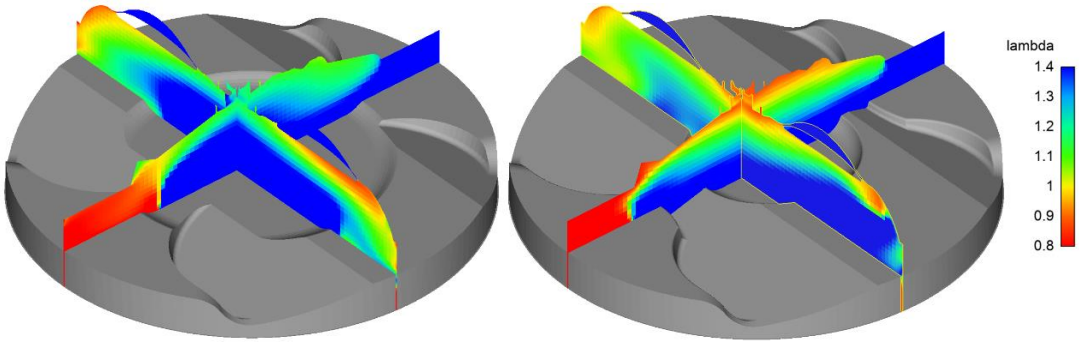

Figure 6-5 Comparison of Relative Air/Fuel Ratio Distribution in Combustion Chamber at 33 deg BTDC of Cycle 2 for Base Piston and Bowl Piston

Figure 6-4 shows that the relative air/fuel ratio at the spark plug electrodes were consistently below 0.9 for the bowl piston whereas the relative air/fuel ratio varied between 0.95 to 1.06. Figure 6-5 shows the mixture distribution at 2nd cycle in the combustion chamber at 33 BTDC.

A parametric study on the piston bowl location was carried out to assess its influence on the enrichment of the mixture in the vicinity of the spark plug electrodes. For the purpose of this study, three different iterations of the bowl location were simulated- the bowl was positioned at the centre of the piston and 4mm towards the exhaust and intake side of the piston. Figure 6-6 shows the results of the simulation where enrichment at the vicinity of the spark plug can be clearly observed for the exhaust side bowl.

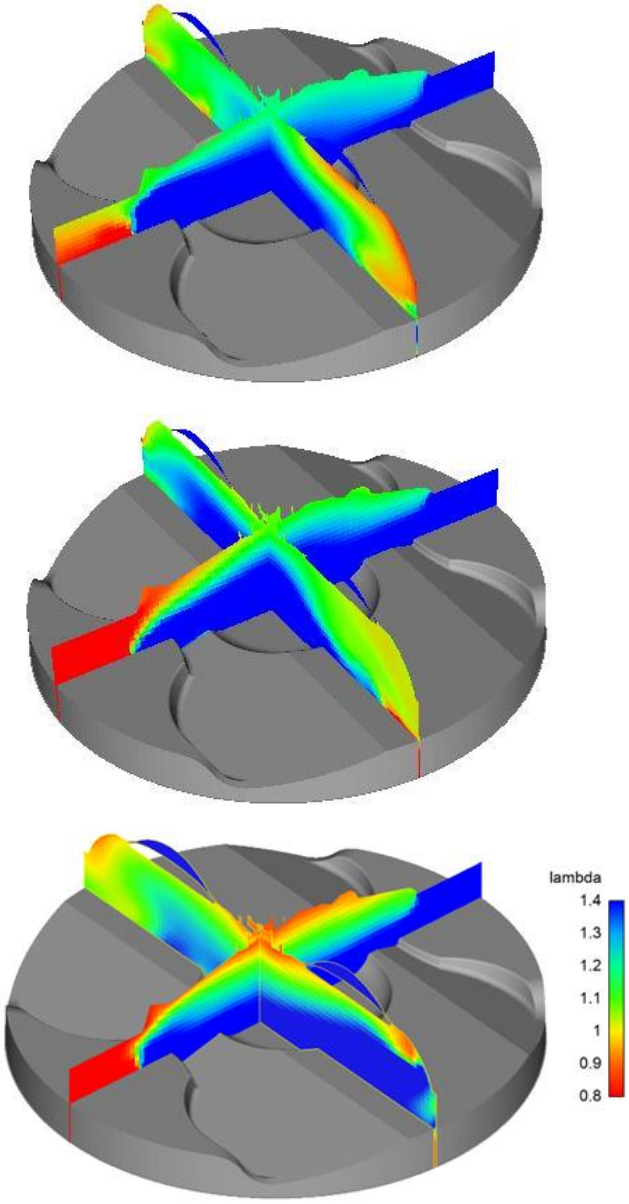

Figure 6-6 Comparison of Relative Air/Fuel Ratio Distribution in Combustion Chamber at 33 deg BTDC of Cycle 2 for Intake Side Bowl (Top), Centre Bowl (Centre) and Exhaust Side Bowl (Bottom)

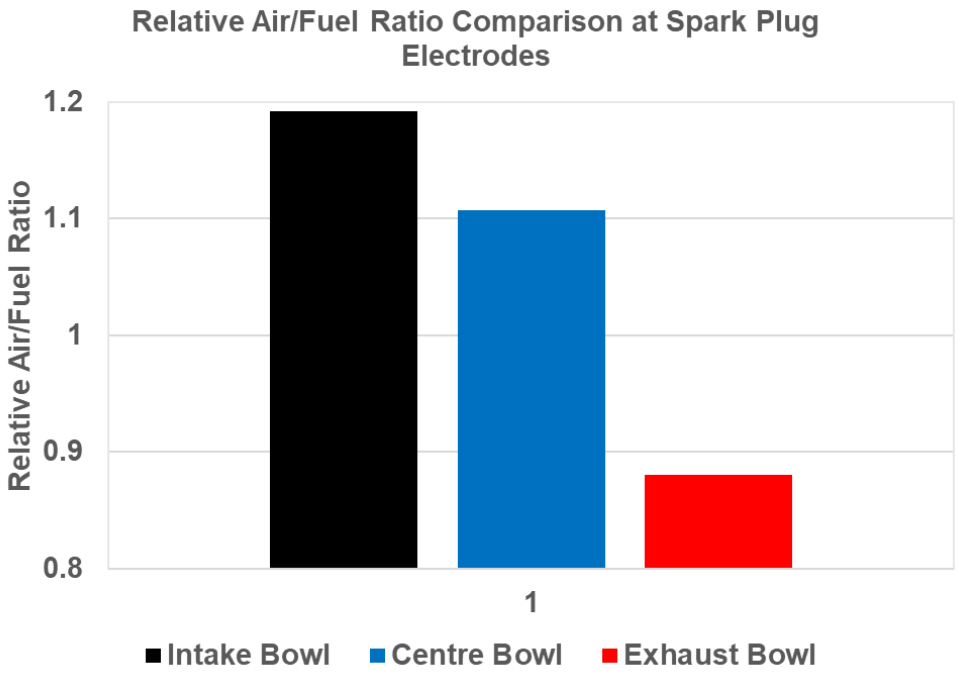

Figure 6-7 Comparison of Relative Air/Fuel Ratio at Spark Plug Electrodes at Spark Timing for Various Bowl Locations

Figure 6-7 shows that the exhaust side bowl demonstrated a higher mixture enrichment near the spark plug electrodes- 35.4% and 25.8% more enrichment when compared with the intake side bowl and centre bowl positions, respectively.

Figure 6-8 and 6-9 show that the heat release for bowl piston design was much higher coupled with a shortened ignition delay when compared with the base piston. It was found that the bowl piston exhibited a shorter ignition delay by 4.31 degrees and a shorter burn duration by 8.29 degrees when compared with the base piston design as shown in Figure 6-10.

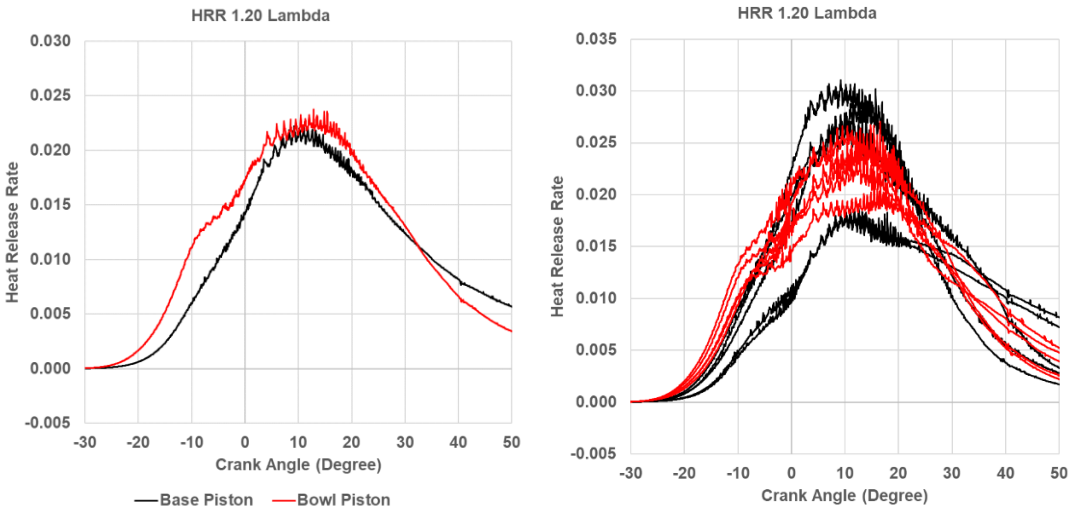

Figure 6-8 Comparison of 5 Cycle Averaged (Left) and Individual Simulated Cycles (Right) of Heat Release Rate for Base Piston (Black) and Bowl Piston (Red)

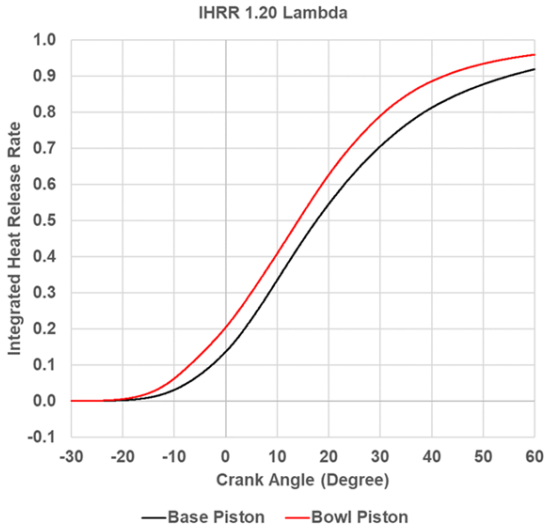

Figure 6-9 Comparison of Simulated Integrated Heat Release Rate for Base Piston and Bowl Piston

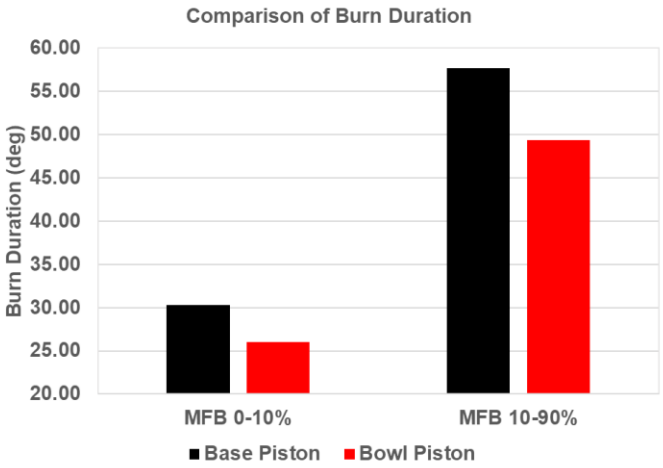

Figure 6-10 Comparison of Simulated Ignition Delay and Burn Duration for Base Piston and Bowl Piston

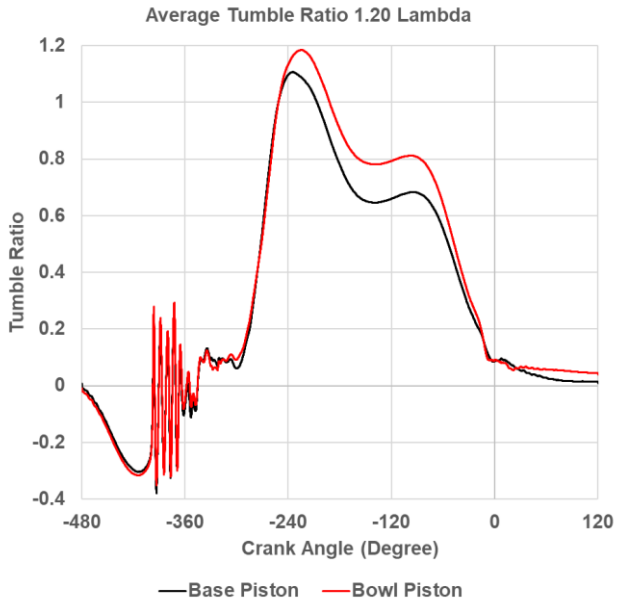

Figure 6-11 Comparison of Simulated In-cylinder Tumble Ratio for Base Piston and Bowl Piston

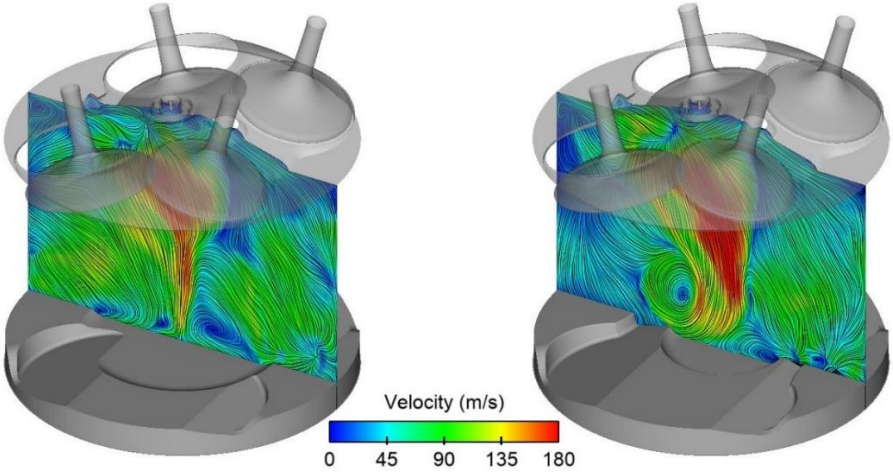

Figure 6-12 Comparison of Simulated In-cylinder Velocities at 240 deg BTDC for Base Piston and Bowl Piston

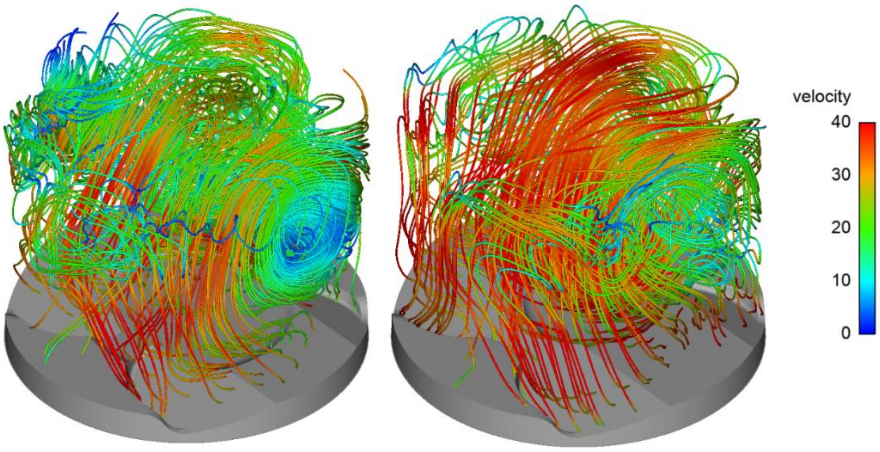

Figure 6-13 Comparison of Velocity Streamlines Depicting In-cylinder Flow at 120 deg BTDC for Base Piston and Bowl Piston

Figure 6-11 shows the comparison of 4 cycle averaged tumble ratio. The tumble ratio plot was observed to contain two components- the first being tumble generation region which can be observed between 360 deg BTDC and 180 deg BTDC, this is where tumble is generated via the intake port when the valves are open, as shown in Figure 6-12. The combustion chamber with bowl piston generated 8.2% higher tumble ratio than the base piston. The high tumble generation can be attributed to the piston bowl design which is able to guide the incoming air flow from the ports by providing an optimum angle of attack for the incoming flow. The higher depth of the bowl design also aids the circular motion of the flow via a higher dilatation which resulted in a well-defined vortex just above the bowl as shown in Figure 6-12.

The second component- the tumble sustenance region, where the tumble is sustained by the combustion chamber until the piston approaches TDC can be observed between 180 deg BTDC and TDC. Figure 6-13 shows the velocity streamlines in the combustion chamber where a higher velocity and lower stagnation regions can be observed in the case of the bowl piston crown design which aids in a 19% improvement in tumble sustenance over the base piston crown design. Figure 6-14 shows that velocity at the vicinity of the spark plug is higher for the bowl piston that the base piston. A higher velocity near the spark plug would aid in faster development of flame kernel thus reducing ignition delay which can be observed in Figure 6-19.

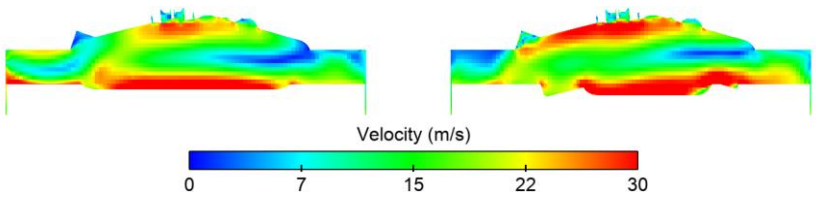

Figure 6-14 Comparison of Simulated In-cylinder Velocities at 33 deg BTDC for Base Piston and Bowl Piston

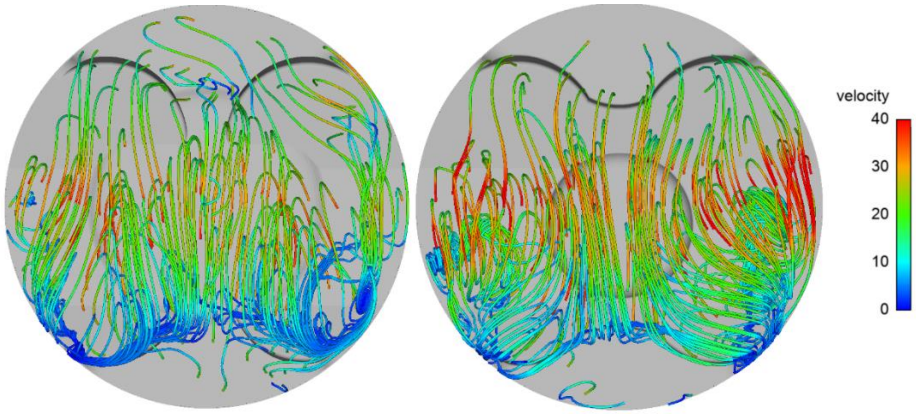

Figure 6-15 Velocity Streamlines Depicting In-cylinder Flow with Emphasis towards Exhaust Valve Pocket Region at 33 deg BTDC for Base and Bowl Piston

Figure 6-15 shows the impact of material removal between the valve pockets. Velocity streamlines show that the stagnation regions around the exhaust valve pockets, which would normally be prone to knocking combustion due to slower combustion in these regions, were significantly reduced in the bowl piston. Results from the pre-chamber ignition simulation results clearly highlight the impact of the material removal which is shown in Figure 6-32.

Figures 6-16, 6-17 and 6-18 show that the turbulent kinetic energy for bowl piston crown design was higher than the base piston crown design from combustion start till the end of combustion. TKE was found to be 12% higher across the combustion chamber at ignition time. Higher turbulence levels are known to improve flame speeds and thus reduce burn duration.

Figure 6-19 shows the comparison of combustion flames for base and bowl piston. It was observed that the flame kernel for the bowl piston developed quicker than the base piston which can be attributed to higher mean flow velocity at the spark plug electrodes. Faster combustion was observed in the case of the bowl piston which can be attributed to high turbulence levels present in the combustion chamber which improved flame speeds.

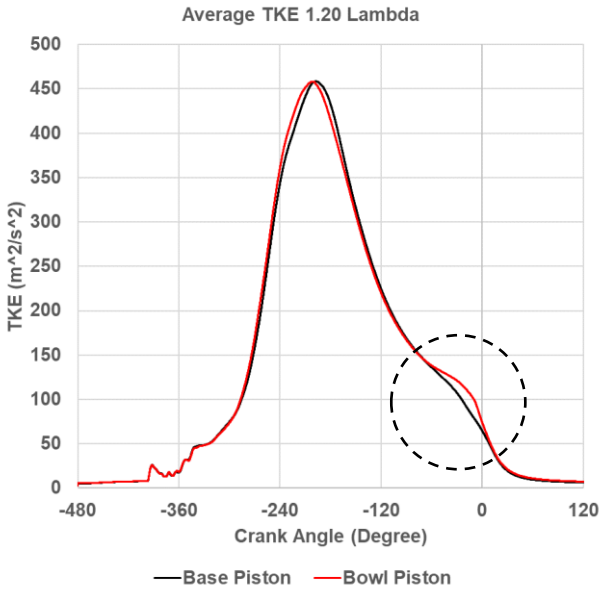

Figure 6-16 Comparison of Simulated Turbulent Kinetic Energy for Base and Bowl Piston

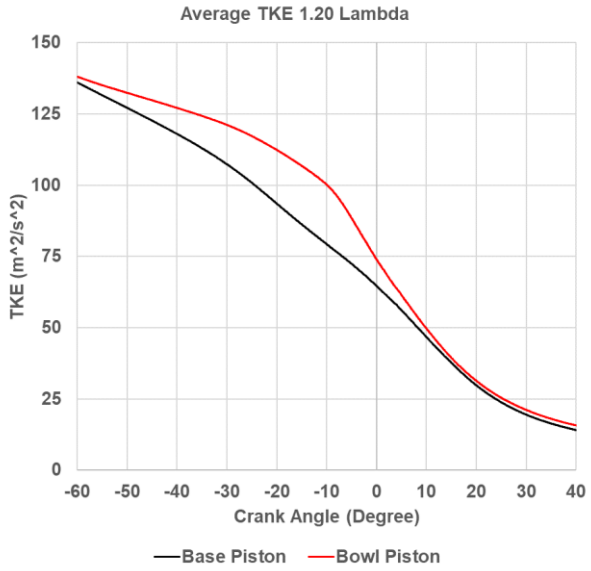

Figure 6-17 Enlarged View of Comparison of Simulated Turbulent Kinetic Energy for Base and Bowl Piston

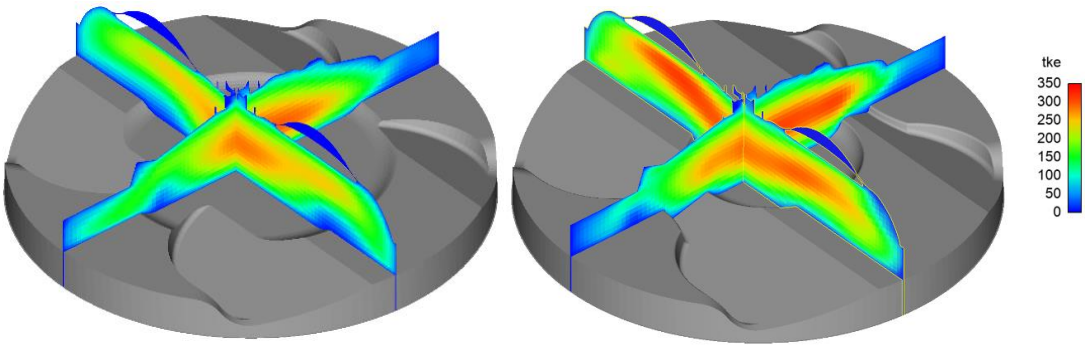

Figure 6-18 Comparison of Simulated Turbulent Kinetic Energy at 33 deg BTDC for Base and Bowl Piston

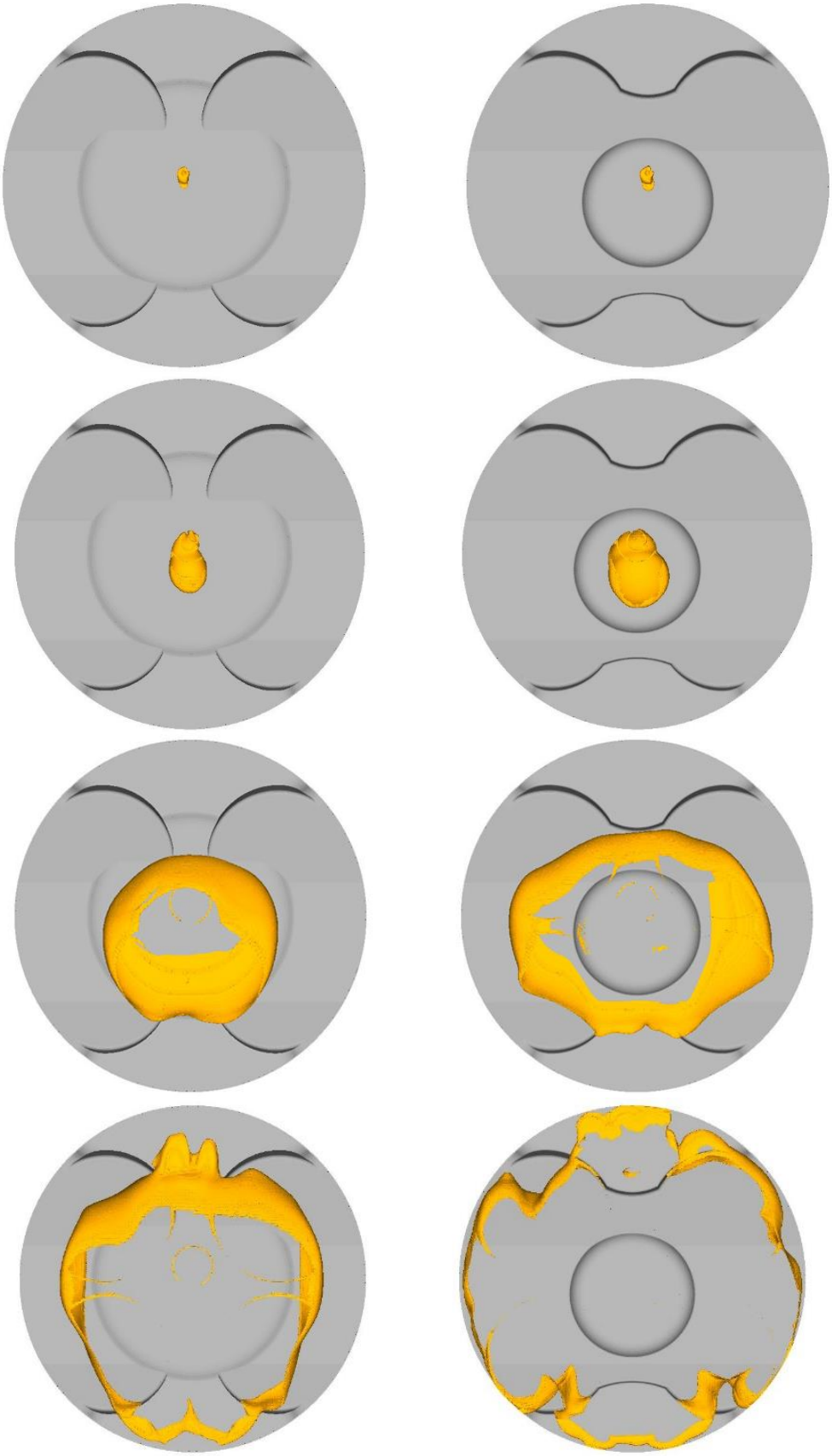

Figure 6-19 Comparison of Combustion Flames for Base Piston (Left) and Bowl Piston (Right) at 28 deg BTDC, 18 deg BTDC, 2 deg BTDC and 20 deg ATDC (Top to Bottom)

6.2 Investigation of the Influence of Piston Crown Design on a Pre-chamber Ignition System via Simulation

To study the impact of pre-chamber ignition, the spark plug was replaced with a 4 hole pre-chamber ignitor which had a volume of 0.8 cm^3 which was optimised via a parallel study – not in the scope of this research thesis. Simulations were run for two cycles each for the base and bowl piston crown designs at an engine speed of 7500 rpm with the engine operating at 1.20 relative air/fuel ratio with an ignition timing of 24 deg BTDC. Results from the 2^{nd} cycle of the simulations are presented for each of the piston crown designs, further cycles were not simulated due to high computational demand. The aim of the simulation exercise was to establish the impact of main chamber flow conditions on a pre-chamber ignited engine.

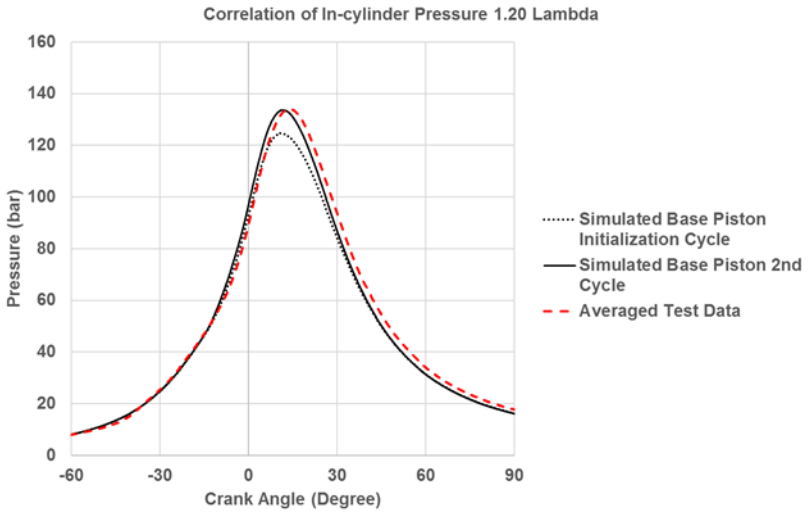

Figure 6-20 Correlation of Simulated In-cylinder Pressure for Base Piston

Figure 6-20 shows the correlation between the 100 cycle average test and simulated in-cylinder pressure data. The simulated in-cylinder pressure cycles stayed close to the average test pressure cycle due to a reduction of cyclic

variation offered by the pre-chamber ignition system. Simulating further cycles would provide more information on cyclic variation however this was not carried out due to simulation models being computationally expensive.

Following correlation, the base piston was replaced with a bowl piston in the simulation. Simulation results showed that the gross IMEP was found to be the same for the base and bowl piston at 22.14 bar for the respective second cycles, however investigation of the simulation results revealed that ignition delay in the case of bowl piston was higher than that of the base piston due to a leaner relative air/fuel ratio in the pre-chamber of the bowl piston case than the base piston due to cyclic variation induced by mean flow in the 3D CFD model which can be cured by simulating more cycles. It was found that for the bowl piston case the pre-chamber had a relative air/fuel ratio of 1.185 at ignition time compared to 1.08 found in the 4 hole pre-chamber of the base piston case. Simulations with the 6 hole pre-chamber ignitor had shown that the pre-chamber was more enriched with the bowl piston than the base piston in multiple cycles as shown in Figure 6-23. However, since the aim of the simulation was to establish the impact of high tumble and turbulence in the main-chamber of a pre-chamber ignition system- further cycles were not simulated as the 2nd cycles of the base and bowl piston had established the impact of in-cylinder flow on combustion, results of which are presented in this section.

Figure 6-21 shows the comparison of simulated in-cylinder pressure and pre-chamber pressure. The pre-chamber peak pressure for the bowl piston was found to generate a lower peak pressure than the base piston case following ignition due to lower enrichment in the pre-chamber as shown in Figure 6-22.

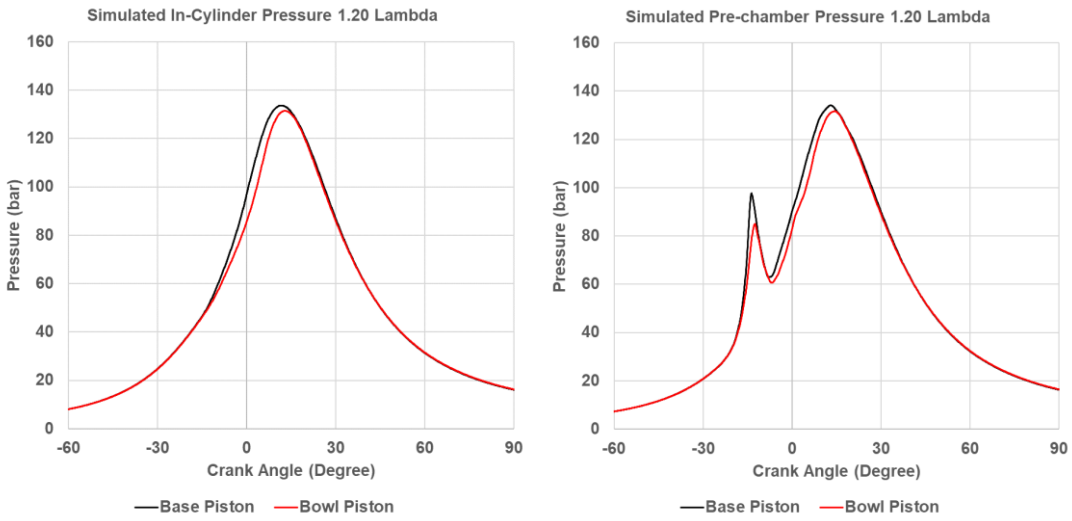

Figure 6-21 Comparison of Simulated In-cylinder (Left) and Pre-chamber (Right) Pressure for Base and Bowl Piston

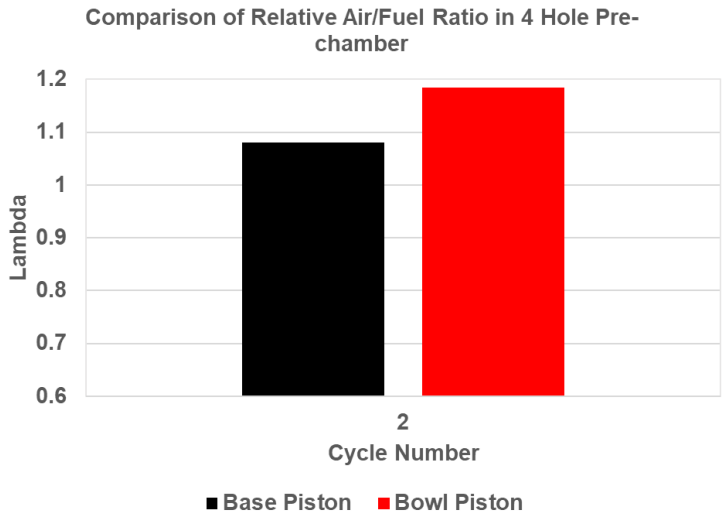

Figure 6-22 Comparison of Fuel Distribution in 4 Hole Pre-chamber for Base and Bowl Piston at Ignition Time

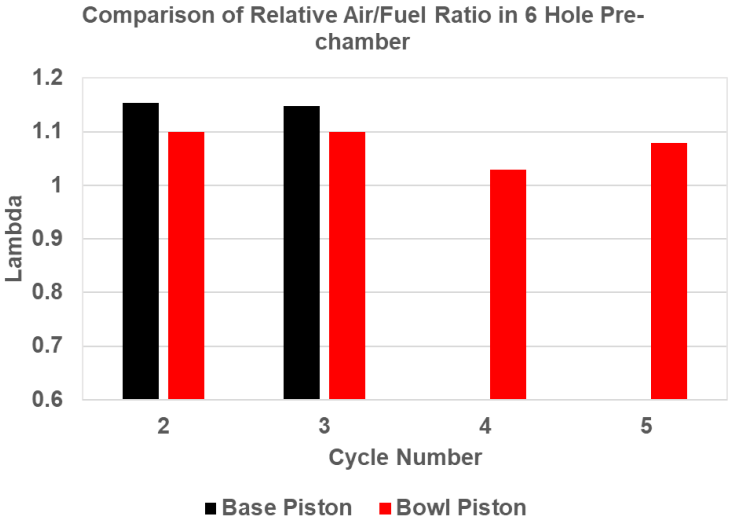

Figure 6-23 Comparison of Fuel Distribution in 6 Hole Pre-chamber for Base and Bowl Piston at Ignition Time

The difference between the pre-chamber peak pressure and main chamber pressure was found to be 48.47 bar for the base piston compared to 34.32 bar for the bowl piston. The lower pressure difference between the pre-chamber and main chamber for the bowl piston was expected to reduce the jet velocity at the nozzles of the pre-chamber and thus reduce penetration of the jet into the main chamber which would in turn reduce the turbulence generated in the main chamber via shear action of the jet flow when compared with the base piston case, resulting in longer burn duration and a longer ignition delay.

A delayed main chamber combustion was thus observed for the bowl piston case which can be visualised via a delayed combustion start as shown in Figure 6-24 and 6-25 which compared the heat release rate and integrated heat release rate for the two piston crown designs.

A higher heat release rate was observed in the case of the bowl piston between 5 deg ATDC and 15 deg ATDC. Figure 6-26 shows that the ignition delay was 2.3 degrees longer for the bowl piston case however the final 10-90% mass fraction burned was only 0.7 degrees longer than the base piston. The MFB 10-75% showed that the bowl piston case had burned the 10% to 75% of mass fraction of the charge mass 1.9 degrees faster than the base piston case. It was found that the main chamber conditions aided the faster combustion in the bowl piston case as there was high turbulence already present in the main chamber due to breakdown of a higher tumble ratio.

Figure 6-27 shows the comparison of tumble ratio between the two piston crown designs and as expected the bowl piston crown design generated and

sustained a higher tumble ratio compared to the base piston as discussed in the previous sections.

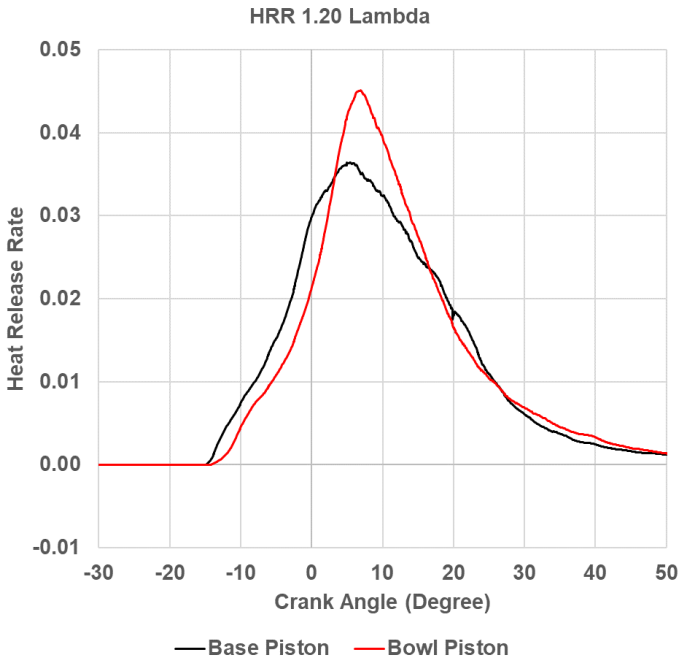

Figure 6-24 Comparison of Simulated Heat Release Rate for Base and Bowl Piston

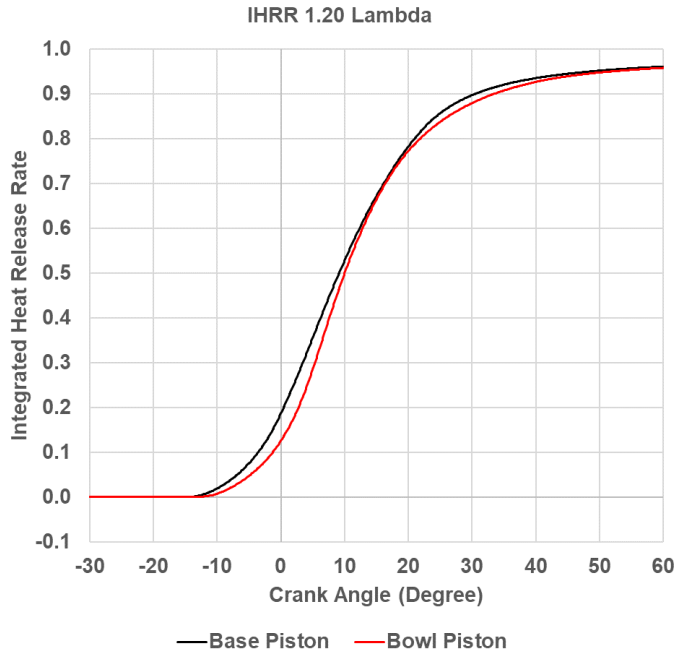

Figure 6-25 Comparison of Simulated Integrated Heat Release Rate for Base and Bowl Piston

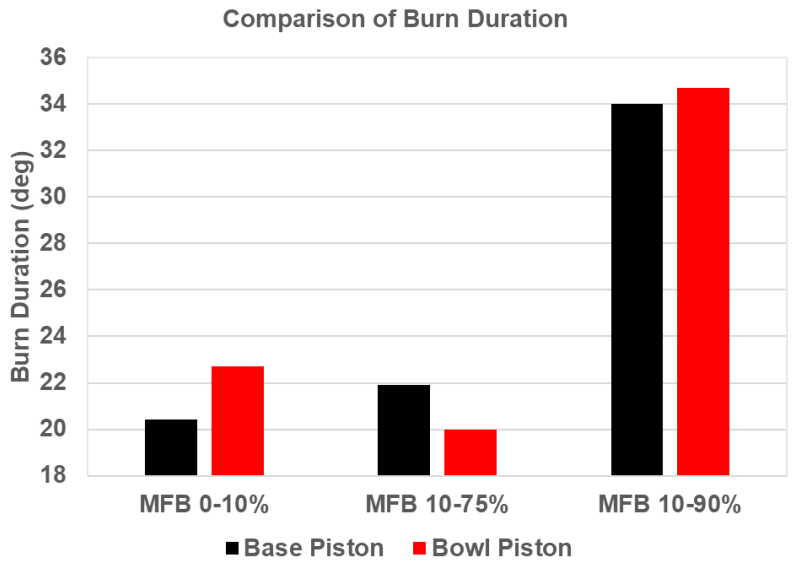

Figure 6-26 Comparison of Simulated Ignition Delay and Burn Durations for Base and Bowl Piston

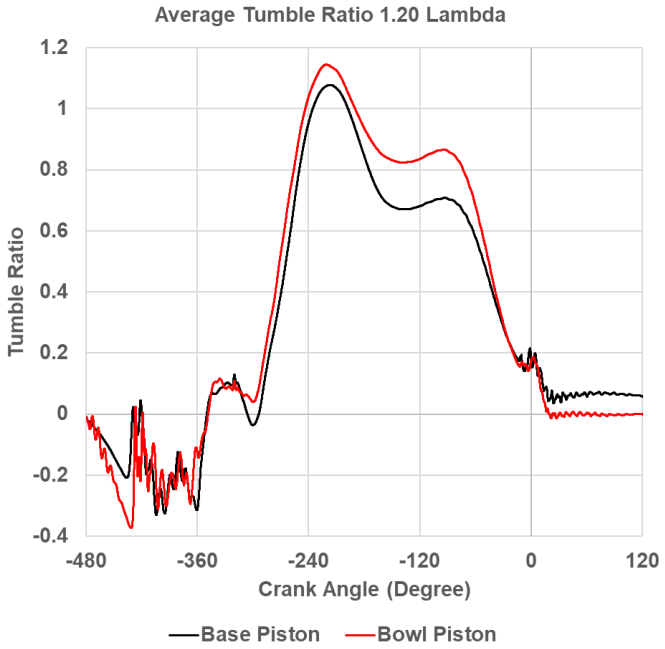

Figure 6-27 Comparison of Simulated In-cylinder Tumble for Base and Bowl Piston

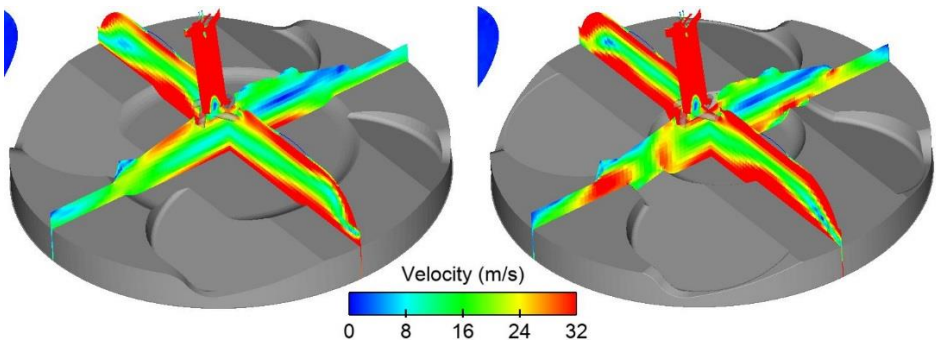

Figure 6-28 Comparison of Simulated In-Cylinder Velocities at 24 deg BTDC for Base (Left) and Bowl Piston (Right)

Figure 6-29 and 6-30 show the comparison of simulated turbulence levels for base and bowl pistons in the second cycle. It was observed that due to poor enrichment of the pre-chamber in the case of bowl piston crown design for the particular simulated cycle, the initial jets from the nozzles of the pre-chamber were delayed and had a lower penetration which can be visualised in Figure 6-32. However, since the turbulent kinetic energy of the main chamber was already 9% higher for the piston bowl crown design at 15 deg BTDC compared to the base piston, the TKE generated by shear action of the jets on the main chamber flow was low- 50% lower than the base piston crown design as observed in Figure 6-30, the overall turbulence levels in the main chamber remained high in the main chamber for the bowl piston throughout the expansion cycle owing to already high turbulence levels present in the main chamber before the jet initiation time. This ensured a faster flame speed after jet ignition of the main chamber contents which aided the reduction of burn duration.

Figure 6-31 shows the TKE generated by the pre-chamber jets in the main chamber via shear action, the flame is shown via a transparent black 1700K temperature isosurface. It was observed that the jets generated TKE only along the direction of the nozzle and the turbulence levels in the shadow regions largely remained undisturbed.

Thus, it was concluded that the main chamber conditions had a sizeable impact on the pre-chamber ignited engine. The main chamber conditions such as the one found in bowl piston would aid in reducing cyclic variations owing to certain cycles that have a poorly enriched pre-chamber. The high turbulence levels present in the main chamber would thus aid in propagating the flame

front in the shadow regions of combustion chamber away from the jets and also aid in generating a higher turbulence via shear action of the jets as the jets further convert the already small eddies in the main chamber to even smaller eddies.

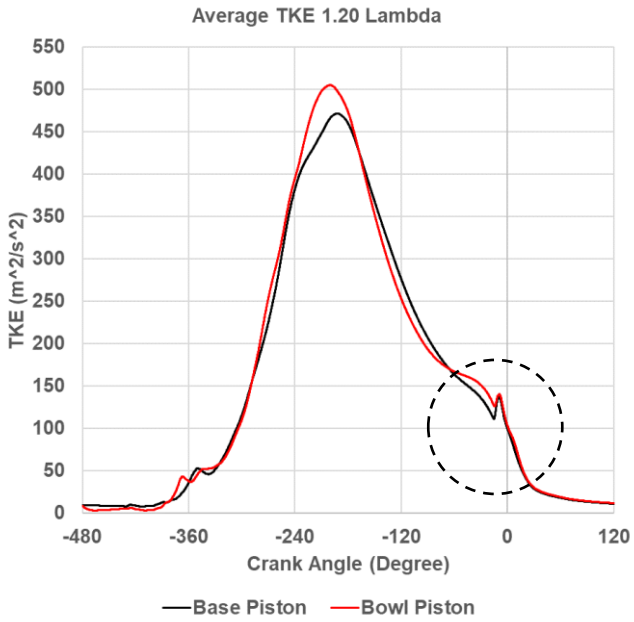

Figure 6-29 Comparison of Simulated Turbulent Kinetic Energy for Base and Bowl Piston

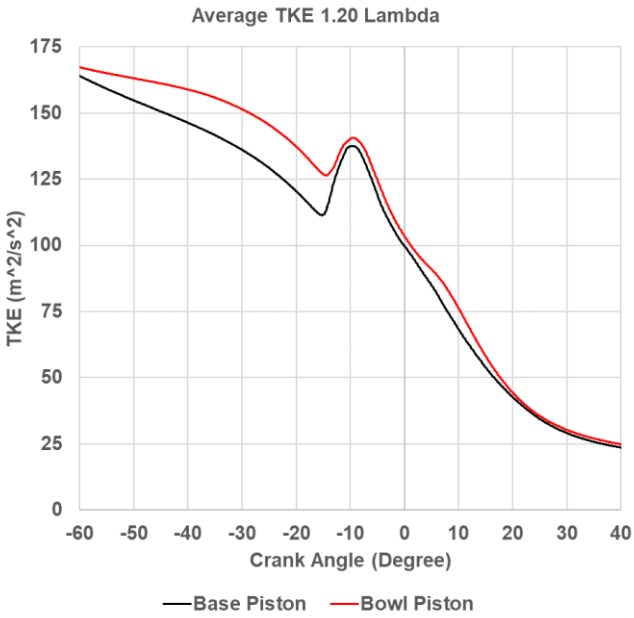

Figure 6-30 Enlarged View of Comparison of Simulated Turbulent Kinetic Energy for Base and Bowl Piston

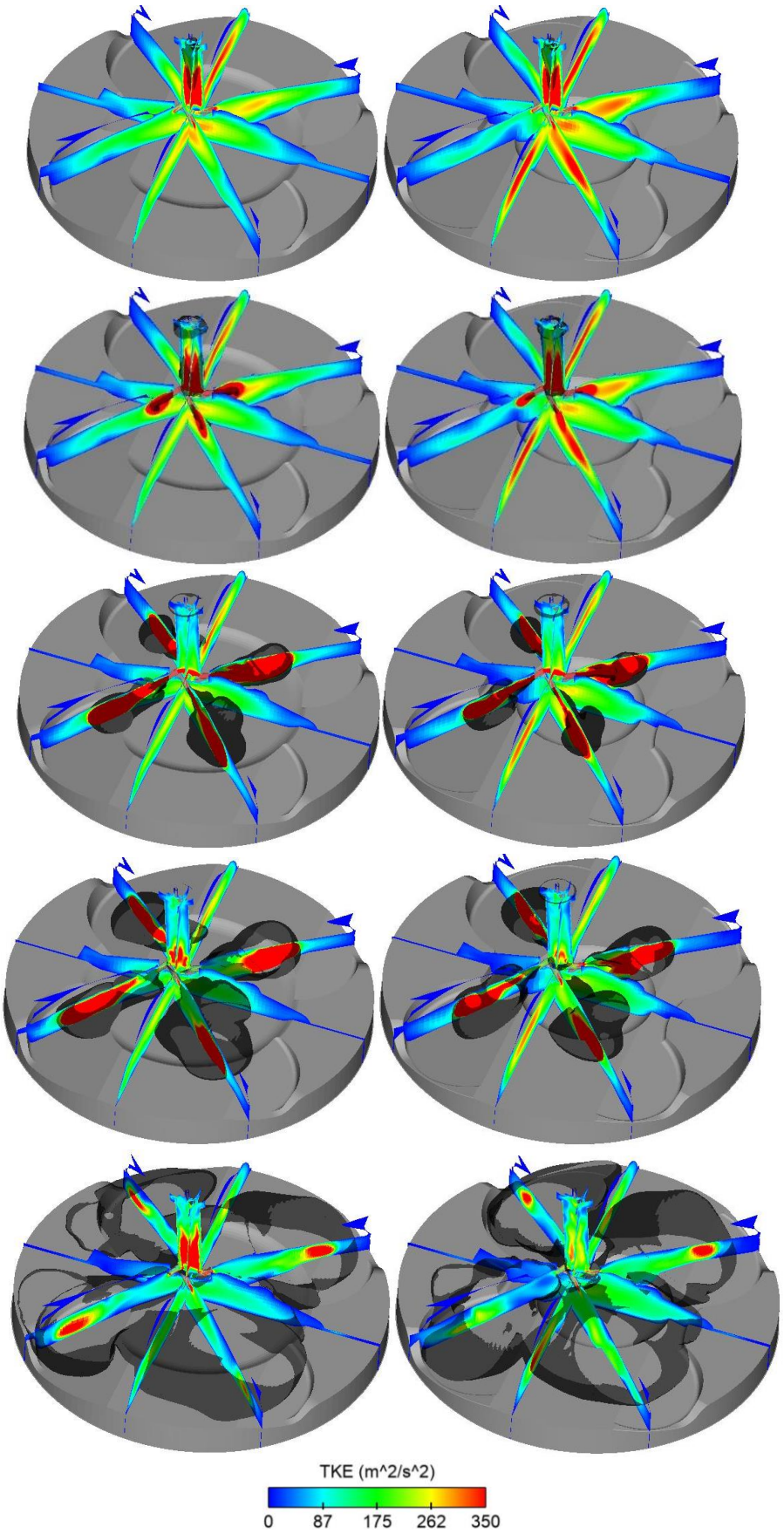

Figure 6-31 Comparison of Simulated Turbulent Kinetic Energy at 18 deg BTDC, 15 deg BTDC, 8 deg BTDC, 4 deg BTDC and 8 deg ATDC for Base (L) and Bowl Piston (R)

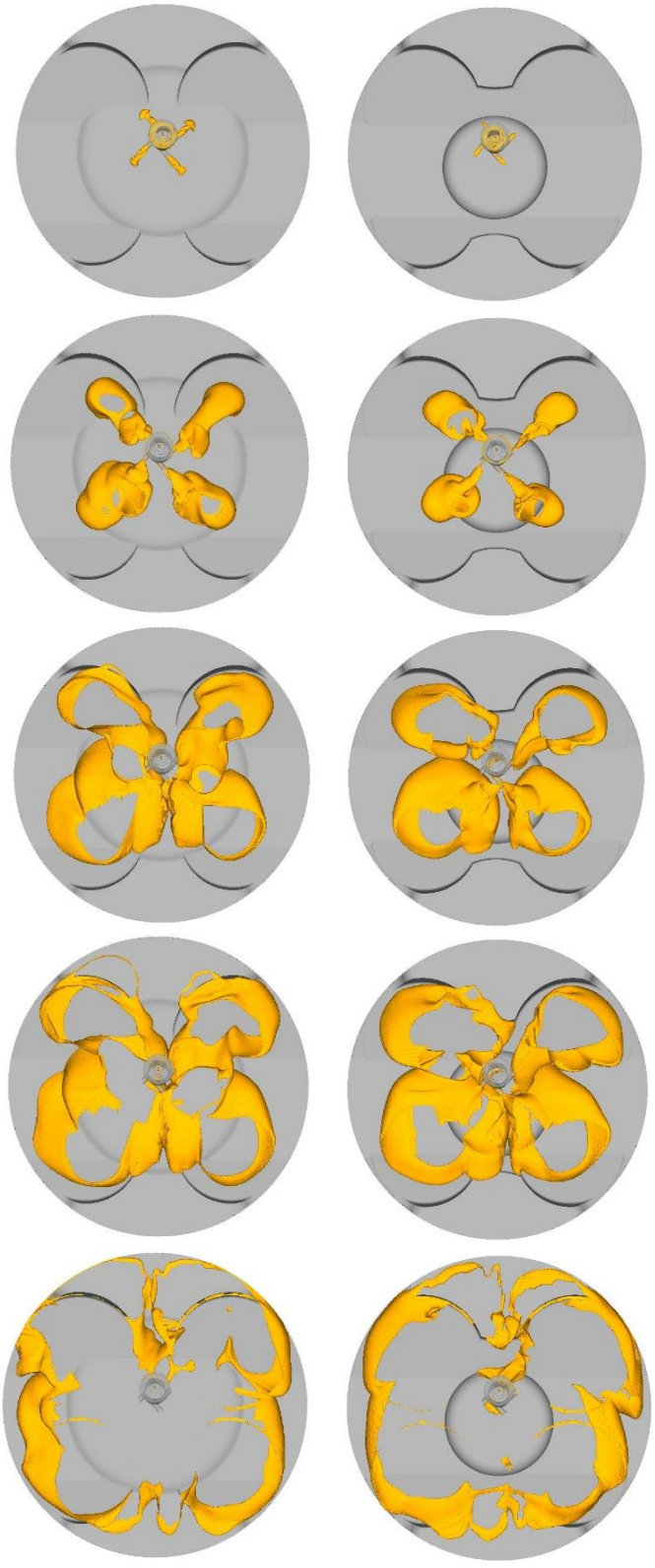

Figure 6-32 Comparison of Combustion Flames for Base (L) and Bowl Piston (R) at 14 deg BTDC, 6 deg BTDC, 2 deg BTDC, 6 deg ATDC and 16 deg ATDC

6.3 Engine Test Results

The bowl piston was manufactured to be tested utilising results from the 3D CFD studies. The base and bowl pistons are shown in figure 6-33.

Figure 6-33 Base Piston Crown (L) and Bowl Piston Crown (R) Designs

The piston crowns were first tested on the spark ignited engine and then the pre-chamber ignited engine, results of which have been presented in the forthcoming sections.

6.3.1 Performance Evaluation of Piston Crown Shape on Combustion for a Spark Ignited Engine

Engine testing was conducted at 7500 rpm where ignition and fuel timings were optimised at relative air/fuel ratios of 1.20, 1.25, 1.30, 1.35 and 1.40 for a fuel flow rate of 13.33 kg/h to calibrate the engine for maximum indicated performance or lowest ISFC which was limited by knock or MBT. The aim was to analyse the performance of the two piston crown designs and how it impacts a spark ignition system.

Figure 6-34 showed that ISFC was reduced by 6.33 g/kWh on average for the bowl piston design with the highest gain at relative air/fuel ratio of 1.30 where

an improvement of 8.89 g/kWh was observed. The bowl piston could not be tested at relative air/fuel ratio of 1.35 and 1.40 due to high number of misfires which led to an unstable engine which can be observed in the form of high COV of gross IMEP in Figure 6-35 at relative air/fuel ratio of 1.30- the most likely cause was that the spark ignition system could not ignite the main chamber charge due to very high velocity and turbulence at the vicinity of spark plug electrodes, as predicted by 3D CFD for the bowl piston case.

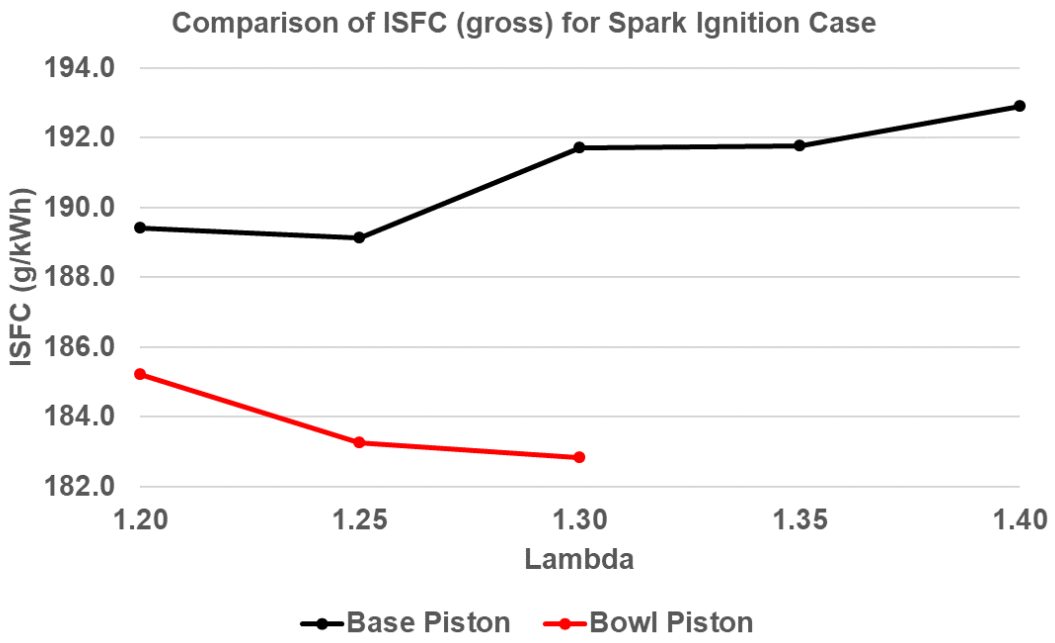

Figure 6-34 Comparison of Gross Indicated Specific Fuel Consumption for Base and Bowl Piston at Various Relative Air/Fuel Ratios

Figure 6-36 and 6-37 shows the comparison between ignition timing and exhaust gas temperatures for base and bowl pistons. A 3.3 degree ignition retard for 3.7 degree reduction in exhaust gas temperatures was observed for the bowl piston case when compared with the base piston case.

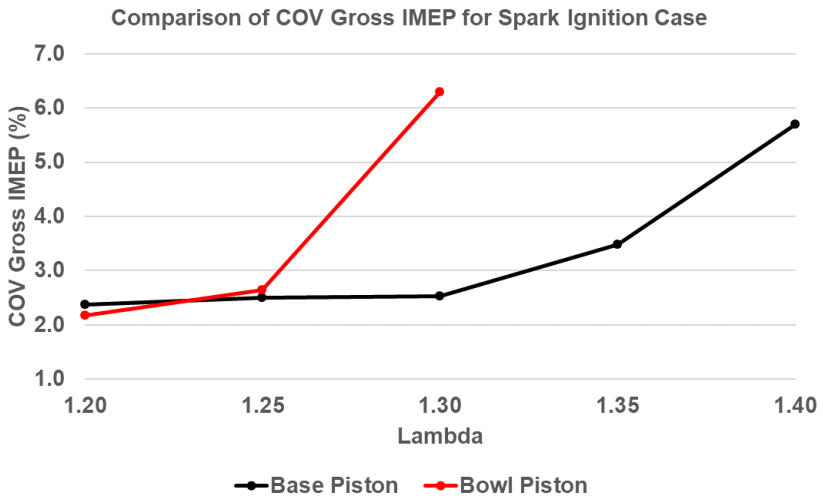

Figure 6-35 Comparison of Coefficient of Variation of Gross IMEP for Base and Bowl Pistons at Various Relative Air/Fuel Ratios

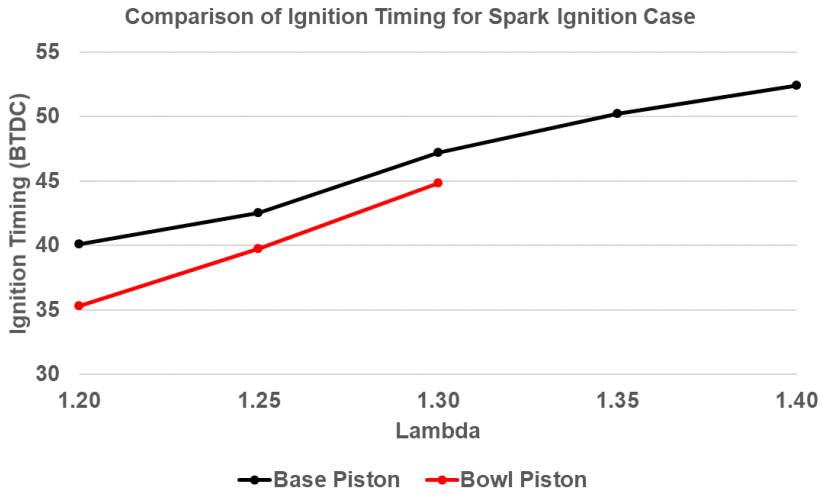

Figure 6-36 Comparison of Ignition Timing for Base and Bowl Pistons at Various Relative Air/Fuel Ratios

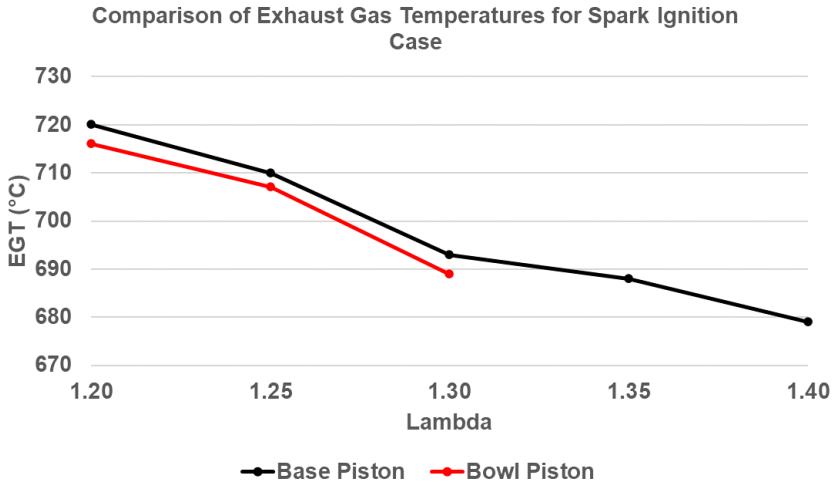

Figure 6-37 Comparison of Exhaust Gas Temperatures for Base and Bowl Pistons at Various Relative Air/Fuel Ratios

Figure 6-38 shows the comparison of 100 cycles of in-cylinder pressure plots for base and bowl pistons. A narrower band of pressure curves were observed after TDC in the case of bowl piston due to reduction in cyclic variation. A high number of misfires are observed for the bowl piston at a relative air/fuel ratio of 1.30 due to insufficient ignition energy available at the spark plug electrodes. Figure 6-39 shows the comparison of average pressure curves where lower pumping losses can be observed before TDC for the bowl piston case due to retarded ignition timings for a higher performance.

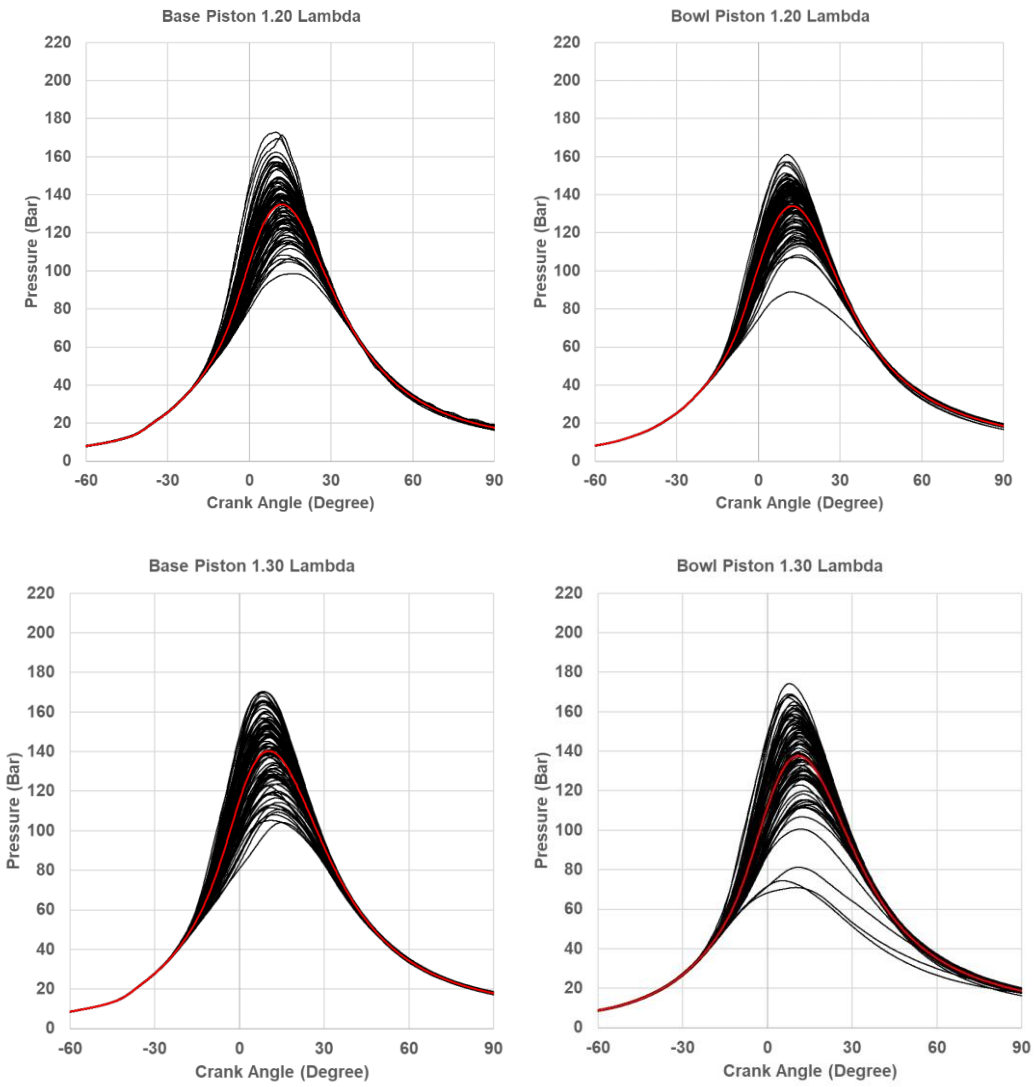

Figure 6-38 100 Cycles In-Cylinder Pressure Plots for Base and Bowl Pistons at Various Relative Air/Fuel Ratios (continued)

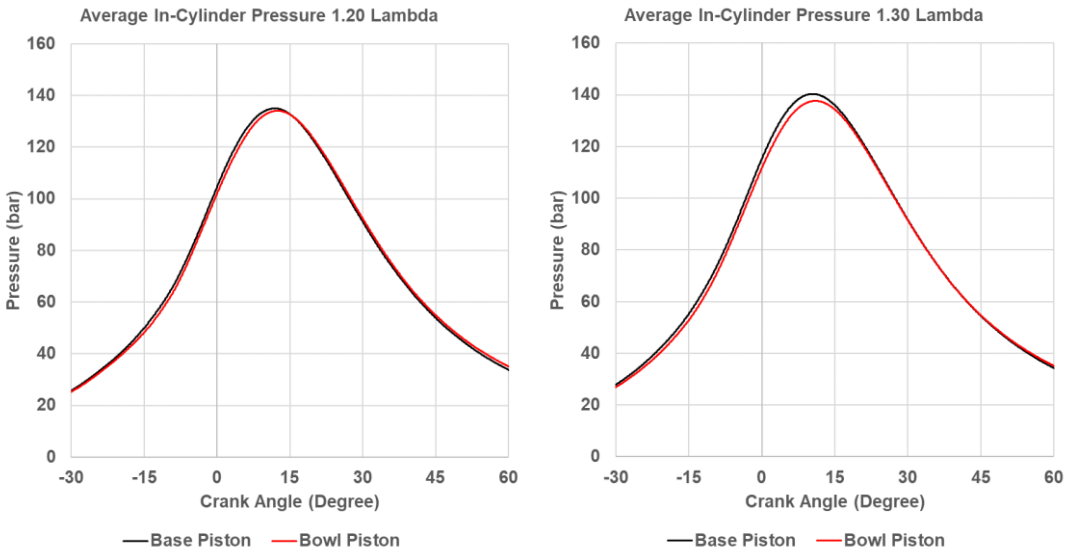

Figure 6-39 100 Cycle Averaged In-cylinder Pressure Plots for Base and Bowl Pistons at Various Relative Air/Fuel Ratios

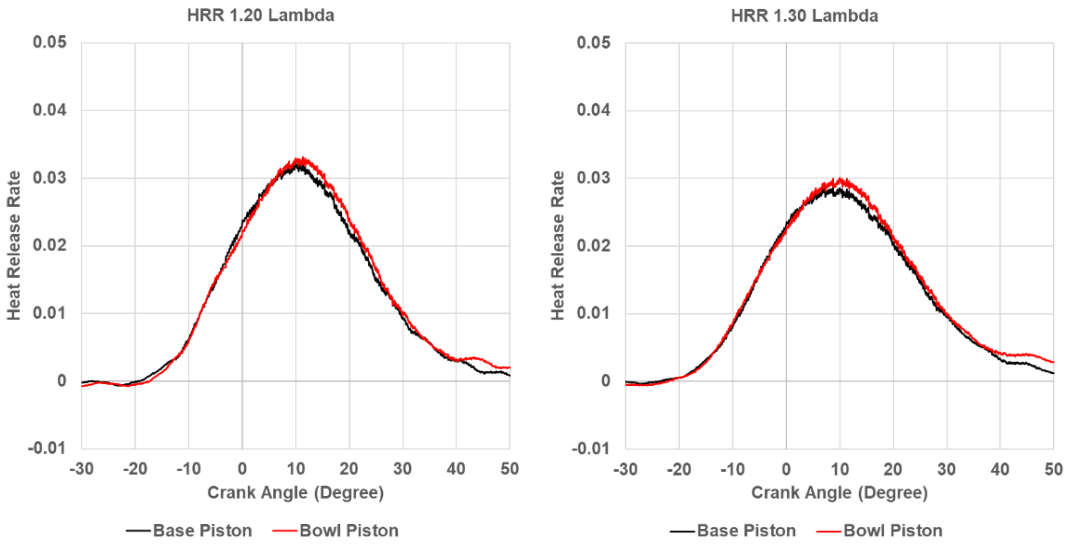

Figure 6-40 100 Cycle Averaged Normalized Heat Release Rate for Base and Bowl Pistons at Various Relative Air/Fuel Ratios

Figure 6-40 and 6-41 show the comparison between normalised heat release rate and integrated heat release rate, where an improvement in both the parameters were observed for the bowl piston case. The integrated heat release rate shows a higher fraction of heat released by 50 deg ATDC for the bowl piston design showing a better combustion efficiency.

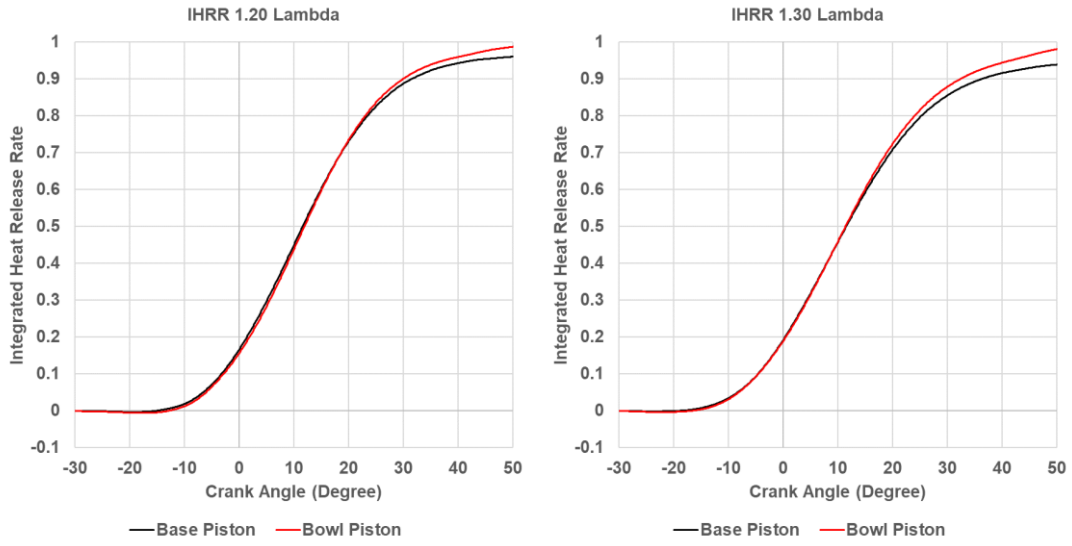

Figure 6-41 100 Cycle Averaged Normalized Integrated Heat Release Rate for Base and Bowl Pistons at Various Relative Air/Fuel Ratios

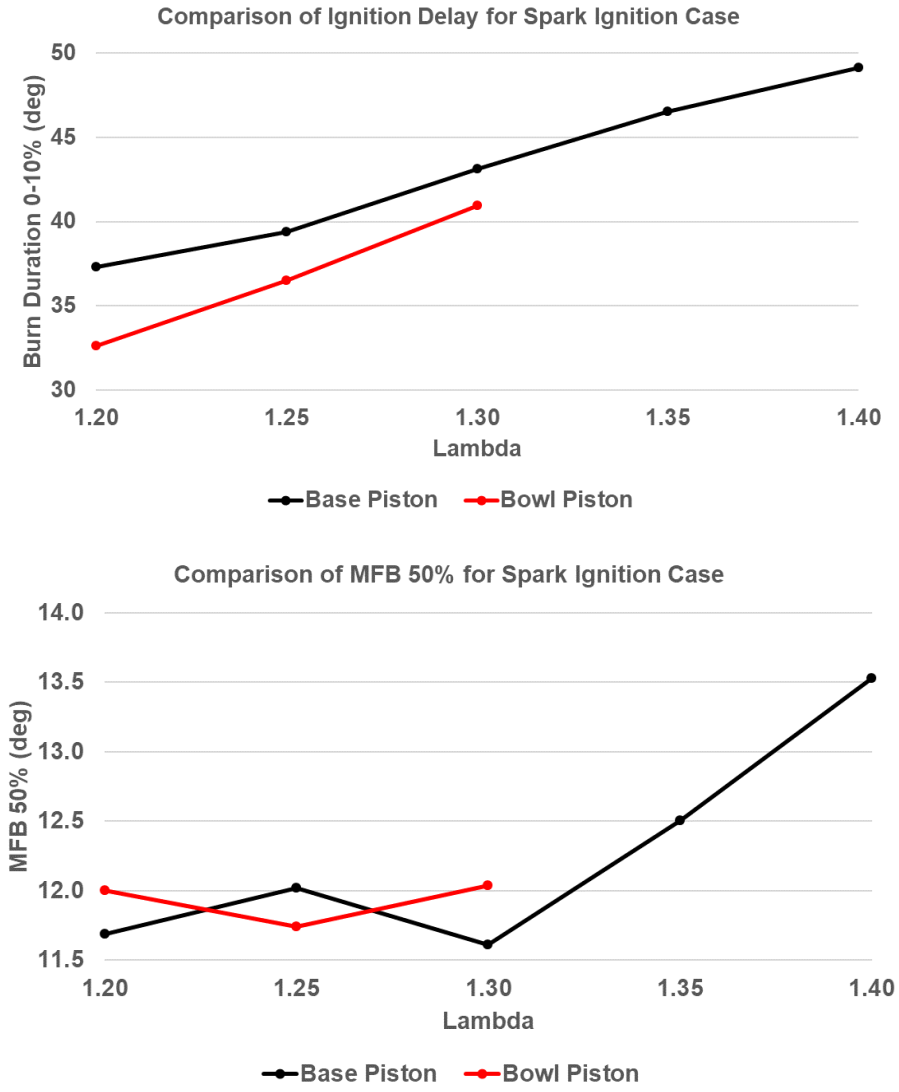

Figure 6-42 Comparison of 100 Cycle Averaged Ignition Delay, 50% Burn Point and Burn Duration for Base and Bowl Pistons at Various Relative Air/Fuel Ratios

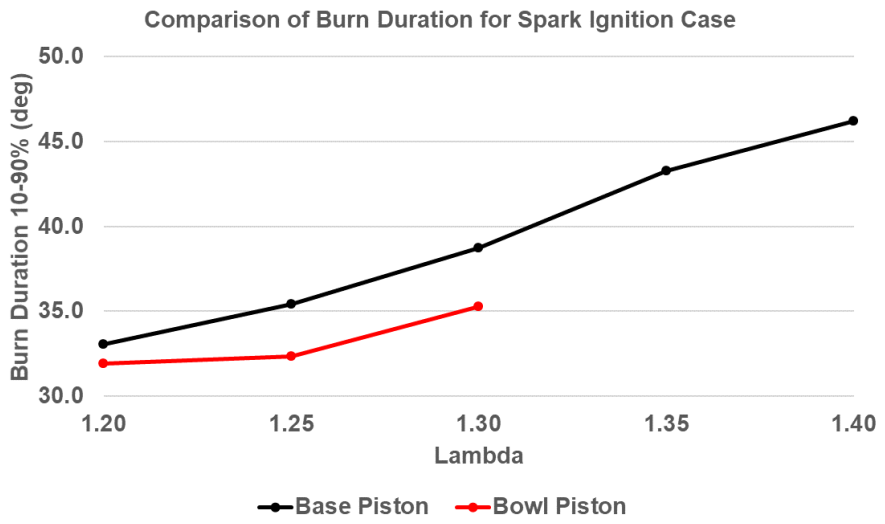

Figure 6-42 Comparison of 100 Cycle Averaged Ignition Delay, 50% Burn Point and Burn Duration for Base and Bowl Pistons at Various Relative Air/Fuel Ratios (Continued)

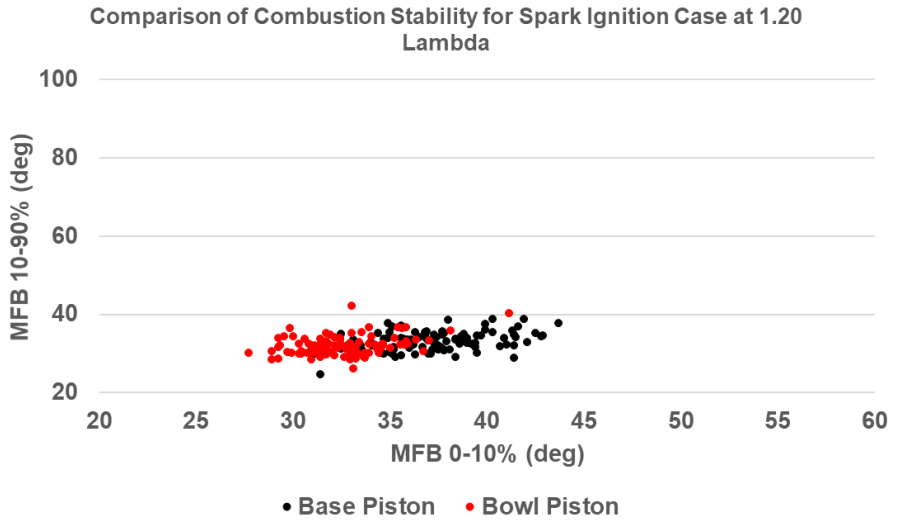

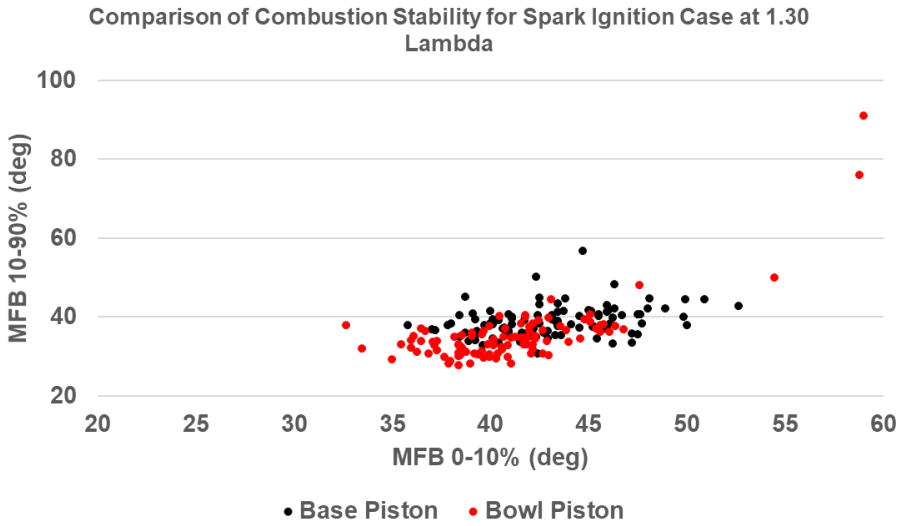

Figure 6-43 Comparison of Combustion Stability for Base and Bowl Pistons at Various Relative Air/Fuel Ratios

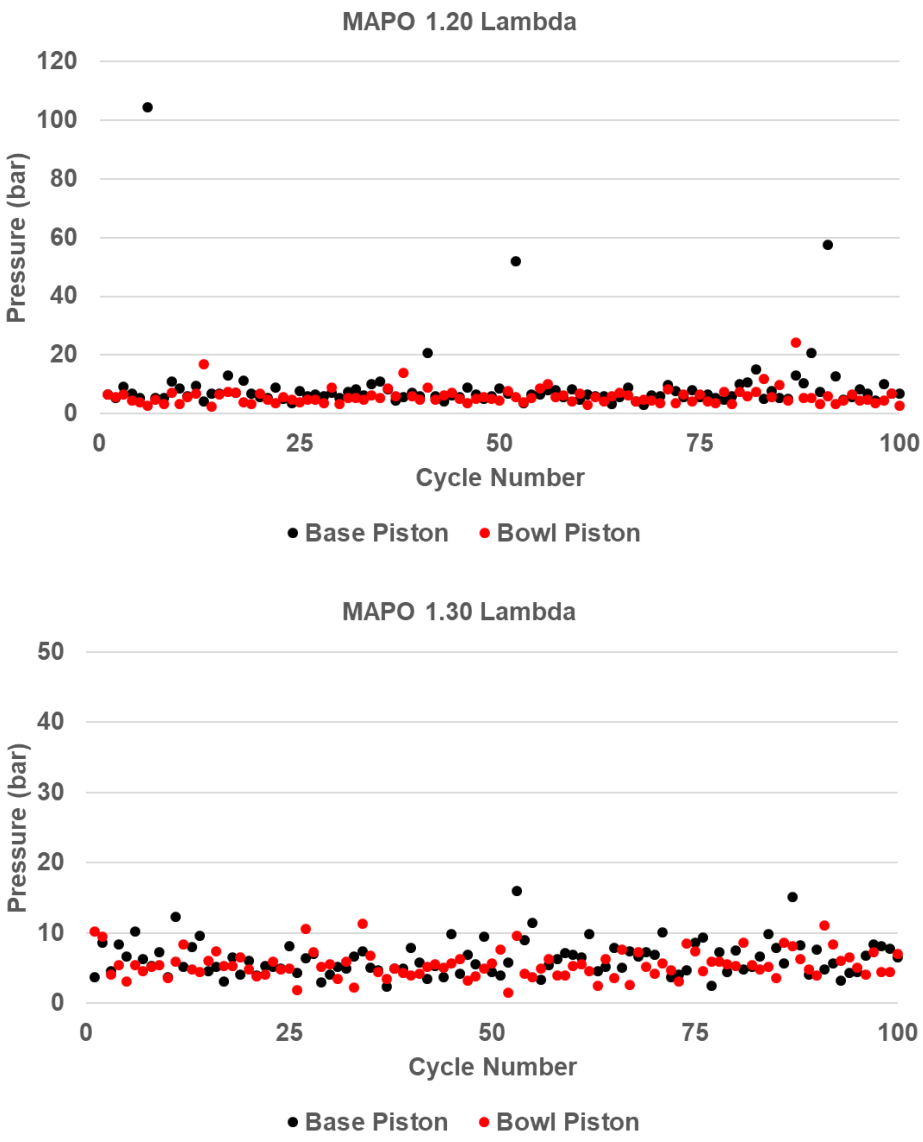

Figure 6-44 Comparison of Maximum Amplitude of Pressure Oscillations for Base and Bowl Pistons at Various Relative Air/Fuel Ratios

Figure 6-42 shows the comparison of various burn characteristics, it was observed that both ignition delay and 10-90% mass fraction burn duration were reduced for all relative air/fuel ratios in the case of bowl piston. Ignition delay was reduced by 3.23 degrees on average for the bowl piston case and the 10-90% mass fraction burn duration was reduced by 2.55 on average.

Figure 6-43 demonstrates the better combustion stability for the bowl piston case as the burn duration points are more concentrated due to lower cyclic variation.

Figure 6-44 shows that the bowl piston exhibited a lower number of knocking cycles compared to the base piston across all relative air/fuel ratios. Super-knock and heavy knocking cycles were more evident in the case of base piston. Comparison of MAPO shows that MAPO for bowl piston reduced by 36.37%, 11.50% and 13.23% at 1.20, 1.25 and 1.30 relative air/fuel ratios, respectively.

Lambda	Base Piston MAPO (bar)	Bowl Piston MAPO (bar)
1.20	9.21	5.86
1.25	7.07	6.26
1.30	6.35	5.51

Table 6-1 Comparison of Average MAPO for Base Piston and Bowl Piston at Lambda 1.20, 1.25 and 1.30

6.3.2 Performance Evaluation of Piston Crown Shape on Combustion for a Pre-chamber Ignited Engine

Engine testing was conducted at 7500 rpm with optimised ignition and fuel timings at relative air/fuel ratios of 1.20, 1.25, 1.30, 1.35 and 1.40 for a fuel flow rate of 13.33 kg/h to calibrate the engine for maximum indicated performance or lowest ISFC which was limited by MBT only as there were no knocking cycles which could be heard via the engine stethoscope. The aim was to analyse the performance of the two piston crown designs and how it impacts a pre-chamber ignition system.

Figure 6-45 showed that ISFC was reduced by 5.69 g/kWh on average for the bowl piston design with the highest gain at relative air/fuel ratio of 1.25 where an improvement of 7.24 g/kWh was observed.

Figure 6-46 shows the comparison of COV of gross IMEP for base and bowl piston crown designs where it was observed that the COV of gross IMEP in the case of the bowl piston was consistently below 2 for relative air/fuel ratio of 1.20 to 1.35 with the highest difference observed at relative air/fuel ratio of 1.40 where COV of gross IMEP of bowl piston was 1.19 lower than the base piston.

Figure 6-47 shows that the ignition timings were distinctly retarded by 3 and 5.6 degrees at the leaner relative air/fuel ratios of 1.35 and 1.40 respectively for the bowl piston case for a lower ISFC. Exhaust gas temperatures were found to be lower for the bowl piston across all relative air/fuel ratios demonstrating efficient combustion.

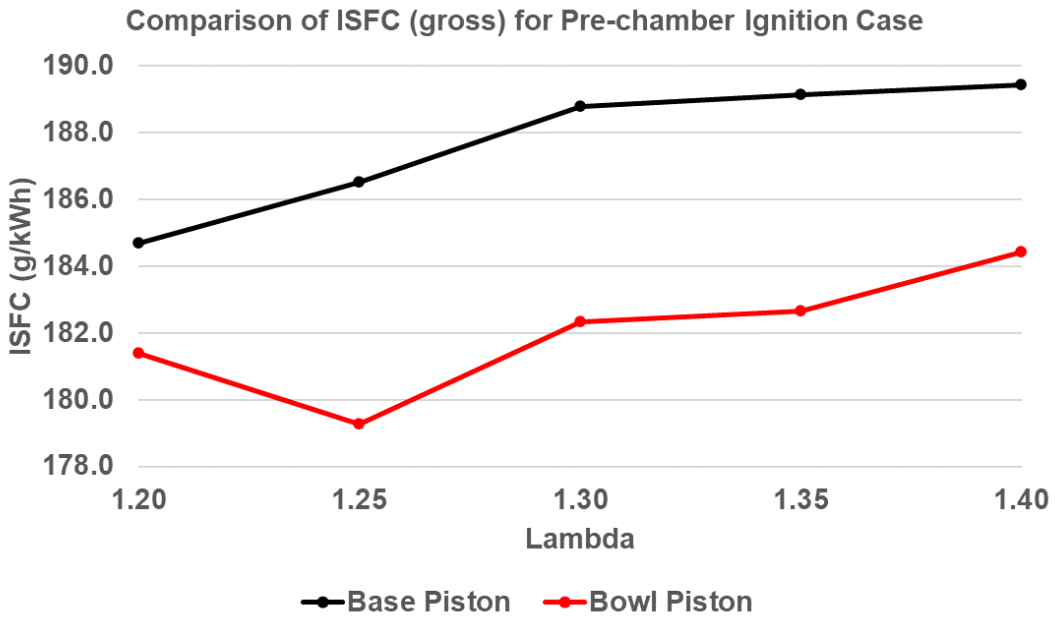

Figure 6-45 Comparison of Gross Indicated Specific Fuel Consumption for Base and Bowl Pistons at Various Relative Air/Fuel Ratios

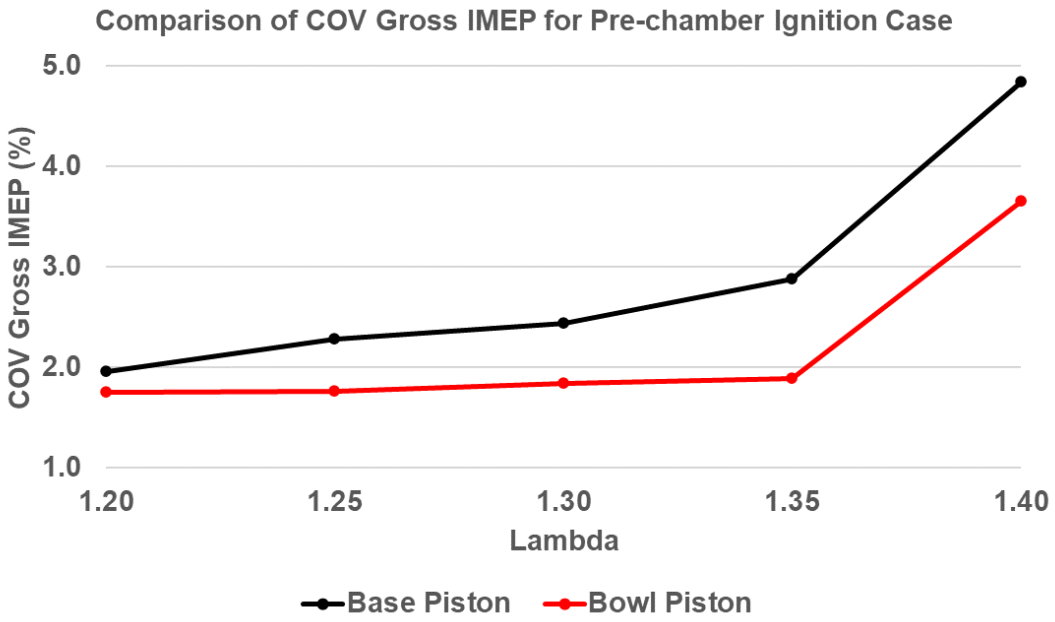

Figure 6-46 Comparison of Coefficient of Variation of Gross IMEP for Base and Bowl Pistons at Various Relative Air/Fuel Ratios

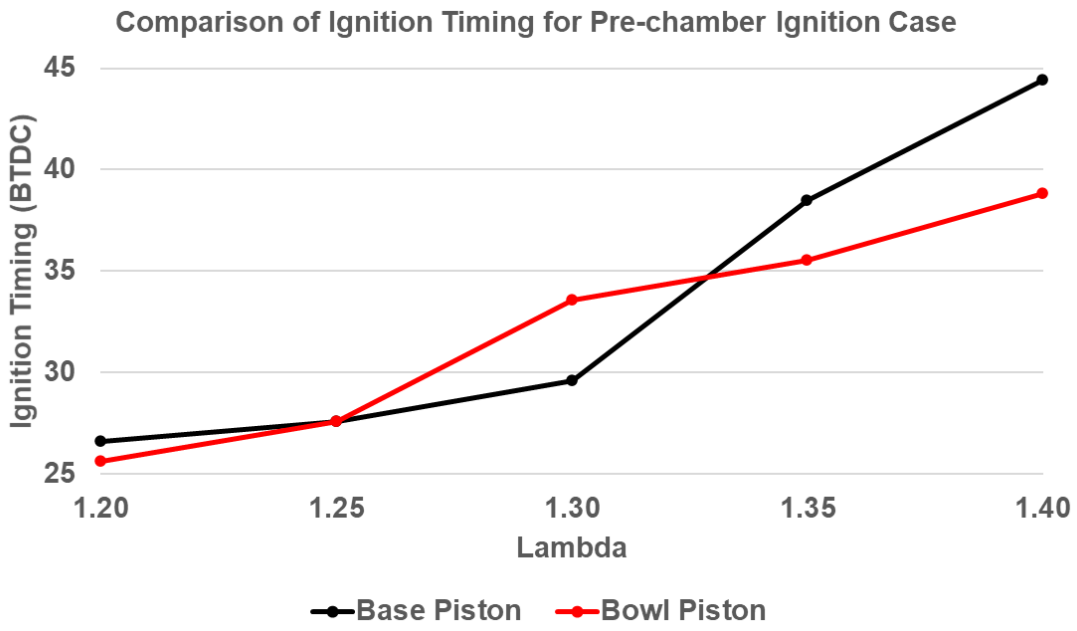

Figure 6-47 Comparison of Ignition Timing for Base and Bowl Pistons at Various Relative Air/Fuel Ratios

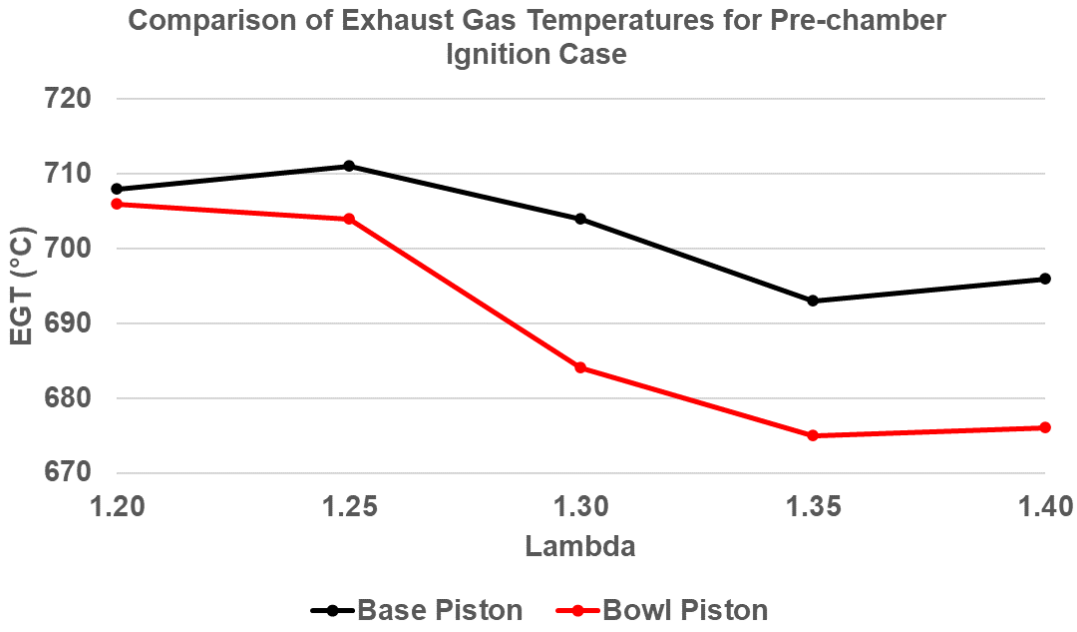

Figure 6-48 Comparison of Exhaust Gas Temperatures for Base and Bowl Pistons at Various Relative Air/Fuel Ratios

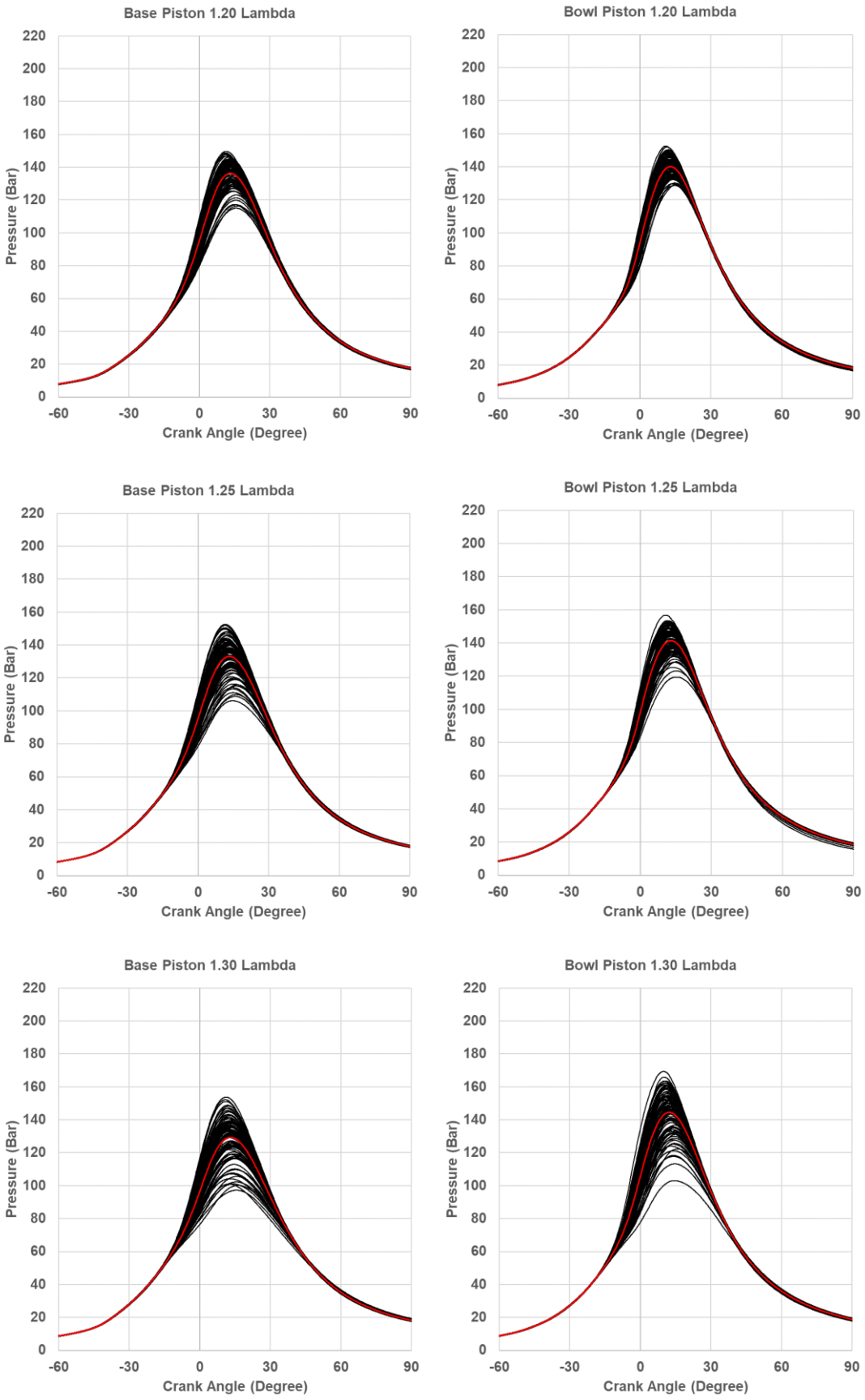

Figure 6-49 100 Cycles In-Cylinder Pressure Plots for Base and Bowl Pistons at Various Relative Air/Fuel Ratios

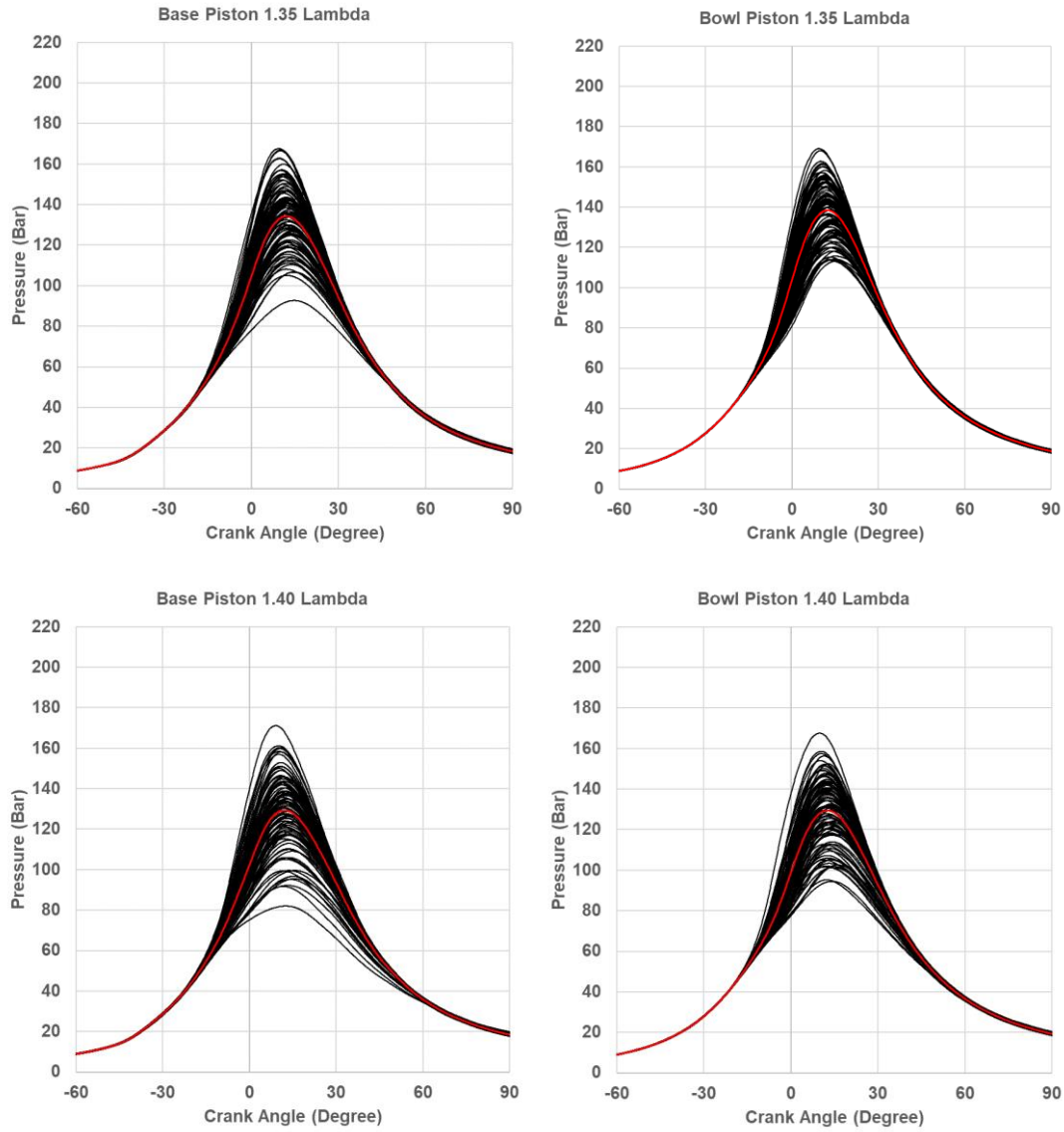

Figure 6-49 100 Cycles In-Cylinder Pressure Plots for Base and Bowl Pistons at Various Relative Air/Fuel Ratios (continued)

Figure 6-49 shows the comparison of 100 cycles of in-cylinder pressure plots for base and bowl pistons. A narrower band of pressure curves were observed after TDC in the case of bowl piston due to reduction in cyclic variation. Figure 6-50 shows the comparison of average pressure curves where lower pumping losses can be observed before TDC for the bowl piston case due to retarded ignition timings and higher peak pressures were observed.

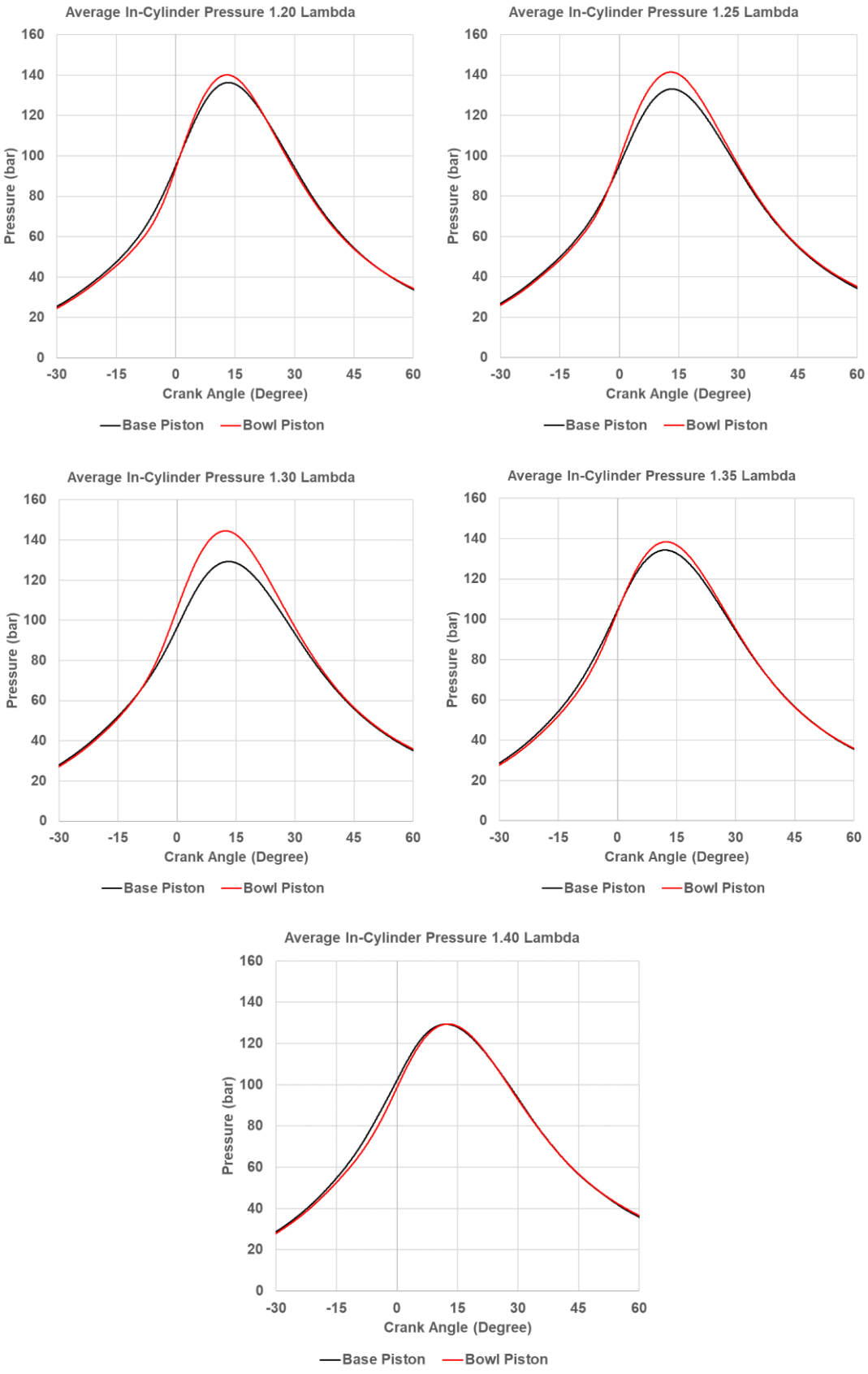

Figure 6-50 100 Cycle Averaged In-cylinder Pressure Plots for Base and Bowl Pistons at Various Relative Air/Fuel Ratios

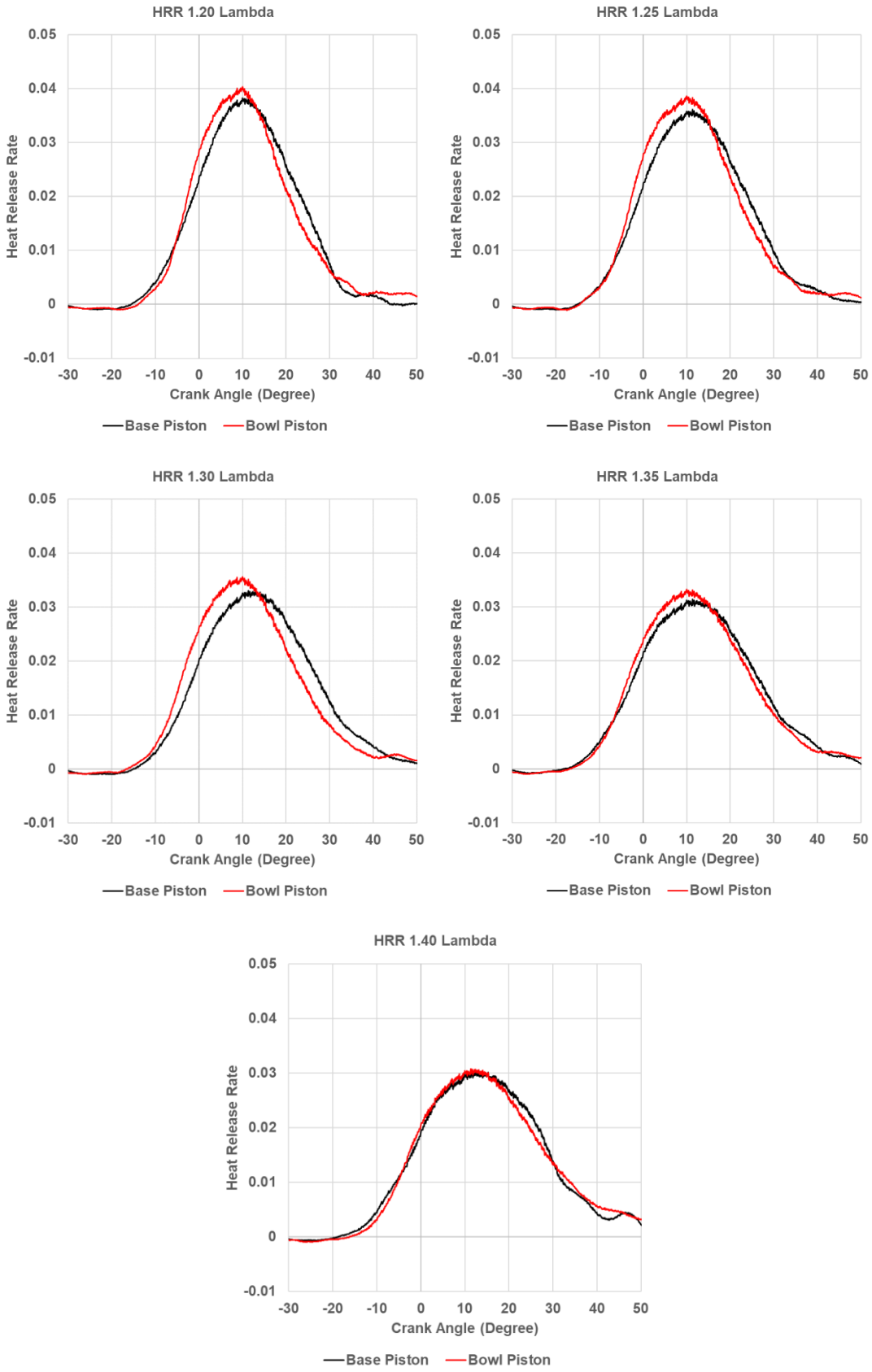

Figure 6-51 100 Cycle Averaged Normalized Heat Release Rate for Base and Bowl Pistons at Various Relative Air/Fuel Ratios

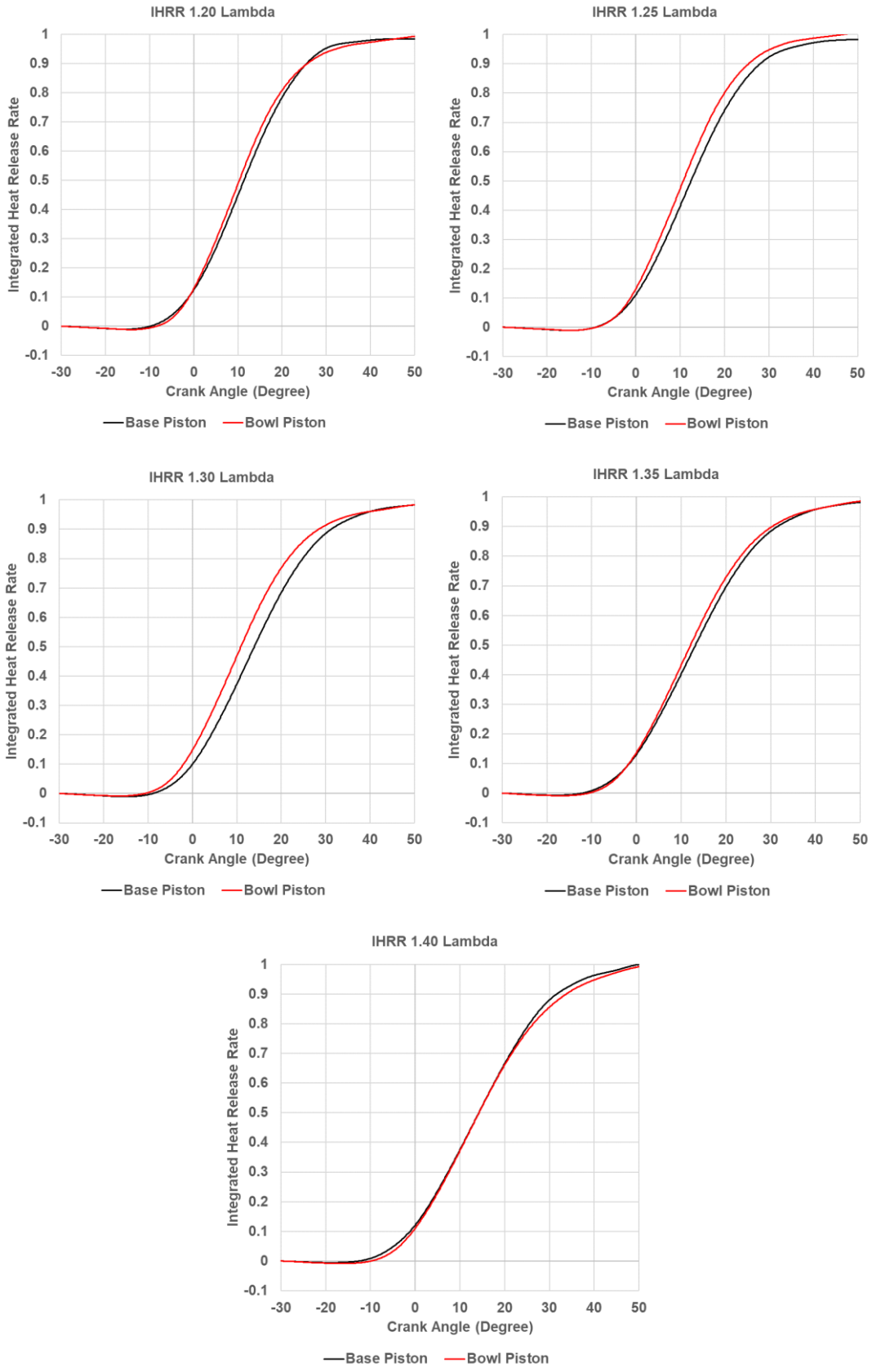

Figure 6-52 100 Cycle Averaged Normalized Integrated Heat Release Rate for Base and Bowl Pistons at Various Relative Air/Fuel Ratios

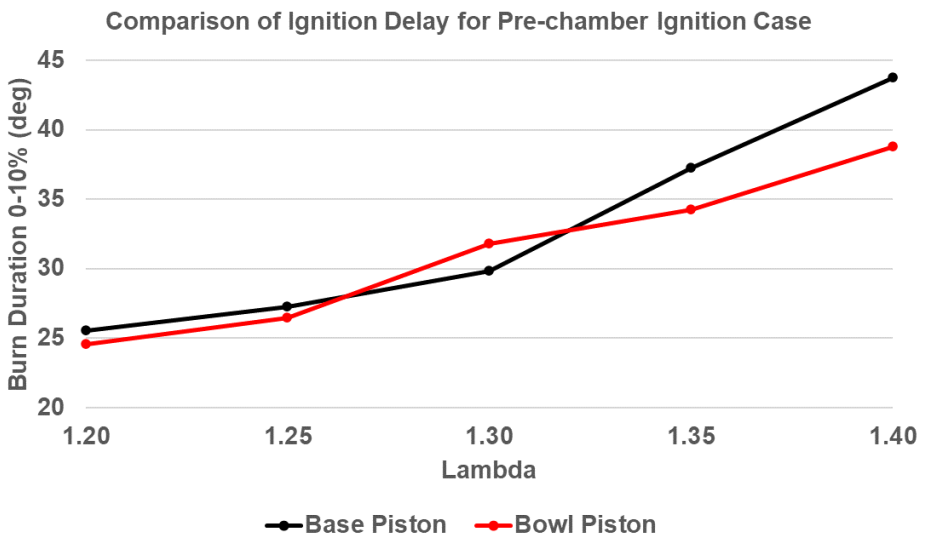

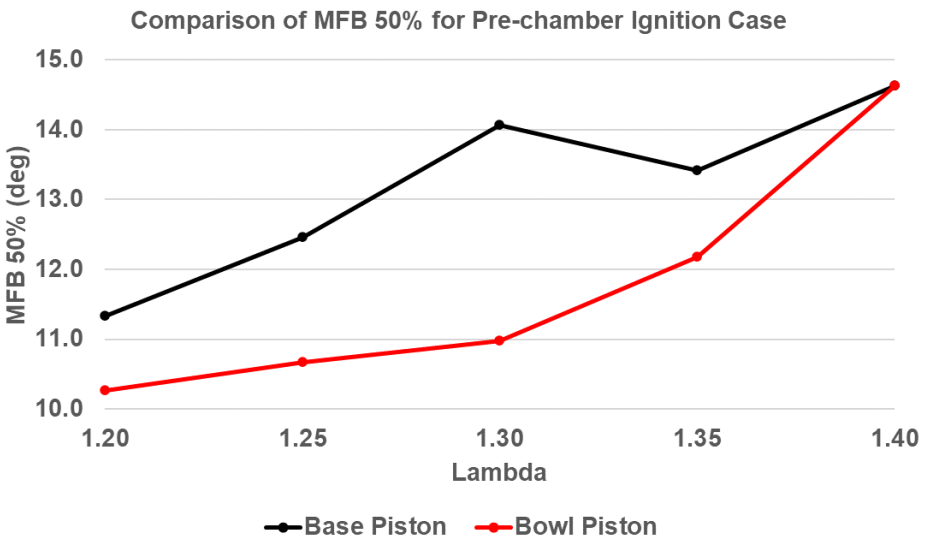

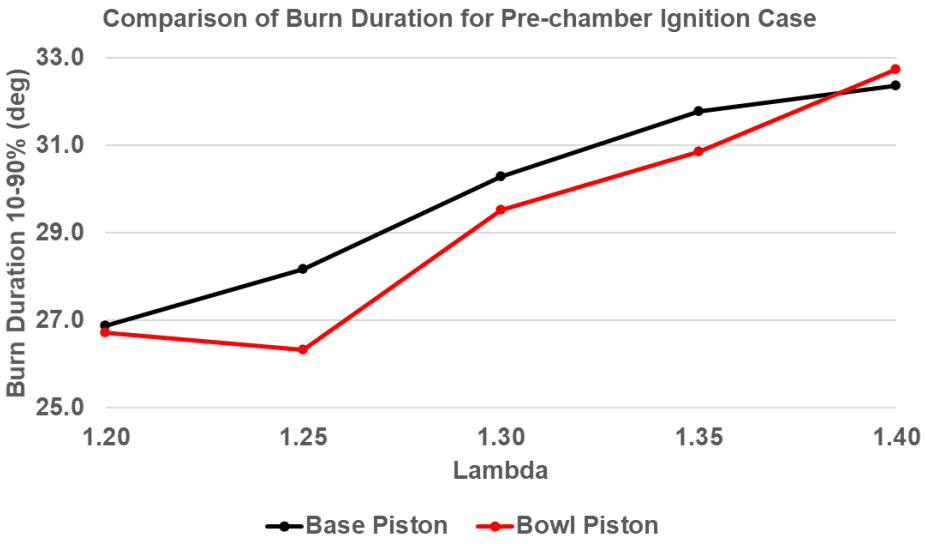

Figure 6-53 Comparison of Cycle Averaged Ignition Delay, 50% Burn Point and Burn Duration for Base and Bowl Pistons at Various Relative Air/Fuel Ratios

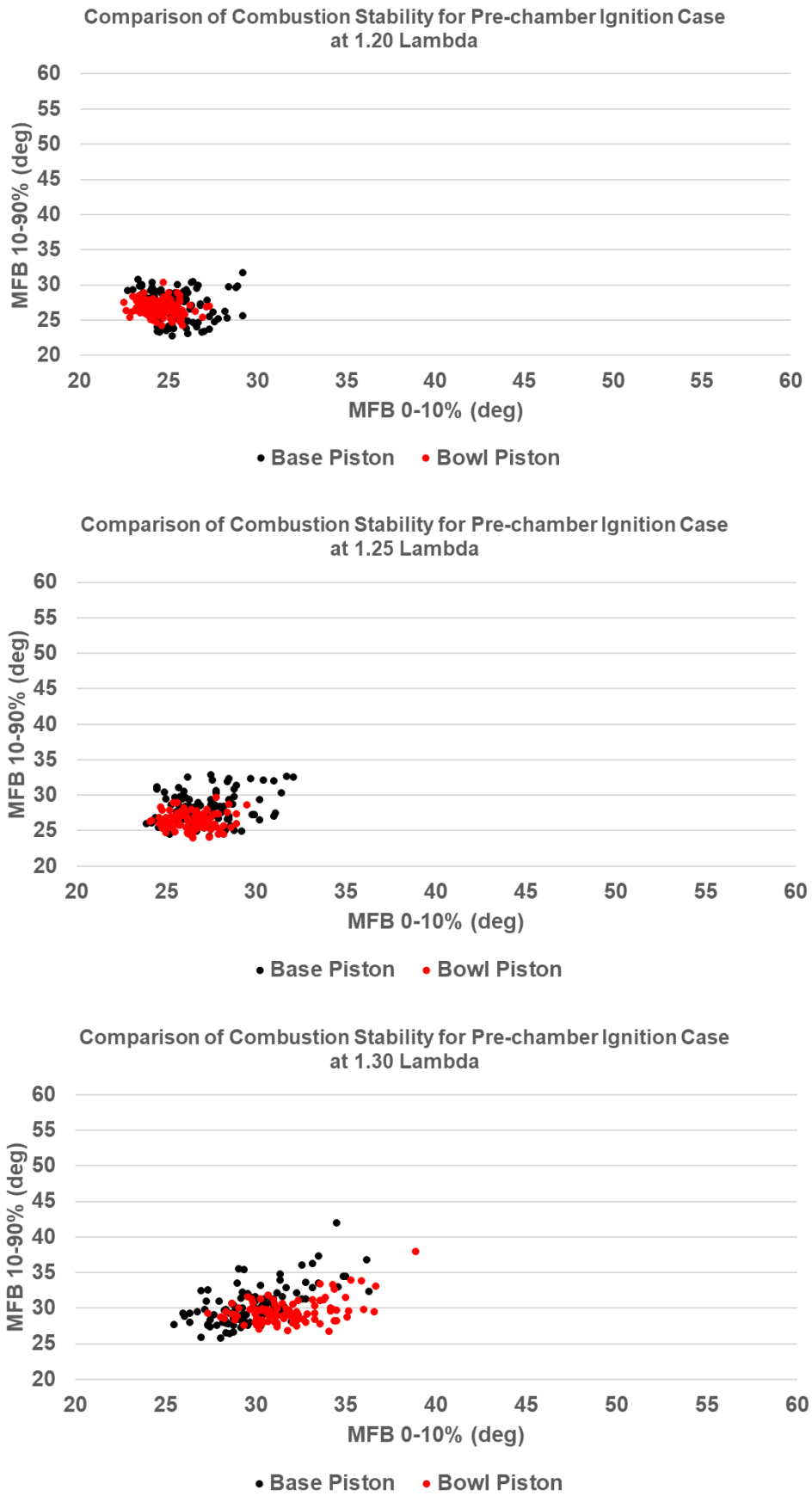

Figure 6-54 Comparison of Combustion Stability for Base and Bowl Pistons at Various Relative Air/Fuel Ratios

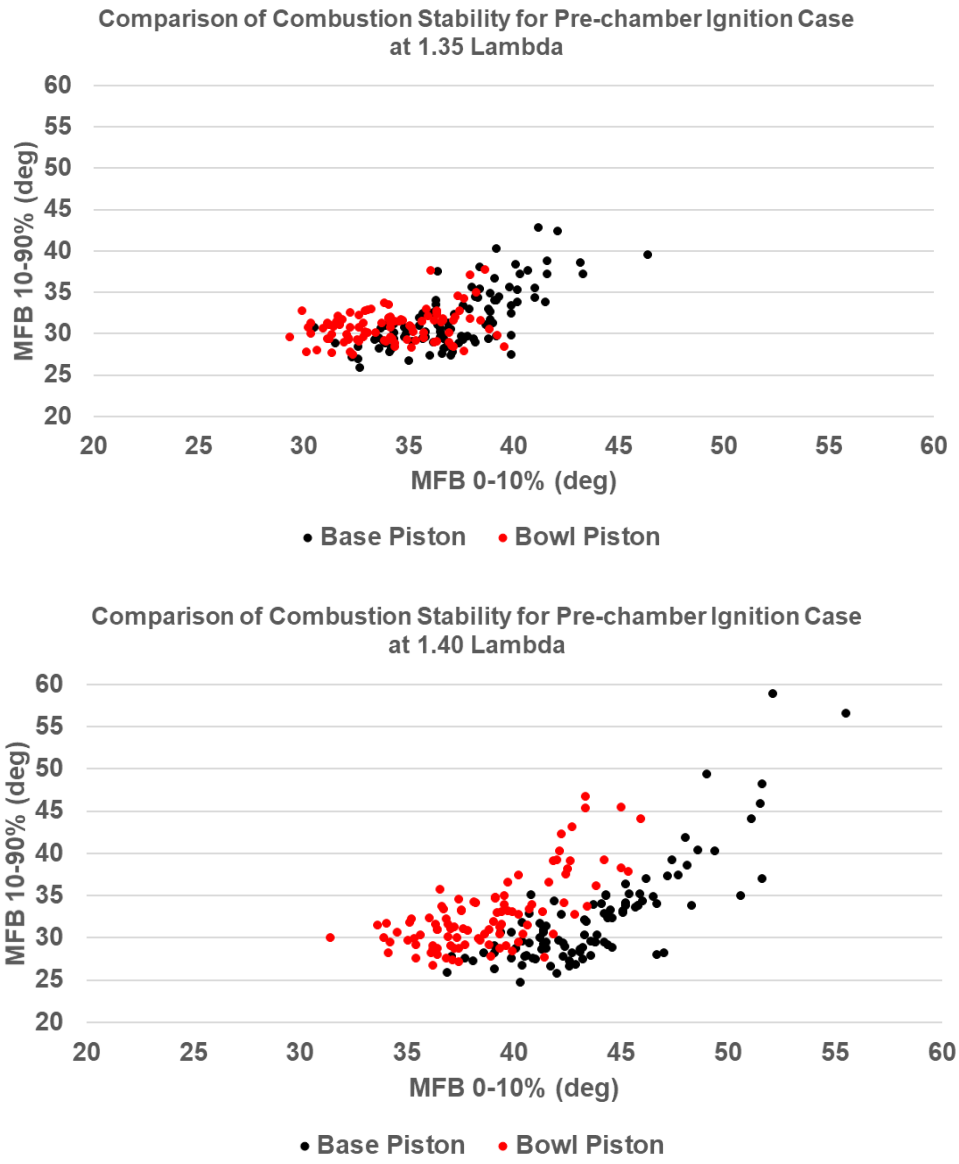

Figure 6-54 Comparison of Combustion Stability for Base and Bowl Pistons at Various Relative Air/Fuel Ratios (continued)

Figure 6-51 and 6-52 show the comparison between normalised heat release rate and integrated heat release rate, where an improvement in both the parameters were observed for the bowl piston case. The integrated heat release rate showed that the burn rate of bowl piston case was faster than the base piston case initially up until approximately 75% mass fraction burn point. A slowdown in burn rate for the bowl piston case was observed from MFB 75%

point onwards due to pre-chamber enrichment as observed in 3D CFD simulations.

Figure 6-53 shows the comparison of various burn characteristics, it was observed that both ignition delay and 10-90% mass fraction burn duration were reduced for all relative air/fuel ratios except for 1.40 in the case of bowl piston. Ignition delay was reduced by 1.55 degrees on average, with the biggest reduction of 5 degrees occurring at a relative air/fuel ratio of 1.40 for the bowl piston case and the 10-90% mass fraction burn duration was reduced by 0.66 on average.

Figure 6-54 demonstrates the better combustion stability for the bowl piston case as the burn duration points are more concentrated due to lower cyclic variation.

Figure 6-55 and Table 6-2 show that the bowl piston exhibited a higher number of high maximum pressure oscillation cycles compared to the base piston across all relative air/fuel ratios which were related to shockwaves from pre-chamber jets and were not knocking cycles as no pinging noise could be heard via the engine stethoscope.

Lambda	Base Piston MAPO (bar)	Bowl Piston MAPO (bar)
1.20	9.90	15.57
1.25	9.78	12.15
1.30	6.25	7.81
1.35	4.75	6.09
1.40	4.39	4.69

Table 6-2 Comparison of Average MAPO for Base Piston and Bowl Piston at Various Relative Air/Fuel Ratios

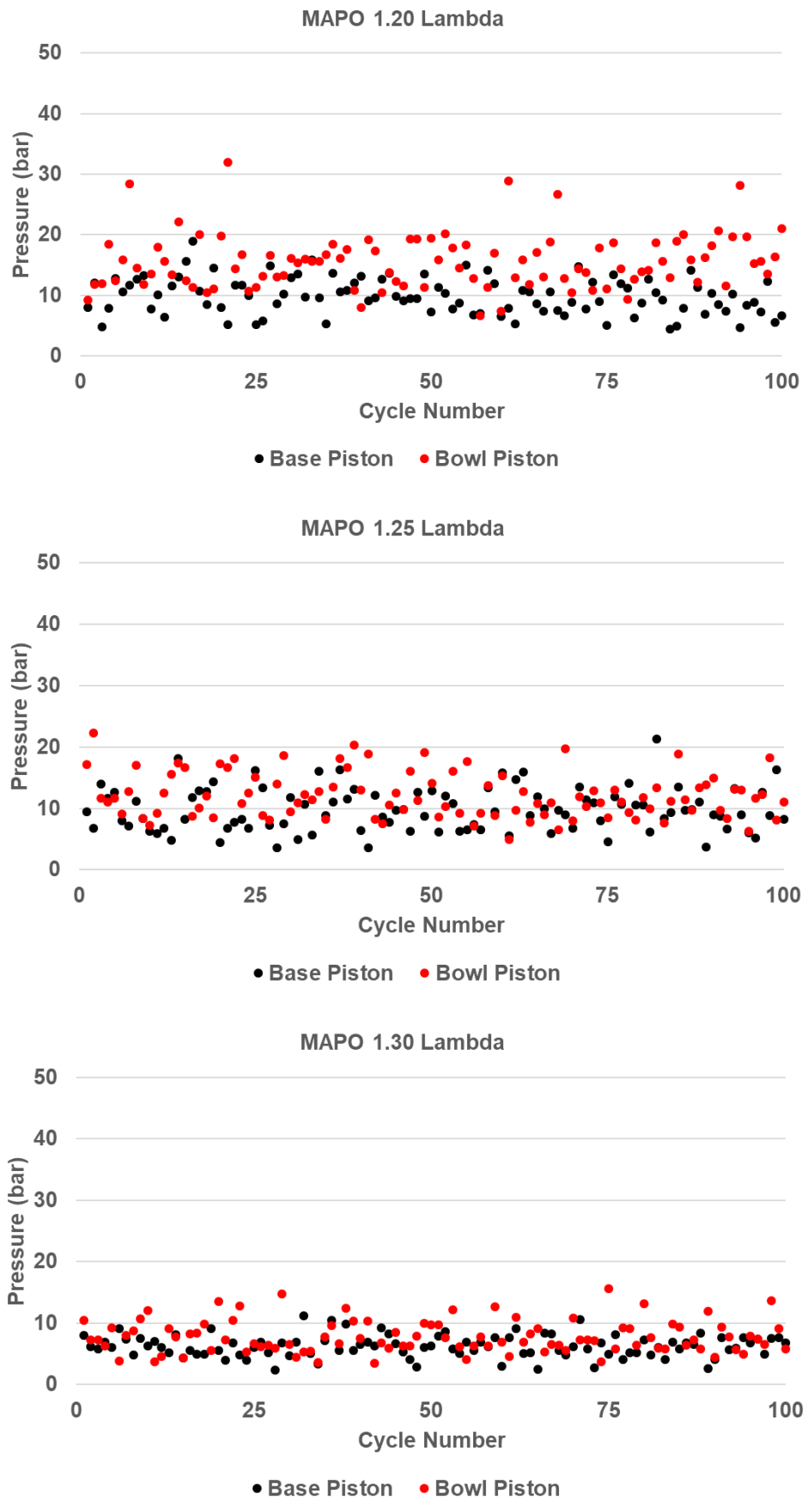

Figure 6-55 Comparison of Maximum Amplitude of Pressure Oscillations for Base and Bowl Pistons at Various Relative Air/Fuel Ratios

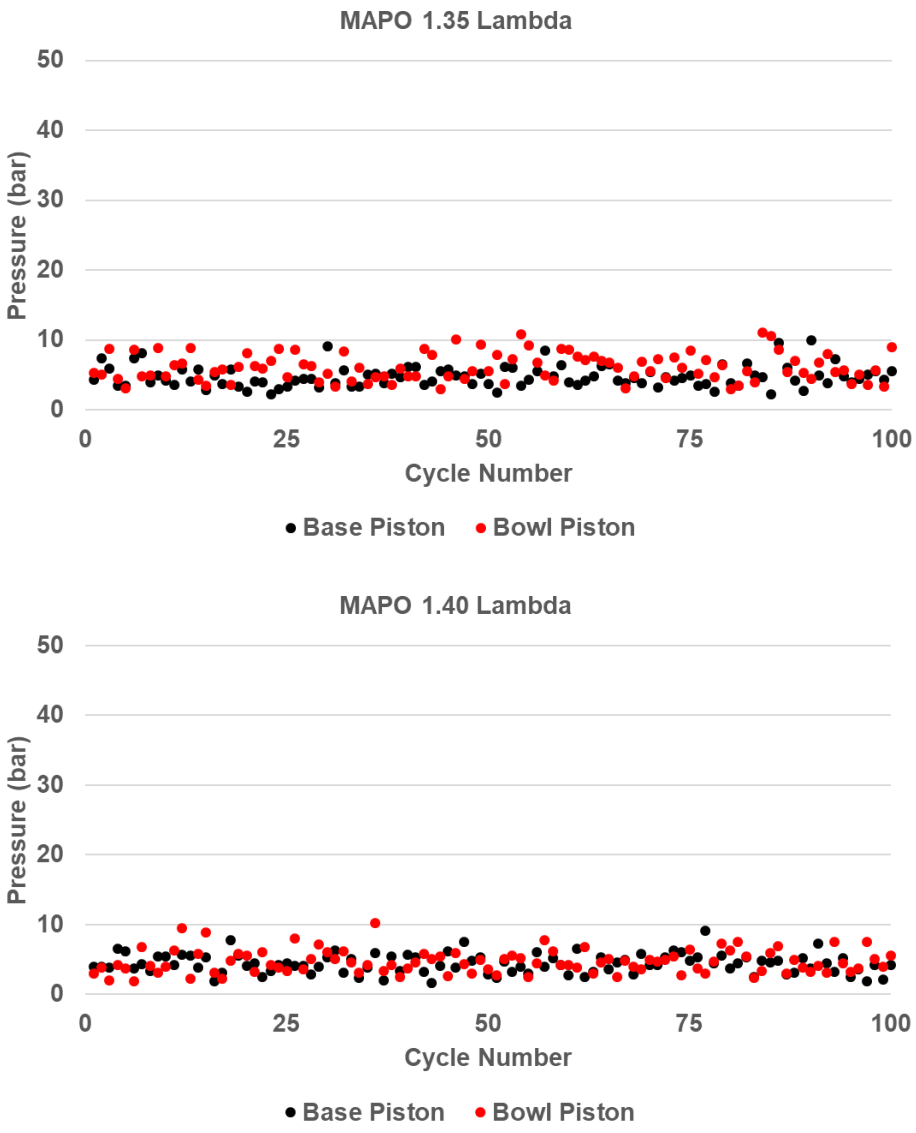

Figure 6-55 Comparison of Maximum Amplitude of Pressure Oscillations for Base and Bowl Pistons at Various Relative Air/Fuel Ratios (continued)

6.4 Discussion of Results

6.4.1 Influence of Piston Crown Design on Pre-chamber Ignited Engine

3D CFD simulation results for pre-chamber ignited engine had shown that the increased tumble ratio and resulting turbulent intensity during compression process aided the main chamber combustion process. The simulated cycles as presented in the simulation results for the 4 hole pre-chamber showed that the main chamber conditions for the bowl piston case compensated for the poor enrichment of the pre-chamber to aid flame propagation for that particular cycle. The 4 hole pre-chamber was expected to be enriched as simulations with the 6 hole pre-chamber had shown significant enrichment with the bowl piston of the pre-chamber over four simulated cycles. However, the poor enrichment of the 4 hole pre-chamber for the particular cycle, due to cyclic variation, resulted in a lower intensity jet and late ejection of jets, as visualised in Figure 6-32, from the pre-chamber into the main chamber, which was expected to slow the main chamber combustion processes due to a lower flame surface area owing to the reduced jet penetration length. However, due to the high turbulence prevalent in the main chamber in the case of bowl piston- the high turbulence allowed the flame surface area to rapidly expand after jet ignition via flame stretching, which can be explained via shorter MFB 10-75% for the case of bowl piston as shown in Figure 6-26, and thus even with a poor ignition start of the main chamber contents, the gross IMEP of the bowl piston case matched with the gross IMEP of the base piston case.

Engine testing results showed a 5.69 g/kWh reduction in gross ISFC on average for the case of bowl piston when compared with the base piston which was attributed to pre-chamber enrichment and reduction in COV of gross IMEP due to better combustion stability. The lower exhaust gas temperatures in the case of bowl piston showed that the overall combustion efficiency was improved. The ignition delay MFB 0-10% comparison showed that the bowl piston had a shorter ignition delay on average in the main chamber compared to the base piston which provides further evidence that the pre-chamber in the bowl piston case is enriched better than the base piston.

The ignition delay vs relative air/fuel ratio trend showed that ignition delay increased with increasing relative air/fuel ratio which can be attributed to the decreasing enrichment of the passive pre-chamber and also the reduction of the pressure difference between the main chamber and pre-chamber due to increasing manifold pressure- which was done to achieve the relative air/fuel ratio target for the fixed fuel flow rate.

The combustion stability plots across all relative air/fuel ratios showed that the slow burning cycles were significantly reduced for the bowl piston case as shown in Figure 6-54. This was attributed to the high turbulent intensity present in the main chamber of the bowl piston case, as suggested by 3D CFD simulation results, which aided in propagating the initial flame front especially in the case of slower than average burning cycles where the low jet intensity and the resulting lower jet penetration would result in a lower initial flame surface area. The findings are consistent with Novella et al. (2020) where the authors have hypothesised in their study that if the jet ejection process was compromised due to any reason which would negatively alter the onset of main

chamber ignition- the main chamber thermodynamic and turbulence conditions, if favourable, would assure a reasonable combustion rate and the overall operation of the engine may not be compromised.

The pre-chamber ignition system was also able to cope with igniting the main-chamber that had a high mean flow velocity at leaner air/fuel ratios with the bowl piston as no misfiring cycles were observed. A high number of misfiring cycles and instability were observed when the engine operated with a bowl piston at a relative air/fuel ratio of 1.30 with the spark ignition system. As operating the engine at relative air/fuel ratio of 1.30, for the same fuel flow rate as relative air/fuel ratio of 1.20, requires a higher manifold pressure- the gas velocity at the intake ports would thus be increased which would lead to a higher tumble ratio which would result in a higher velocity and higher turbulent intensity at the spark plug electrodes during ignition timing. As the bowl piston crown design alone was expected to substantially increase the mean flow velocity and turbulent intensity at the spark plug electrodes compared to the base piston as found in 3D CFD results as shown in Figure 6-14, a further increase in manifold pressure would thus result in further increasing the mean flow velocity and turbulent intensity at the spark plug electrodes in the case of the bowl piston compared to the base piston. Thus, the misfires can be attributed to high turbulence level which restricts the flame kernel's growth and thus lead to blowing off the spark plasma channel which in turn cuts the supply of energy to the mixtures required for ignition. It was thus concluded that a higher ignition energy source was required to ignite the mixture beyond relative air/fuel ratio of 1.30 for the bowl piston design- which was achieved with the pre-chamber ignition system as the pre-chamber was shielded from main

chamber flow conditions and furthermore the pre-chamber ignition mode has a much higher ignition energy due to multiple jet ignition sites which was able to overcome the drawbacks of spark ignition system.

The overall 10-90% burn duration for the bowl piston with the pre-chamber ignitor did not show much improvement over the base piston and only an average of 0.66 degrees. It was also observed at relative air fuel ratio of 1.40 that the 100 cycle averaged burn duration for the bowl piston was longer than that of the base piston. Further investigation revealed that because the pre-chamber was more enriched and as the combustion process inside the pre-chamber contributed to no actual work output- less fuel energy was available in the main chamber as a result of which the integrated heat release rate was shown to take a longer time to reach 90% burn point. Comparison of the MFB 10-75% duration showed that the bowl piston design had a faster rate of heat release and thus shorter burn duration by an average of 1.25 degrees when compared with the base piston as shown in Figure 6-56.

The MFB 10-90% vs relative air/fuel ratio trend showed that burn duration increased with increasing relative air/fuel ratio which can be attributed to the reduction in flame speeds in the main chamber of the engine. Operating in leaner conditions reduces flame temperature and affects the reaction rate thus reducing the flame speeds which would increase the overall burn duration. As the ignition delay was also found to be increasing with leaner operation, the jet velocity and penetration would be reduced thus reducing the initial flame area via jet ignition in the main chamber which would contribute to a longer burn duration.

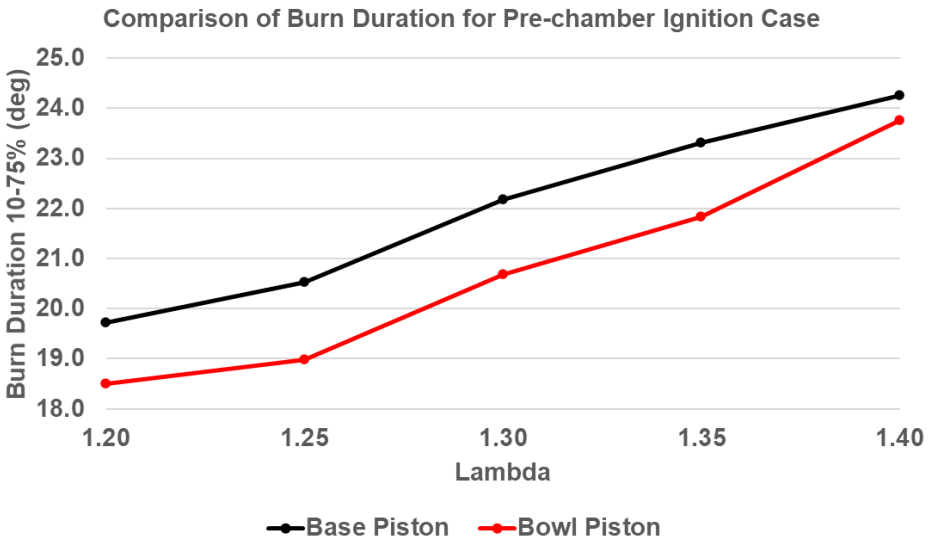

Figure 6-56 Comparison of Cycle Averaged Mass Fraction Burn Duration of 10-75% for Base and Bowl Pistons at Various Relative Air/Fuel Ratios

Figure 6-57 shows the comparison between the high pass filtered pressure oscillations in the main chamber for the base piston and bowl piston at various relative air/fuel ratios. It was observed that the pressure oscillations in the bowl piston case had a higher amplitude than the base piston case. Since the pre-chamber jet ejection results in rapid compression of the gas ahead of the tip of the jet- this results in the generation of shockwaves.

An observation was made- that the shockwaves were not a result of knocking combustion or end gas autoignition as no knocking sounds were heard via the engine stethoscope whilst the engine was in operation.

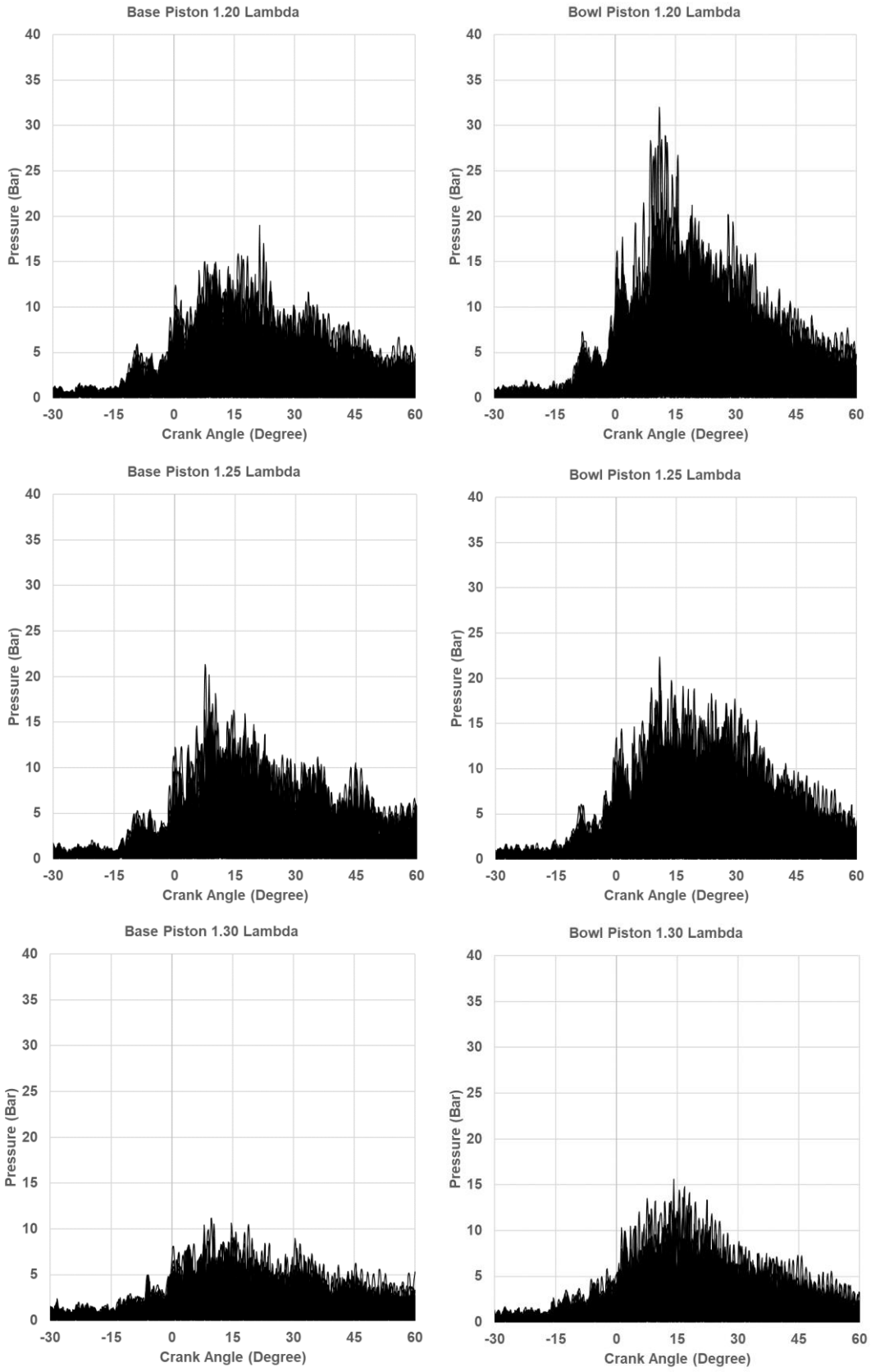

Figure 6-57 Comparison of 100 Overlaid High Pass Filtered Raw Absolute Pressure Signals for Base and Bowl Pistons at Various Relative Air/Fuel Ratios

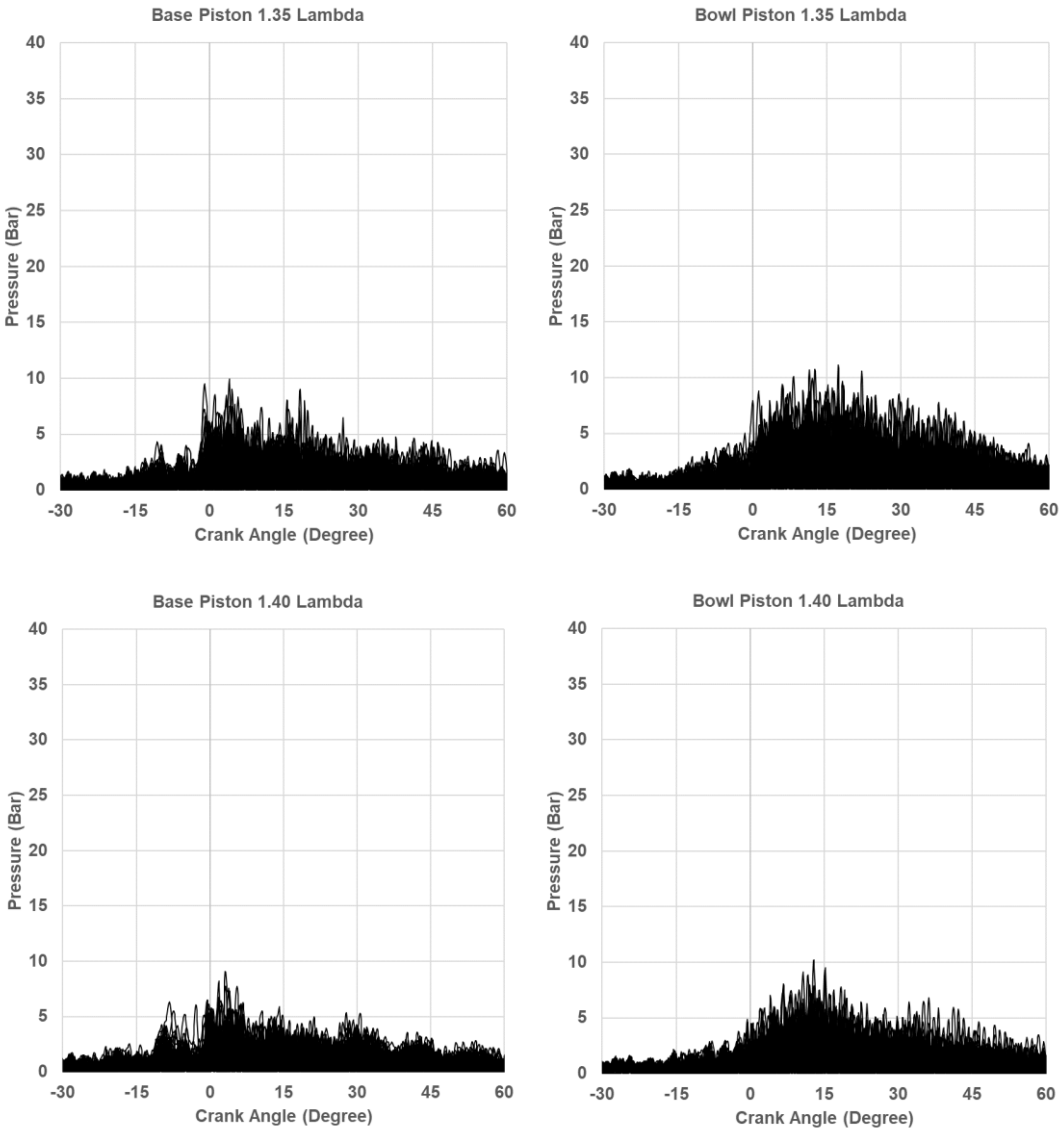

Figure 6-57 Comparison of 100 Overlaid High Pass Filtered Raw Absolute Pressure Signals for Base and Bowl Pistons at Various Relative Air/Fuel Ratios (continued)

As the pre-chamber jet velocity is a function of enrichment of the pre-chamber, a better enrichment would mean a higher jet velocity which would in-turn lead to a more rapid compression of the gas ahead of the tip of the jet thus resulting in higher amplitude shockwaves. This phenomenon was observed in the comparison between the maximum amplitude of high pass filtered pressure oscillations for the base and bowl piston, shown in Figure 6-58, where the bowl piston exhibited higher amplitude pressure oscillations as the pre-chamber in the bowl piston was more enriched than the base piston.

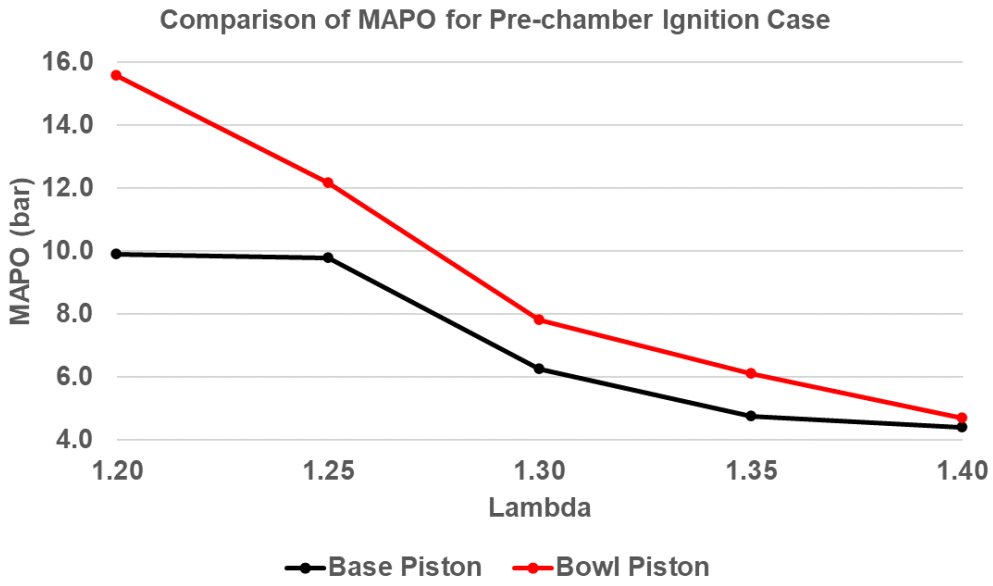

Figure 6-58 Comparison of Average MAPO for Base and Bowl Pistons at Various Relative Air/Fuel Ratios

7. Investigation of the Influence of Back-Pressure on a Pre-chamber Ignited Engine

The residual gas fraction contained in an engine cylinder during compression stroke of a 4-stroke engine is determined by the exhaust and inlet processes. The amount of residual gas fraction contained in the engine cylinder from the previous cycle affects the engine combustion processes through its influence on charge mass, temperature and dilution. Residuals have a significant influence on flame propagation in the combustion chamber via dilution effect as there is very little oxygen content in the residual gas. The residual gas dilutes the fuel/air mixture and thus reduces the flame propagation speed. Furthermore, the non-uniform spatial distribution of residual gas may cause misfire if the residual gas resides around the spark plug at the time of ignition. Thus concentrations of residual gas are known to have profound effects on the performance of an engine. The residual gas fraction is primarily a function of inlet and exhaust pressures, speed, compression ratio, valve timing, and exhaust system dynamics. (Heywood, 1998; Senecal et al., 1996)

As there is very limited knowledge available in literature regarding the influence of residuals in a high speed passive pre-chamber ignited engine, this chapter aims to study the influence of residuals on combustion in a passive pre-chamber ignited engine via alteration of the exhaust back pressure.

7.1 Investigation of Influence of Back Pressure via Engine Testing

To study the influence of back-pressure on combustion, the engine was set to be tested at 6000 rpm at 1.20 relative air/fuel ratio with an absolute exhaust back-pressure of 1.2 bar and 2 bar generated by controlling a back-pressure valve, forthwith referred to as a 'Low Back-pressure' a 'High Back-pressure' condition, respectively, in the engine testing results with both spark and pre-chamber ignition systems. The ignition timings were limited by engine knocking and/or maximum spark advance for best torque.

Comparison of gross ISFC as shown in Figure 7-1 showed that gross ISFC increased with higher back-pressure for both spark and pre-chamber ignited engine cases. Gross ISFC was found to have increased by 4.41 g/kWh and 1.72 g/kWh for spark and pre-chamber ignition cases, respectively.

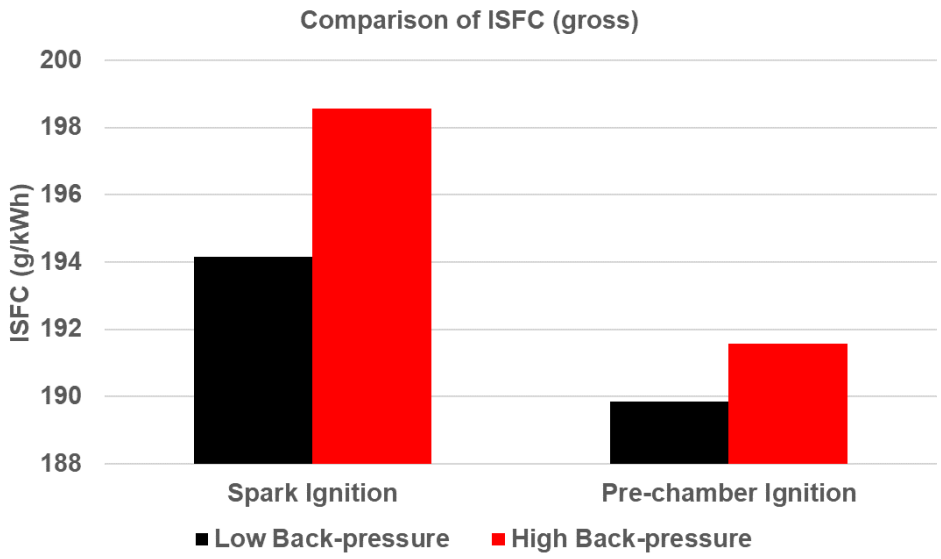

Figure 7-1 Comparison of Gross Indicated Specific Fuel Consumption at Low and High Back-pressures for Spark and Pre-chamber Ignited Engine

Comparison of COV of gross IMEP as shown in Figure 7-2 showed that the COV of gross IMEP increased at high back-pressure condition for both the spark and pre-chamber ignited engine by 0.53 and 0.93, respectively.

Ignition timings were retarded for both spark ignition and pre-chamber ignition cases at high back-pressure case compared to the low back-pressure case as shown in Figure 7-3. The spark timing was retarded by 1.21 degrees and 5.04 degrees for spark ignition and pre-chamber ignition, respectively.

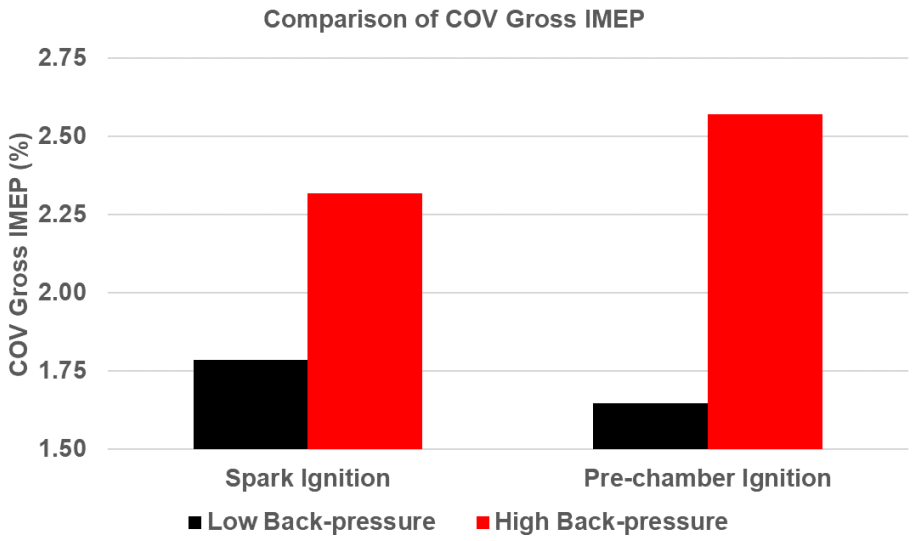

Figure 7-2 Comparison of Coefficient of Variation of Gross IMEP at Low and High Back-pressures for Spark and Pre-chamber Ignited Engine

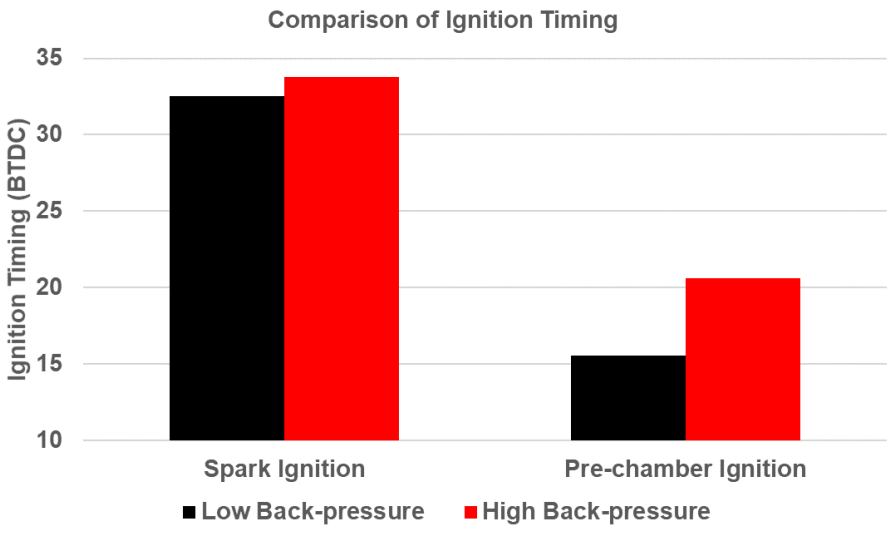

Figure 7-3 Comparison of Ignition Timing at Low and High Back-pressures for Spark and Pre-chamber Ignited Engine

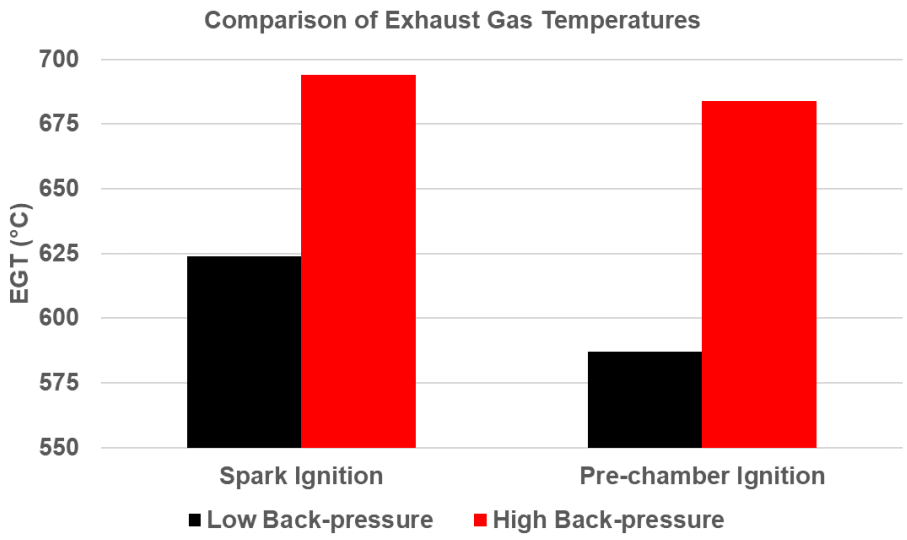

Figure 7-4 Comparison of Exhaust Gas Temperatures at Low and High Back-pressures for Spark and Pre-chamber Ignited Engine

Exhaust gas temperatures were found to be considerably higher for the high back-pressure case than the low back-pressure case for both spark and pre-chamber ignition systems. The exhaust gas temperatures were found to be 70 °C and 97 °C higher for the high back-pressure case compared to the low back-pressure case for spark ignition and pre-chamber ignition, respectively.

Figure 7-5 shows the comparison of 100 cycles of in-cylinder pressure plots for spark and pre-chamber ignition systems with high and low back-pressures applied. A narrower band of pressure curves were observed for the low back-pressure case for both spark and pre-chamber ignition signifying a low cyclic variation when compared with the high back-pressure cases. A higher number of lower than average pressure cycles were observed for the cases of spark and pre-chamber ignition systems at higher back-pressure which was reflected in the average pressure plots as shown in Figure 7-6.

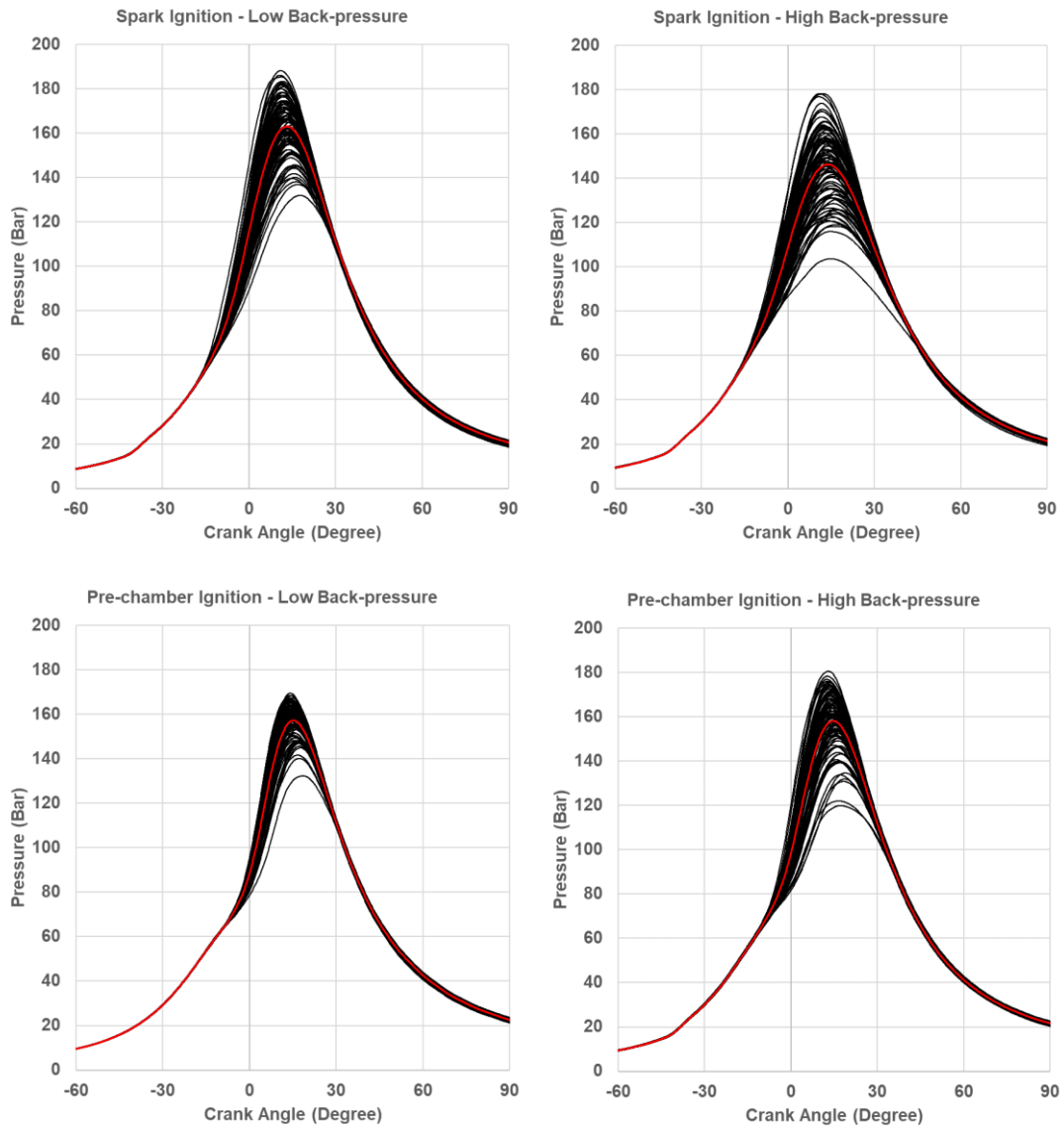

Figure 7-5 Comparison of 100 Cycles of In-cylinder Pressure Plots at Low and High Back-pressures for Spark and Pre-chamber Ignited Engine

Figure 7-7 and 7-8 show the comparison of normalised heat release rate and integrated heat release rate where a higher peak heat release rate and evidence of faster combustion was observed for the low back-pressure case for both spark and pre-chamber ignition cases.

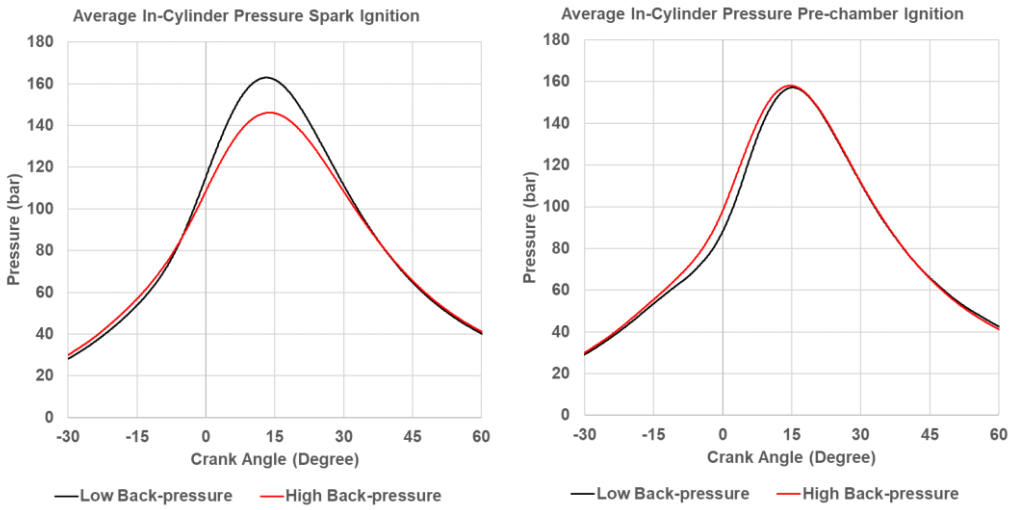

Figure 7-6 Comparison of 100 Cycle Averaged In-cylinder Pressure Plots at Low and High Back-pressures for Spark and Pre-chamber Ignited Engine

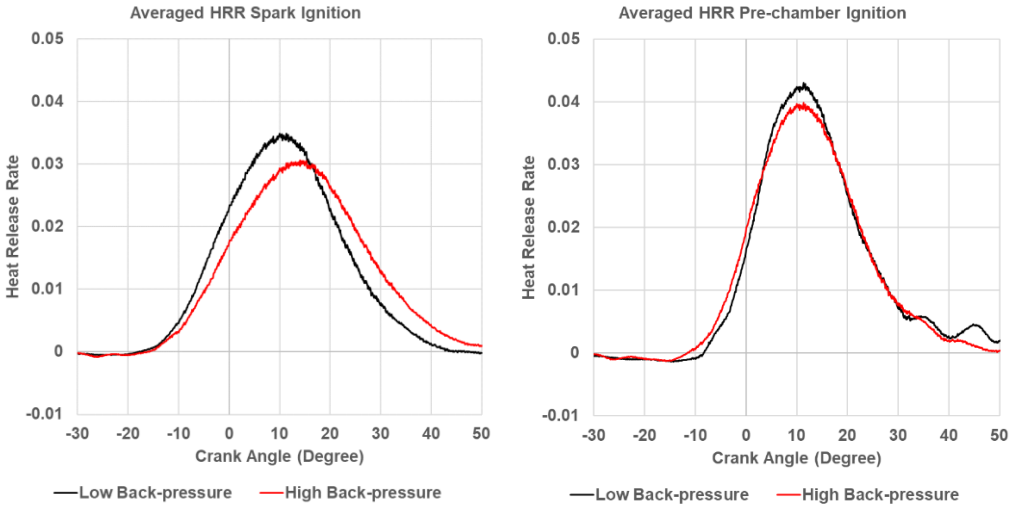

Figure 7-7 Comparison of Normalised Heat Release Rate at Low and High Back-pressures for Spark and Pre-chamber Ignited Engine

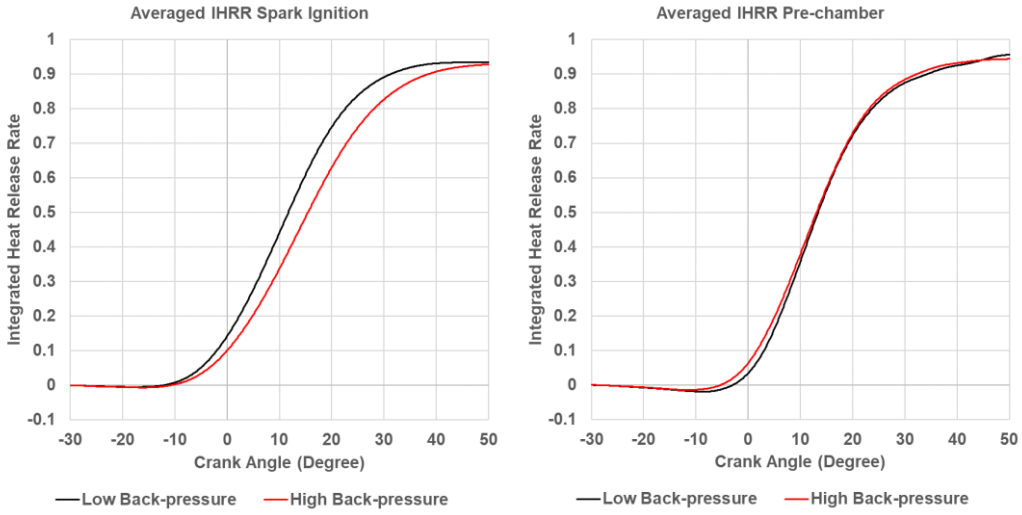

Figure 7-8 Comparison of Normalised Integrated Heat Release Rate at Low and High Back-pressures for Spark and Pre-chamber Ignited Engine

Figure 7-9 shows the comparison of various burn characteristics, it was observed that the ignition was delayed for both spark and pre-chamber ignition cases when the back-pressure was high. Ignition was delayed by 3.33 degrees and 3.83 degrees for spark and pre-chamber ignition cases, respectively at higher back-pressure. MFB 50% point was delayed by 3.84 degrees for the spark ignition case at high back-pressure, which was limited by knock limited spark advance and the MFB 50% point was advanced by 0.22 degrees for the pre-chamber case with high back-pressure, which was limited to maximum advance for best torque. The MFB 10-90% burn duration was increased by 5.79 degrees for the spark ignition case at high back-pressure compared to the low back-pressure case. For the pre-chamber case the MFB 10-90% burn duration was reduced by 1.02 degrees at high back-pressure when compared with the low back-pressure case.

Figure 7-10 shows the comparison between the MFB 10-75% burn duration for spark and pre-chamber ignition at low and high back-pressure where the MFB 10-75% burn duration was found to be higher by 2.81 degrees and 0.77 degrees the spark and pre-chamber ignition cases at high back-pressure, respectively, when compared with the low back-pressure case.

The comparison of combustion stability, shown in Figure 7-11, shows that combustion is more stable for the low back-pressure case for both spark and pre-chamber ignition cases as the deviation in ignition delay and MFB 10-90% burn duration were found to be lower and more concentrated in the plots when compared to the high back-pressure case.

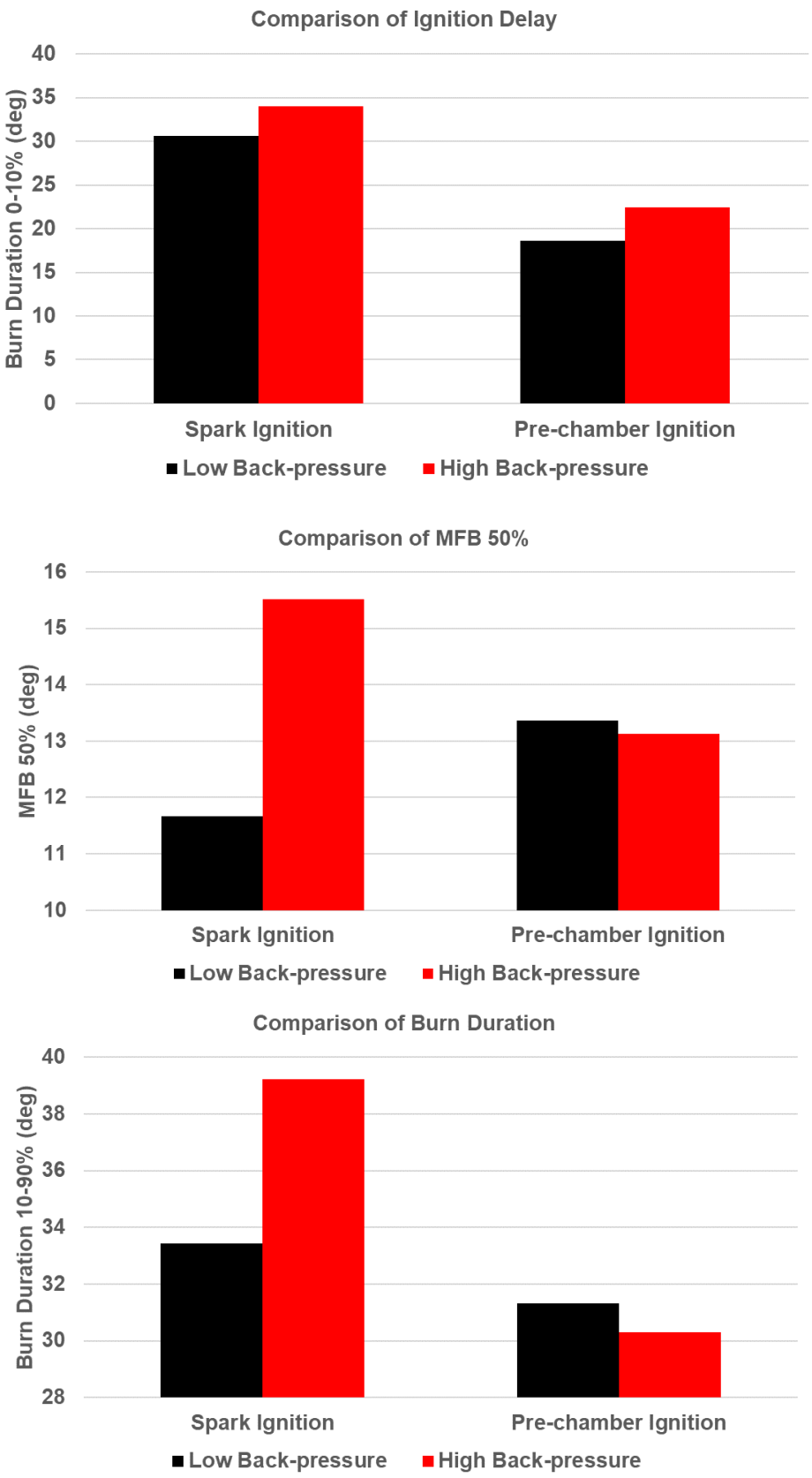

Figure 7-9 Comparison of 100 Cycle Averaged Ignition Delay, MFB 50% and 10-90% Burn Duration at Low and High Back-pressures for Spark and Pre-chamber Ignited Engine

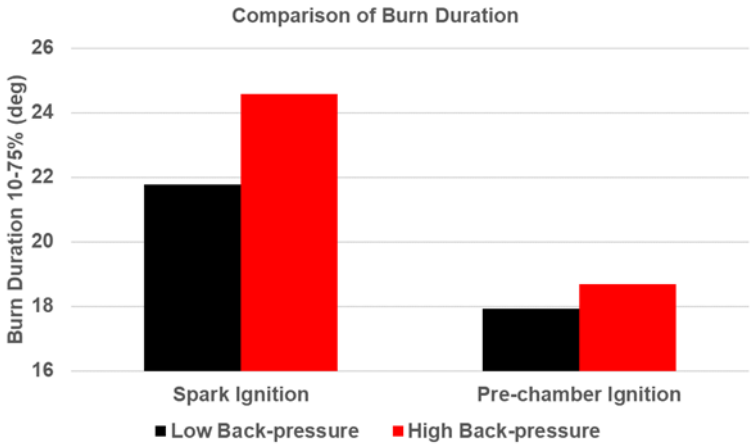

Figure 7-10 Comparison of 100 Cycle Averaged 10-75% Burn Duration at Low and High Back-pressures for Spark and Pre-chamber Ignited Engine

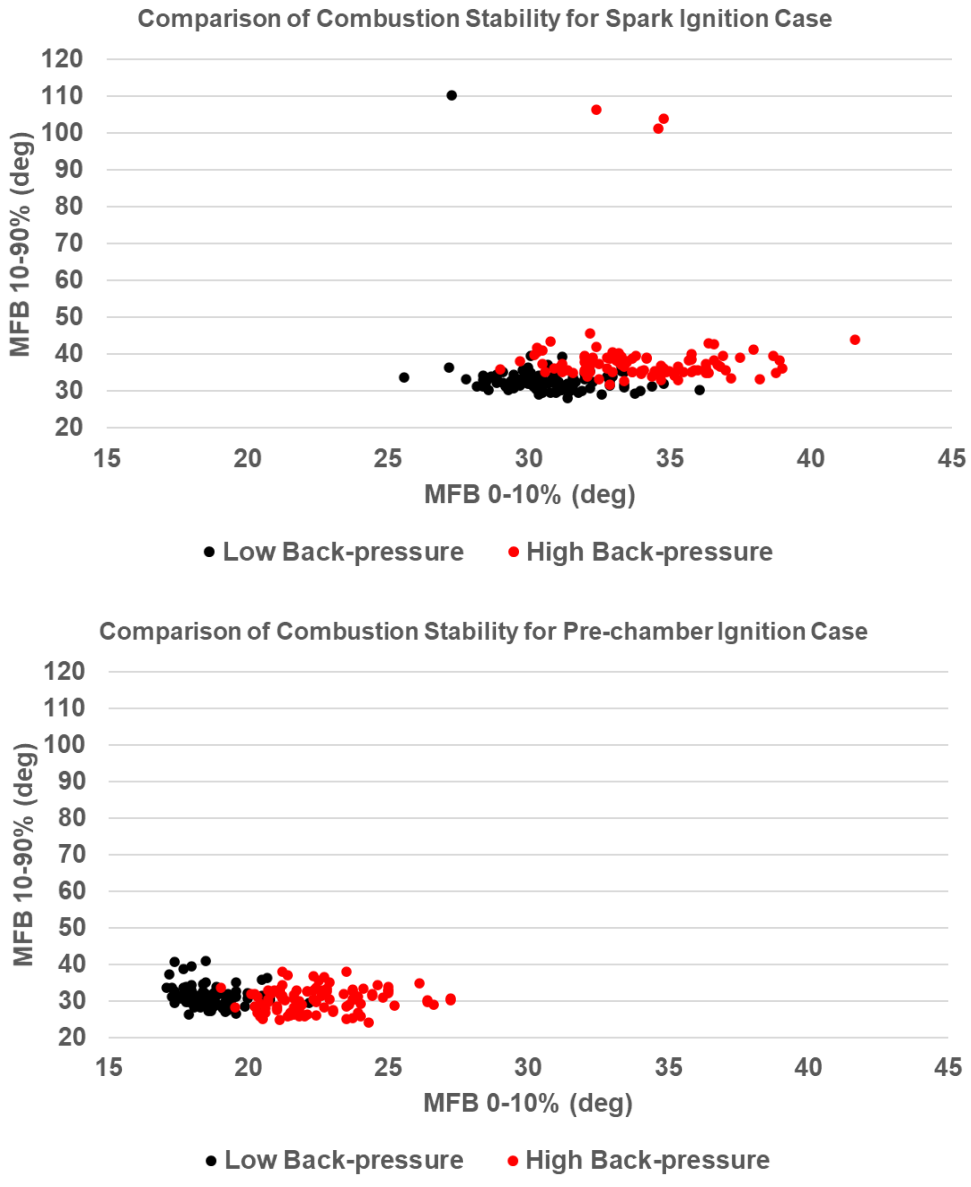

Figure 7-11 Comparison of Combustion Stability at Low and High Back-pressures for Spark and Pre-chamber Ignited Engine

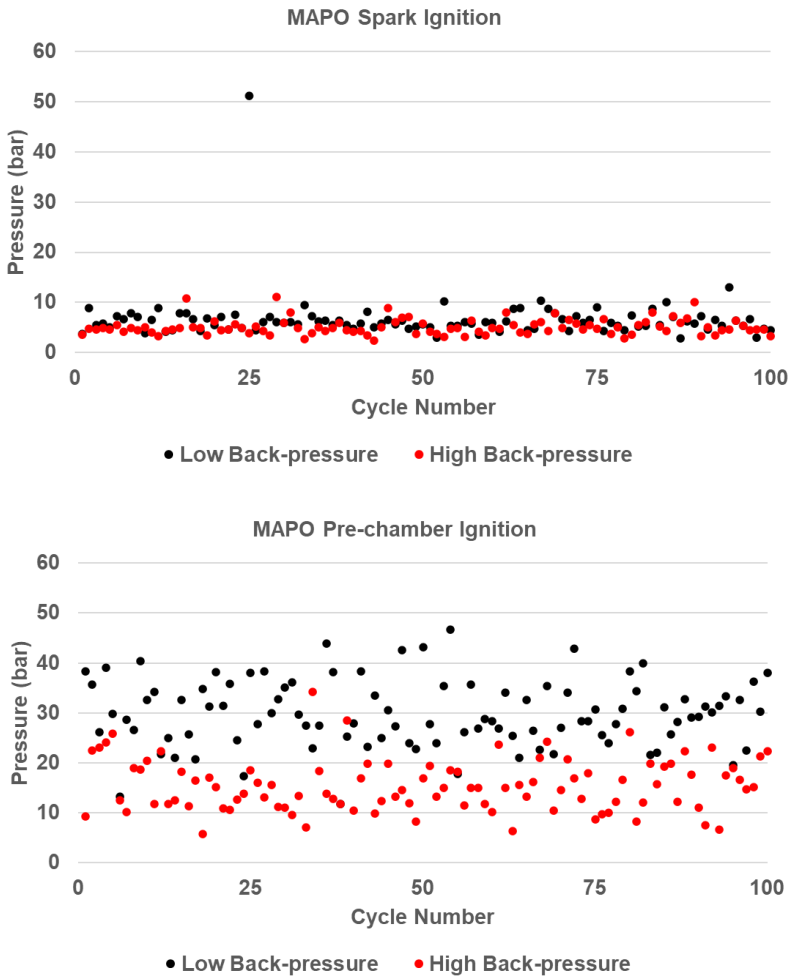

Figure 7-12 Comparison of Maximum Amplitude of Pressure Oscillations at Low and High Back-pressures for Spark and Pre-chamber Ignited Engine

Ignition System	Average Low Back-pressure MAPO (bar)	Average High Back-pressure MAPO (bar)
Spark Ignition	6.64	5.08
Pre-chamber Ignition	29.91	15.5

Table 7-1 Comparison of Average MAPO for Spark and Pre-chamber Ignition cases at Low and High Back-pressure

Comparison of MAPO, as shown in Figure 7-12 and Table 7-1, for the spark ignition case showed that the average MAPO was identical for the low back-pressure and high back-pressure cases. Average MAPO value was slightly

higher for the low back-pressure case due to 1 heavy knocking cycle in the 100 cycles. The MAPO for the pre-chamber ignition case at low back-pressure was found to be twice of the high back-pressure case, which was also observed in the 100 overlaid high pass filtered raw absolute pressure signals as shown in Figure 7-13.

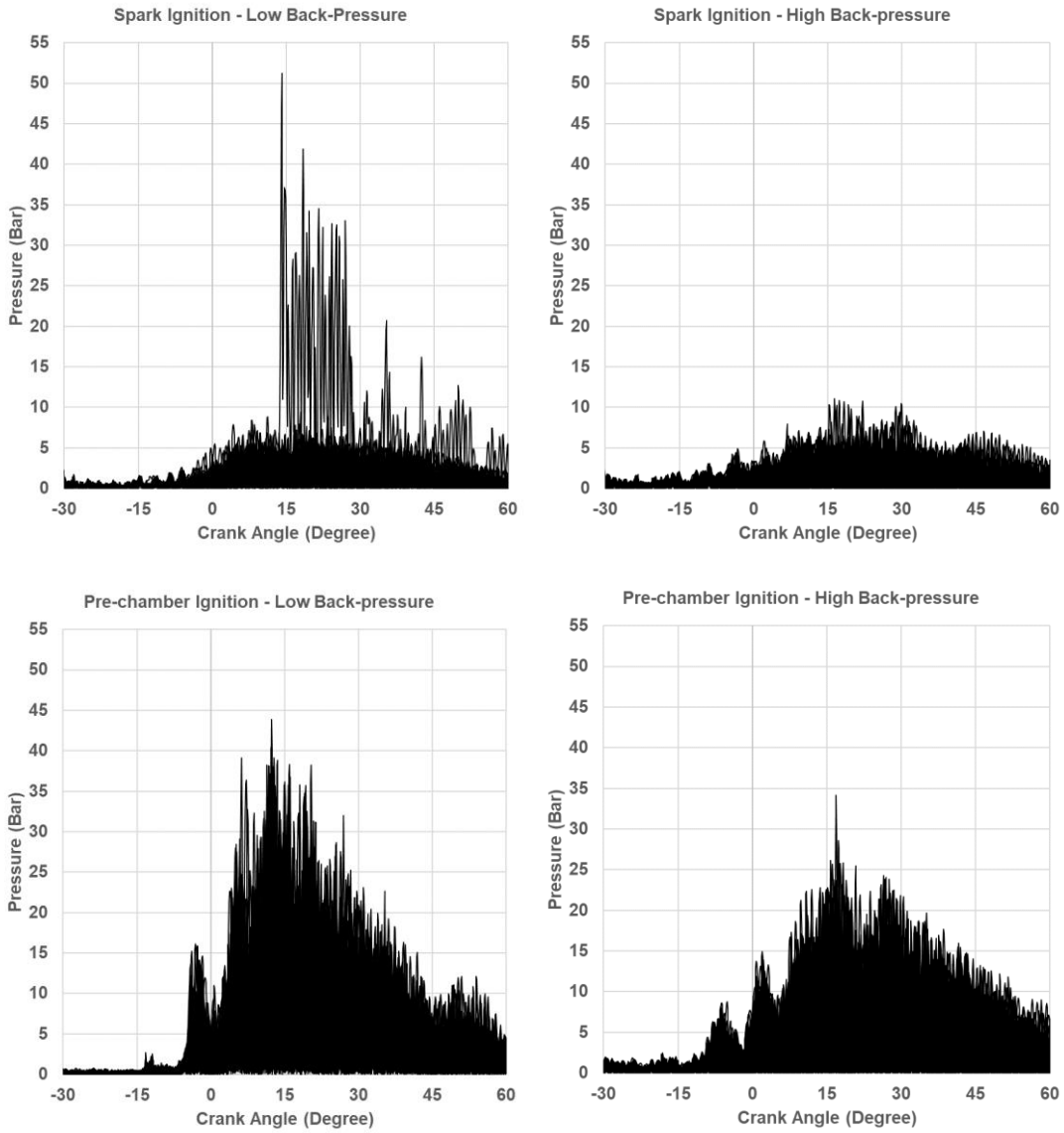

Figure 7-13 100 Overlaid High Pass Filtered Raw Absolute Pressure Signals at Low and High Back-pressures for Spark and Pre-chamber Ignited Engine

7.2 Investigation of Influence of Back Pressure via Simulation

The in-cylinder pressure data obtained from engine testing was correlated with a combination of 1D CFD and 3D CFD models to understand the influence of exhaust back-pressure on engine performance via simulation methods. A 1D GT power model with a SI Wiebe combustion model was utilised for this study, due to a low computational cost compared to 3D CFD, to calculate residual concentration in the combustion chamber. The combustion model was tuned to match the test in-cylinder pressure data for the low and high back-pressure cases. 3D CFD data was used to obtain pre-chamber burn characteristics to be input into the 1D CFD model.

7.2.1 Correlation of Spark Ignition Simulation Models with Engine Test Data

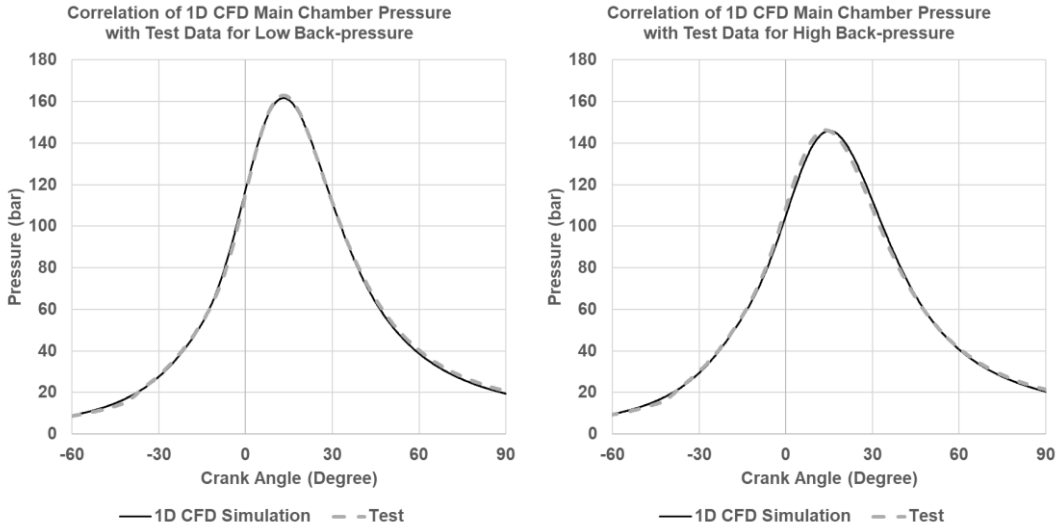

Figure 7-14 Correlation of 1D CFD Main Chamber Pressure with Test Data for Spark Ignition Case with Low and High Back-pressures

Figure 7-14 shows the correlation of in-cylinder pressure of the 1D CFD model with engine test data. The SI Wiebe combustion model was calibrated for the

engine operating at 1.20 relative air/fuel ratio with a speed of 6000 rpm at a fuel flow rate of 13.32 kg/h with low and high back-pressure of 1.2 and 2 bar, respectively.

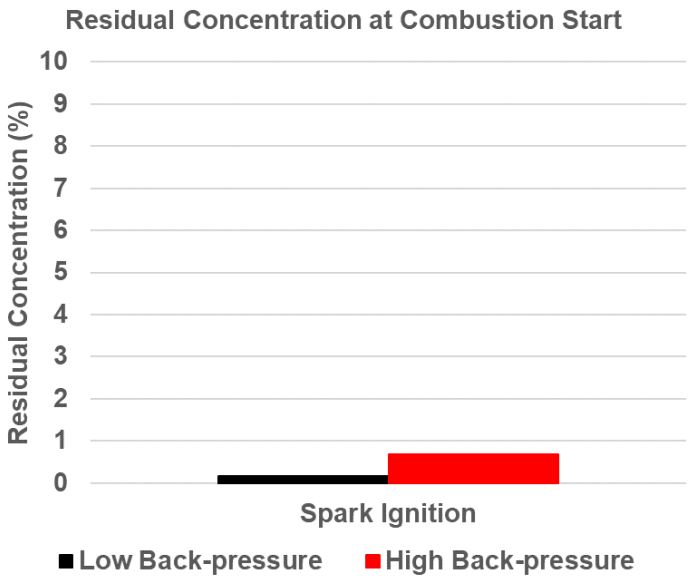

Figure 7-15 Simulated Residual Concentration at Combustion Start for Spark Ignition Case with Low and High Back-pressures

The simulated residual concentration at combustion start for spark ignition case was found to be 0.16% and 0.68% at low and high back-pressure, respectively.

7.2.2 Correlation of Pre-chamber Ignition Simulation Models with Engine Test Data

A 3D CFD model was developed for the pre-chamber ignited high back-pressure case to correlate with test data to obtain the pre-chamber instantaneous pressure and burn conditions to input into the 1D CFD model as a pressure sensor was not attached to the pre-chamber in the test setup. Figure 7-16 shows the correlation of the 3D CFD simulated main chamber pressure with test data where the ignition timing was set to 16 deg BTDC. Figure 7-17 shows the correlation for the 1D CFD simulated pre-chamber

pressure with the 3D CFD simulated pre-chamber pressure data for the high back-pressure case.

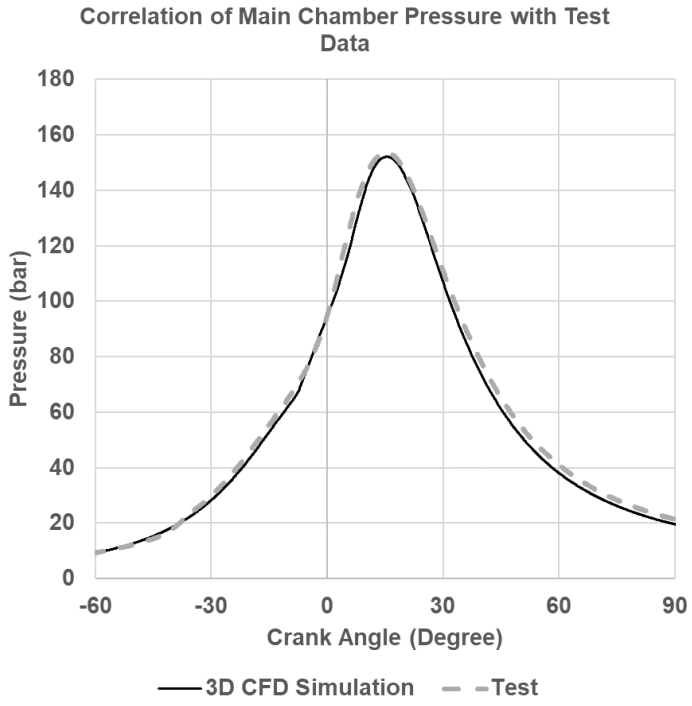

Figure 7-16 Correlation of 3D CFD Main Chamber Pressure with Test Data for Pre-chamber Ignition Case at High Back-pressure

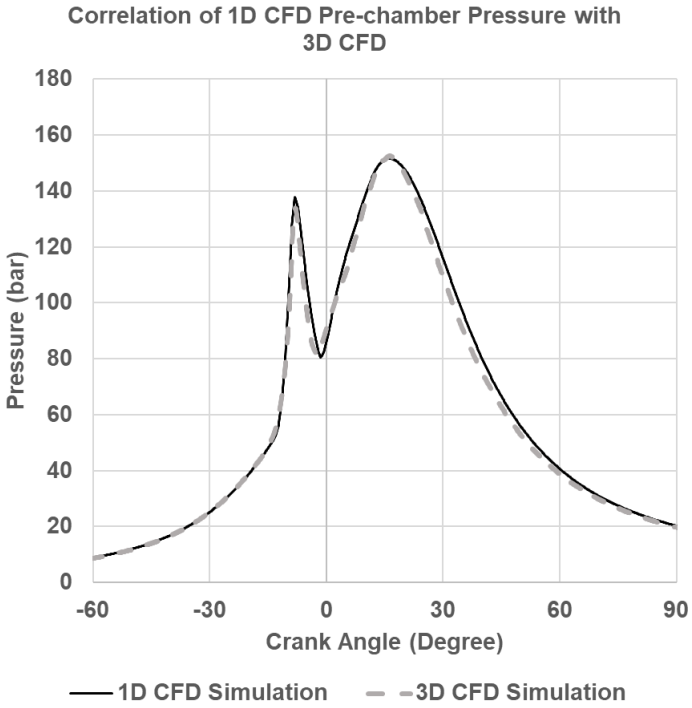

Figure 7-17 Correlation of 1D CFD Pre-chamber Pressure with 3D CFD Simulated Pre-chamber Pressure for Pre-chamber Ignition Case at High Back-pressure

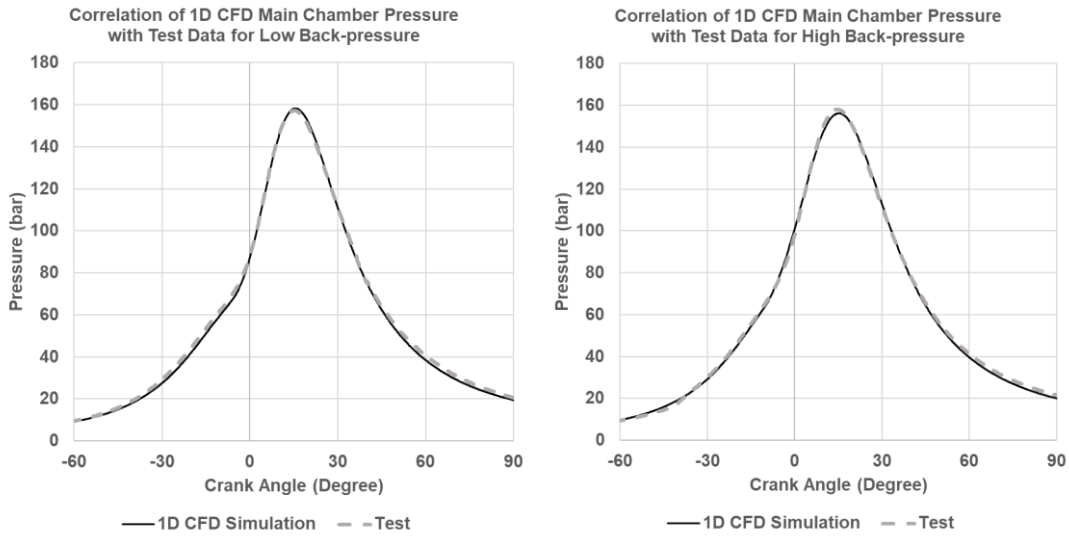

Figure 7-18 Correlation of 1D CFD Pre-chamber Pressure with Test Data for Pre-chamber Ignition Case at High Back-pressure

Figure 7-18 shows the correlation of the main-chamber in-cylinder pressure which was simulated in 1D CFD with Test Data at low and high back-pressure. Figure 7-19 shows the comparison of simulated residual concentration at combustion start where the residual concentration was found to be 0.18% in the main-chamber and 4.40% in the pre-chamber at low back-pressure case and 0.74% in the main-chamber and 7.20% in the pre-chamber at high back-pressure.

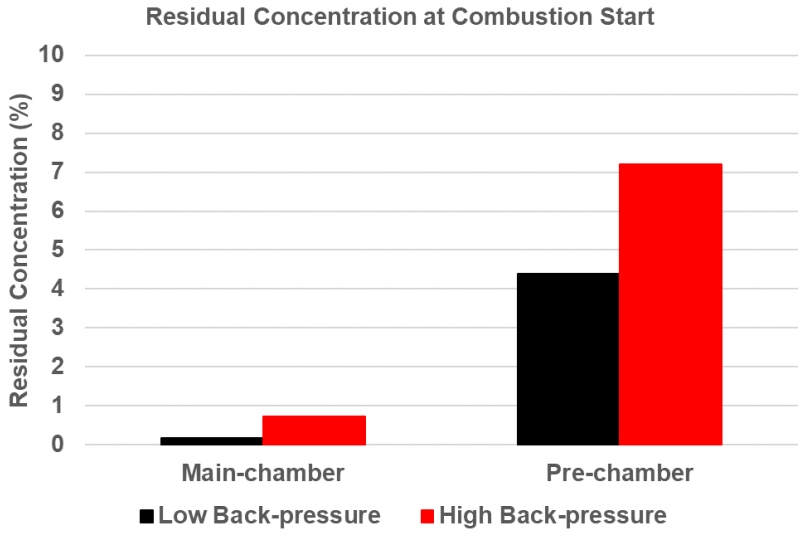

Figure 7-19 Simulated Residual Concentration at Combustion Start in the Pre-chamber and Main-chamber for Pre-chamber Ignition Case with Low and High Back-pressures

7.3 Discussion of Results

Engine test results for spark and pre-chamber ignition cases suggested that the performance of engine reduces with increasing back-pressure. Results showed that the trends observed in the case of spark ignited engine from the transition from low to high back-pressure were found to be similar to the trends observed in the pre-chamber ignited engine.

Gross ISFC and COV of gross IMEP were found to be higher for the high back-pressure case compared to the low back-pressure case. Ignition delay, exhaust gas temperature and burn duration were also found to be higher for the high back-pressure case coupled with a poor combustion stability for both spark and pre-chamber ignited engines which were attributed to high cyclic variation and slow flame propagation speeds due to increasing residuals.

Increasing the back-pressure was expected to increase the residual gas concentration in the main chamber, which was confirmed by the 1D CFD simulation results- the residual concentration in the main chamber was found to be 0.17% for low back-pressure cases and 0.71% for high back-pressure cases on average at combustion start. However, a large difference of residual concentration was found in the pre-chamber for the low and high back-pressure cases, where the residual concentration was found to be 2.8 percentage points higher for the high back-pressure case when compared to the low back-pressure case at combustion start. The difference in residual concentration can be attributed to the pre-chamber ingesting a higher residual gas fraction from the main-chamber in the high back-pressure case during intake stoke including the intake and exhaust valve overlap period, between

300 deg CA and 400 deg CA, and up until end of compression stroke, between -180 deg CA to ignition timing, as observed in Figure 7-20.

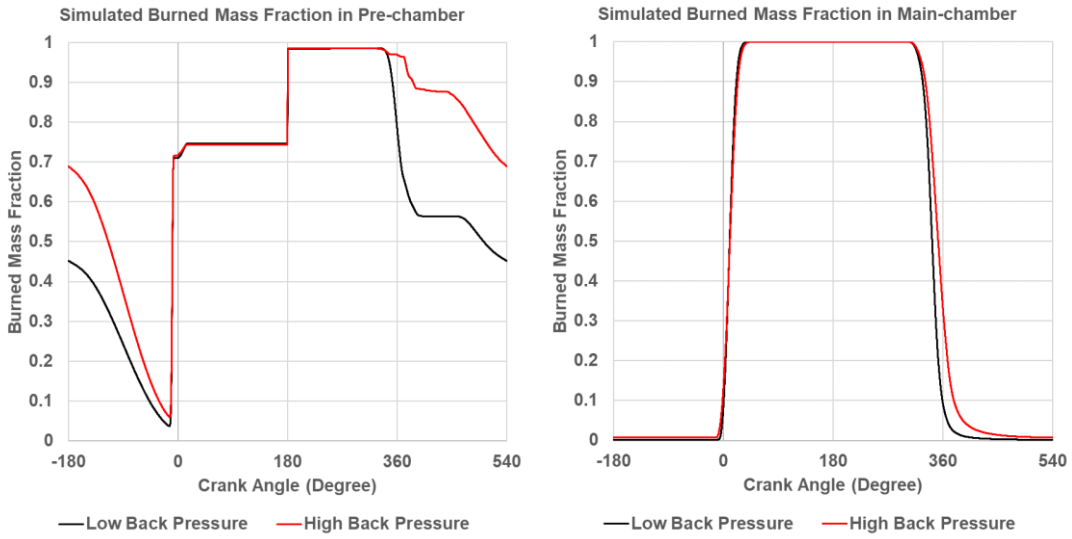

Figure 7-20 Simulated Instantaneous Residual Mass Fraction in the Pre-chamber and Main-chamber for Pre-chamber Ignition Case with Low and High Back-pressures

Recent study by Novella et al. (2020) have shown that the passive pre-chamber ignited engine is less tolerant of residuals and has a much limited EGR dilution limit compared to a spark ignited engine, thus the residual concentration level admitted by the engine was limited by the pre-chamber combustion performance. A higher residual concentration in the pre-chamber during combustion would lead to the flame beginning in the thickened flame regime where the eddies in the pre-chamber can penetrate into the diffusive layer of the flame which would enlarge the flame front thickness resulting in decreased laminar flame speeds and also compromising the flame stability- which explains the drop in performance of the engine with increasing ignition delay at high back-pressure case for the pre-chamber ignited engine. To counter the reduced flame speeds in the pre-chamber, further advancing of the spark timing was found to be ineffective due to the worsening of the pre-chamber flow and thermochemical conditions within the pre-chamber due to

the increasing residual concentration in the pre-chamber when one moves from TDC to 180 deg BTDC as shown in Figure 7-20. However, it was observed that the drop in performance of the pre-chamber ignited engine was lower in magnitude compared to the spark ignited engine as shown in Figure 7-1. This was attributed to the faster burn rate offered by the pre-chamber ignitor due to ignition at multiple sites in the main-chamber.

The comparison of average of maximum amplitude of pressure oscillations for the pre-chamber ignited engine, as shown in Table 7-1, demonstrates the influence of residual concentration inside the pre-chamber at combustion start. The average MAPO value for the low back-pressure case was found to be almost twice than that of the high back-pressure case which shows that the case with lower residuals generated a higher pressure inside the pre-chamber which resulted in a high jet velocity thus causing high amplitude of pressure oscillations. This observation is also complimented by the shorter ignition delay observed in the low back-pressure case, as shown in Figure 7-9, which shows that a faster combustion took place inside the pre-chamber due to more favourable conditions available for combustion.

Based on the findings of this study, a parametric study on the valve overlap period is recommended, which was not in the scope of this study, for the high back-pressure case to reduce the residual concentration in the main-chamber during intake stroke and thus aid in reducing the residual concentration in the pre-chamber to improve performance of the engine, as a valve overlap period has a very significant influence on the residual concentration in the main-chamber as suggested by Heywood (1998).

8. Investigation of the Influence of Compression Ratio on a Pre-chamber Ignited Engine

As a spark ignited internal combustion engine is governed by the Otto cycle, the indicated fuel conversion efficiency of an Otto cycle depends on the compression ratio and the specific heat ratio.

The indicated fuel conversion efficiency increases with increasing compression ratio and increases as specific heat ratio. As the pre-chamber ignited engine had shown a significant improvement in performance over the spark ignited engine as shown in previous chapters, potential gains via a higher compression ratio of the combustion chamber for a pre-chamber ignited engine were investigated in this chapter. The high compression ratio for this study was achieved via elimination of the piston bowl from the base piston design as shown in Figure 8-1.

A compression ratio of 15, compared to 14.1 achieved by the base piston crown design, was achieved by the high CR piston crown design for the spark ignited engine which was reduced to 14.7, compared to 13.8 achieved by the base piston crown design, when the 4 hole 0.8 cc pre-chamber was fitted due to additional volume added into the combustion chamber.

Figure 8-1 Base Piston Crown (L) and High CR Piston Crown (R) Designs

8.1 Investigation of Influence of Compression Ratio via Engine Testing

Engine testing was conducted at 7500 rpm on the high CR piston with optimised ignition and fuel timings at relative air/fuel ratios of 1.20, 1.25, 1.30, 1.35 and 1.40 for a fuel flow rate of 13.33 kg/h to calibrate the engine for maximum indicated performance or lowest ISFC which was limited by MBT or knock limited spark advance as few knocking cycles were observed at certain operating points. The aim was to analyse the influence of compression ratio and how it impacts a pre-chamber ignition system which was undertaken by comparing the results of high CR piston against the low CR pistons- the base and bowl piston crown designs- results of which were discussed in detail in chapter 6.

Figure 8-2 showed that gross ISFC for the high CR piston was reduced by 9.20 g/kWh and 3.51 g/kWh on average when compared with the low CR base piston crown and bowl piston crown designs, respectively.

Figure 8-3 shows the comparison of COV of gross IMEP where it was observed that the COV of gross IMEP in the case of the high CR piston was lower than the base piston but higher than the bowl piston case from relative air/fuel ratio of 1.20 to 1.30. The COV of gross IMEP had an average of 2.03% for the high CR piston case compared to 2.22% for the base piston case and 1.78% for the bowl piston case from 1.20 to 1.30 relative air/fuel ratio. However, the COV of gross IMEP for the high CR piston was much higher compared to both the base and bowl piston cases at 1.35 and 1.40 relative air/fuel ratios.

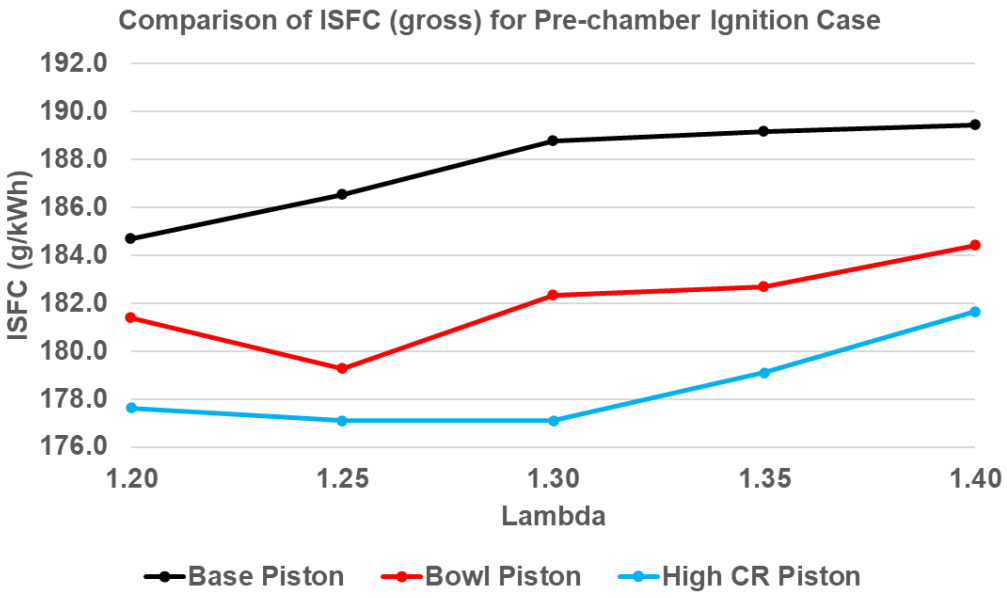

Figure 8-2 Comparison of Gross Indicated Specific Fuel Consumption for Base, Bowl and High CR Pistons at Various Relative Air/Fuel Ratios

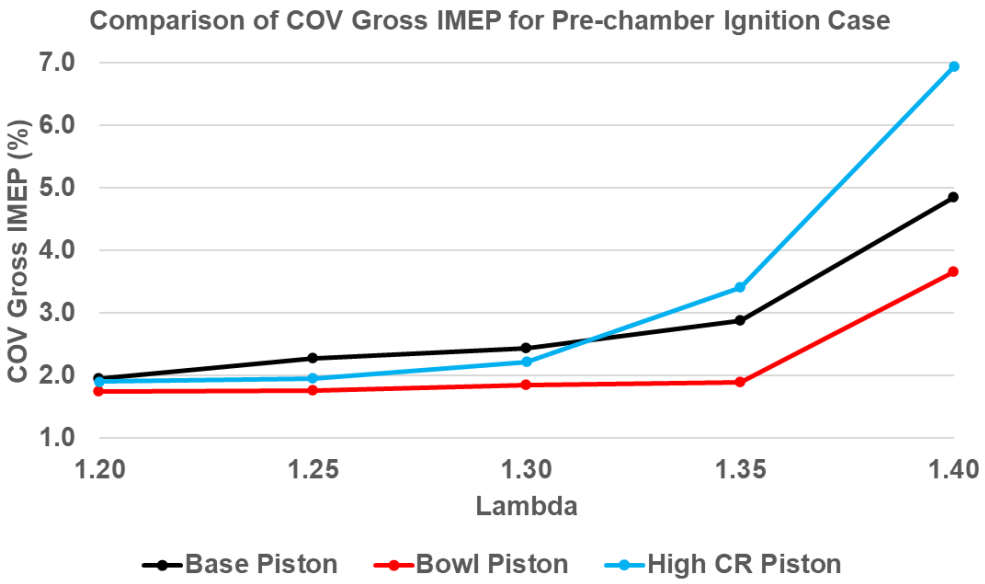

Figure 8-3 Comparison of Coefficient of Variation of Gross IMEP for Base, Bowl and High CR Pistons at Various Relative Air/Fuel Ratios

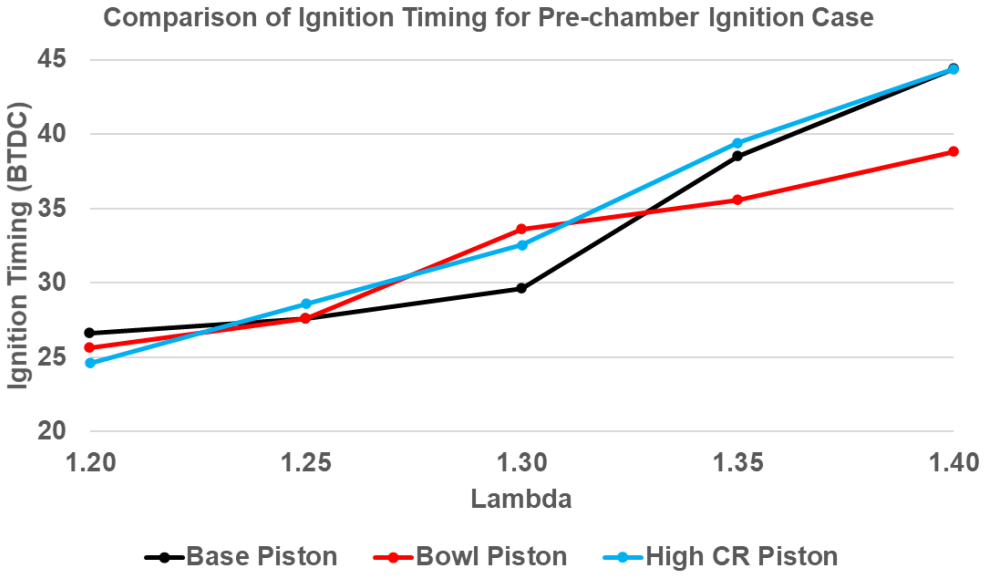

Figure 8-4 Comparison of Ignition Timing for Base, Bowl and High CR Pistons at Various Relative Air/Fuel Ratios

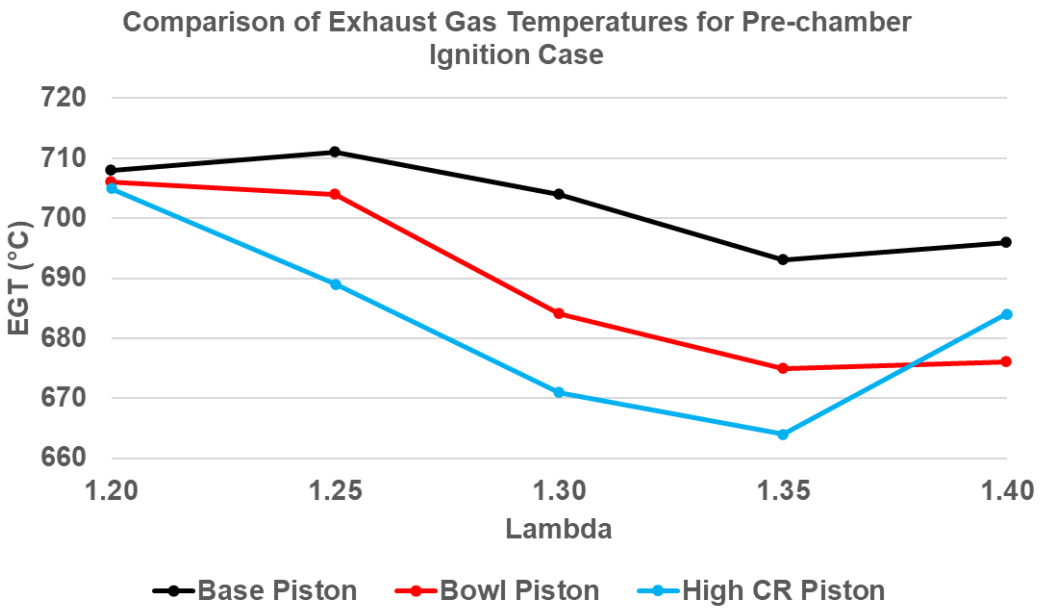

Figure 8-5 Comparison of Exhaust Gas Temperatures for Base, Bowl and High CR Pistons at Various Relative Air/Fuel Ratios

Figure 8-4 shows that the ignition timings were initially retarded at relative air/fuel ratio of 1.20, however the ignition timings for the high CR piston were relatively advanced at the leaner air fuel ratios when compared to the base and bowl piston cases. Exhaust gas temperatures, shown in Figure 8-5, were found to be lower for the high CR piston case across all relative air/fuel ratios except for relative air/fuel ratio of 1.40 where the exhaust gas temperature was found to be slightly higher than the bowl piston case.

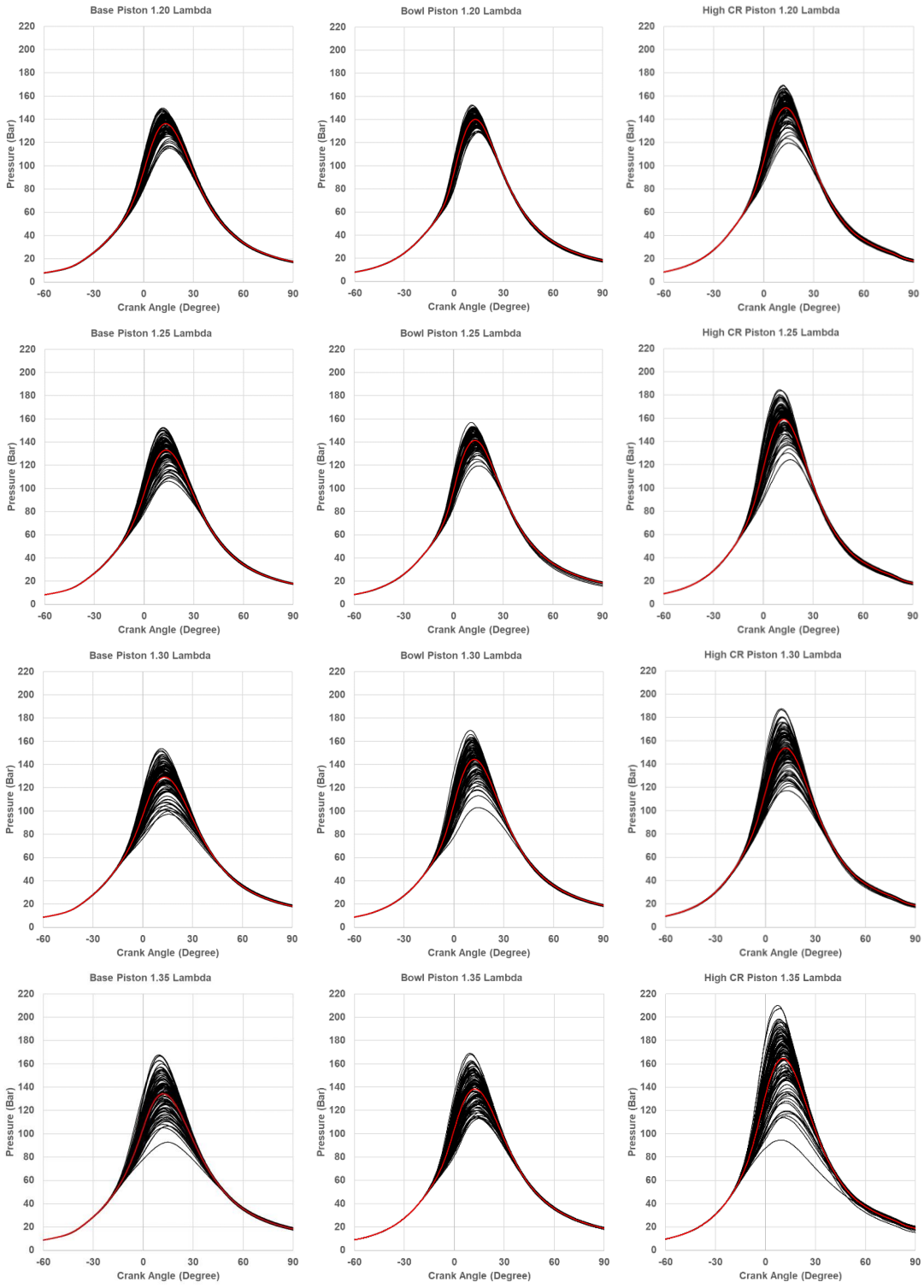

Figure 8-6 100 Cycles In-Cylinder Pressure Plots for Base, Bowl and High CR Pistons at Various Relative Air/Fuel Ratios

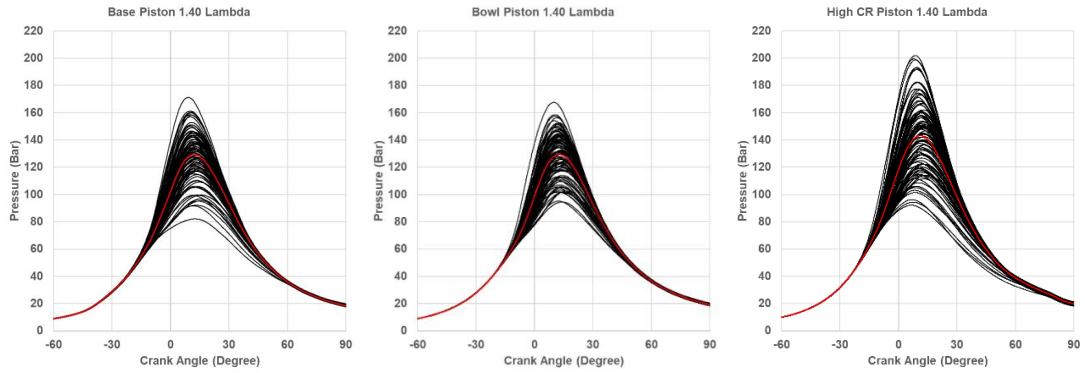

Figure 8-6 100 Cycles In-Cylinder Pressure Plots for Base, Bowl and High CR Pistons at Various Relative Air/Fuel Ratios (continued)

Figure 8-6 shows the comparison of 100 cycles of in-cylinder pressure plots for base and bowl pistons. A wider band of peak pressure curves were observed after TDC in the case of high CR piston at leaner relative air/fuel ratios of 1.35 and 1.40 due to increase in cyclic variation.

Figure 8-7 shows the comparison of average pressure curves where higher pumping losses (before TDC) and high peak pressures (after TDC) were observed for the high CR piston case due to higher compression ratio.

Figure 8-8 and 8-9 show the comparison between normalised heat release rate and integrated heat release rate, where an improvement in both the parameters were observed for the high CR piston case at all relative air/fuel ratios except for 1.40 where a reduction in burn rate for the high CR piston case was observed.

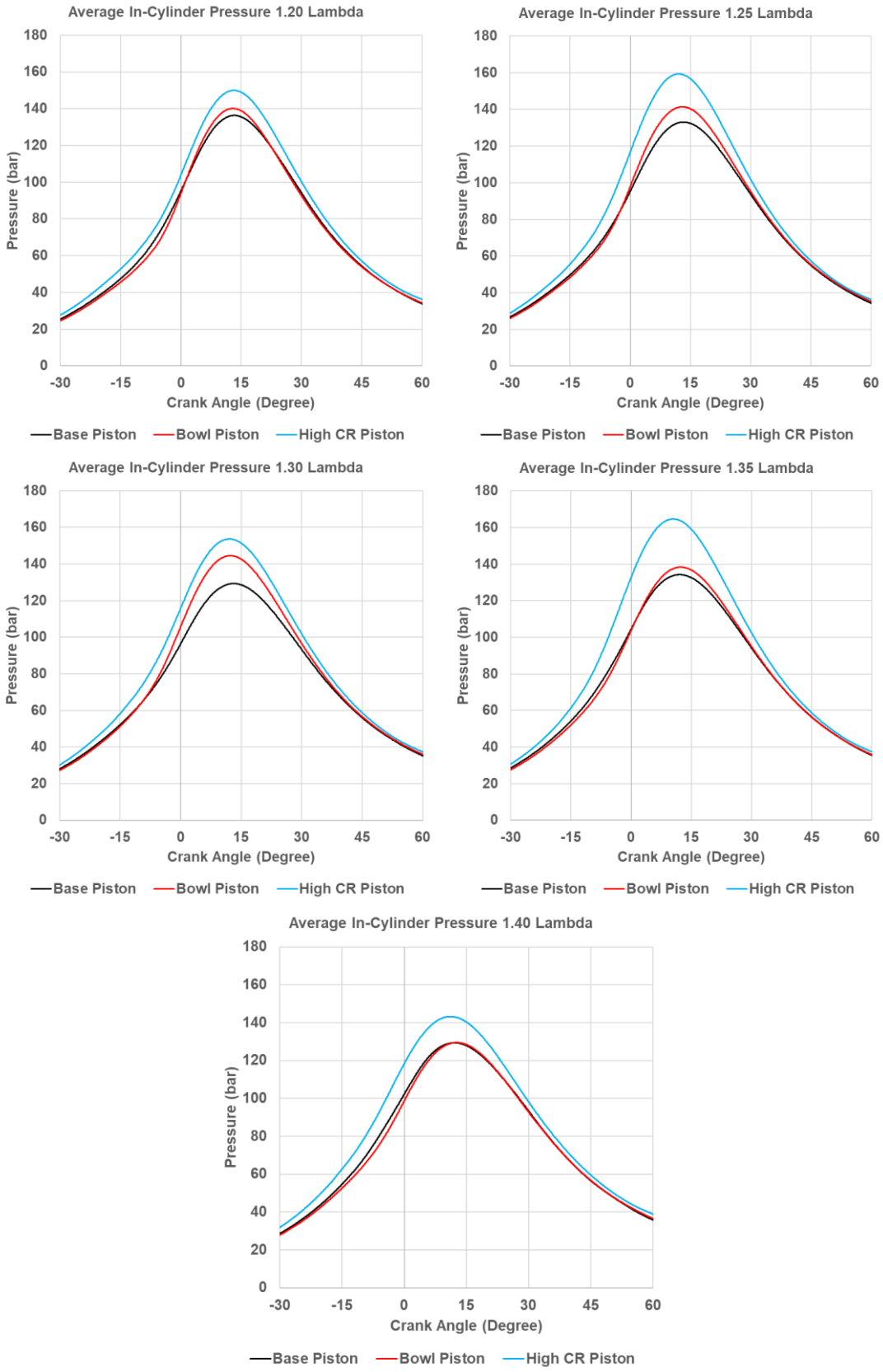

Figure 8-7 100 Cycle Averaged In-cylinder Pressure Plots for Base, Bowl and High CR Pistons at Various Relative Air/Fuel Ratios

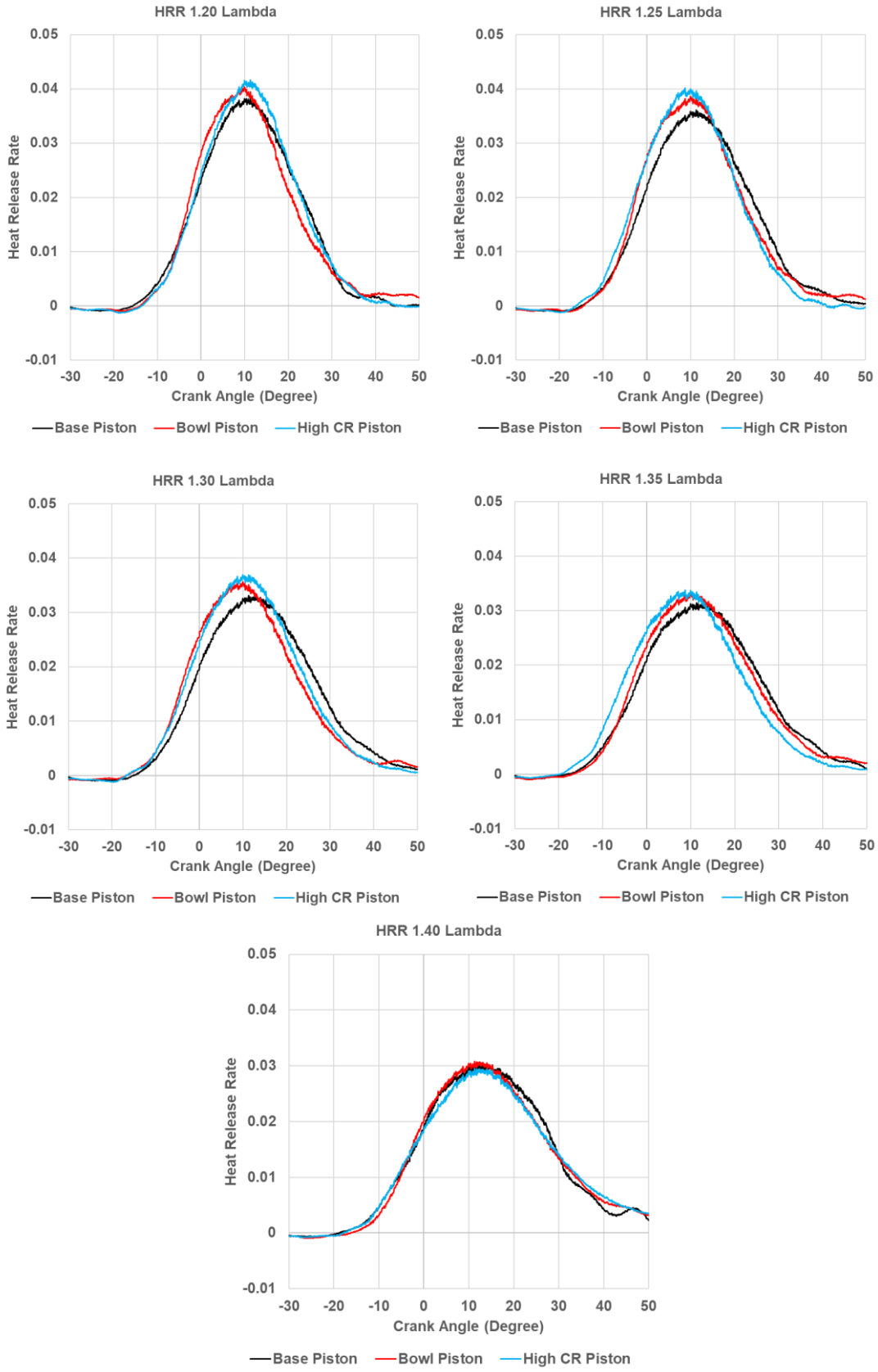

Figure 8-8 100 Cycle Averaged Normalized Heat Release Rate for Base, Bowl and High CR Pistons at Various Relative Air/Fuel Ratios

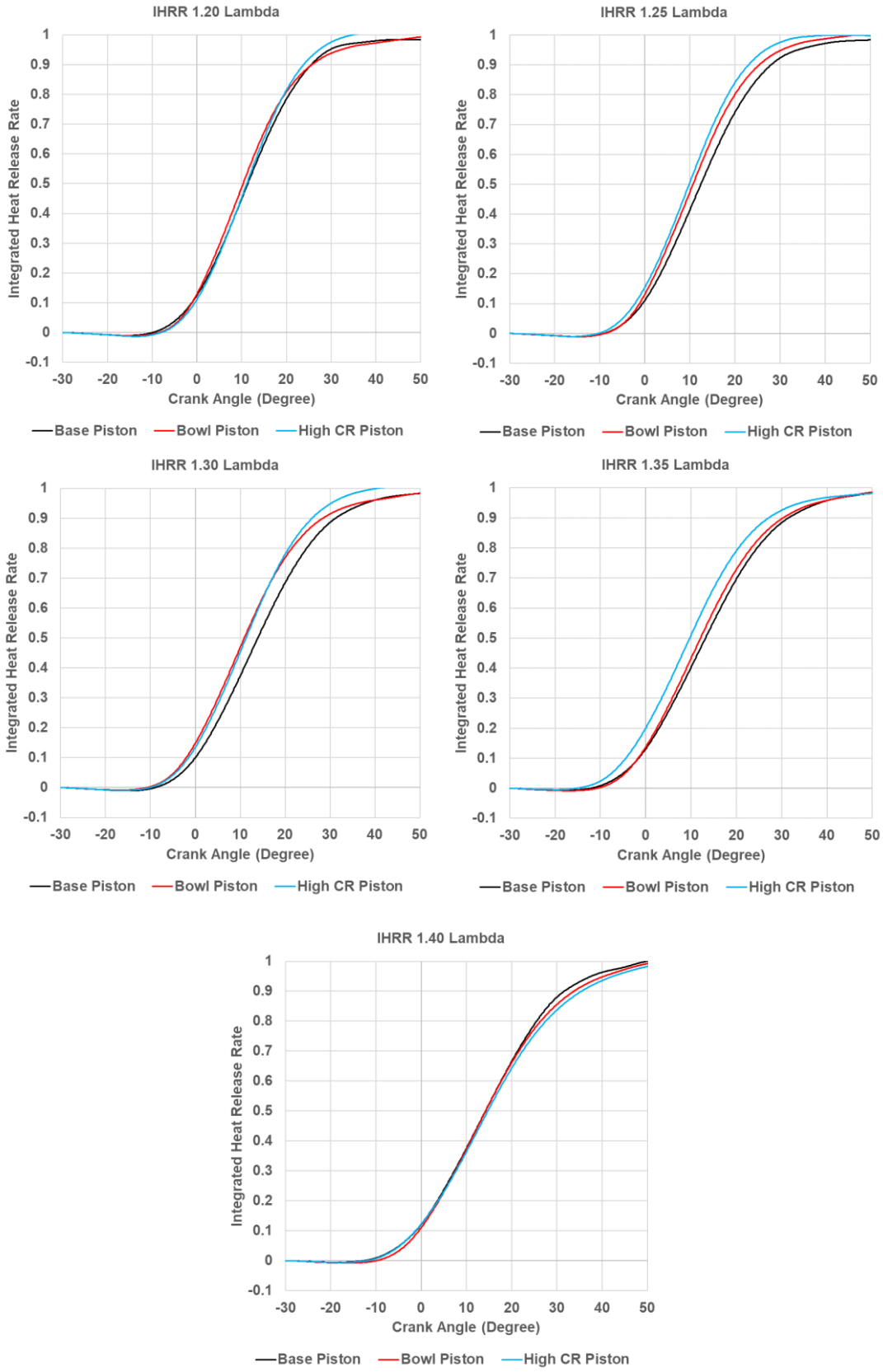

Figure 8-9 100 Cycle Averaged Normalized Integrated Heat Release Rate for Base, Bowl and High CR Pistons at Various Relative Air/Fuel Ratios

Figure 8-10 shows the comparison of various burn characteristics, where it was observed that the average ignition delay for the high CR piston case was found to be similar to the bowl piston case from relative air/fuel ratio of 1.20 to 1.30 however, ignition delay was found to have increased in the case of the high CR piston at 1.35 and 1.40 relative air/fuel ratio when compared with the bowl piston case.

A significant reduction in the burn duration was observed for the high CR piston case from 1.20 to 1.35 relative air/fuel ratio when compared with both base and bowl piston however, an increase in burn duration was observed at relative air/fuel ratio of 1.40 for the high CR piston case compared to both base and bowl piston.

Figure 8-11 shows that the burn duration points are more concentrated initially for the high CR piston from relative air/fuel ratio of 1.20 to 1.30 however, combustion was found to be less stable at relative air/fuel ratio of 1.35 and 1.40 when compared with the base and bowl piston cases. The variation in ignition delay and MFB 10-90% burn duration were evident in the standard deviation plots, shown Figure 8-12 and 8-13 where the high CR piston showed a higher deviation for both ignition delay and MFB 10-90% burn duration at leaner relative air/fuel ratios of 1.35 and 1.40.

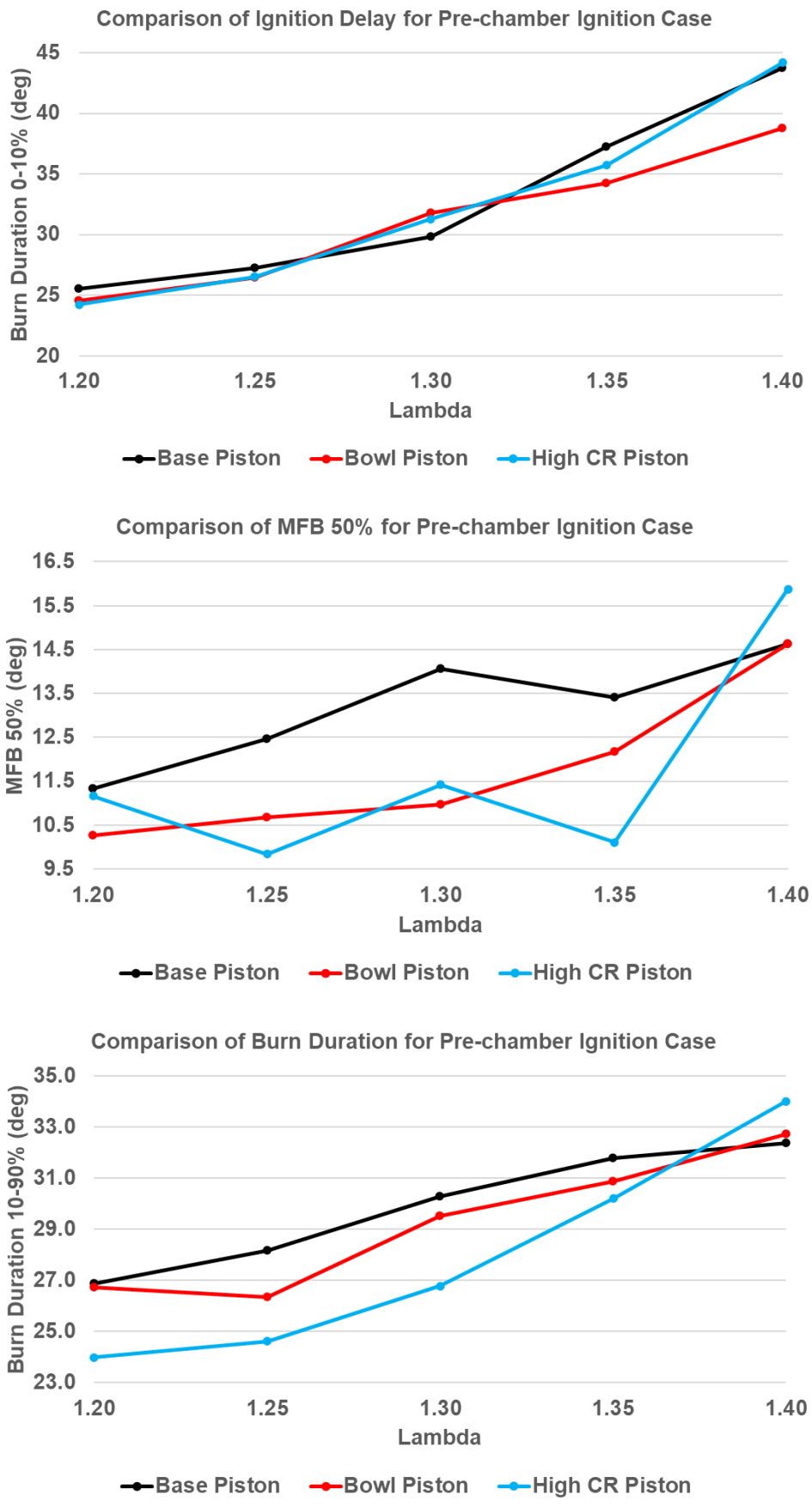

Figure 8-10 Comparison of Cycle Averaged Ignition Delay, 50% Burn Point and Burn Duration for Base, Bowl and High CR Pistons at Various Relative Air/Fuel Ratios

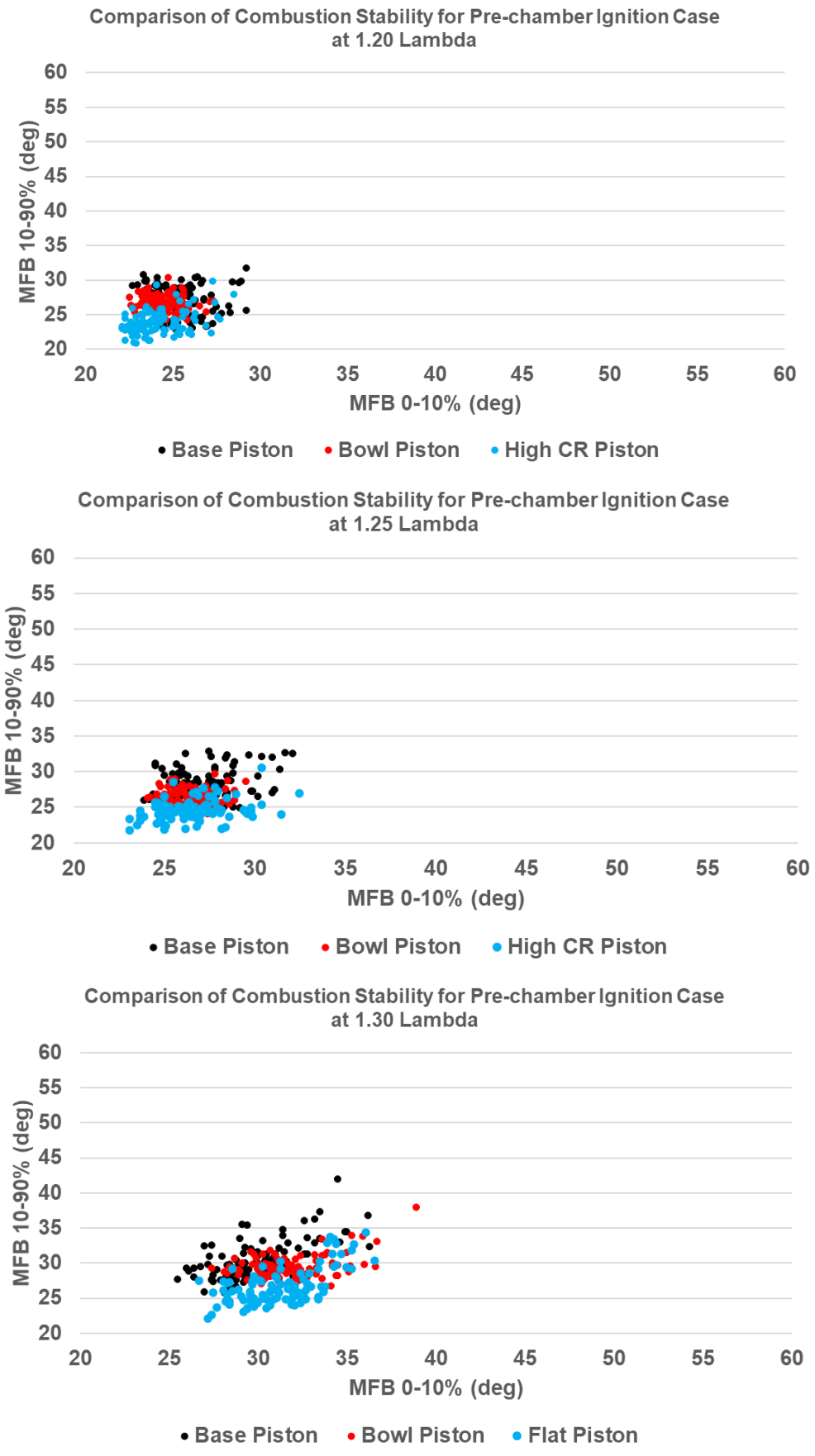

Figure 8-11 Comparison of Combustion Stability for Base, Bowl and High CR Pistons at Various Relative Air/Fuel Ratios

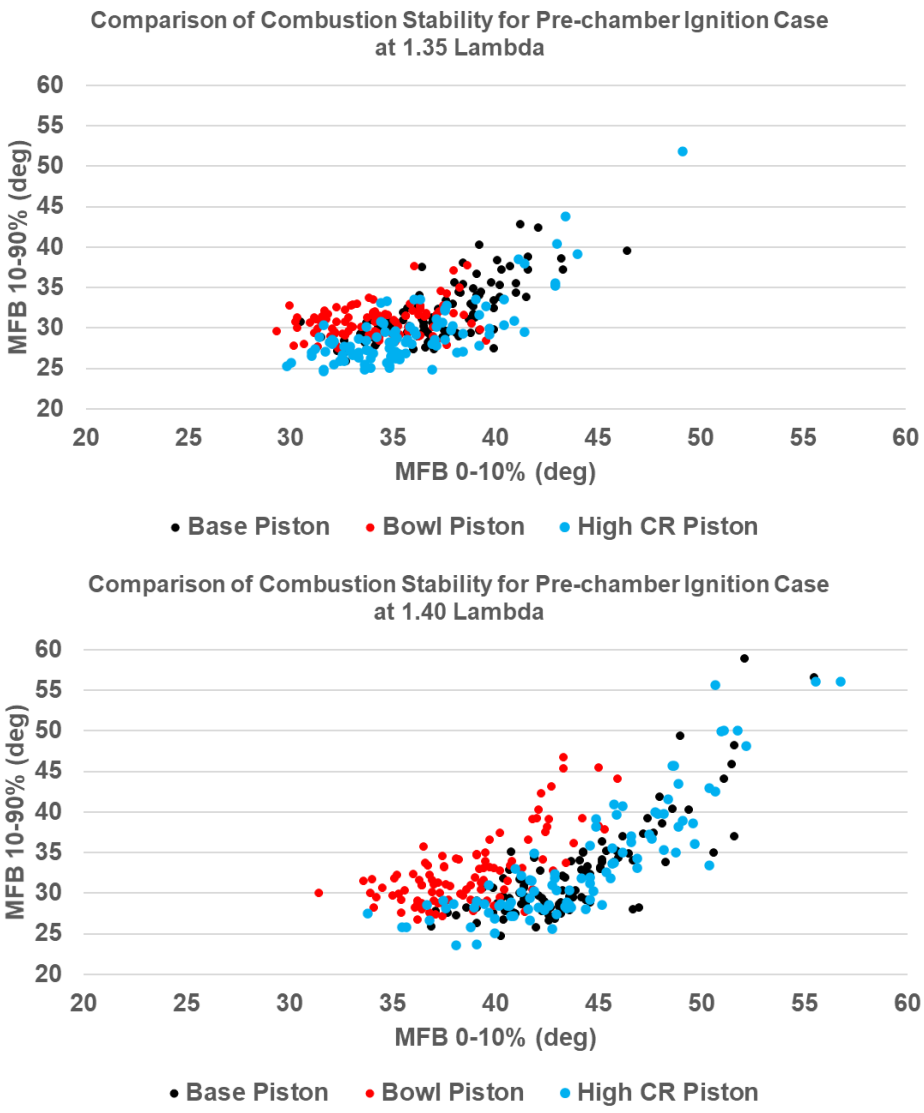

Figure 8-11 Comparison of Combustion Stability for Base, Bowl and High CR Pistons at Various Relative Air/Fuel Ratios (continued)

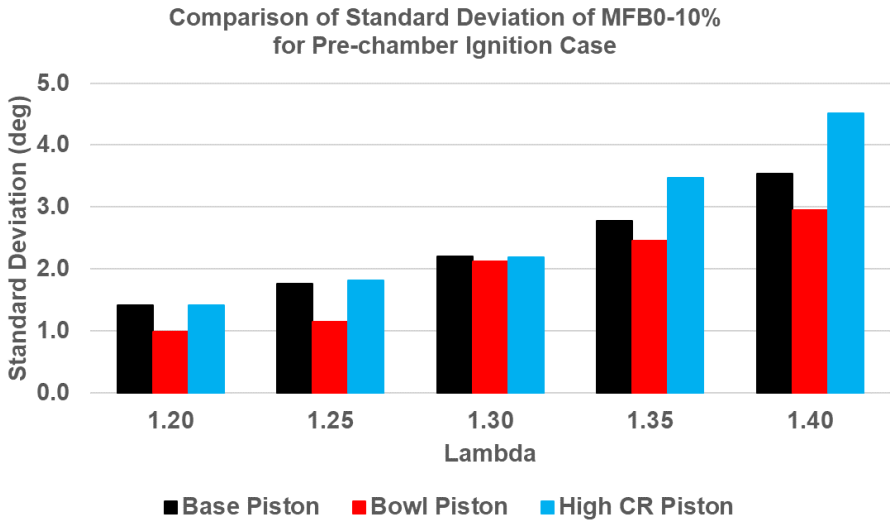

Figure 8-12 Comparison of Standard Deviation of MFB 0-10% for Base, Bowl and High CR Pistons at Various Relative Air/Fuel Ratios

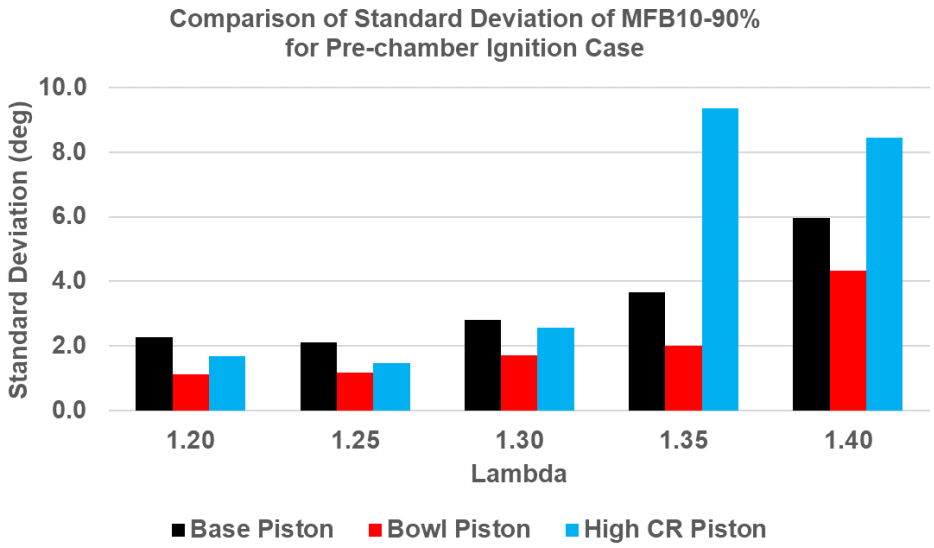

Figure 8-13 Comparison of Standard Deviation of MFB10-90% for Base, Bowl and High CR Pistons at Various Relative Air/Fuel Ratios

Table 8-1 and Figure 8-14 show that the high CR piston exhibited a lower number of high maximum pressure oscillation cycles compared to the bowl piston across all relative air/fuel ratios. A few knocking cycles were observed in the case of high CR piston at relative air/fuel ratio of 1.35 which can be observed via the outliers in the MAPO plot – the consequence of which resulted in a higher average MAPO compared to the base and bowl piston at this operating point.

Lambda	Base Piston MAPO (bar)	Bowl Piston MAPO (bar)	High CR Piston MAPO (bar)
1.20	9.90	15.57	12.55
1.25	9.78	12.15	8.98
1.30	6.25	7.81	7.03
1.35	4.75	6.09	6.84
1.40	4.39	4.69	3.69

Table 8-1 Comparison of Average MAPO for Base, Bowl and High CR Pistons at Various Relative Air/Fuel Ratios

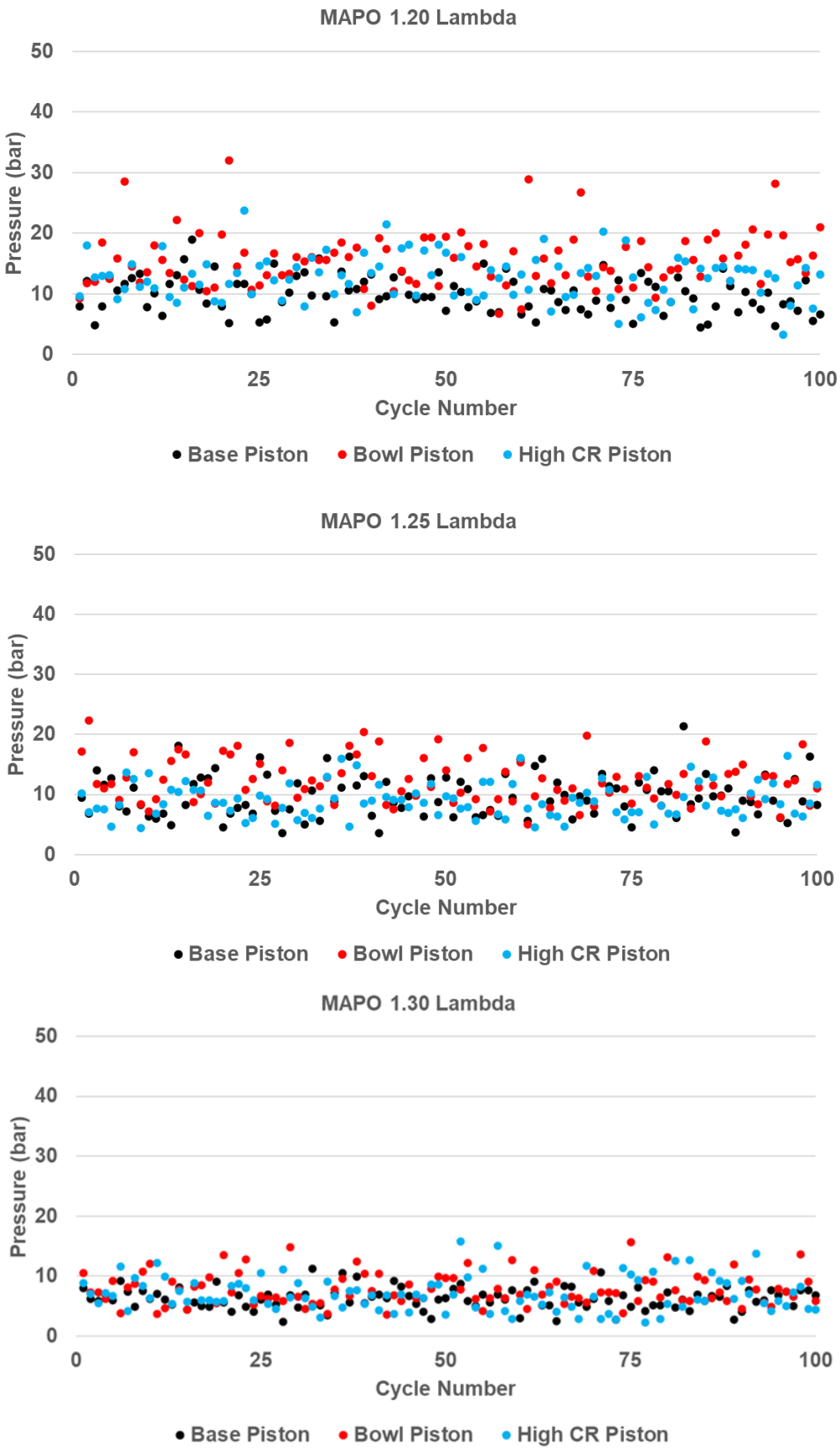

Figure 8-14 Comparison of Maximum Amplitude of Pressure Oscillations for Base, Bowl and High CR Pistons at Various Relative Air/Fuel Ratios

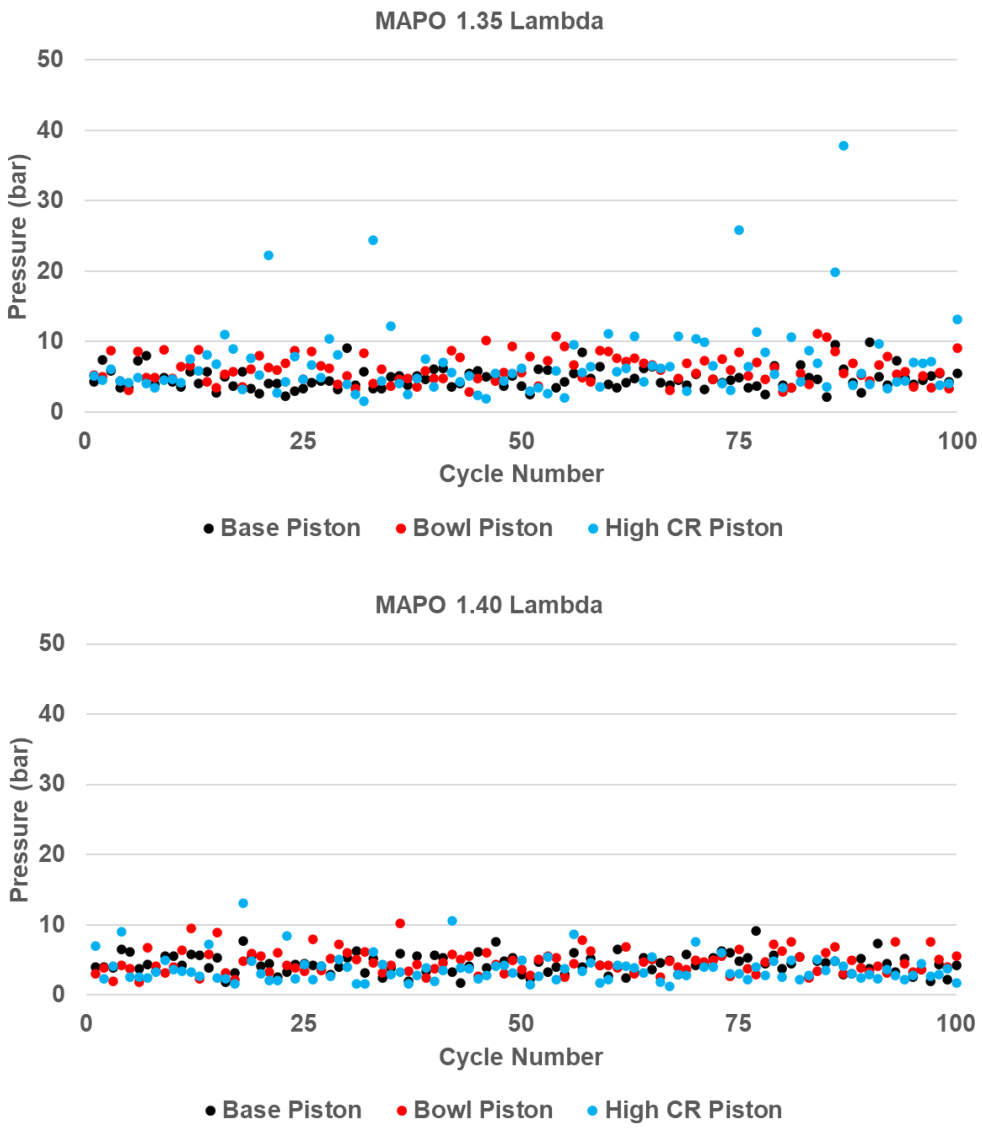

Figure 8-14 Comparison of Maximum Amplitude of Pressure Oscillations for Base, Bowl and High CR Pistons at Various Relative Air/Fuel Ratios (continued)

8.2 Study of Base Piston and High Compression Ratio Piston Engine Test Results via Simulation

1D CFD and 3D CFD simulation was utilised to gain understanding of the causes of experimental results observed to understand the influence of compression ratio on engine performance. A 1D GT power model with a SI Wiebe combustion model was utilised for this study which was correlated against base piston and high CR piston test data. The combustion model was tuned to match the test in-cylinder pressure data for the low and high back-pressure cases.

Figure 15 shows the correlation of the 1D simulated main chamber in-cylinder pressure data to the engine test data for the base piston. Figure 16 shows the correlation of the 1D simulated in-cylinder pressure data to the engine test data for the high CR piston. The pre-chamber SI Wiebe combustion model was not altered for all relative air/fuel ratios as only the residual concentration at spark timing, a function of pre-chamber breathing, was of interest and this would not be affected by combustion inside the pre-chamber as all contents in the cylinder are assumed to be completely burned at exhaust valve opening time.

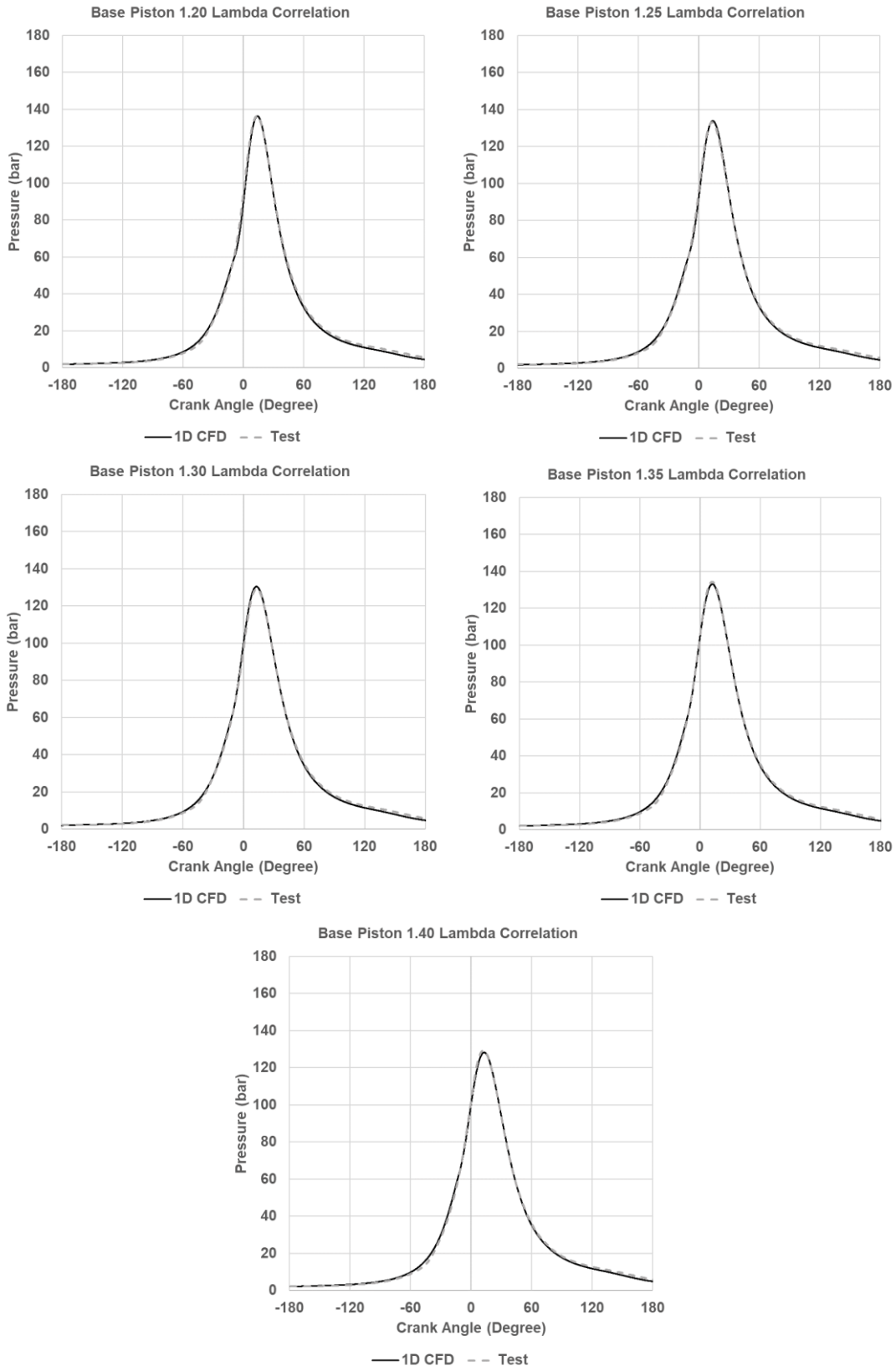

Figure 8-15 Correlation of 1D CFD Main Chamber Pressure with Test Data for Base Piston Case at Various Relative Air/Fuel Ratios

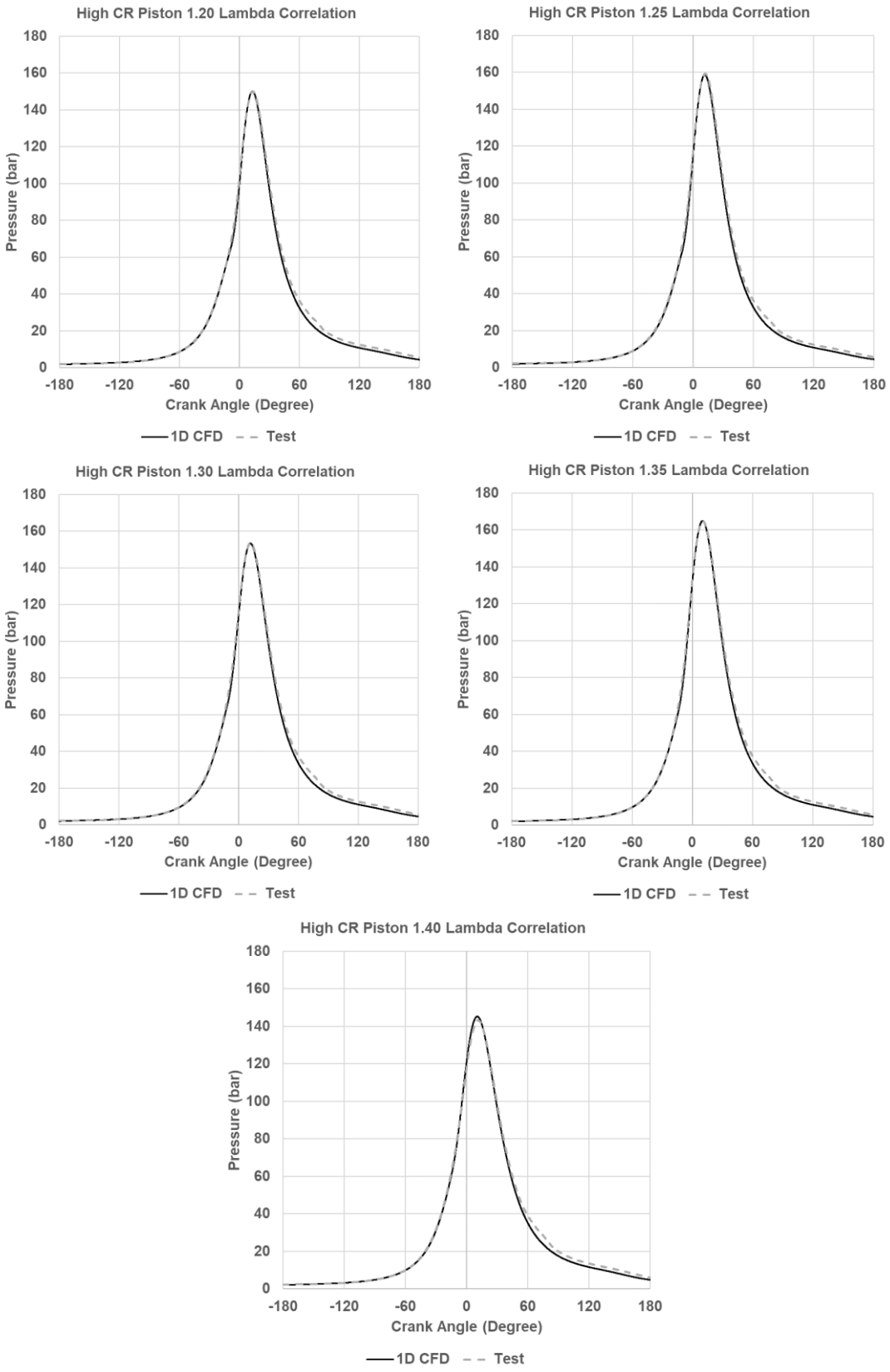

Figure 8-16 Correlation of 1D CFD Main Chamber Pressure with Test Data for High CR Piston Case at Various Relative Air/Fuel Ratios

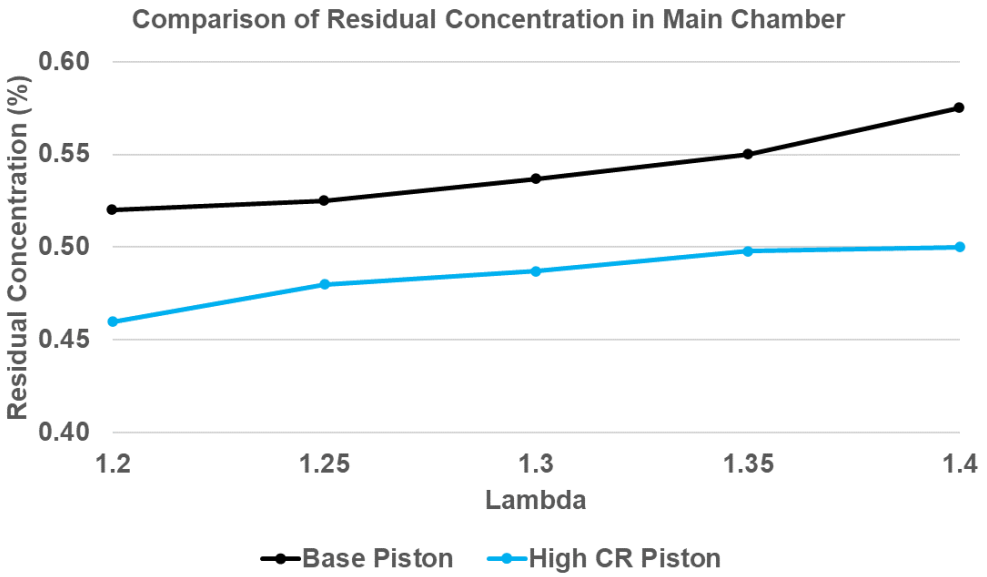

Figure 8-17 Comparison of Simulated Residual Concentration in Main Chamber for Base and High CR Piston at Various Air/Fuel Ratios

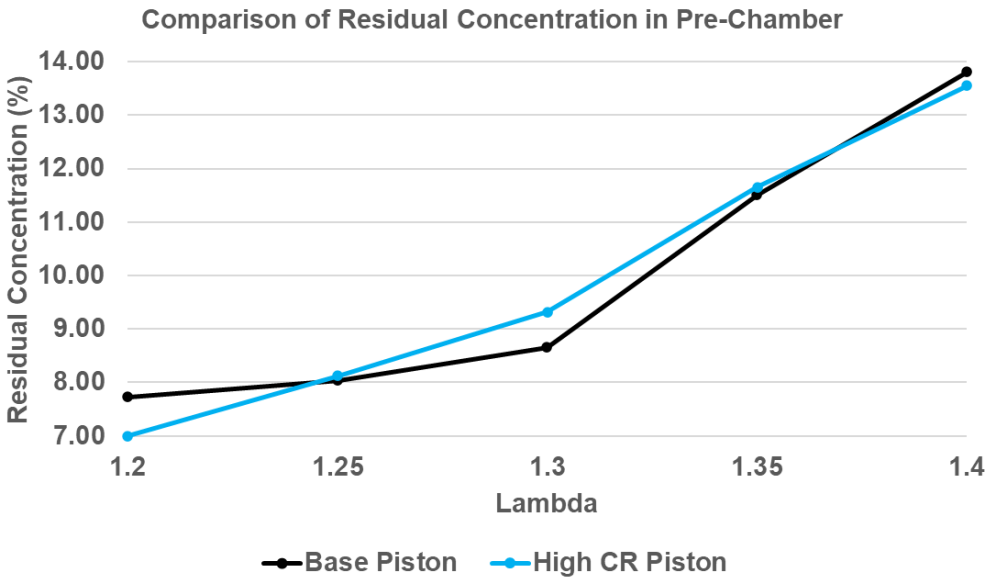

Figure 8-18 Comparison of Simulated Residual Concentration in Main Chamber for Base and High CR Piston at Various Air/Fuel Ratios at Ignition Timing

Figure 8-17 and 8-18 show the comparison of simulated residual concentration in main chamber and pre-chamber at combustion start, respectively, for base and high CR piston where it was observed that the high CR piston demonstrated a lower residual concentration in the main-chamber. A lower residual concentration in the pre-chamber was also observed for the high CR piston case when same instants were compared for the base and high CR

piston however, due to advanced ignition timings at relative air/fuel ratios of 1.25, 1.30 and 1.35, this led to the combustion starting at unfavourable times for the high CR piston case where the thermochemical conditions were found to be poor- led to higher residuals at combustion start at certain air/fuel ratios for the high CR piston case as demonstrated in Figure 8-18.

Figure 8-19 and 8-20 compare the simulated tumble ratio and turbulence in the main chamber for base and bowl piston where it was observed that the tumble and turbulence generated by the high CR piston were lower than that of the base piston due to the flat piston surface which was unable to sustain the tumble in the combustion chamber thus resulting in a lower breakdown of tumble ratio at TDC leading to lower turbulence generation.

The tumble ratio for the high CR piston was reduced by 8.89% and 23.72% during tumble generation phase and sustenance phase, respectively, when compared with the base piston. The turbulence generation by the high CR piston was reduced by 12.69% at combustion start when compared with the base piston case.

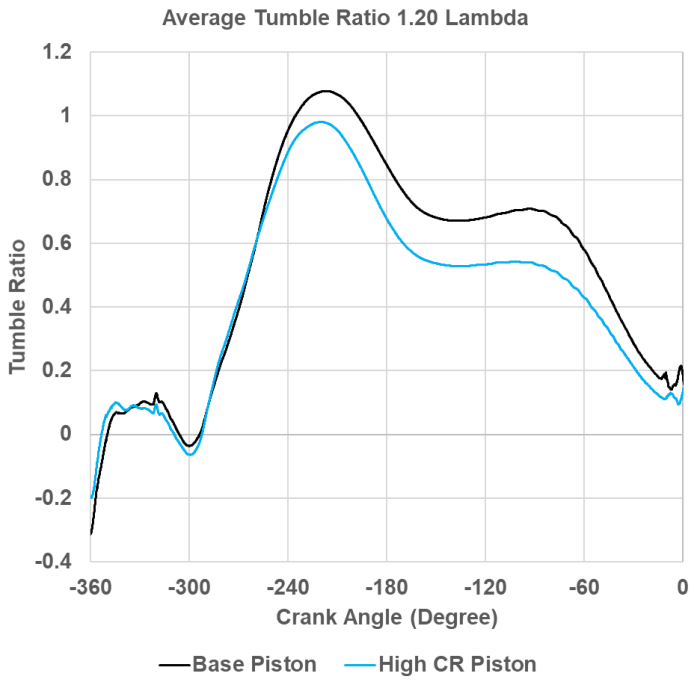

Figure 8-19 Comparison of Simulated Tumble Ratio for Base and High CR Piston

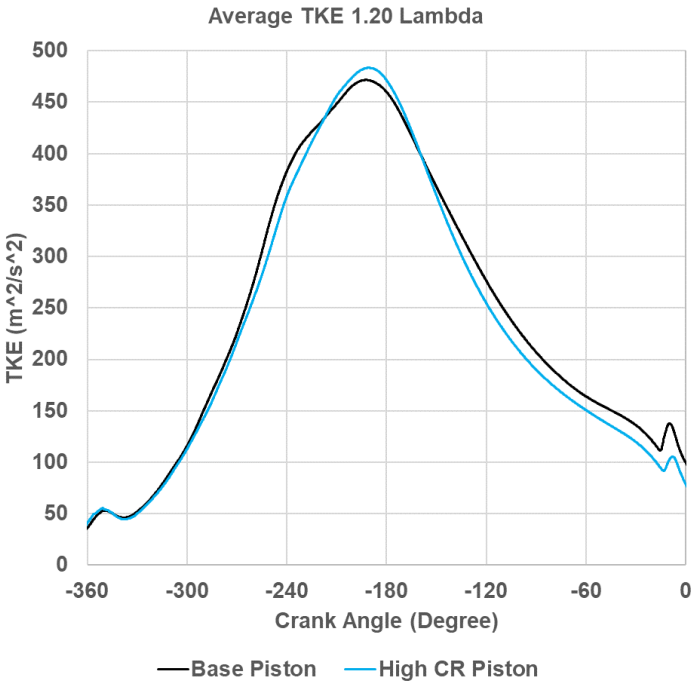

Figure 8-20 Comparison of Simulated Turbulent Kinetic Energy for Base and High CR Piston

8.3 Discussion of Results

Engine test results showed a 9.20 g/kWh and 3.51 g/kWh reduction in gross ISFC on average for the case of high CR piston when compared with the low CR base piston and bowl piston cases as shown in Figure 8-2. The improvement in ISFC for the high CR case shows that the indicated fuel energy conversion efficiency was improved compared to the low CR cases which was also evident due to the reduction in exhaust gas temperatures for the high CR case as shown in Figure 8-5. The improvement in efficiency can be attributed to the increase in temperature, as shown in Figure 8-21, of the charge at ignition time due to a higher compression which has the ability to improve laminar flame speeds and the improvement in ISFC can also be attributed to the reduced mass fraction of the residual gases compared to the low compression ratio case as increasing the compression ratio results in reduction of the residual mass concentration in the main chamber (Heywood, 1998). The higher flame speeds resulted in a lower ignition delay and burn duration of the flame in majority of the relative air/fuel ratio points tested on the engine as observed in Figure 8-10.

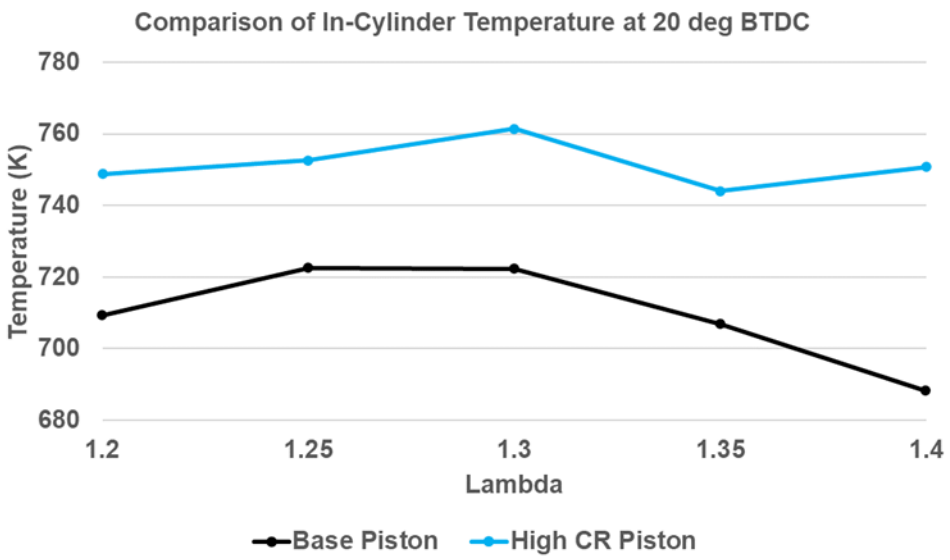

Figure 8-21 Comparison of In-cylinder Temperature at 20 deg BTDC

The magnitude of reduction in ISFC for the high CR piston case compared to the base and bowl piston cases shows the importance of in-cylinder aerodynamics and pre-chamber enrichment. Although the high CR attained a higher thermal efficiency compared to the base and bowl piston, the COV of gross IMEP plot as shown in Figure 8-3 shows that the lean limit was compromised due to poor in-cylinder aerodynamics and poor pre-chamber enrichment. The flat piston crown shape of the high CR piston led to reduction in tumble and turbulence as found in 3D CFD study of the high CR flat piston, as shown in Figure 8-19 and 8-20, which has the ability to significantly affect mixture preparation and pre-chamber enrichment.

Thus the increased COV of gross IMEP and longer ignition delay especially at leaner relative air/fuel ratios of 1.35 and 1.40 was attributed to low turbulence due to low tumble and lower pre-chamber enrichment which led to reduction in flame speeds in the main-chamber due to lower turbulence levels and lower ignition energy available at jet ejection time due to poor pre-chamber enrichment. The low turbulence level in the main chamber also lead to an

increase in the number of lower than average pressure cycles, shown in Figure 8-6, across all relative air/fuel ratio. This led to a reduction in combustion stability which was observed in the comparison of standard deviation of ignition delay and MFB 10-90% burn duration where it was observed that the high CR piston case had a higher standard deviation for both ignition delay and MFB 10-90% burn duration across all relative air/fuel ratios when compared with the bowl piston case as observed in Figure 8-11 and 8-12. However, when the high CR piston was compared with the base piston case- a lower burn duration was observed for the same ignition delay, from relative air/fuel ratio of 1.20, 1.25 and 1.30, which can be attributed to the higher flame speeds for the high CR case.

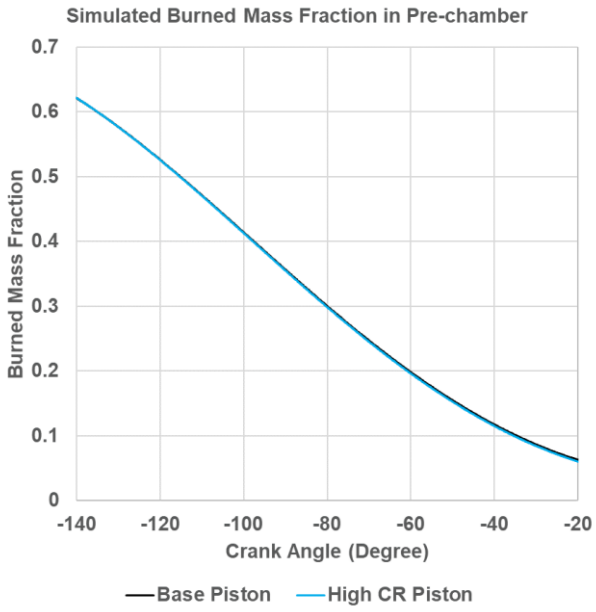

Figure 8-22 Simulated Instantaneous Residual Mass Fraction in the Pre-chamber for Base and High CR Piston at Relative Air/Fuel Ratio of 1.20

The higher CR case also demonstrated a lower residual concentration in the main chamber as observed in the 1D simulation results as shown in Figure 8-17. However, due to an advanced ignition timing for the high CR case compared to the low CR base piston case at relative air/fuel ratios 1.25, 1.30,

1.35 – the residual concentration in the pre-chamber was found to be higher in the high CR case due to advanced ignition timings leading to worsening thermochemical conditions at combustion start which further contributes to longer ignition delay of the main chamber leading to higher variation in various parameters such as burn duration and gross IMEP. Figure 8-22 shows the instantaneous residual concentration in the pre-chamber for base and high CR piston cases where an increase in the residual concentration was observed from TDC to inlet valve closing time thus resulting in unfavourable conditions in the pre-chamber for an advanced ignition timing.

Figure 8-23 shows the comparison between the high pass filtered pressure oscillations in the main chamber for the base piston, bowl piston and high CR piston at various relative air/fuel ratios. It was observed that the amplitude of pressure oscillations for the high CR piston case had a lower amplitude than the bowl piston case. As the pre-chamber jet velocity is a function of enrichment of the pre-chamber which affects the amplitude of pressure oscillations in the main-chamber originating from the pre-chamber jets, as discussed in the previous chapters, this phenomenon was observed in the comparison between the maximum amplitude of high pass filtered pressure oscillations for the bowl and high CR piston where the high CR piston exhibited lower amplitude pressure oscillations which shows that the pre-chamber in the high CR piston was less enriched than the bowl piston.

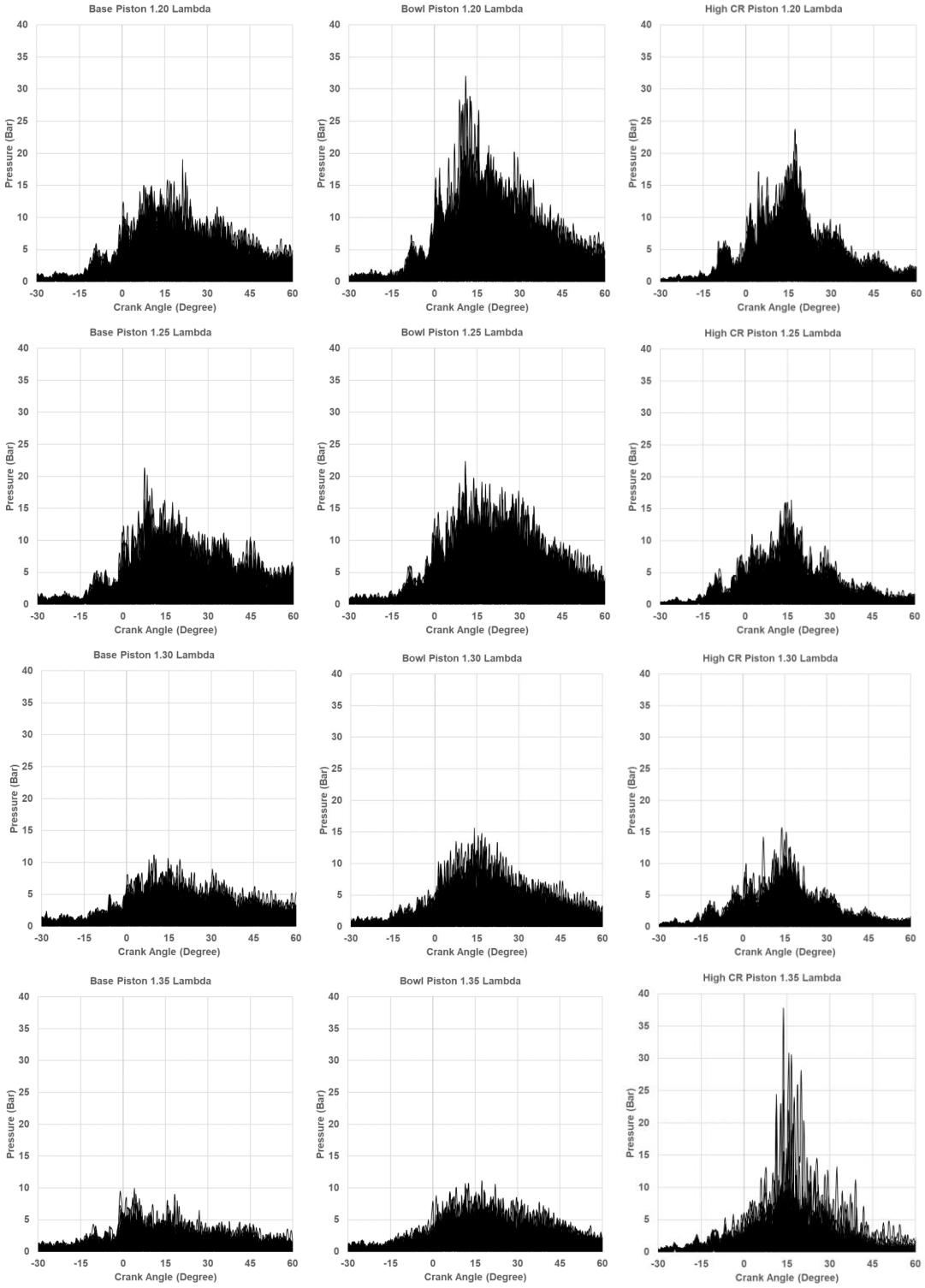

Figure 8-23 Comparison of 100 Overlaid High Pass Filtered Raw Absolute Pressure Signals for Base, Bowl and High CR Pistons at Various Relative Air/Fuel Ratios

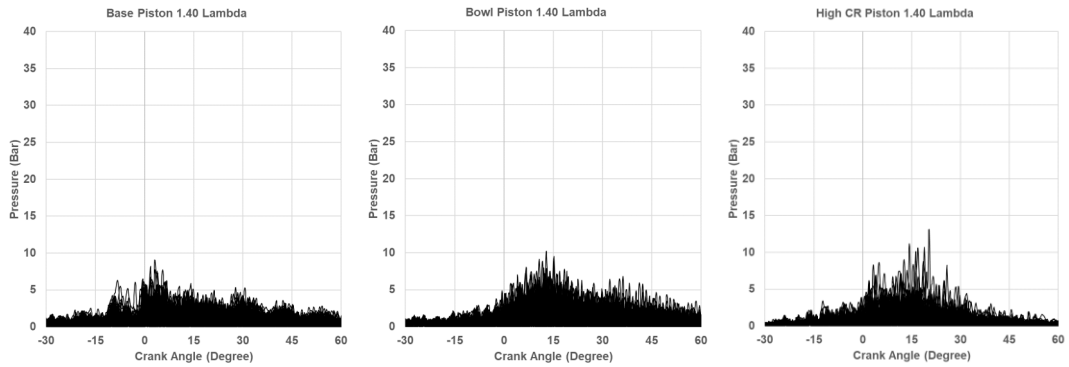

Figure 8-23 Comparison of 100 Overlaid High Pass Filtered Raw Absolute Pressure Signals for Base, Bowl and High CR Pistons at Various Relative Air/Fuel Ratios (continued)

Comparison of average MAPO shown in Figure 8-24 shows that the average value of MAPO for the high CR piston case was lower than that of the bowl piston except for the relative air/fuel of ratio 1.35 where a few knocking cycles were observed which resulted in the average MAPO value of high CR piston at relative air/fuel ratio of 1.35 being higher than the bowl piston average MAPO value.

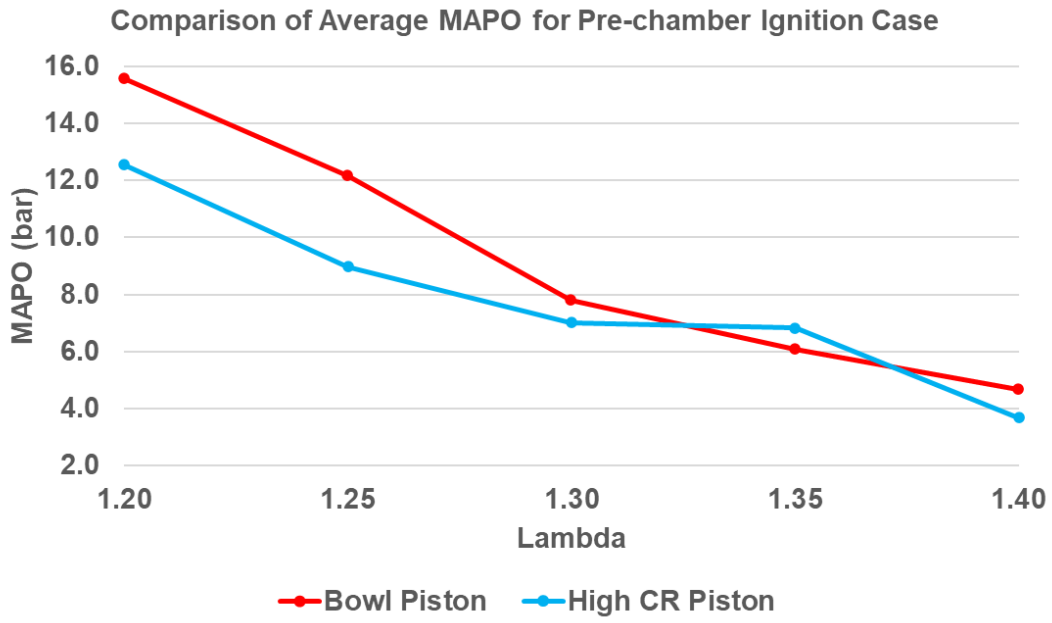

Figure 8-24 Comparison of Average MAPO for Bowl and High CR Piston

Knocking due to end-gas auto-ignition was observed in 5 cycles at relative air/fuel ratio of 1.35 – where the knocking combustion was believed to have been caused due to the end gas residing at a higher temperature due to higher compression and also due to a very high cyclic variation at the particular operating point where the faster than average burning cycles resulted in inducing end-gas auto-ignition. To compare the knock pressure cycles, non-knocking cycles were compared with knocking cycles. Figure 8-25 shows the absolute high pass filtered pressure signal for a non-knocking cycle and Figure 8-26 shows the absolute high pass filtered pressure cycle for knocking cycle number 21, 33, 75, 86 and 87. The first spike in the pressure signal denotes the knock initiation time where it was observed that the 5 knocking cycles had a knock initiation time between 11.2 deg CA and 17.2 deg CA. Table 8-2 shows the knock initiation time for the knocking cycles.

Cycle Number	Knock Initiation Time (deg CA)
21	11.2
33	11.3
75	12.9
86	17.2
87	13.8

Table 8-2 Knock Initiation Time for Knocking Cycles

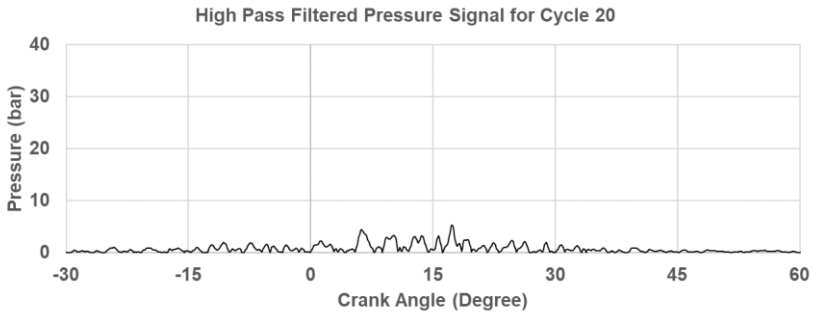

Figure 8-25 High Pass Filtered Pressure Signal for a Non-Knocking Cycle for High CR Piston

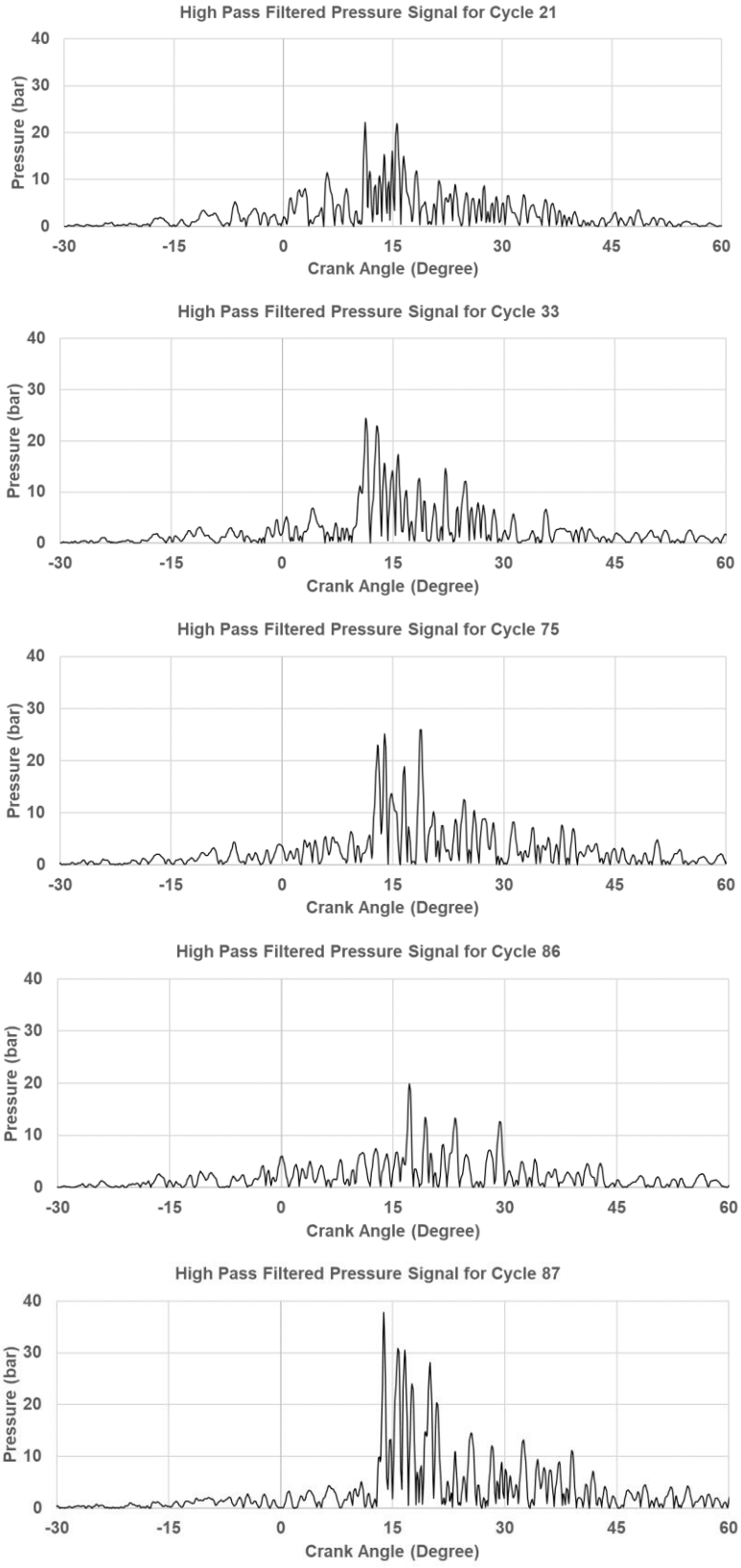

Figure 8-26 High Pass Filtered Pressure Signal for Knocking Cycles for High CR Piston

The 1D correlated pressure plots of the low CR and high CR case was utilised to study the unburned gas temperature at 1.35 relative air/fuel ratio. Figure 8-27 shows the comparison of instantaneous unburned gas temperature where it was found that the high CR case had a higher unburned gas temperature compared to the low CR base piston case between 20 deg BTDC and 30 deg ATDC. Thus, the higher temperature and pressure due to increased compression ratio provides favourable conditions for the end gas to auto-ignite which resulted in the 5 knocking cycles for high CR piston case.

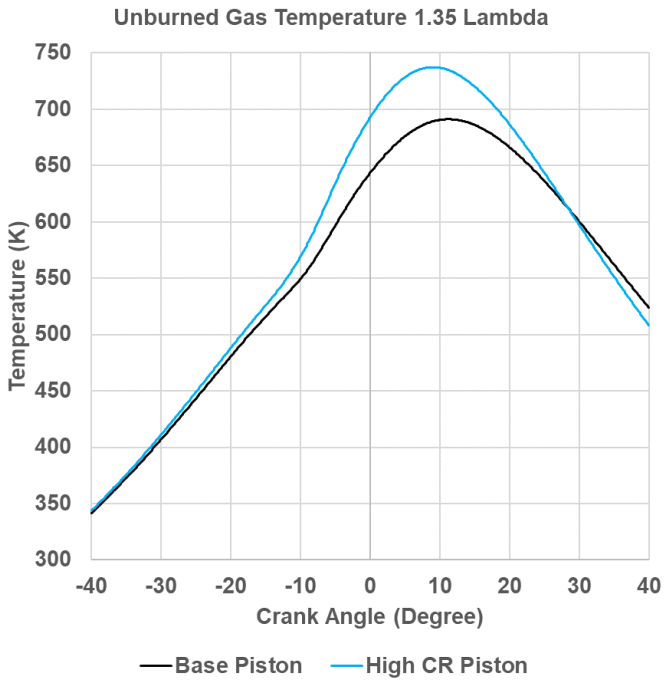

Figure 8-27 Comparison of Instantaneous Unburned Gas Temperature for Base and High CR Piston

9. Summary and Conclusions

A series of studies were conducted to evaluate the impact of in-cylinder conditions on a turbocharged gasoline pre-chamber ignited engine, as a means to improve the engine's full load thermal efficiency.

9.1 In-cylinder Flow Conditions

The influence of port generated tumble and piston crown shape were studied on both spark and pre-chamber ignited engines to evaluate the impact of alteration of in-cylinder flow conditions. The key conclusions that were drawn from the studies are summarised below.

- Higher tumble ratio and the resulting higher turbulence resulted in a lower cyclic variation of gross IMEP and faster combustion for a pre-chamber ignited engine. A lower gross ISFC was thus achieved with the high tumble case. A better combustion stability with a lower cyclic variation of gross IMEP was observed for the high tumble case due to reduction of the number of slow cycles owing to faster combustion compared to the low tumble case thus proving that in-cylinder flow has a significant influence on combustion in the main chamber of a pre-chamber ignited engine.
- An optimised piston crown geometry to aid combustion in a pre-chamber ignited engine was developed which had shown that a smaller diameter bowl with increased depth resulted in enriching the pre-chamber that resulted in higher jet velocities and penetration which led to a reduction in ignition delay, reduced number of slow burning cycles

thus reducing cyclic variation of gross IMEP. The lean limit was thus extended via faster combustion due to high turbulence generated at TDC- all of which resulted in a lower gross ISFC when compared with the base piston crown geometry. It was also concluded that the combustion chamber geometry and ports for a pre-chamber ignited engine could be designed to have a very high tumble ratio at leaner relative air/fuel ratios without the risk of flame kernel blowoff which would result in misfires and high cyclic variation as in the case with spark ignited engines.

- The revised piston crown geometry (bowl piston) led to an increase of the best indicated thermal efficiency by 1.47 percentage points compared to the base piston crown geometry. The engine fitted with the base piston crown geometry resulted in a best indicated thermal efficiency of 48.73% compared to 50.20% obtained with the engine utilising the revised piston crown geometry (bowl piston).

9.2 Effect of Exhaust Back-pressure

The effect of back pressure was studied on spark and pre-chamber ignition systems to evaluate the effect of exhaust back pressure on combustion. Studies concluded that the main chamber residual concentration increased at ignition timing for both spark and pre-chamber ignited engine at high back-pressure which resulted in the increase of ISFC due to poor combustion stability as a result of longer ignition delay and slow burn rate. A higher back-pressure resulted in nearly double the residual concentration in the pre-chamber when compared against the low back-pressure case. The higher

residual concentration in the pre-chamber led to slower burn rate in the pre-chamber which resulted in lower pressure generated inside the pre-chamber thus leading to reduction of the jet velocities and jet penetration which led to a high variation of ignition delay in the main chamber – negatively affecting performance.

9.3 Effect of Compression Ratio

The effect of compression ratio was studied on the pre-chamber ignited engine by altering the piston crown geometry. The high compression ratio flat piston crown shape which had a compression ratio of 14.7 was studied against two piston crown shape designs which had a compression ratio of 13.8 each.

- Results concluded that the indicated thermal efficiency of the engine improved by 0.62 percentage points with the higher compression ratio engine having a best indicated thermal efficiency of 50.82% compared to the lower compression ratio engine which had a best indicated thermal efficiency of 50.20%.
- The flat piston crown shape led to poor pre-chamber enrichment at leaner relative air/fuel ratios leading to a higher variation in ignition delay. A reduced tumble and turbulence in the main-chamber due to the flat piston crown shape led to an increased cyclic variation of gross IMEP thus emphasising the need for a combustion chamber redesign to support a pre-chamber ignition system.

9.4 Original Contribution to Knowledge

The research work presented in this thesis has shown that a higher tumble ratio in the main-chamber aided in improving the main-chamber combustion processes for a pre-chamber jet ignited engine. The higher tumble ratio resulted in the reduction of cyclic variation and reduction in ISFC which fills a significant gap in literature regarding the influence of in-cylinder flow in a passive pre-chamber ignited engine.

The research work presented also fills the void in literature regarding the influence of residual concentration and compression ratio on a passive pre-chamber ignited lean burn engine where little to no research can be found in literature.

9.5 Suggestions for Future Work

Based on the conclusions of various studies presented in this thesis, the following suggestions were made for future work.

- A parametric study on the intake and exhaust valve overlap period is required to reduce the residual concentration in the pre-chamber which has the potential to further improve performance.
- A higher compression ratio resulted in improving the indicated thermal efficiency of the pre-chamber ignited engine however a high cyclic variation and lower combustion stability was observed which was found to be due to lower pre-chamber enrichment and low tumble and turbulence generated by the flat piston. A high compression ratio pent-roof piston crown shape with a bowl is proposed to reduce the cyclic variation and improve combustion stability which has the potential to further improve thermal efficiency of the engine.
- A study on the interaction of shockwaves generated by the pre-chamber jets and main chamber turbulent eddies is proposed as it is currently unknown on how the amplitude of shockwaves are affected by the main chamber turbulence levels and vice versa as literature published by Chen and Donzis (2019) and Rotman (1991) suggests that the shockwaves result in increasing the turbulent kinetic energy when passing through a medium and the shockwaves get distorted when passing through a medium having a high turbulent kinetic energy.

10. References

1. AER Ltd (2016) Project 60B. Available from: https://www.aerltd.com/our-engines/project-60b/ [Accessed May 19, 2020].

2. Anderson, E. K., Attard, W. P., Brown, A., Litke, P., Grinstead, K. and Hoke, J. (2013) Experimental Study of a Pre-Chamber Jet Igniter in a Turbocharged Rotax 914 Aircraft Engine. Warrendale, PA: SAE International.

3. Asad, U., Kumar, R., Han, X. and Zheng, M. (2011) Precise instrumentation of a diesel single-cylinder research engine, Measurement, 44 (7), pp. 1261-1278. DOI: 10.1016/j.measurement.2011.03.028.

4. Attard, W. P., Bassett, M., Parsons, P. and Blaxill, H. (2011) A New Combustion System Achieving High Drive Cycle Fuel Economy Improvements in a Modern Vehicle Powertrain. Warrendale, PA: SAE International.

5. Attard, W. P. and Blaxill, H. (2012a) A gasoline fueled pre-chamber jet ignition combustion system at unthrottled conditions, SAE International Journal of Engines, 5 (2), pp. 315-329. DOI: 10.4271/2012-01-0386.

6. Attard, W. P. and Blaxill, H. (2012b) A Lean Burn Gasoline Fueled Pre-Chamber Jet Ignition Combustion System Achieving High Efficiency and Low NOx at Part Load. Warrendale, PA: SAE International.

7. Attard, W. P. and Blaxill, H. (2011) A single fuel pre-chamber jet ignition powertrain achieving high load, high efficiency and near zero NOx emissions, SAE International Journal of Engines, 5 (3), pp. 734-746. DOI: 10.4271/2011-01-2023.

8. Attard, W. P., Blaxill, H., Anderson, E. K. and Litke, P. (2012) Knock limit extension with a gasoline fueled pre-chamber jet igniter in a modern vehicle powertrain, SAE International Journal of Engines, 5 (3), pp. 1201-1215. DOI: 10.4271/2012-01-1143.

9. Attard, W. P., Fraser, N., Parsons, P. and Toulson, E. (2010) A turbulent jet ignition pre-chamber combustion system for large fuel economy improvements in a modern vehicle powertrain, SAE International Journal of Engines, 3 (2), pp. 20-37. DOI: 10.4271/2010-01-1457.

10. Attard, W. P., Kohn, J. and Parsons, P. (2010) Ignition energy development for a spark initiated combustion system capable of high load, high efficiency and near zero NOx emissions, SAE International Journal of Engines, 3 (2), pp. 481-496. DOI: 10.4271/2010-32-0088.

11. Attard, W. P. and Parsons, P. (2010a) Flame kernel development for a spark initiated pre-chamber combustion system capable of high load, high efficiency and near zero NOx emissions, SAE International Journal of Engines, 3 (2), pp. 408-427. DOI: 10.4271/2010-01-2260.

12. Attard, W. P. and Parsons, P. (2010b) A normally aspirated spark initiated combustion system capable of high load, high efficiency and near zero NOx emissions in a modern vehicle powertrain, SAE International Journal of Engines, 3 (2), pp. 269-287. DOI: 10.4271/2010-01-2196.

13. Attard, W. P., Toulson, E., Huisjen, A., Chen, X., Zhu, G. and Schock, H. (2012) Spark Ignition and Pre-Chamber Turbulent Jet Ignition Combustion Visualization. Warrendale, PA: SAE International.

14. AVL List GmbH (2020) AVL CONCERTO 5 User Manual.

15. Ayala, F. A. (2006) Combustion lean limits fundamentals and their application to a SI hydrogen-enhanced engine concept. ProQuest Dissertations Publishing. Available from: https://search.proquest.com/docview/304947676 [Accessed Jul 1, 2018].

16. Benajes, J., Novella, R., Gomez-Soriano, J., Martinez-Hernandiz, P. J., Libert, C. and Dabiri, M. (2019) Evaluation of the passive pre-chamber ignition concept for future high compression ratio turbocharged spark-ignition engines, Applied Energy, 248 , pp. 576-588. DOI: 10.1016/j.apenergy.2019.04.131.

17. Biswas, S. (2017a) Mechanisms of Pre-Chamber Hot Turbulent Jet Ignition of Ultra-Lean Mixtures. United States - Indiana. Available from: https://search.proquest.com/docview/1958941884/abstract/D6C8D8FF179E4238PQ/1 [Accessed Apr 2, 2020].

18. Biswas, S. (2017b) Mechanisms of Pre-Chamber Hot Turbulent Jet Ignition of Ultra-Lean Mixtures. ProQuest Dissertations Publishing.

19. Biswas, S. (2018) Physics of Turbulent Jet Ignition. 1st ed. 2018 ed. CH: Springer.

20. Biswas, S. and Qiao, L. (2016) Prechamber hot jet ignition of ultra-lean H2/air mixtures: Effect of supersonic jets and combustion instability, SAE International Journal of Engines, 9 (3), pp. 1584-1592. DOI: 10.4271/2016-01-0795.

21. Bunce, M. and Blaxill, H. (2014) Methodology for Combustion Analysis of a Spark Ignition Engine Incorporating a Pre-Chamber Combustor. Warrendale, PA: SAE International.

22. Bunce, M. and Blaxill, H. (2016) Sub-200 g/kWh BSFC on a Light Duty Gasoline Engine. Warrendale, PA: SAE International.

23. Bunce, M., Blaxill, H., Kulatilaka, W. and Jiang, N. (2014) The Effects of Turbulent Jet Characteristics on Engine Performance Using a Pre-Chamber Combustor. Warrendale, PA: SAE International.

24. Chen, C. H. and Donzis, D. A. (2019) Shock–turbulence interactions at high turbulence intensities, Journal of Fluid Mechanics, 870, pp. 813-847. DOI: 10.1017/jfm.2019.248.

25. Chinnathambi, P., Bunce, M. and Cruff, L. (2015) RANS Based Multidimensional Modeling of an Ultra-Lean Burn Pre-Chamber

Combustion System with Auxiliary Liquid Gasoline Injection. Warrendale, PA: SAE International.

26. Chinnathambi, P. and Bunce, M. (December 1, 2015) The Effects of Pre-Chamber-Initiated Lean-Burn Combustion on Engine Efficiency and Emissions, in: IMechE,Royal College of Physicians, London, December 2015London: IMechE.

27. Convergent Science (2017) Converge Manual. Convergent Science.

28. Cooper, A., Harrington, A., Bassett, M., Reader, S. and Bunce, M. (2020) Application of the Passive MAHLE Jet Ignition System and Synergies with Miller Cycle and Exhaust Gas Recirculation.

29. CORPORATION, T. M. (2018) CAR DETAILS | WEC | WEC. Available from: http://toyotagazooracing.com/wec/cars/2018-2019/index.html [Accessed May 19, 2020].

30. Couet, S., Higelin, P. and Moreau, B. (2001) APIR: A New Firing Concept for the Internal Combustion Engines - sensitivity to knock and in-cylinder aerodynamics. Warrendale, PA: SAE International.

31. Davis, G. C., Krieger, R. B. and Tabaczynski, R. J. (1974) Analysis of the Flow and Combustion Processes of a Three-Valve Stratified Charge Engine with a Small Prechamber. Warrendale, PA: SAE International.

32. EDF Energy (2019) Electric cars and the environment. Available from: https://www.edfenergy.com/for-home/energywise/electric-cars-and-environment [Accessed May 16, 2020].

33. FIA (2019) https://www.fia.com/regulation/category/110. Available from: https://www.fia.com/regulation/category/110 [Accessed May 19, 2020].

34. FIA Sport / Technical Department (2019) 2020 Technical Regulations for LMP1 Prototype Hybrid. FIA Sport / Technical Department.

35. Gamma Technologies (2019) Engine performance application manual.

36. Gentz, G., Thelen, B., Litke, P., Hoke, J. and Toulson, E. (2015) Combustion visualization, performance, and CFD modeling of a pre-chamber turbulent jet ignition system in a rapid compression machine, SAE International Journal of Engines, 8 (2), pp. 538-546. DOI: 10.4271/2015-01-0779.

37. Granet, V., Vermorel, O., Lacour, C., Enaux, B., Dugué, V. and Poinsot, T. (2012) Large-eddy simulation and experimental study of cycle-to-cycle variations of stable and unstable operating points in a spark ignition engine, Combustion and Flame, 159 (4), pp. 1562-1575. DOI: 10.1016/j.combustflame.2011.11.018.

38. Gupta, H. C. and Bracco, F. V. (1982) The origin of pressure oscillations in divided chamber engines, Combustion and Flame, 48, pp. 33-49. DOI: 10.1016/0010-2180(82)90114-6.

39. Hamori, F. (2006) Exploring the limits of hydrogen assisted jet ignition. Available from: http://minerva-access.unimelb.edu.au/handle/11343/39036 [Accessed Apr 1, 2020].

40. Harrison, M. F. and Dunkley, A. (2004) The acoustics of racing engine intake systems, Journal of Sound and Vibration, 271 (3), pp. 959-984. DOI: 10.1016/S0022-460X(03)00773-9.

41. Heisler, H. (1995) Advanced engine technology. 1. publ. ed. London: Elsevier Science & Technology.

42. Heywood, J. B. (1998) Internal combustion engine fundamentals. New York: McGraw-Hill.

43. Hua, J., Zhou, L., Gao, K. and Feng, Z. (2020) Effects on cycle-to-cycle variations and knocking combustion of turbulent jet ignition (TJI) with a small volume pre-chamber, SAE International, (2020-01-1119).

44. Joshi, A. (2020) Review of Vehicle Engine Efficiency and Emissions. SAE International.

45. Kalghatgi, G. T. and Bradley, D. (2012) Pre-ignition and 'super-knock' in turbo-charged spark-ignition engines, International Journal of Engine Research, 13 (4), pp. 399-414. DOI: 10.1177/1468087411431890.

46. Kimura, N., Kobayashi, H. and Ishikawa, N. (2018) Study of gasoline pre-chamber combustion at lean operation. DOI: 10.5445/IR/1000088589.

47. Li, Y., Zhao, H., Peng, Z. and Ladommatos, N. (2001) Analysis of Tumble and Swirl Motions in a Four-Valve SI Engine. Warrendale, PA: SAE International.

48. Liu, Y., Jia, M., Xie, M. and Pang, B. (2013) Development of a new skeletal chemical kinetic model of toluene reference fuel with application to gasoline surrogate fuels for computational fluid dynamics engine simulation, Energy & Fuels, 27 (8), pp. 4899-4909. DOI: 10.1021/ef4009955.

49. Marinov, N. M. (1999) A detailed chemical kinetic model for high temperature ethanol oxidation, International Journal of Chemical Kinetics, 31 (3), pp. 183-220. DOI: 10.1002/(SICI)1097-4601(1999)31:3<183::AID-KIN3>3.0.CO;2-X.

50. Mazda (2019) SKYACTIV-X. Available from: https://www.mazda.co.uk/why-mazda/skyactiv-x/ [Accessed May 20, 2020].

51. Mercedes, A. H. (2017) The Most Powerful F1 Mercedes Ever! « Mercedes AMG HPP. Available from: https://www.mercedes-amg-hpp.com/the-most-powerful-f1-mercedes-ever/ [Accessed May 16, 2020].

52. Norman C. Blizard and James C. Keck (1974) Experimental and theoretical investigation of turbulent burning model for internal

combustion engines, SAE Transactions, 83, pp. 846-864. Available from: https://www.jstor.org/stable/44721435.

53. Novella, R., Pastor, J., Gomez-Soriano, J., Barbery, I., Libert, C., Rampanarivo, F., Panagiotis, C. and Dabiri, M. (2020) Experimental and Numerical Analysis of Passive Pre-Chamber Ignition with EGR and Air Dilution for Future Generation Passenger Car Engines. Warrendale, PA: SAE International.

54. P. K. Senecal, E. Pomraning, K. J. Richards, T. E. Briggs, C. Y. Choi, R. M. McDavid and M. A. Patterson (2003) Multi-dimensional modeling of direct-injection diesel spray liquid length and flame lift-off length using CFD and parallel detailed chemistry, SAE Transactions, 112 , pp. 1331-1351. Available from: https://www.jstor.org/stable/44741357.

55. Pomraning, E., Richards, K. and Senecal, P. K. (2014) Modeling Turbulent Combustion Using a RANS Model, Detailed Chemistry, and Adaptive Mesh Refinement.

56. Probst, D., Wijeyakulasuriya, S., Pomraning, E., Kodavasal, J., Scarcelli, R. and Som, S. (2019) Predicting cycle-to-cycle variation with concurrent cycles in a gasoline direct injected engine with large eddy

simulations, Journal of Energy Resources Technology, 142 (4). DOI: 10.1115/ICEF2018-9722.

57. Robinet, C., Higelin, P., Moreau, B., Pajot, O. and Andrzejewski, J. (1999) A New Firing Concept for Internal Combustion Engines: “I'APIR”. Warrendale, PA: SAE International.

58. Roethlisberger, R. P. and Favrat, D. (2002a) Comparison between direct and indirect (prechamber) spark ignition in the case of a cogeneration natural gas engine, part I: Engine geometrical parameters, Applied Thermal Engineering, 22 (11), pp. 1217-1229. DOI: 10.1016/S1359-4311(02)00040-6.

59. Roethlisberger, R. P. and Favrat, D. (2002b) Comparison between direct and indirect (prechamber) spark ignition in the case of a cogeneration natural gas engine, part I: Engine geometrical parameters, Applied Thermal Engineering, 22 (11), pp. 1217-1229. DOI: 10.1016/S1359-4311(02)00040-6.

60. Rotman, D. (1991) Shock wave effects on a turbulent flow, Physics of Fluids A: Fluid Dynamics, 3 (7), pp. 1792-1806. DOI: 10.1063/1.857960.

61. S. D. Hires, R. J. Tabaczynski and J. M. Novak (1978) The prediction of ignition delay and combustion intervals for a homogeneous charge, spark ignition engine, SAE Transactions, 87, pp. 1053-1067. Available from: https://www.jstor.org/stable/44611083.

62. Sakai, Y., Kunii, K., Tsutsumi, S. and Nakagawa, Y. (1974) Combustion Characteristics of the Torch Ignited Engine. Warrendale, PA: SAE International.

63. Scarcelli, R., Richards, K., Pomraning, E., Senecal, P. K., Wallner, T. and Sevik, J. (2016) Cycle-to-Cycle Variations in Multi-Cycle Engine RANS Simulations. United States.

64. Senecal, P. K., Xin, J. and Reitz, R. D. (1996) Predictions of Residual Gas Fraction in IC Engines.

65. Serrano, D., Zaccardi, J., Müller, C., Libert, C. and Habermann, K. (2019) Ultra-lean pre-chamber gasoline engine for future hybrid powertrains, SAE International Journal of Advances and Current Practices in Mobility, 2 (2), pp. 607-622. DOI: 10.4271/2019-24-0104.

66. Soltic, P., Hilfiker, T. and Hänggi, S. (2019) Efficient light-duty engine using turbulent jet ignition of lean methane mixtures, International Journal of Engine Research, , pp. 146808741988983. DOI: 10.1177/1468087419889833.

67. Song, R., Gentz, G., Zhu, G., Toulson, E. and Schock, H. (2017) A control-oriented model of turbulent jet ignition combustion in a rapid compression machine, Proceedings of the Institution of Mechanical Engineers, Part D: Journal of Automobile Engineering, 231 (10), pp. 1315-1325. DOI: 10.1177/0954407016670303.

68. Song, R., Vedula, R. T., Zhu, G. and Schock, H. (2017) A control-oriented combustion model for a turbulent jet ignition engine using liquid fuel, International Journal of Engine Research, pp. 1468087417731698. DOI: 10.1177/1468087417731698.

69. Spicher, U. and Heidenreich, T. (2009) 2 - Stratified-charge combustion in direct injection gasoline engines, in: 2 - Stratified-charge combustion in direct injection gasoline engines, in: Advanced direct injection combustion engine technologies and development, Elsevier Ltd, pp. 20-44.

70. Stadler, A., Sauerland, H., Härtl, M. and Wachtmeister, G. (2020) The Potential of Gasoline Fueled Pre Chamber Ignition Combined with Elevated Compression Ratio.

71. Swamy, K. R., Harne, V., Gunjegaonkar, D. S. and Gopalkrishnan, K. V. (2001) Study and Development of Lean Burn Systems on Small 4-Stroke Gasoline Engine. Warrendale, PA: SAE International.

72. T. Morel, C. I. Rackmil, R. Keribar and M. J. Jennings (1988) Model for heat transfer and combustion in spark ignited engines and its comparison with experiments, SAE Transactions, 97, pp. 348-362. Available from: https://www.jstor.org/stable/44547379.

73. Toulson, E., Huisjen, A., Chen, X., Squibb, C., Zhu, G., Schock, H. and Attard, W. P. (2012) Visualization of propane and natural gas spark ignition and turbulent jet ignition combustion, SAE International Journal of Engines, 5 (4), pp. 1821-1835. DOI: 10.4271/2012-32-0002.

74. Toulson, E., Schock, H. J. and Attard, W. P. (2010) A Review of Pre-Chamber Initiated Jet Ignition Combustion Systems. Warrendale, PA: SAE International.

75. Toulson, E., Watson, H. C. and Attard, W. P. (2007a) The Effects of Hot and Cool EGR with Hydrogen Assisted Jet Ignition. Warrendale, PA: SAE International.

76. Toulson, E., Watson, H. C. and Attard, W. P. (2009a) Gas Assisted Jet Ignition of Ultra-Lean LPG in a Spark Ignition Engine. Warrendale, PA: SAE International.

77. Toulson, E., Watson, H. C. and Attard, W. P. (2007b) The Lean Limit and Emissions at Near-Idle for a Gasoline HAJI System with Alternative Pre-Chamber Fuels. Warrendale, PA: SAE International.

78. Toulson, E., Watson, H. C. and Attard, W. P. (2009b) Modeling Alternative Prechamber Fuels in Jet Assisted Ignition of Gasoline and LPG. Warrendale, PA: SAE International.

79. Truffin, K., Angelberger, C., Richard, S. and Pera, C. (2015) Using large-eddy simulation and multivariate analysis to understand the sources of combustion cyclic variability in a spark-ignition engine, Combustion and Flame, 162 (12), pp. 4371-4390. DOI: 10.1016/j.combustflame.2015.07.003.

80. Uyehara, O. A. (1995) Prechamber for Lean Burn for Low NOx. Warrendale, PA: SAE International.

81. Wakai, K. (1993) Effect of small hydrogen jet flame on augmentation of lean combustion. Available from: https://doi.org/10.4271/931943.

Appendix

A1 In-cylinder Pressure Sensor Specifications

Measuring Range	0-1000 bar
Overload	1000 bar
Sensitivity	1.5 pC/bar
Linearity	≤ ± 0.5%
Calibrated Ranges	0-300 bar
Natural Frequency	> 400 kHz
Acceleration sensitivity	≤ 0.0005 bar/g
Shock Resistance	≥ 2,000 g
Insulation Resistance	≥ 1*10^13 Ω
Capacitance	7 pF
Sensor operating temperature range	-40 – 350 °C
Thermal sensitivity change	≤ 4%
Load change drift	4 mbar/ms
Cyclic temperature drift	≤ ± 1.5 bar
Thermo shock error Δp	≤ ± 0.8 bar
Thread diameter	M5x0.5
Cable connection	M3x0.35
Weight	1.6 grams
Mounting torque	1.5 Nm

Table A-1 Specifications of In-cylinder Pressure Sensor AVL GO15DK Gen1 (AVL List GmbH, 2020)

A2 AVL Calcgraf Model

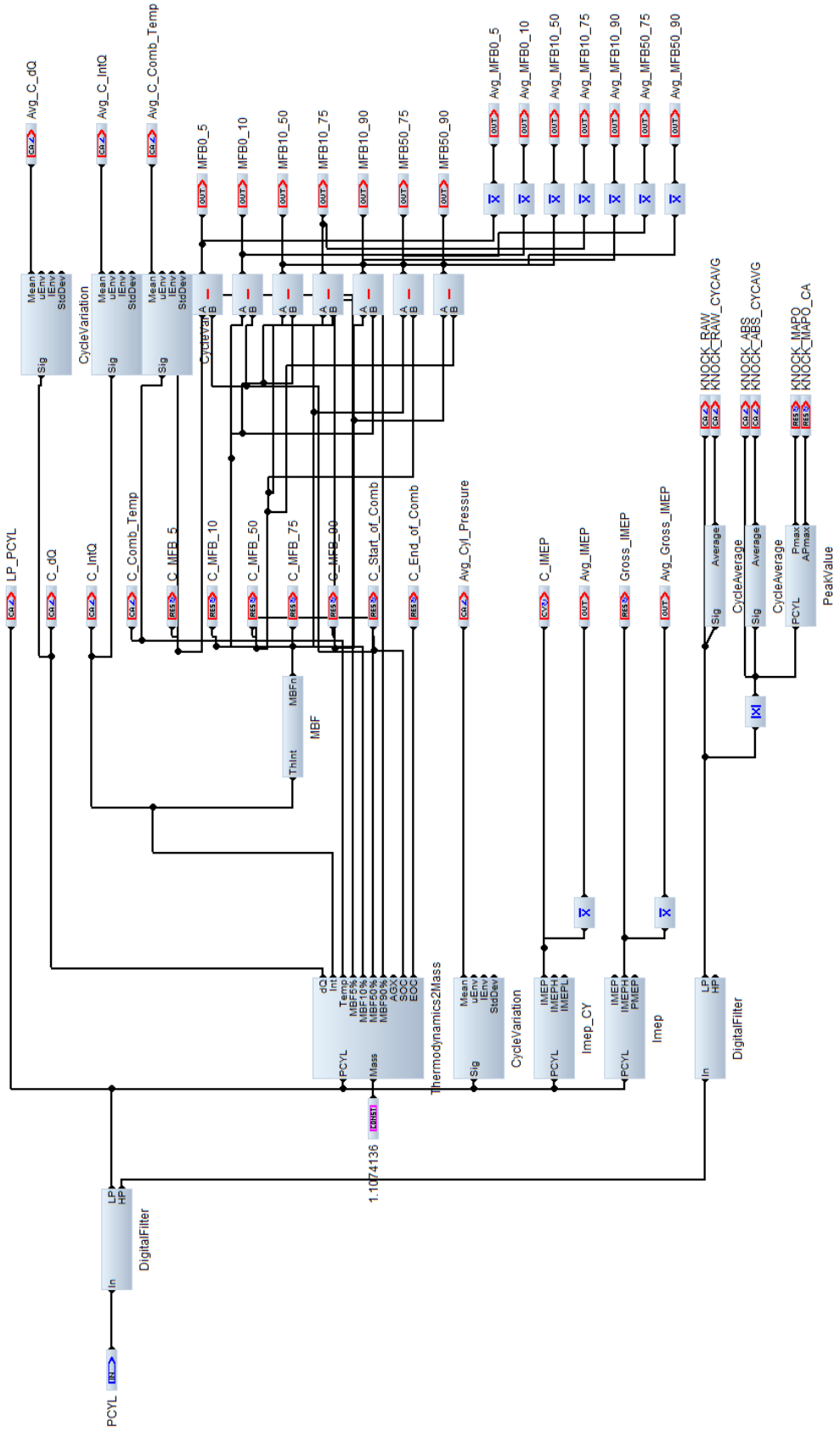

Figure A-1 AVL Calcgraf Model for Combustion Calculations

A3 Experimental Errors and Accuracy of Results

A3.1 Cyclic Temperature Drift

As the membrane of the sensor is periodically heated by the combustion in the cylinder- the local temperature at the membrane changes periodically. The change in local temperature at the membrane is exacerbated by a pre-chamber ignition system where a jet originating from the pre-chamber may be directed at the pressure sensor. The output signal of the pressure sensor thus gives an incorrect pressure value due to change of temperature. The maximum misreading within one cycle due to this thermal effect is called cyclic temperature drift or thermal shock error (AVL List GmbH, 2020). The manufacturer states that the maximum drift value of the in-cylinder pressure sensor is ± 1.5 bar as shown in Table A-1. However, these values were measured at 9 bar IMEP and 1500 rpm on a typical gasoline engine which was very different to the engine utilised in this research project and thus there may be a higher error of the maximum drift value which has not been quantified.

A3.2 Crank Position Determination Time Error

Due to high torsional oscillations at the flywheel of the single cylinder engine, a crank determination time error was observed in the areas of the missing teeth in the crank angle encoder - which was a part of the flywheel. The maximum error in calculation of gross IMEP was found to be 0.12 bar.